The Effects of Particle Size on CO_2 reduction in Packed Bed Dielectric Barrier Discharge Plasma Reactors

By:

Thomas D Butterworth

A thesis submitted in partial fulfilment of the requirements for the degree of

Doctor of Philosophy

The University of Sheffield

Faculty of Engineering

Department of Chemical and Biological Engineering

Submission Date

16th July 2015

Acknowledgments

First and foremost, I would like to thank my supervisors, Dr. Rachael Elder and Prof. Ray Allen, for believing in my abilities, supporting me, and listening to my crazy ideas. The academic freedom that you have allowed me has been both the greatest gift, and the greatest challenge I have ever received.

I owe a thank you, and possibly an apology, to Prof. Chris Hardacre at QUB, to whom I was very insistent that it would not be possible to create plasma discharges in 150 μm powders. It looks like we were both right!

I would also like to say a special thank you to Dr. Corinne Howse, who is without a doubt the best (and only) project manager I have ever had. I am very grateful for the support you have given me, especially during the last year. Good luck with the new baby! (This is also my way of making up for not signing your maternity leave card due to being at a conference)

The 4CU group is full of some fantastically talented and creative people and I am grateful to be a part of it. So thank you to all of the members of 4CU for providing me with inspiration, help, and thought provoking discussion.

Thank you to the EPSRC for the financial support, and to the EPSRC instrument loan pool. On the extremely slim chance that anyone from the EPSRC is reading this, please resurrect the loan pool. It is a very valuable service.

Thank you to all of the technicians who have helped me along the way: Oz, Mark, Usman, Stuart, Steve, Andy, Adrain. In particular I should thank Clif, who sadly passed away shortly after making my 1st generation of plasma reactor.

I would not have been able to do half of the work in my thesis without Dr. Josselin Noirel introducing me to Mathematica over 4 years ago. Thank you for your constant help and support along the way!

There is also an endless list of colleagues and friends in the department to whom I am extremely grateful, you make the university an excellent environment to work in and be a part of. In particular I have to mention Dharana, Pratik, Kay, Alison, Pelayo, Matt, and Jen who have probably listened to me ranting more than anyone else.

I owe my parents, Simon and Liz, and grandparents, Tony and Jennifer, a big thank you (and a lot of money) for their seemingly endless emotional (and financial) support. I'm sure you are probably very relieved to think I now have a paid job lined up.

Finally, I want to thank my beautiful girlfriend Ema for being the most amazing support since I met her. I really don't think I couldn't have maintained my motivation during the final months of this project without you.

Abstract

Utilisation of CO_2 emissions for production of synthetic fuels as an energy storage vector has the potential to be an economically viable mechanism to assist in the mitigation of anthropogenic climate change. Packed bed plasma reactors (PBRs) are a potential technology that could be utilised for reduction of CO_2 to CO as one of the steps in the fuel production process. Current understanding of the behavior of plasma discharges within PBRs is very poor, and the effects of many of the parameters that can be varied are still unknown.

This thesis aims to investigate the effects of particle size (180 μm to 2000 μm - random shape) of two different commonly used packing materials (Al_2O_3 and $BaTiO_3$) on the conversion of CO_2 in PBRs. The reactor behavior is observed through determination of product gas composition and plasma power consumption in order to determine CO_2 conversion and reactor efficiency. Electrical characterisation techniques are used to determine reactor burning voltage, and capacitances. These capacitances are subsequently used to quantify the occurrence of reactor partial discharging over a range of different operating conditions.

The results indicate that smaller particles (down to 180 μm) can significantly increase CO_2 conversion by up to 70%, provided that the voltage applied is sufficiently high to generate a discharge in the void spaces of the packing material. However, with decreasing particle size, the reactor burning voltage is found to increase exponentially, as well as the tendency of the reactor towards partial discharging. Consequently, there are two recommendations:

    I.   Higher electric field strengths should be used by researchers working with packed bed reactors

   II.   Reactor capacitances, including the effective dielectric capacitance, should be reported for all packed bed reactor experiments in order to determine whether partial reactor discharging behavior is occurring

1 Introduction

There is strong evidence to suggest that the average global atmospheric temperature is rising due to increasing anthropogenic emissions of greenhouse gases, particularly CO_2 from the combustion of fossil fuels. It is anticipated that that this climate change will have serious, wide ranging, and negative impacts upon our environment. The predicted humanitarian impacts are a rise in sea levels as the polar ice caps melt, as well as extreme changes to weather patterns leading to drought, famine, and disease. The increasing atmospheric concentrations of CO_2 are predicted to have a strong negative impact on ecosystems, due to both climate change and acidification of the oceans. Immediate attempts to mitigate climate change would also be economically beneficial in the long term, as imminent action is predicted to cost 1% of global gross domestic product (GDP) now, as opposed to 15 - 20% for the foreseeable future if a policy of adaptation is implemented [1].

Global energy demand is increasing, whilst simultaneously reserves of increasingly valuable fossil fuels are being consumed. Presuming that governments take action in order to avoid climate change, the future energy supply is likely to be composed of a greater proportion of renewable energy sources, coal and gas fired power stations with "carbon capture" technology, and nuclear energy. In order for the proportion of renewable energy generation to increase to a high level, the problems of intermittent supply should be addressed. One possible solution to climate change, fossil fuel consumption, and intermittent supply of renewable energy is through carbon dioxide utilisation.

It may be possible to capture CO_2 from energy generation or other industrial sources, and to convert it into synthetic fuels during off peak hours, or at times when energy supply exceeds demand. This would effectively act as a store of chemical energy. This fuel could then be used either for energy generation, or to meet the requirements of the haulage and aviation industries for liquid fuels with high energy densities that would require no adaptation to alternative, and currently undeveloped technologies.

Non-thermal plasma technology for CO_2 reduction has the potential to operate at relatively low temperatures, at atmospheric pressures, with extremely fast kinetics, high selectivities and high efficiencies. The use of non-thermal plasma for the reduction of CO_2 to CO was a popular research topic in Russia in the late 1970s to 1980s, where much of the foundation of modern CO_2 plasma chemistry was established. Recently the subject has regained its popularity as addressing the problem of climate change becomes an ever pressing concern. Packed bed plasma reactors are one of a handful of methods that have recently attracted attention for their

potential as a plasma based CO_2 utilisation technology. A small number of publications exist on the subject that have demonstrated some promising results, although significant further research is required in order to assess whether the potential of the packed bed plasma reactor can be realised. Despite the large volume of publications on the use of packed bed reactors, and their increasing prevalence in the emerging topic of plasma catalysis, they are still poorly understood due to the wide range and complexity of the parameters that define their behaviour. For these two reasons, this thesis investigates some of the important parameters that control the characteristics of packed bed reactors from the perspective of CO_2 utilisation.

1.1 Anthropogenic climate change

It is widely acknowledged by the scientific community that anthropogenic climate change caused by the emission of greenhouse gases is a significant problem. A recent study found that 97.1% of publications on the topic of climate change endorsed the position that it is caused by human activity [2]. The assessment of the Intergovernmental Panel on Climate Change (IPCC) is considered to be representative of the scientific community.

In their 2014 report [3], the IPCC carried out a thorough meta analysis on a wide range of publications that report evidence, implications, or predictions related to climate change and greenhouse gas emissions. The report offers a succinct summary of the cause of climate change, "[Human influence] is extremely likely to have been the observed cause of warming since the mid 20th century." Further to this it is stated that, "It is extremely likely that [warming since the mid 20th century] was caused by the anthropogenic increase in greenhouse gas concentrations and other anthropogenic forcings together."

The report summarises some of the impacts that have already been observed:

- The period from 1983 – 2013, was very likely to have been the warmest 30 year period in the past 800 years in the Northern Hemisphere, and likely to be the warmest 30 year period in the past 1400 years. The average global surface temperature has risen by 0.85 °C between 1880 and 2012.

- Warming of the oceans accounts for 90% of the global energy accumulation between 1971 and 2010. The average global ocean surface temperature (<75 m) has warmed at a rate of 0.11 °C per decade between 1971 and 2010.

- Oceans have experienced increased evaporation or precipitation in some areas, leading to either localised increases in salinity or freshwater respectively.

- Oceanic uptake of CO_2 emissions has caused the pH of ocean surface water to decrease by 0.1, equivalent to a 26% increase in the concentration of H^+ ions.

- From the period 1979 – 2012 the rate of decrease in arctic sea ice was in the region of 3.5 – 4.1% per decade. With the extent of the summer sea ice minimum decreasing at a rate of 9.4 – 13.6% per decade. Additionally there have been observed changes in snow cover in the Northern Hemisphere, with decreases occurring at a rate of per 1.6% and 11.7% per decade, for March and April, and June respectively. Permafrost temperatures have been observed to rise, with a decrease in the extent and thickness in some regions.
- Sea level rise is seen to be occurring at an increasing rate since the start of the 20th century. Between 1901 and 2010, average rate of sea level increase was at 1.7 mm per year, compared with a rate of 3.2 mm per year between 1993 and 2010. This is attributed to melting of arctic sea ice, glacier mass loss, ocean thermal expansion and changes in land water storage.

The 2014 IPCC report on climate change gives a number of possible projected situations based on emissions scenarios known as representative concentration pathways (RCPs). There are 4 RCP categories, RCP2.6, RCP4.5, RCP6.0 and RCP 8.5 [3].

A summary of some of the predicted changes in sea levels and average atmospheric surface temperatures is shown in Table 1.

Table 1: IPCC predictions for temperature change and sea level rise in 2100 relative to 1986 - 2005 levels of temperature, sea level and CO_2 concentrations. Data taken from [3].

Case		Temperature Change		Sea Level Rise	
Number	Description	Most Likely	Range	Most Likely	Range
RCP2.6	Emissions peak in 2010-2020 and subsequently decline	1.0	0.3 – 1.7	0.40	0.26 – 0.55
RCP4.5	Emissions peak around 2040 and subsequently decline	1.8	1.1 – 2.6	0.47	0.32 – 0.63
RCP6.0	Emissions peak around 2080 and subsequently decline	2.2	1.4 – 3.1	0.48	0.33 - 0.63
RCP8.5	Emissions rise throughout 21st century	3.7	2.6 – 4.8	0.63	0.45 – 0.82

In the IPCC's 2014 report they also predict, with varying degrees of certainty, a range of possible consequences for society, ecosystems, the environment and the economy. A summary of the IPCC's prediction from the 2007 report is shown in Figure 1.
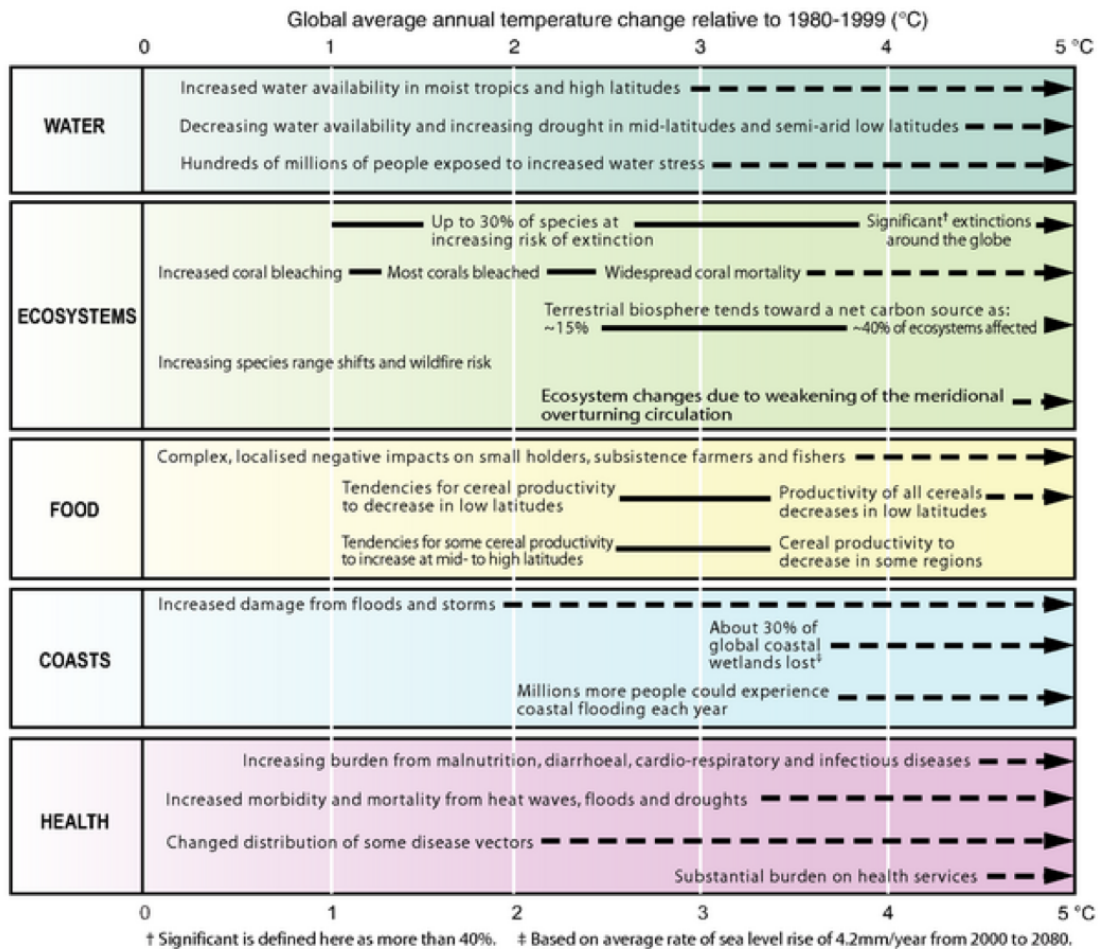
Figure 1: IPCC predictions of the impacts of climate change, based on a temperature change relative to 1980 - 1999 levels [4]. N.b. A more detailed and up to date table of predictions is given in the 2014 report, but it is too long (and too depressing) to fit into the scope of this thesis.

In order to mitigate the effects of climate change it is necessary to minimise emissions of greenhouse gases (GHGs). The 1997 Kyoto protocol [5] was the first international agreement that set out targets for reductions of GHG emissions, the target was a reduction in emissions of 5.2% from 1990 by 2008 – 2012. Although the term of the Kyoto protocol has now expired, it was agreed at the 2010 United Nations Framework Convention on Climate Change (UNFCCC), in Cancún, Mexico, that a legally binding deal to reduce emissions by all countries will be implemented by 2020, with the specifics of the deal established by 2015 at the Paris UN climate change conference [6].

Subsequently the UK government has passed the Climate Change Act 2008 [7], which stated that the UK would reduce its emissions of GHGs by 80% by 2050, and 33% by 2020. The aim of this reduction in emissions is to stabilise CO_2 concentrations at 450 – 475 ppm. The expectation is that this deal will result in an overall global average surface temperature rise of 2°C. In order to meet both national and international targets for reduction in emissions of GHGs there will not be a single solution to the problem. Multiple technologies will have to be developed for each sector

in order to resolve the problem. Primarily, this research is concerned with developing new technologies to mitigate CO_2 emissions from the energy sector.

In the UK in 2013 the energy sector was the biggest emitter of CO_2, producing 178.5 out of the 464.3 million tonnes of CO_2 (38.4%) released into the atmosphere [8]. The is similar to other global statistics for CO_2 emissions, with the global figure for the energy sector's contribution to CO_2 emissions in 2001 standing at 37.2% of a total 28 billion tonnes of CO_2. Global energy consumption is predicted to increase by 84%, from 19.1 trillion kWh in 2008 to 35.2 trillion kWh in 2035. The Department of Energy and Climate Change (DECC) predict that the UK's net electricity consumption is going to show only a marginal increase by 2030, to 31 million tonnes of oil equivalent (Mtoe), when compared to 2010 levels of 28 Mtoe. However, this prediction is based on the assumption that rising energy prices and imposed constraints on efficiency of energy use will limit energy consumption. Both the DECC and the U. S. Energy Information Administration (USEIA) predict increases in the consumption of fossil fuels and consequently production of CO_2, with the global outlook illustrated by Figure 2.
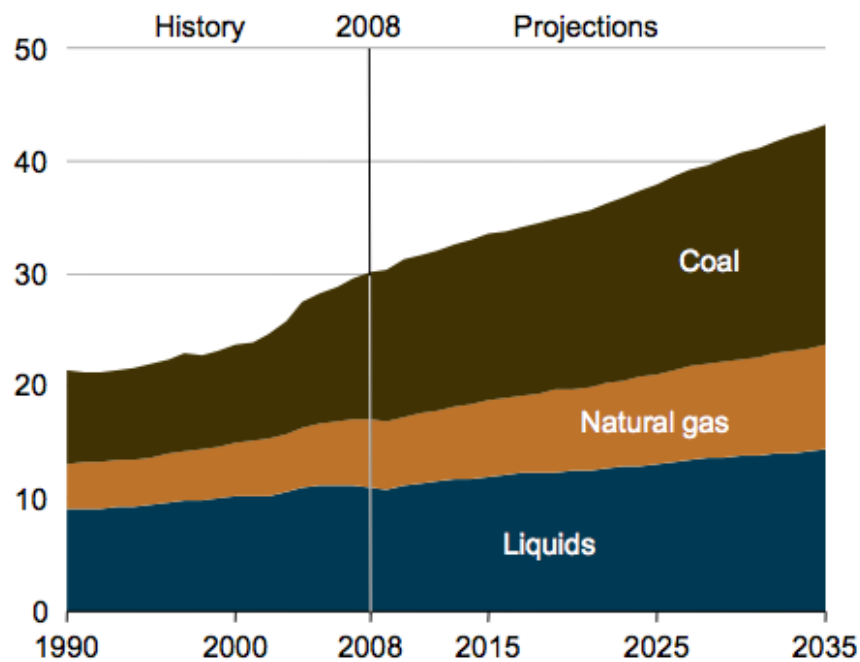
Figure 2: Projected emissions of CO_2 (Given in billions of tonnes) from fossil fuels by the energy industry [9].

The requirement to significantly reduce emissions of CO_2 presents a significant challenge for science and engineering. Projected increases in energy demand driven by a desire for "cheap" fossil fuel energy sources have the potential to release unprecedented levels of CO_2 into the atmosphere that will create environmental, humanitarian, and economic costs that we cannot afford.

1.2 Carbon Capture and Utilisation

One of the assumptions made by the DECC in their projections of energy generation is that Carbon dioxide Capture and Storage (CCS) will be a commercially available technology by 2025. At the point when these projections were made CCS as a concept was, from the perspective of politics and the media, very much *in vogue*. An alternative, yet inherently associated technology, Carbon dioxide Capture and Utilisation (CCU) could be economically advantageous compared with CCS. The purpose of CCU is to convert CO_2 into value added products. Due to the massive amounts of CO_2 emitted annually, an idealistic product produced using a CCU process must have both a high demand and high economic value. Additionally the CCU process itself can only be economically viable by having a good conversion of CO_2 to products, at a high thermodynamic efficiency with the capacity to operate with a large throughput.

CO_2 is thermodynamically a very stable molecule. The image in Figure 3 shows the enthalpy of formation of a molecule compared with the carbon oxidation state for a number of common carbon based molecules. Figure 3 shows that CO_2 is the most oxidised form of carbon, with a relatively high enthalpy of formation. To convert CO_2 to any of the other compounds shown in Figure 3 requires a net energy input.

Figure 3: Enthalpy of formation and carbon oxidation state for CO_2 and some other common carbon based molecules [10]

Although the high energy input required to convert CO_2 to value added products appears to be disadvantageous, if the products are considered to be a store of chemical energy this paradigm can be reversed. T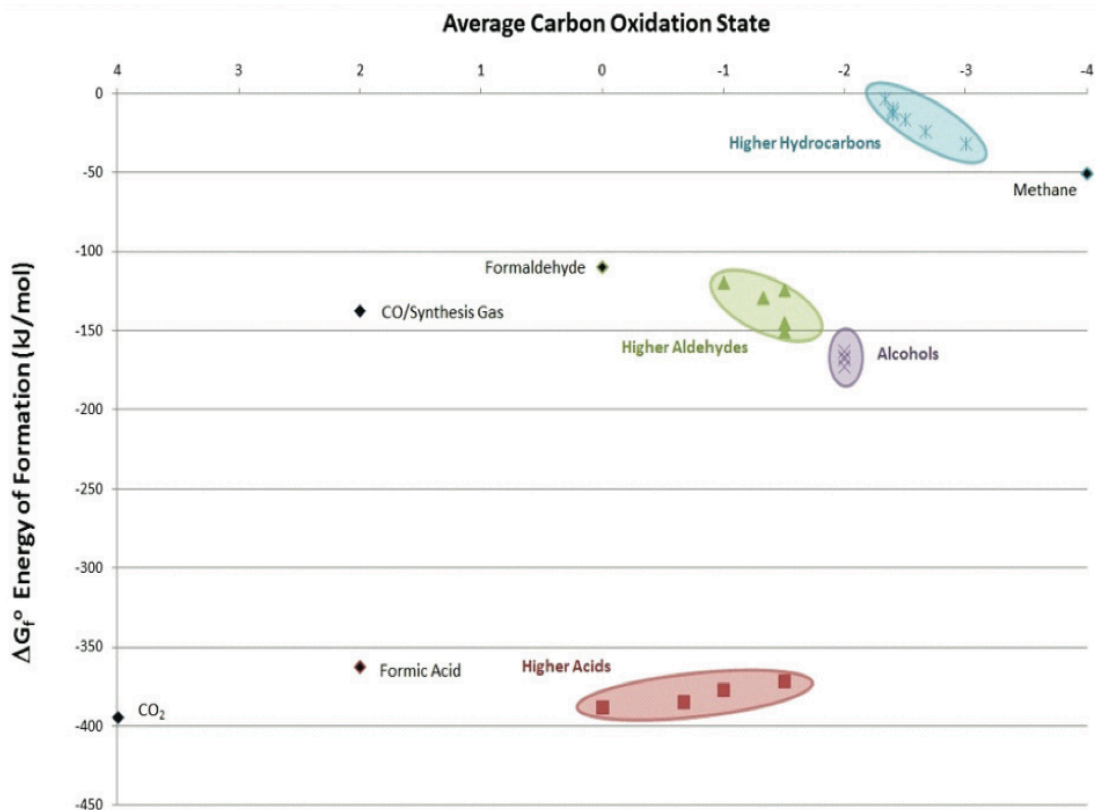herefore, one of the most important possible pathways for CCU is the production of synthetic fuels from CO_2 as a method of energy storage. Hydrocarbon fuels are high value, high demand products that are high energy density stores of chemical energy. Energy storage however only becomes economically viable under 3 circumstances:

1. When supply of energy is greater than demand, for example at night time
2. When the electricity supply is far from the area of demand, such that electricity transmission by power lines leads to very large energy losses
3. Limitations caused by insufficient energy densities of batteries imposes a limit on range and power of haulage and aviation, so chemical fuels are still required

Intermediate term (hours to days) energy storage is considered to be an important factor for increasing future renewable energy generation, as it would allow renewable energy supply to exceed demand without as much energy being wasted. This is a strong economic and environmental argument for development of energy storage techniques. Due to their inherent connection, the problem of energy storage can be coupled with the need to develop low carbon transportation and haulage methods. The commonly proposed solutions for low carbon transportation energy sources are batteries and hydrogen fuel cells. Batteries have a high round trip efficiency, 85 – 95% for Li-ion batteries compared with 64% for a hydrogen PEM fuel cells [10]. However batteries with current technology are expensive, have a limited life span, uncertain safety, and have a low energy density.

Range	Diesel	100% electric with Li-ion battery
500 km 7.5-tonne distribution operations	90 l 76 kg	2.3 m³ 4.7 t
3000 km 44-tonne long distance operations	990 l 836 kg	26 m³ 52 t

Calculation: consumption 20 l/100 km /33 l/100 km, efficiency: diesel engine = 40%, electronic motor = 80%, energy content diesel = 11.8 kWh/kg
Li-ion battery = 0.19 kWh/kg, weight diesel = 0.845 kg/l, Li-ion battery = 2kg/l

Figure 4: A comparison of conventional diesel and Li-ion battery powered methods for heavy goods vehicles. Image taken from [10].

Hydrogen fuel cells are limited by the expense of installing new hydrogen storage and distribution systems, the low energy density of hydrogen, and the inherent low safety of storing dense, pressurized stores of hydrogen. Hydrocarbon fuels, on the other hand, already have a very well established infrastructure, and have energy densities that are many times higher than hydrogen and batteries. Figure 4 illustrates this by comparing the weight and volume occupied by Li-ion batteries and diesel fuel for heavy goods vehicles.

Economic viability of converting CO_2 into synthetic hydrocarbon fuels is dependent upon the cost of extracting and processing naturally occurring hydrocarbon fuels, such as oil and gas. As the cost of extracting hydrocarbons increases as a result of difficult to access and remote fossil fuels supplies, combined with public pressure over the safety of shale gas fracking and Arctic oil exploration, CO_2 utilisation for the production of hydrocarbons becomes increasingly economically viable. The DECC have published a document that reviews and predicts a number of scenarios for future oil prices. The 2030 case is based on the 2011 average oil price being $110 per barrel, with the middle scenario projected cost being $129 per barrel. The predictions for the low and high cost scenarios are $75 and $170 per barrel respectively. It is important to acknowledge that these cost projections are based to some extent on the development of alternative energy and fuel sources. The low cost scenario is based upon climate change policy driving investment in alternative energy sources and reduction of CO_2 emissions, which is in itself the purpose of this research.

There are also strong economic arguments for reducing CO_2 emissions as soon as possible in order to reduce future costs resulting from the consequences of climate change. A number of publications have predicted the long term economic and environmental consequences of climate change, including The Stern Review [1], published for the UK government, and The Garnaut Climate Change Review [11]. Both reports calculate that the cost of operating with a "business as usual" model, i.e. not trying to reduce CO_2 emissions, have much greater long term financial consequences than trying to reduce emissions now. The Stern Review [1] estimates that the cost of reducing emissions sufficiently so that CO_2 concentration will be limited to a 550 ppm target value will cost 1% of GDP now, whilst the cost of inaction on climate change will cost 5 – 20% of GDP each year for the forseeable future.

1.3 Fuel from CO_2

It is clear that immediate action on the reduction of CO_2 emissions is of vital importance for future economic and environmental stability. It is likely that carbon neutral synthetic hydrocarbons will be important in the transition to a low carbon economy. Hydrocarbons clearly cannot be synthesized from CO_2 alone, as a source of hydrogen atoms is required. The idyllic

source of these hydrogen atoms should be environmentally benign, economically viable and must have very low associated emissions of CO_2. There has been an abundance of research previously carried out into using methane as a co-reactant with CO_2 to produce synthesis gas (A.k.a. "Syngas" – a mix of H_2 and CO used in the production of chemicals and liquid fuels), a process known as "dry reforming". Dry reforming of methane has been extensively studied with noble metal catalysts [12], and with various plasma technology based methods including catalytic systems [13]. Reforming of methane however requires extraction and utilization of hydrocarbons, so the outcome is overall net CO_2 emissions and is therefore neither environmentally benign nor sustainable. As an alternative source of hydrogen for the production of hydrocarbons, water may be a viable alternative to methane. It is one of the most abundant molecules on earth, and so does not require any extraction. One of the more promising methods for clean hydrogen production is via electrolysis of water, using either low temperature polymer electrolyte membranes (PEM) [14] or in high temperature (> 700°C) solid oxide electrolysis cells (SOECs), coupled with simultaneous CO_2 reduction [15]. SOECs are the mature technology for CO_2 reduction to CO, however they are limited by the high cost of cells, high temperature of operation (making them reliant on very high temperature sources of heat such as nuclear power or steel production), and the long-term durability of the cells leading to a significant decrease in performance and efficiency.

1.4 Plasma CO_2 utilisation

Plasma is often defined as the "4th state of matter" having a higher enthalpy and entropy than solids, liquids and gases. Plasma is an ionised gas, i.e. electrons are dissociated from gaseous species forming positive (ions) and negative (ions and electrons) charge carriers. Plasma can be broadly categorised into 2 distinct types, fully ionised and weakly ionised plasmas, where "weakly ionised" plasma is defined as less than 1% ionisation. Weakly ionised plasmas are used for plasma chemistry, as their temperature is relatively low, typically less than about 3,000 K. Weakly ionised plasmas can be further sub-categorised into another 2 types, thermal (known as equilibrium) and non-thermal (or non-equilibrium).

In plasma, arguably the most important species is the electron as it can be used to control the behavior of the plasma, and ultimately how the input energy to the plasma is utilised. A thermal plasma is characterised by the electrons and heavier species being in a thermal equilibrium, i.e. having equal energy or temperature. Free electrons gain energy from the electric field during their mean free path, defined as the average distance between collisions with other particles. Individual collisions between energetic electrons and heavy particles cause the electrons to lose only a small fraction of their energy due to the relatively much higher mass of the heavy

particles. This means that there needs to be sufficient time and energy for thermal equilibrium to be established. If the electron temperature is significantly greater than the temperature of the heavy particles, then the plasma is non-thermal. Thermal and non-thermal plasmas typically have different applications, with thermal plasmas being more powerful, and non-thermal being more selective for chemical processes. Plasma technology becomes viable under 2 circumstances:

1. The reactions are possible, but kinetically hindered without a plasma
2. Reactions are impossible due to an extreme chemical equilibrium

Hence non-thermal plasma processes are of the greatest interest to this research. Given the uncertainty of the future of nuclear energy, and the possible advantages plasma chemistry has to offer, the development of a method to reduce CO_2 by plasma chemistry is justified.

One of the more promising non-thermal plasma technologies for CO_2 reduction is the packed bed dielectric barrier discharge (DBD) reactor. These reactors have demonstrated some promising experimental results showing good CO_2 conversion and process efficiency under operation with moderate reaction conditions (P_{atm} and $25 < T (°C) < 150$) that would be favourable to industry. Therefore the reactor type studied in this thesis is the packed bed DBD applied to the problem of CO_2 reduction.

1.5 Research Aim

Whilst carrying out early experimental work for this thesis, and subsequently re-reviewing the available literature on packed bed reactors, it became apparent that the understanding of the relationship between particle size in a packed bed reactor and the behavior of the plasma is currently very poorly understood. Many publications have investigated the usage of packing materials, but none have endeavored to truly understand how such a fundamental property such as particle size impacts the plasma chemistry or the physical nature of the plasma discharge. With this in mind the aim of this thesis is to firstly, observe the changes that occur to a plasma chemical process when particle size is varied; and secondly, to try to understand the cause of these changes.

1.6 Thesis Structure

Chapter 2 introduces the theory of plasma chemistry that is relevant to the content of this thesis, such as the theory of electrical breakdown, important concepts in plasma chemistry, and the mechanisms of formation and loss of reactive species. Three different types of plasma reactors are introduced, the corona discharge, the dielectric barrier discharge (DBD), and the packed bed reactor, and the mechanisms of operation of these reactors are discussed. A particular emphasis is placed on operation and mechanisms of packed bed reactors.

Chapter 3 is the literature review, and presents the latest knowledge regarding dissociation mechanisms of CO_2 in plasmas, as well as a critical review of CO_2 dissociation in corona reactors, DBDs, and packed bed reactors. Methods of analysing electrical characteristics of reactors are also reviewed with a view to implementation in the experimental section of the thesis.

Chapter 4 presents the experimental method and set-up, including development of the experiment, and methods for gas and reactor electrical analysis, and analysis of the reactor packing materials.

Chapter 5 shows the first set of experimental results – measurements of CO_2 conversion, power consumption, reactor operating efficiency, and temperature. These results are analysed and a number of critical research questions are posed.

Chapter 6 features further analysis and discussion of the results obtained in chapter 6, using further data obtained from electrical characterisation of the reactor in order to assist the analysis, and to diagnose the behavior of the reactor.

Chapter 7 presents the summary and conclusions of the thesis work

Chapter 8 gives suggestions for future work

Appendices and references follow

2 Theory of Plasma Chemistry

2.1 Theory Introduction

The purpose of this section is to present the theory of plasma chemistry that is essential to understand the content of this thesis. As plasma chemistry is a very broad and complex subject, this aim of this chapter is to reduce the wide scope presented by the available textbooks and literature on plasma chemistry in order to produce a succinct guide to packed bed dielectric barrier discharges. Fundamental plasma theory such as the mechanism of electrical breakdown, electron reactions and molecular processes are explained first. Subsequently, this theory is related to three different, but related, types of plasma reactor: the corona discharge, the DBD, and the packed bed DBD. Although carbon dioxide is, to a certain extent, considered throughout this section, the chemistry and related literature is dealt with primarily in the review in chapter 3.

2.1.1 Catalysis and non-thermal plasma

One of the benefits of the packed bed reactor is the possibility to add heterogeneous catalytic materials into the reactor. The field of plasma catalysis is very much in its infancy, hence there are many unknowns about how the behavior of a plasma catalytic system deviates from a more traditional thermal or pressure activated catalyst system. Non-thermal plasma systems are characterised by high populations of chemically reactive species, such as radicals, ions, an excited states (discussed further in section 2.2) that are able to participate in reactions that would typically not occur in a more conventional chemical reactor. This presents a challenge to current understanding of catalytic systems and the current models of catalyst reaction mechanisms. The two most commonly referred to catalyst models are the Langmuir-Hinshelwood and Eley-Rideal mechanisms. Both of these mechanisms are induced by the interactions of neutral, non-excited species with a catalyst surface.

In plasma catalysis it is believed that the catalyst packed reactor becomes activated in some way by the presence of the plasma, this may occur by:

- Inducing the formation of reactive species in the gaseous phase
- Activation of the catalyst itself through temporarily inducing enhanced surface reactivity
- A combination of both mechanisms

The logical outcome of this assumption is that the mechanism of plasma catalysis has at least one additional step where excitation of either the catalyst surface or gaseous species occurs. Hence the possibility of alternative reaction mechanisms should be considered, which will consequently lead to the requirement to identify new catalysts that are specifically developed for the requirements of plasma chemistry.

Another outcome of the "plasma activated catalysts" assumption, and the outcome that is more relevant to the work of this thesis, is related to the lifetimes of the excited and reactive states found in plasmas. Some of the excited species found in plasma (such as vibrationally and electronically excited states, discussed further in sections 2.2.1 - 2.2.7) can very quickly relax down to lower energy states, over time frames in the region of picoseconds to nanoseconds. Therefore, if the plasma-catalytic effects are due to excited species, it is essential that these species are able to interact with catalytic surfaces before relaxation occurs. One of the key paradigms of catalytic systems is the requirement for a high surface area to volume ratio of the catalyst. This paradigm becomes even more important in a plasma catalytic system due to the short species lifetimes, meaning that the area of the gas-plasma interface should be maximised. Consequently, this implies that small, tightly packed catalyst particles would be optimal for a plasma catalytic system. However, as predicted by Paschen's law (discussed further in section 2.1.3), small particle sizes are likely to inhibit the initiation of electrical breakdowns in the void spaces of the packing if an insufficient electric field strength is applied. Therefore, there is a balance to be achieved between the high surface area to volume ratio required for optimal performance of the catalytic system, and the constraints on minimum packed bed void size predicted by Paschen's law.

2.1.2 Initiation of electrical breakdown

Typically, gases are considered to be good electrical insulators due to the extremely low concentration of unbound electrons in the gas. If a continuous DC electric field is applied to the gas, any free electrons (That originate from external sources, e.g. background ionising radiation, photo ionization, etc.) are accelerated in the direction of the anode. If, whilst the electron is being accelerated, it gains sufficient kinetic energy before the end of its free path, it will cause an ionisation event in the next molecule it collides with, generating a further free electron. Although there are a number of possible ionisation reactions, the most common is shown in Equation 1, known as direct electron impact ionisation. It is typically the mechanism by which non-thermal plasma discharges are initiated:

$$e + A \rightarrow 2e + A^+$$
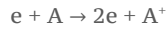
Equation 1

The original electron, and the now liberated second electron are again accelerated by the electric field and the process continues creating an avalanche. Positive ions generated by ionisation drift back towards the cathode, and upon collision with the cathode can generate more electrons by secondary electron emission. This mechanism is known as the Townsend breakdown mechanism, and is illustrated by Figure 5.
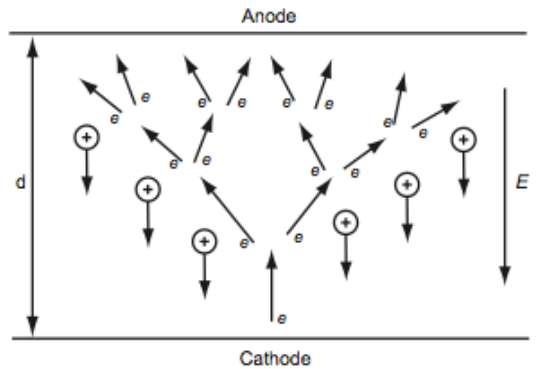
Figure 5: Townsend mechanism of electrical breakdown, showing the formation of an electron avalanche (Image taken from [16])

A stronger electric field (i.e. greater potential difference) accelerates electrons at a faster rate, giving it more energy per unit length travelled than a weak field. If the electron is travelling in a lower pressure gas, or a gas with a smaller molecular size it will have a longer mean free path (defined as the average distance between collisions) allowing it to gain more energy before its next collision. Noble gases have the highest ionisation energies of any group in the periodic table, for example Helium's is 24.6 eV, and Argon's is 15.8 eV (Compared with CO_2 at 13.8 eV). This implies that noble gases would be the most difficult gases to ionise in plasmas, however they also have the longest mean free path due to their small size, and also the impossibility of an electron collision at low energy leading to internal molecular processes (Such as vibrational excitation, discussed in section 2.2.2). As a result of this noble gases tend to be relatively easy to ionise, and consequently the addition of noble gases to a gas mixture can effectively reduce the breakdown voltage of a gas, increase the electron density and average electron energy and thereby (along with other mechanisms) enhance plasma-chemical reactions.

2.1.3 Paschen's Law

Paschen's law relates the minimum breakdown voltage of a gas to the electrode spacing and system pressure in a pair of parallel electrodes subjected to a constant DC voltage. Figure 6 shows theoretical Paschen curves for CO_2 and argon at atmospheric pressure.

It can be calculated that the mean free path of an electron in argon at atmospheric pressure is approximately 2.7 µm.[1] From examining the Paschen curve in Figure 6, it can be seen that for argon at electrode spacings less than 13.7 µm (a point known as the Paschen minimum) that the breakdown voltage begins to increase very rapidly, before approaching infinity below about 5.1 µm. This is due to the electrode spacing approaching the size of the mean free path of the electron, i.e. 2.7 µm compared with 5.1 µm. The electric field strength becomes infinitely large for multiple ionising electron collisions to occur over the length of the electrode spacing as electron molecule collisions become increasingly rare. To the right of the Paschen minimum, breakdown voltage of the gas increases due to electron collisions becoming increasingly common, and consequently not being able to gain sufficient energy between collisions to reach the first ionisation energy.
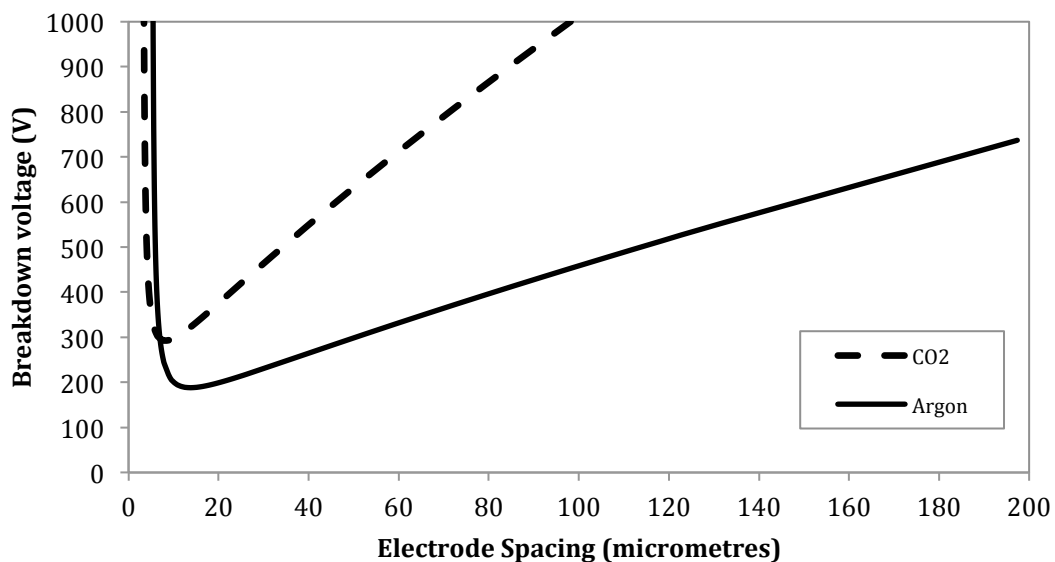
Figure 6: Theoretical Paschen curves for CO_2 and argon at atmospheric pressure

The theoretical Paschen curves shown in Figure 6 are based on the Townsend breakdown criteria, shown in Equation 2. If the value of the terms on the left hand side of the equation are greater than 1, the discharge becomes self sustaining.

$$\gamma\left[\exp(\alpha d)-1\right]>1$$

Equation 2

The plots in Figure 6 correspond to the minimum breakdown voltage at any given electrode spacing (at atmospheric pressure) for which the Townsend breakdown criteria is satisfied for the

---

[1] The number of argon atoms per cm^3 = Avogadro's number ÷ Molecular weight of argon × Density of argon
= 6.023e23 ÷ 40 × 1.662e-3 = 2.5e19 atoms/cm^3
Based on the hard sphere model, the radius of an argon atom is 70 pm, giving a cross sectional area of ~1.5e-16 cm^2.
Therefore the mean free path of an electron is 1/(1.5e-16×2.5e19) = 2.7 µm

specified gas. In Equation 2 the symbols α and γ are the Townsend ionization coefficients, and d is the electrode spacing. The primary Townsend ionization coefficient, α, is the number of ionization events per electron generated per unit length along an electric field. The tertiary Townsend coefficient, γ, is related to the number of electrons extracted per positive ion colliding with the cathode. The value for γ used to produce the Paschen curves shown in Figure 6 is 0.01, and is a representative approximation of the typical values that can be expected from a copper cathode with argon gas [17]. Values for α can be calculated for a gas using the semi-empirical relationship shown in Equation 3:

$$\frac{\alpha}{p} = A\exp\left(-\frac{B}{E/p}\right)$$

Equation 3

where A and B are constants for any given gas. E is the electric field and p is the pressure. The parameter E/p (also observed as E/ n_0, where n_0 is the number of particles) is known as the reduced electric field. The values of A and B used for argon and CO_2 are shown in Table 2:

Table 2: Values for A and B for calculation of semi-empirical Townsend coefficient, α. Taken from [16].

	Argon	CO$_2$
A, $\dfrac{1}{cm\cdot Torr}$	12	20
B, $\dfrac{v}{cm\cdot Torr}$	180	466

From Figure 6 it can be seen that the theoretical minimum breakdown voltage for CO_2 is approximately 1.5 times larger than for argon, a similar trend also applies for all points to the right of the Paschen minimum.

It is expected that CO_2 diluted with different concentrations of argon will change the breakdown potential of the gas. The Paschen curve is a consequence of electron transport properties in a relatively uniform electric field, with well defined gas properties. In a packed bed reactor, the electric field and electron transport properties will be non-uniform due to dielectric effects, switching electric fields, and variations in local gas composition. This will affect the localised gas breakdown voltage, and this will change with different particle sizes (and shapes), applied potential difference, gas composition and packing materials.

2.1.4 Electron energy distribution

The electron is the medium by which the majority of energy is transferred into the plasma. Free electrons generated by ionization reactions are accelerated by the electric field accumulating kinetic energy. However, the electric field in the plasma is inhomogeneous, and the free path of electrons varies, consequently electrons have a distribution of energies. The energy of an electron is very important, as the energy of an incident electron during a collision with another species dictates the outcome of the interaction. A commonly referred to parameter in plasma chemistry is therefore the electron energy distribution function (EEDF). The EEDF of a non-thermal plasma typically shows a strong negative exponential distribution and has a significant effect on plasma chemical reactions rates.

The EEDF is strongly dependent upon gas composition. Molecular gases, such as CO_2, allow the possibility of vibrational excitation reactions that occur at relatively low energy levels (about 1-2 eV), where as monatomic gases do not have this possibility. Consequently the EEDF in each gas under the same applied electric field would be very different.

Experimental determination of the EEDF is difficult, particularly for non-thermal plasmas, so quite often ideal statistical distributions are used as approximations, for example a Maxwellian or Druyvesteyn distribution as shown in Figure 7.
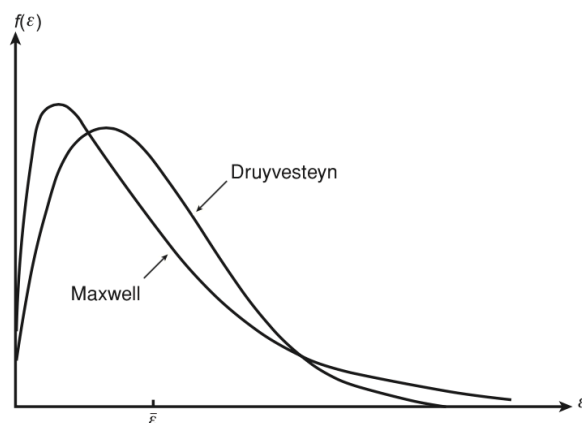
Figure 7: Maxwellian and Druyvesteyn distributions of EEDF, with electron energy, ε, and EEDF, f(ε). The 2 distributions have the same mean electron energy, indicated by $\bar{\varepsilon}$. [16]

The importance of the EEDF can be appreciated when it is compared to the possible range of interactions of an electron with a species over a range of energies. Figure 8 and Figure 9 show the electron interaction cross sectional data for CO_2 and argon. The EEDF of a plasma discharge and the cross sections of the gaseous species present in the discharge are inherently co-dependent upon each other. Further explanation of the possible reactions that can be induced by these electron collisions is given in section 2.2.

The cross section of a species can be considered as an imaginary area that depends upon incident electron energy. If that electron is then to pass through that imaginary cross sectional area at the end of its mean free path, the reaction will occur. The probability of a reaction occurring can be calculated by dividing the cross section of the reaction of interest at a specified electron energy by the total of all reaction cross sections for the species at that energy.
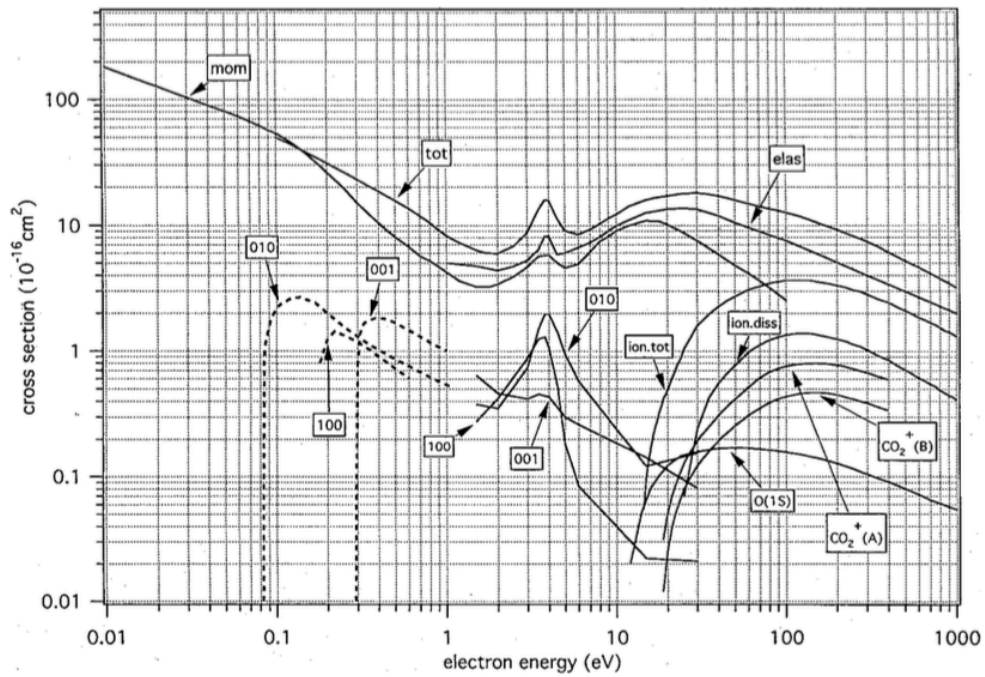
Figure 8: Electron interaction cross sections for CO_2. At any given electron energy, upon an electron passing through the "cross section" of a CO_2 molecule a reaction will take place. The probability of the reaction that will take place is determined by taking the reaction cross section at the specified electron energy, and dividing by the sum of all reaction cross sections at that energy. The cross sections in the graph lead to the the following possible reactions: momentum transfer (mom), elastic scattering (elas), vibrational excitation (0's), ionisation (ion tot & ion diss), and electronic excitation. These reactions are explained in further detail in section 2.2.1 [18]

24
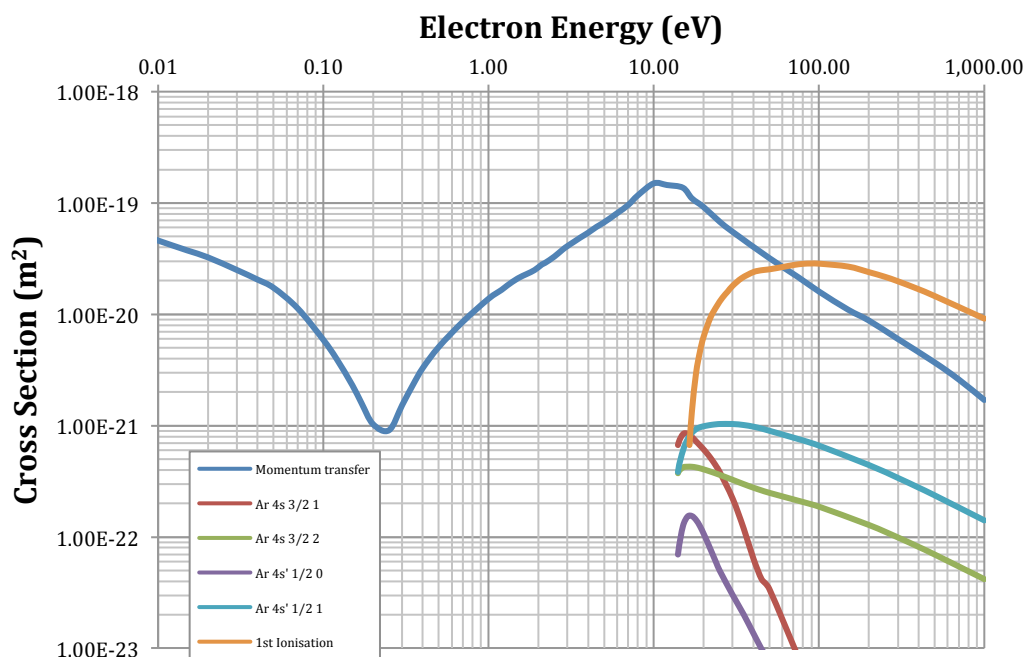
Electron Energy (eV)

Figure 9: Electron interaction cross sections for argon. This graph shows momentum transfer, electronic excitation and 1st ionisation energy. Note that vibrational excitation reactions are not possible in argon as it is a monatomic gas. The very large decrease in cross section between 0.1 and 1 eV allows electron to more easily reach the higher energies required for ionization in argon compared to CO_2. Note that a large number of lower probability electronic excitation reactions are not included in this graph, all of which have a threshold energy greater than 12.9 eV. This data is taken from [19] using the LxCat database at lxcat.net.

2.2 Plasma reaction chemistry

There are a wide range of possible reactions that can take place within a plasma system. Due to the large number of different possible reactions, it is important to be aware of all of them, but for this review it is only necessary to understand the mechanisms behind some of the reactions. Some of the range of possible reactions are listed below, whilst the reactions that are considered to be of greater importance for this work are discussed further in sections 2.2.2 to 2.2.7. In the following list, *A* and *B* represent atoms of different species, whilst A_2 and B_2 represent molecules. Electrons are represented by e, *M* is a temporary collision partner, *S* is a solid surface, an asterix (*) represents and excited species, and charged particles are indicated by either $^+$ or $^-$. It is easy to become preoccupied with the significance of a particular set of reactions whilst ignoring others, a problem that appears to be rife in the plasma modeling community. An understanding of the possible reactions mechanisms can be useful to pose hypotheses concerning the behavior of a plasma system, so some brief explanation of each reaction is given as well as some idea of how it contributes to the chemistry of the plasma. However, due to the complexity of the system the reality is that the contribution of each reaction to the overall chemistry cannot be determined without a combination of accurate analytical techniques accompanied by a detailed and

representative model. Please note, many plasma chemical reactions are included, but the list is not exhaustive.

1. Electron – Molecule reactions

- Excitation: Excitation reactions include all forms of molecular and atomic excitation (Vibrational, electronic, etc) and are responsible for the majority of chemistry that takes place within a plasma. They are discussed further in sections 2.2.2 & 2.2.3.

$$e + A_2 \rightarrow A_2^* + e$$
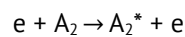
- Dissociation by direct electron impact: This is dissociation of a molecule through one collision with an electron. There are a number of possible mechanisms for this, all of which occur via electronic excitation.

$$e + A_2 \rightarrow 2A + e$$
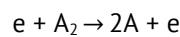
- Electron attachment: Can have a significant role in electron losses when electron energy is not sufficiently high for dissociative attachment, and the pressure is above 0.1 atm. Typically this is a 3 body process involving the excitation of a 3rd reaction partner.

$$e + A_2 \rightarrow A_2^-$$
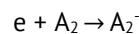
- Dissociative attachment: This mechanism has a very specific electron energy requirement, for CO_2 and O_2 the threshold is ~ 2 eV, and CO is ~ 6.5 eV.

$$e + A_2 \rightarrow A^- + A$$
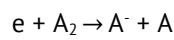
- Ionisation: This is discussed in section 2.1.2.

$$e + A_2 \rightarrow A_2^+ + 2e$$
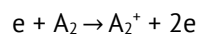
- Dissociation ionization: This mechanism only occurs when electron energy is relatively high and substantially exceeds the ionization potential of the molecule, meaning that dissociative ionization is one of the less common plasma processes.

$$e + A_2 \rightarrow A^+ + A + 2e$$
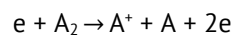
- Recombination: These reactions are exothermic and typically have no activation energy. They energy emitted can lead to dissociation, radiation emission, or the transfer of energy to a 3rd body electron.

$$e + A_2^+ \rightarrow A_2$$
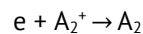
- Electron impact detachment: This process is very similar to to ionization by direct electron impact, and is important for plasma with a high level of ionization. However it can occur at lower incident electron energies than ionization reactions, with cross sections being very high for electron energies ~ 10eV.

$$e + A_2^- \rightarrow A_2 + 2e$$
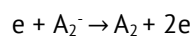
2. Atom – Ion – Molecule reactions

- Penning ionization: This process takes place when the electronic excitation of a metastable species exceeds the ionization potential of another atom. For example in the case of argon and CO_2, Ar has multiple electronic excitation levels with relatively high cross sections that exceed the ionization potential of CO_2. This process can have very large cross sections, and can therefore be a significant contribution to ionization in mixed gases.

$$M^* + A \rightarrow A^+ + M + e^-$$
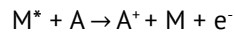
- Penning dissociation: This process occurs by a similar mechanism to penning ionization, but leads to the dissociation of a molecule rather than ionization.

$$M^* + A_2 \rightarrow 2A + M$$
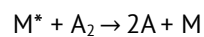
- Charge Transfer: The exchange of an electron to / from a positive / negative ion and a neutral. The cross section for these reactions are large.

$$A^{+/-} + B \rightarrow A + B^{+/-}$$
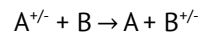
- Ion Recombination: Losses of charged particles are predominantly due to ion – ion recombination. At atmospheric pressure the mechanism typically proceeds by a three body process , and typically has a very fast reaction rate.

$$A^+ + B^- \rightarrow A + B^*$$
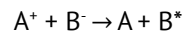
- Collisional Detachment

$$M + A_2^- \rightarrow A_2 + M + e$$
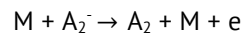
- Associative detachment: An important mechanism in non-thermal discharges, typically has quite high rate coeffecients. In electronegative gases, such as CO_2, associative electron detachment can be much faster than ion-ion recombination [20].

$$A^- + B \rightarrow AB + e$$

- Neutral Recombination:

$$A + B + M \rightarrow AB + M$$

- Synthesis:

$$A + B \rightarrow AB$$

$$A^* + B \rightarrow AB$$
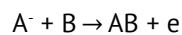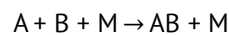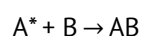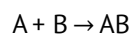
3. Heterogeneous reactions – These may be of particular importance in plasma catalysis, although the associated mechanisms are currently not known. Further discussion of plasma catalysis is given in section 2.1.1.

- Neutral Recombination

$$S\text{-}A + A \rightarrow S + A_2$$
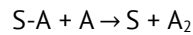
- Metastable De-excitation

$$S + M^* \rightarrow S + M + h\nu$$
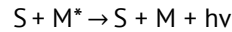
- Neutral Abstraction

$$S\text{-}B + A \rightarrow S + AB$$

- Sputtering

$$S\text{-}B + M^* \rightarrow S^+ + B + M$$
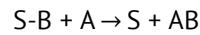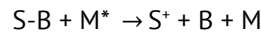
2.2.1 Reactions of excited species

Excited atoms and molecules play a significant role in plasma chemistry, with a large proportion of electron-molecule and electron-atom collisions leading to the formation of excited species over a wide range of electron energies. Collisions between increasingly energetic electrons and neutral particles can cause excitation of rotational, translational, vibrational and electronic excitation modes in an atom or molecule. Rotational excitation peaks at about 0.1 eV in most species, with values reaching as high as $10^{-16}\,cm^2$. Rotational and translational excitation does not lead to plasma chemical reactions taking place, and effectively causes the gas temperature to increase. Results from modeling of CO_2 plasmas suggest that the greatest proportion of electron energy is transferred to vibrational and electronic excitation, hence they are considered at greater length [21].

2.2.2 Vibrational excitation of molecules by electron impact

Vibrational excitation is one of the most important processes when considering molecular non-thermal plasma chemical processes. This is for two important reasons; firstly, reactions from vibrationally excited molecules contribute significantly to the kinetics of plasma chemistry, and secondly, a very large proportion of energy between electrons and molecules is transferred to modes of vibrational excitation. There are 3 significant modes of vibrational excitation in tri-atomic molecules, such as CO_2 and H_2O, shown in Figure 10: Symmetric (v1), bending (v2) and asymmetric (v3).

The notation used to describe the modes of vibration is given in the form:

$$(n_{v1}, n_{v2}, n_{v3})$$

Where n is an integer corresponding to the discrete energy level occupied in that specific mode of excitation, with the ground state n=0, and each subsequent energy level being given 1, 2, 3... etc. For example the 1st asymmetric bending mode would be written as (001). If a molecule increases or decreases in energy between one of its adjacent discrete energy levels, this is known as a one quantum change in energy. Similarly multiple changes in energy levels are known as multi-quantum energy change. This terminology is applicable to other types of excitation with discrete energy levels, for example electronic excitation.

Vibrational excitation is not caused by elastic collisions between electrons and molecules, this is due to the very large difference in mass between an electron and a molecule. Instead, vibrational excitation is the result of a resonant process proceeding through the formation of a non-stable negative ion. The theoretical maximum cross section for vibrational excitation of a molecule with an incident electron having energy ~ 1eV is around 10^{-19} cm^2, where as experimental values are about 10^{-16} cm^2 [16]. This unexpectedly large cross section is explained by the resonant exchange process previously described.

The rate coefficients for formation of vibrationally excited species by electron impact tend to be at their highest value for relatively low electron energies, about 1 – 3 eV. These values typically correspond to a maximum in the electron energy distribution in non-thermal plasmas, explaining why a large proportion of the energy in non thermal discharges goes into vibrational excitation.

2.2.3 Electronic excitation of neutral species by electron impact

Direct electronic excitation of neutral particles by electron impact typically requires much higher electron energies than vibrational excitation, typically greater than 10 eV. Despite electronic excitation requiring relatively high electronic energies, it is an important process to consider in plasma chemistry as it can lead to dissociation of a molecule in a single stage, or through a

series of intermediate steps through metastable excited species. Where dissociation through vibrational excitation is of particular importance for a limited number of gases (CO_2 and CO included), dissociation through electronic excitation becomes more important where a gas may be limited in its rate of dissociation through vibrational excitation as in the case of water vapour. The reasons for the limitations of vibrational excitation in the dissociation of water vapour are explained in section 2.2.6.

The energy efficiency of CO_2 dissociation through electronic excitation is limited to approximately ~25% [16]. However, through a mechanism of dissociation through preliminary vibrational excitation this efficiency can be increased. Although this reaction mechanism is still limited by the relatively low electron energy distributions of non-thermal plasmas, as well as the possibility of simultaneous excitation of alternative modes that do not ultimately lead to dissociation.

2.2.4 Relaxation processes of excited molecules and atoms

Transfer of energy from excited species to other molecules or atoms in a plasma is known is relaxation. An awareness of the fundamentals of relaxation processes is required in order to understand the processes as well as the limitations of dissociation through vibrational or electronic excitation. The relaxation processes that will be discussed are vibrational-translational (VT) relaxation, vibrational-vibrational (VV) relaxation, and electronic relaxation.

2.2.5 VV Relaxation

VV relaxation is the process by which vibrational energy exchange occurs by collisions between molecules in the system, leading to highly vibrationally excited molecules. These highly vibrationally excited molecules can play an important role in non-thermal plasma as the kinetics of the system can be dependent upon the fraction and concentration of these molecules. It is important to note that formation of these highly excited molecules does not typically occur by direct electron impact. Resonant VV relaxation occurs between 2 molecules of the same type, for example between 2 CO_2 molecules. Generally speaking, single quantum VV relaxation is a much faster process than VT relaxation at room temperature, with typical rate constant ranging from $10^{-10} - 10^{-13}$ cm^3s^{-1}, which results in large populations of highly vibrationally excited molecules. For some molecules, such as CO_2 (001), VV relaxation is due to multipole or dipole interactions, so called long distance forces. These long distance forces lead to very fast rates of VV relaxation in these molcules, in fact collisions can occur more frequently than the species rate of gas-kinetic collisions at room temperature. For example, the ratio of the VV relaxation rate coefficient to the gas kinetic collision value in CO_2 (001) is 4; because of this highly vibrationally

excited CO_2 molecules can rapidly populate a system, a phenomenon known as the Treanor effect (shown in Figure 11), a property that can be very desirable in a plasma chemical system requiring dissociation of CO_2.
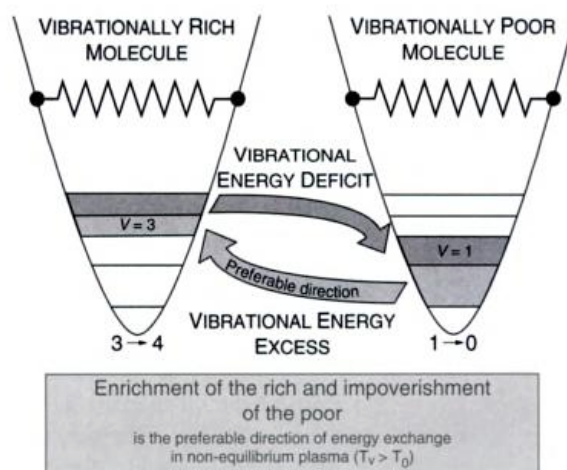
Figure 11: The process of VV relaxation leading to overpopulation of highly vibrationally excited states (The Treanor effect). This requires vibrational temperature to exceed translational temperature. The Treanor effect is known as "capitalism of molecular life". Image taken from [20].

2.2.6 VT Relaxation

Energy transfer from vibrational to translational modes in a molecule is known as VT relaxation. Trasnlational energy is the most commonly understood form of the meaning of kinetic energy, i.e. linear motion. In collisions at low gas temperatures between vibrationally excited molecules there is very little energy transfer, hence rates of VT relaxation are generally slow. It is, however, important to consider VT relaxation in plasma systems. This is because the contribution of vibrational excitation towards dissociation reactions is of particular importance for reaction kinetics, as described in section 2.2.5 and 3.1, hence as VT relaxation occurs simultaneously with VV relaxation it is effectively wasting energy that could be contributing to dissociation reactions.

Typical rates of adiabatic VT relaxation are shown in Table 3.

Table 3: Approximate rate coefficients of fast adiabatic VT relaxation for single component gasses at room temperature, based on the Landau-Teller formula. Data taken from Fridman's Plasma Chemistry [20], P. 70.

Molecule	Rate Coefficient (cm^3s^{-1})
O_2	5×10^{-8}
H_2O	3×10^{-12}
CO_2	5×10^{-15}
CO	1×10^{-18}

The rate coefficient for VT relaxation in H_2O (3×10^{-12} cm^3s^{-1}) is similar to its coefficient of VV relaxation (1×10^{-12} cm^3s^{-1}), this is problematic as it leads to a reduction in the maximum efficiency of H_2O dissociation by vibrational excitation. This limit can be shown to be ~60% for

H_2O, as opposed to about ~95% for CO_2. In order to minimise the energy loss by VT relaxation it is necessary to have a relatively high degree of ionisation as determined by Equation 4.

<div align="center">Equation 4</div>

$$\frac{n_e}{[H_2O]} > 10^{-4}$$

Equation 4 is based on the ratio of the VT relaxation rate to the rate of vibrational excitation by direct electron impact. When the value of $n_e/[H_2O]=10^{-4}$ then the rate of VT relaxation is approximately equal to the rate of vibrational excitation by electron impact, hence stimulation of plasma chemical processes by vibrational excitation in water takes place for levels of ionization above this value. CO_2 reduction is also limited by VT relaxation, and similarly can be overcome by high levels of ionization, however for CO_2 this value is significantly lower than that for water at approximately $n_e/[H_2O]=3 \times 10^-$ [16].

Fast non-adiabatic VT relaxation occurs in collisions involving chemical reactions for which there are 4 possible mechanisms, VT relaxation through: molecular collisions with atoms, intermediate formation of long life complexes, relaxation in symmetrical exchange reactions, and heterogeneous reactions. The rate coefficients of these reactions is in the range of about 10^{-10} to 10^{-13} cm^3s^{-1}, making them significantly faster than typical rates of VT relaxation, and similar to the rates of VV relaxation. The mechanism of heterogeneous VT relaxation proceeds through adsorption of molecules onto a surface, so may be of particular interest in consideration of reaction mechanisms for plasma-catalytic processes or when trying to prevent further reactions occurring within a plasma chemical system.

2.2.7 Relaxation of electronically excited species

The relaxation of electronically excited species occurs through emission of radiation (which becomes useful for measuring EEDF in plasma diagnostics), super elastic collisions (energy transfer back to plasma electrons, and collisions with other particles. The dominant mechanism of electronic relaxation in non-thermal plasma is through collisions with other heavy particles. Additionally, although to a lesser extent, relaxation to vibrational and translational degrees of freedom, with typical cross sections being about ~10^{-14} cm^2.

2.3 Non-equilibrium plasma reactor types

There are a wide range of different types of non-equilibrium plasma reactors available, some of which have been developed recently and are relatively poorly understood, whilst some varieties of non-thermal plasma reactor have widespread, large scale, industrial use. Within each variety

of reactor there can also be major differences in terms of reactor geometries and operating conditions used that can have a significant influence on the behavior of the plasma, and consequently the performance of the reactor.

The purpose of this section of the review is to explain the characteristics and the theory of the behavior of each relevant reactor type in order to give context to the literature review and the experimental chapters. The atmospheric pressure reactor types that are discussed in this review are the corona discharge, dielectric barrier discharge (DBD), and packed bed reactors.

2.3.1 Corona Discharge

One of the earliest identified and most studied types of plasma discharges is the corona. It has found widespread, very large scale industrial application in the form of the electrostatic precipitator [23]. The characteristic geometry of the corona discharge is an asymmetric pair of electrodes such that an inhomogeneous electric field is produced. For example, in a point to plane type geometry the electric field close to the point electrode typically has an electric field strength that far exceeds the electrical breakdown strength of the gas due to the small radius of curvature of the electrode. As a result of this geometry, the corona discharge develops from the point electrode towards the planar one, with the highest plasma densities being in the vicinity of the point electrode. Corona plasmas can be driven by positive or negative, DC or pulsed DC power sources, with the driving potential difference typically being applied to the electrode with the highest radius of curvature.
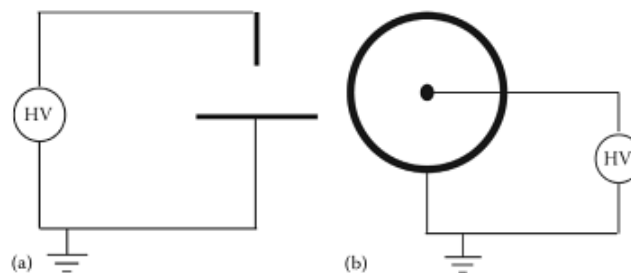
Figure 12: Typical electrode configurations for a corona plasma. (a) shows a point to plane geometry, and (b) shows a coaxial geometry. Adapted from [24].

Coronas driven by continuous DC power sources are limited in power as a result of the possible transition from being a corona discharge to an arc discharge at high voltages. In order to overcome this limitation pulsed DC power sources are used, so that the pulse duration is shorter than the time required for an avalanche of electrons to reach the ground electrode, and consequently cause a transition to a spark or arc discharge. Typically the required pulse duration is in the 10 – 300 ns region, and also requires very fast rise times (0.5- 3 kV/ns), although this depends upon gas composition, temperature and gap size [24, 25]. Fridman [16] states that the

fast rise times lead to high mean electron energies, which decrease the fraction of electron energy that contributes to vibrational excitation, with greater energy going towards electronic excitation and ionization.

The application of positive or negative driving voltages also has a strong effect on the nature of the plasma discharge as it changes the mechanism of the electrical breakdown. The polarity of the applied voltage can affect the size of the plasma region, the number density of electrons, and also change the relationship between gas temperature and electron density in the reactor [26, 27].

A limitation of common corona discharge geometries, such as the point to plane and wire type geometries are non-optimal gas contacting, a process termed "electrical sneakage" [28]. This is the gas effectively bypassing the plasma discharge due the inhomogeneity and non-dispersed nature of the plasma discharge. This problem can be addressed by the usage of multiple-stage reactors, for example through the application of similar multiwire geometries to corona discharges as found in electrostatic precipitators.

2.3.2 Dielectric Barrier Discharge (DBD) reactors

The DBD is another very well studied and industrially useful plasma reactor type, finding application in the production of ozone for the disinfection and decontamination of water [29]. The DBD reactor geometry is characterised by a pair of electrodes, typically in a planar or coaxial arrangement that are separated by one or more dielectric layers. Figure 12 shows typical geometric configurations used in DBDs.
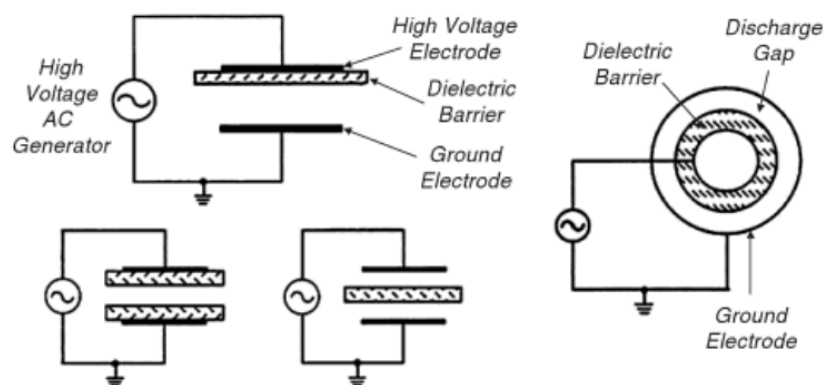
Figure 13: Common dielectric barrier discharge reactor configurations. Image taken from [30].

The dielectric layer is a non-electronically conducting layer that is polarizable in an electric field. The polarisability of the material is quantified by the (dimensionless) dielectric constant, represented by ε, where a higher value indicates a greater susceptibility to polarization. Typical

34

values are in the range of 1 – 10 for materials such as glass and plastics, whilst values can reach as high as 10,000 for ferroelectric materials, discussed further in section 2.3.3. The presence of the dielectric layer prevents the discharge from transitioning between being a non-equilibrium discharge to an arc. Although if a sufficiently high potential difference is applied the dielectric material itself will breakdown (above its dielectric strength, measured in kV/mm) and an arc discharge will occur regardless.

The discharge gap in a DBD typically is in the range from millimetres to centimetres. Average electron densities are 10^{14} - 10^{15} cm^{-3}, whilst average electron energy can be 1 – 10 eV [31]. There are two types of discharge possible in a DBD, a filamentary mode of operation and a homogenous glow mode. The homogenous glow mode is of most interest for surface treatment and thin film deposition and typically occurs at reduced pressures or with very high concentrations of noble gases, it is very difficult to achieve in electronegative gases and its control is unreliable [30, 31]. The filamentary mode of operation is characterized by many micro-discharges that take place over the surface of the electrodes. Over every cycle of the applied AC voltage, the microdischrages remain in the same place. The image in Figure 14 shows the microdischarges observed in a DBD from an end on perspective. Note the approximately even spacing and size of the microdischarges, this is caused by the electric field generated by the microdischarges repelling other microdischarges in the DBD.
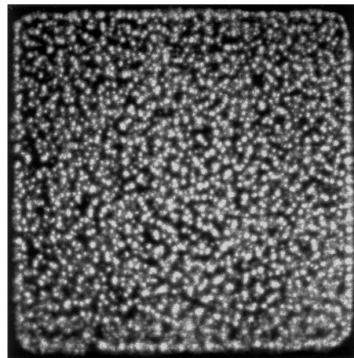
Figure 14: End-on view of microdischarges in atmospheric-pressure air in a DBD (original size: 6 cm x 6 cm, exposure time: 20 ms). Image taken from [31].

After the initial electron avalanche from electrical breakdown occurs, as discussed in section 2.1.2, a thin ionization channel that rapidly propagates between the electrodes is initiated, this is known as a streamer. It is caused by the low mass, and consequently fast, electrons causing ionization of heavy, slow moving molecules in the gas that leave a positive "tail" to the electron avalanche. The positively charged species, due to their slow movement, remain in the discharge gap after the AC half cycle is complete and the applied voltage returns to zero. As polarity of the applied field is reversed, and once sufficient charge builds up on the dielectric layer, the streamer will take place in the reverse direction, following the trail left by the remaining

positively charged ions in the gap remaining from the previous microdischarge. The ionization channel of a microdischarge is approximately cylindrical, and typically has a radius of about 100 µm [31], an image showing a sketch of an individual microdischarge is given in Figure 15.
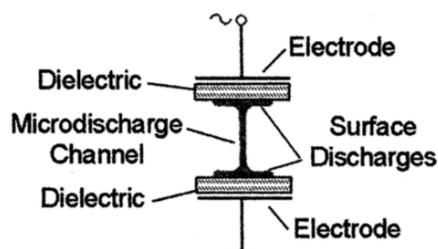
Figure 15: Schematic of an individual microdischarge, showing the microdischarge channel itself as well as surface discharges propagating over the surface of the dielectric material. Image adapted from [31]

2.3.3 Packed bed reactors

Packed bed reactors refer to any plasma discharge in which a packing material is incorporated into the plasma discharge in order to attempt to enhance the properties of the plasma. This "catch all" term therefore includes microwave, radiofrequency and other discharge types, but for the context of this thesis "packed bed reactor" refers only to corona and DBD discharge types that feature a packed bed, unless explicitly stated otherwise. A packed bed reactor of either the corona or DBD type actually typically shares some characteristic properties of each. In a packed bed reactor the geometry used is typically co-axial or planar, with the spaces between the electrodes occupied by the packing material. Quite often the packing material will be a dielectric material such as a ceramic, and may be coated with a catalyst, hence in a corona this can act as a dielectric layer. The particles themselves can enhance localized electric field strengths between 10 – 250 times [32], with some shapes of particles also believed to further enhance electric fields [33]. Hence, this localized enhancement of electric field strengths gives the discharge some corona like properties, as this is where the plasma discharges occur, leading to intense microdischarges.

A packing material may be selected for the reactor for a number of reasons: to enhance the electric field, to increase the electron density, to act as a catalyst, to act as an absorbent for reaction products, or to quench reactions and dissipate heat. A packing material that is incorporated into the plasma discharge will typically change the properties of the discharge by multiple mechanisms. It has been reported by several publications [34-36] that the combination of plasma and catalyst has improved the process characteristics in such a way that the effects on energy efficiency, conversion and product selectivity are greater than the sum of using either a catalyst of plasma independently, I.e. the effects are synergistic. It is therefore a challenging

36

problem for a plasma chemist to determine the origin of an observed change in the effects of the plasma.

Plasma catalysis is an emerging area of research, and there is a great deal of uncertainty over the mechanisms that occur in plasma catalytic systems, although a number of theories for the observed synergistic enhancements have been proposed. Neyts & Bogaerts [35] have summarised some of the theorised mechanisms that may lead to synergistic effects between plasma and catalysts, this is shown in Figure 16.
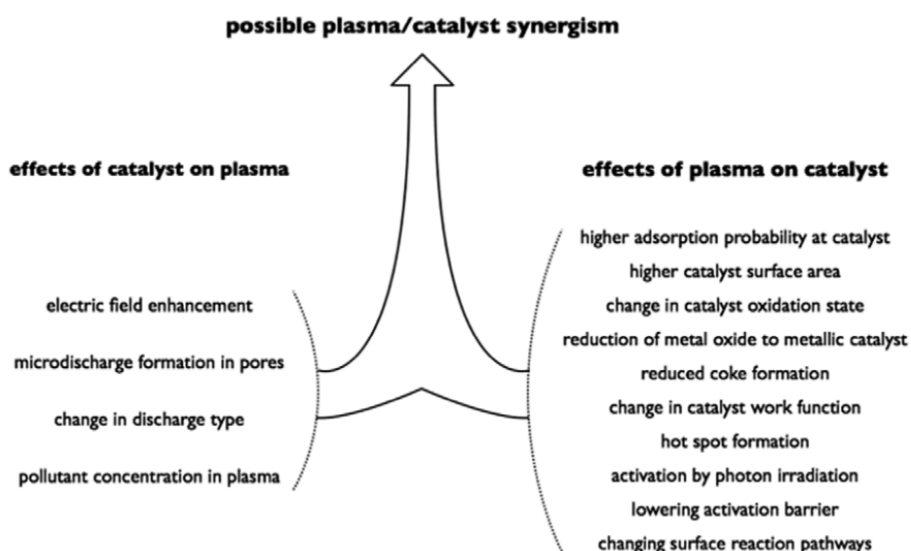
Figure 16: Summary of effects that occur between plasma discharges and catalysts that may lead to synergistic enhancement of a plasma - chemical reaction [35]

The plasma-catalyst interactions relevant to this thesis that are shown in Figure 16 are discussed in more detail in the remainder of this section.

Dielectric materials interact with electric fields and can cause enhancement of the fields, with the highest field strengths found between the contact points of the dielectrics. This effect is illustrated by Figure 17.
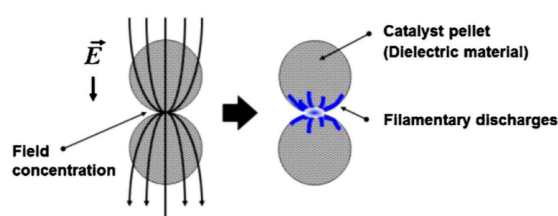
Figure 17: Local electric field enhancement caused by dielectric materials. Adapted from [37].

Through increasing the dielectric constant of a material, enhancement of the localised electric field is also increased. This enhancement of electric field is linked to dielectric constant of the material, as well as particle size and shape. Figure 18 shows the theoretical enhancement of

electric fields in packed bed reactors, with the reactor cross sectional average electric fields increasing by up to 1.5 times for dielectric constants greater than 100 [38].
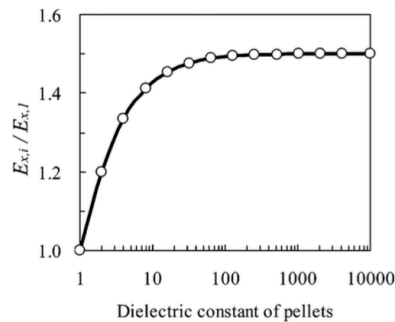
Figure 18: Enhancement of electric field as a function of dielectric constant of pellets. The value $E_{x,i}/E_{x,1}$ is effectively the cross sectional averaged augmentation factor of the electrical field. Image taken from [38].

A popular example of materials with very high dielectric constants are ferroelectrics. Ferroelectric materials are a relatively well-studied packing material for packed bed reactors, the most frequently used example being barium titanate, $BaTiO_3$. Ferroelectric materials are a group of pyroelectric crystals that are characterized by their spontaneous polarization. These materials can be polarized both positively and negatively, with the switching of the polarisation achieved by reversing the applied electric field as it is in an AC field [39]. The response of the polarization to the applied electric field follows a hysteresis loop, as shown in Figure 19. Additionally ferroelectric materials have very high dielectric constants, from 100 – 10,000, meaning that they can store a large charge on their surface.
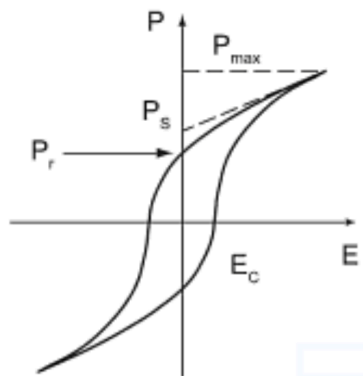
Figure 19: Typical P-E hysteresis loop of a ferroelectric material. Where P_r is remnant polarisation, P_{max} is the maximum polarization, E_c is the coercive field and P_s is the spontaneous polarization. Image adapted from [40].

The polarization reversal leads to a "non compensated" charge on the surface of the ferroelectric that leads to very strong localized electric fields ($E > 10^7$ V/cm) [41], and hence can accelerate electrons to very high energies, however the plasma density is relatively low [38]. As ferroelectric materials are crystalline they undergo phase transitions at certain temperatures,

38

these phase transitions can remove the ferroelectric properties of the crystal, and the point at which this takes place is known as the Curie point. The Curie point of some ferroelectric materials can be quite low, with that of $BaTiO_3$ typically being approximately 127°C.

Ferroelectric materials also posses other properties that are of interest for the development of a plasma reactor, whether they are used as a dielectric material in a DBD or as the packing in a ferroelectric packed bed reactor (FPBR). Rosenman et al [42] reviewed researched published on an unusual property of ferroelectric materials, ferroelectric electron emission (FEE), a summary of some of their conclusions is presented here. Two types of FEE have been found to occur, "weak" and "strong" characterized by the difference in their observed emission current densities, up to 10^{-7} A/cm^2 and 100 A/cm^2 respectively, a reported difference of 9 – 12 orders of magnitude. The weak ferroelectric emission is stimulated by pyroelectric or piezoelectric effects, or by spontaneous polarization inversion and occurs only in the ferroelectric phase, i.e. below the Curie point. Weak electron emission occurs from a ferroelectric when it is negatively charged and uncoated by an electrode.

Strong electron emission from ferroelectrics occurs under quite different circumstances to the weak electron emission. There are two distinct domains required, an uncoated electrode region, and a ferroelectric coated electrode region, typically applied in a grid or striped pattern. A high voltage pulse is applied causing an electric field both normal to, and tangential to the electrode. The electric field that is normal to the electrode occurs at the ferroelectric coated region, whilst the tangential field occurs on the uncoated electrode. As a result of the normal electric field a number of effects occur, dielectric polarization, ferroelectric polarization switching, and field enforced phase transition, dependent on the phase of the ferroelectric material, whilst the tangential electric field results in an electron avalanche and surface flashover. It is proposed that the high current densities are caused by plasma formation, which is followed by strong electron emission. Rosenman et al [42] state that there is "no unanimous opinion about the strong electron emission effect. Due to the lack of detailed knowledge…".

Similarly, Kemp & Kovaleski [43], found that it was possible to reduce the breakdown voltage in a ferroelectric plasma source by up to 75% by adjusting the frequency of the applied applied AC voltage close to the resonant mechanical frequency of a number of different PZT disks, both in a vacuum and atmospheric pressure. They attribute this reduction in voltage to electron emission caused by electron emission cause by the piezoelectric effect induced by the radial mechanical vibrations at the resonant frequency, which they found to be at 235 kHz using impedance spectroscopy.

The electron emission phenomena found in ferroelectric materials may be of benefit for increasing electron density and plasma density in a reactor, whilst reducing breakdown voltage and consequently decreasing power requirement and potentially increasing efficiency.

In packed bed reactors, plasma surface interactions become very important. Surfaces can be a source of significant losses for plasma active species as the ratio of surface area to plasma volume increases. In order to maintain a plasma discharge it is important to maintain levels of ionization and electron density in the gas. Hence, to counteract the quenching effects of surface dominated discharges it may be possible to enhance surface emission of electrons. This may be achieved through the usage of low work function materials, or materials that have high values for secondary electron emission. The work function of a material is the minimum thermodynamic energy required to extract an electron from the surface of a material in a vacuum, and it is already considered to be important in thermionic emission applications, for example light bulbs and arc welding. Thermionic emission however only becomes important at high temperatures, typically above 1,000 K. Through field emission of electrons it is possible to directly extract electrons from cold metal surfaces in strong electric fields ($> (1/3) \times 10^6$ V/cm) due to the quantum mechanical effect, electron tunneling [16], it is this effect that would be of interest to non-equilibrium plasma applications.

Secondary electron emission has 4 possible mechanisms, secondary ion-electron emission, potential electron emission induced by metastable atoms, photo electron emission, and secondary electron-electron emission [16]. Secondary ion-electron emission is considered to be the most important. There are two further mechanisms of secondary ion-electron emission, one of which only becomes significant at ion energies about 1 keV, so is not considered here. The mechanism that is dominant at low ion energies is the Penning mechanism of secondary ion-electron emission, this is similar to the mechanism of Penning ionization described in section 2.2. When an ion approaches a surface it can extract an electron from it if the ionization potential (*I*) exceeds the work function (*W*). If the ionization energy is high enough it can be possible to extract more than one electron from the surface. The secondary ion-electron emission (*γ*) can be estimated by the formula [16]:

$$\gamma \approx 0.016 \, (I - 2W)$$

Equation 5

Neither low work function materials, nor secondary electron emission have been significantly investigated for non-equilibrium plasmas, although there are a couple of publications that demonstrate a tentative relationship between work function, secondary electron emission and electron densities. In a comparison between Al_2O_3 and MgO dielectric barriers in atmospheric pressure air, it was observed that the material with the highest secondary ion-electron

coefficient (MgO, γ = 0.11) at equal applied powers an increase in electron density and density of electronically excited species occurs when compared to Al_2O_3 (γ = 0.099) [44]. Similarly, the authors of a study using microcrystalline diamonds (a material with an extremely low work function) tentatively suggested that the surface effects, such as secondary electron emission, should have a positive effect on the discharge [45]. This was then subsequently supported by a different research group demonstrating increased current densities at reduced applied potential differences using nanodiamond based, very low work function materials in microplasma devices [46]. The potential of these methods to enhance plasma density in packed bed (and other surface dominated) discharges is an interesting prospect, and is very much a worthwhile avenue for further research.

Another possible approach in packed bed plasma reactors could be to use the packing materials as an absorbent for reaction products or metastable species, and consequently reduce the occurrence of reverse reactions that may limit conversion in the reactor, as well as maintaining a favourable reaction equilbrium. Plasma reactions involving oxygen containing molecules will inherently generate highly reactive oxygen species, for example CO_2 plasmas have been demonstrated to generate high concentrations of atomic oxygen [47] (remarkably in the cited study the concentrations were observed to be higher than singlet oxygen in oxygen containing plasmas). Modeling of CO_2 plasmas also shows that during an electrical breakdown singlet oxygen concentration reaches similar levels to CO concentration, before rapidly recombining with other species to produce molecular oxygen, ozone, or CO_2 [21]. Using a packing material in this way would therefore be sacrificial, and consequently it would be likely to require subsequent regeneration that is likely to render any industrial scale process prohibitively expensive due to the extra energy cost. It would, however, be an academically interesting investigation.

3 Literature Review

3.1 Plasma reduction of CO$_2$

The aim of this section is to cover the current understanding and state of the art technology for CO$_2$ dissociation in plasmas. The parameters that would be of interest to a chemical engineer, i.e. conversion, efficiency, power, selectivity, flow-rates, operating temperature and pressure for each reactor are discussed. These parameters are inherently related to some of the plasma chemistry concepts described in chapter 2. This relationship between the internal plasma chemical processes and the observed effects on important chemical engineering parameters are discussed, and the causes of these relationships is used to outline the limitations and possibilities for each different reactor geometry evaluated.

Dissociation of carbon dioxide to carbon monoxide and monatomic oxygen is an endothermic process and is represented by Equation 6:

$$CO_2 \rightarrow CO + O, \quad \Delta H = 5.5 \text{ eV / molecule or } 530.6 \text{ kj / mol}$$

Equation 6

where the carbon dioxide is reduced to carbon monoxide and molecular oxygen, this reaction can be expressed by Equation 7:

$$CO_2 \rightarrow CO + \tfrac{1}{2} O_2, \qquad \Delta H = 2.9 \text{ eV / molecule or } 279.8 \text{ kj / mol}$$
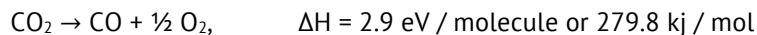
Equation 7

The efficiency (η) of this reaction is expressed using Equation 8:

$$\eta = \frac{\Delta H}{E_{CO}}$$

Equation 8

where E_{CO} is the energy cost of generating one mole of carbon monoxide in the reactor, and ΔH is the enthalpy change of the reactions shown in Equation 7.

The energy efficiency of CO$_2$ dissociation in thermal plasmas is thermodynamically limited to a maximum of 43%, this is due to thermal plasmas being in thermal equilibrium, i.e. the electron temperature is equal to the temperature of heavier species. Equilibrium plasma dissociation of CO$_2$ proceeds via the thermal decomposition mechanism at 2500 – 3000 K at 0.16 atm [16]. In order to preserve the reaction products and prevent reverse reactions, the products of the

reaction must be cooled extremely rapidly, at rates of $10^8 - 10^9$ Ks^{-1}, in order for the maximum dissociation efficiency to be attained.

In non equilibrium plasmas, the primary modes of CO_2 dissociation are through the vibrational and electronic modes. The transfer of energy to vibrational modes in CO_2 plasmas has been the focus of a number of research groups in recent years due to the theoretical efficiency of dissociation being as high as 95%. There are 3 causes for this high efficiency that are described in Fridman's plasma chemistry [16]:

1. At plasma electron temperatures between 1 and 2 eV, 95% of the energy input into the plasma can be transferred to the asymmetric stretch mode of vibrational excitation in CO_2.

2. Dissociation of CO_2 and its related reactions are endothermic. Vibrational excitation is the most effective mechanism to stimulate these reactions.

3. The vibrational energy required to dissociate CO_2 is exactly equal to the O=CO bond energy of 5.5 eV, i.e. the activation energy of the reactions is zero.

There are very few reactor types that transfer their energy predominantly to vibrational modes, with the most commonly cited examples being moderate pressure microwave plasma discharges [48, 49], and atmospheric pressure gliding arc plasmas [50, 51], which have achieved experimental efficiencies as high as 90% and 43% respectively.

Dissociation of CO_2 by electronic excitation is another important reaction mechanism, particularly at high electron energies. For example, for CO_2 dissociation in a dielectric barrier discharge, where electron temperature is typically in the region of 2 – 3 eV, modeling data suggests that only 12% of the electron energy is transferred to vibrational states, whilst 79% is transferred to electronic excitation [21]. Maximum energy efficiency of CO_2 reduction by electronic excitation is approximately 25% [16].

There is often a trade off between conversion and efficiency of CO_2 reduction in a plasma reactor. This is due to the mechanisms by which CO_2 dissociation takes place at different electron energies. The most efficient plasma reactor described in literature, the supersonic flow moderate pressure microwave plasma, operates at an efficiency of 90%, with the dominant CO_2 dissociation reaction mechanism proceeding by vibrational excitation [48]. The efficiency of the reactor is highest at a specific energy input of ~ 0.3 eV / molecule, using Equation 7 it can be seen that this must limit the conversion of CO_2 to approximately 10%.

3.1.1 Corona Discharge

As stated in section 2.3.1, the corona discharge is a reactor type that has been widely used by industry and is relatively well understood. It is therefore a good starting point when considering non-equilbrium plasma discharges. Boukhalfa et al [52] were the first group to investigate dissociation of CO_2 in a corona discharge. Using a point to plane type discharge they investigated positive and negative coronas in pure CO_2, and air + 3% CO_2. The maximum conversion of CO_2 obtained was about 6.7% for the air + 3% CO_2 system (based on the yield of CO of 200 ppm). The higher conversion achieved using air with CO_2 compared to the pure CO_2 system is attributed to the presence of excited nitrogen, N_2^*, transferring its energy to CO_2 leading to a dissociation reaction taking place, i.e. Penning dissociation as described in section 2.2. This increase in conversion is commonly observed in many reactor types using additional nitrogen or noble gases [53-57].

The increase in conversion is attributable not just to the Penning dissociation mechanism suggested by Boufhalka et al [52], but also due to the longer mean free path of an electron in noble gases leading to higher electron energies and densities, and a charge transfer mechanism leading to CO_2 dissociation by electron – ion recombination as suggested by Ramakers et al [58]. The mechanism for this is given by the consecutive reactions shown in Equation 9 and Equation 10:

$$Ar^+ + CO_2 \rightarrow Ar + CO_2^+$$

Equation 9

$$CO_2^+ + e^- \rightarrow CO + O$$
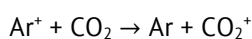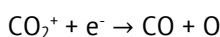
Equation 10

In the case of the charge transfer reaction given in Equation 9, the reaction is exothermic, and consequently very fast, for gases (eg. Ar – 15.7 eV, He – 24.6 eV and N_2 – 15.6 eV) where the ionization energy exceeds that of CO_2 (13.6 eV).

The CO_2 corona discharge has been extensively studied, in both positive [59-61] and negative [59, 62, 63] coronas, with positive nano-second pulses [64], and in the presence of catalysts [65, 66]. The highest claimed efficiency for a non-catalysed corona systems is 502.5 kJ/mol energy input (~56%) by Horváth et al [59], with CO_2 conversions up to 10%. However, they are somewhat ambiguous regarding the method of calculating reactor power consumption, and provide an incorrect value for the theoretical limit to efficiency (393.5 kj/mol). Despite this, it can be considered that typical corona discharge conversions and efficiencies are the region of < 10 % and < 12 % respectively. Typical reduced electric fields are in the region of 100 – 200 Td,

suggesting that the CO_2 dissociation reaction mechanism is likely to be dominated by electronic excitation similarly to a DBD [21].

The work of Wen & Jiang [65] and Liu et al [66] both use catalysts within the corona discharge, and each show relatively high CO_2 conversions (23% and 18% respectively) compared with non-catalysed corona discharges. Their work is discussed further in section 3.1.3.

3.1.2 Dielectric Barrier Discharge

Zheng et al [54], Paulussen et al [67], Wang et al [55], and Ramakers et al [58] each used a coaxial geometry DBD to dissociate CO_2. The discharge gap in the reactors varied from 1 – 11 mm, the frequency of the applied AC voltage was in the range from 2.2 kHz to 90 kHz, and voltages up to 14 kV were applied. All of the authors found similar trends, for example as there is an increase in the concentration of CO_2 in the carrier gas (which was either argon [54, 58] or helium [55, 58]) then the absolute percentage of CO_2 conversion decreases whilst the efficiency increases. Similarly, the effect of the flowrate (and consequently residence time) of gas into the reactor, shows that lower flowrates lead to an increase in conversion, but a decrease in efficiency. The effect of applied power also follows a simple trend, as the power is increased, the conversion of CO_2 increases as efficiency decreases.

The effect of frequency of the AC voltage on conversion and efficiency does not follow such a simple trend. Paulussen et al [67] who tested the greatest range in frequency, from 10 – 90 kHZ found that the highest conversion they achieved, and one of the highest achieved between all of the authors, was 30% at 60 kHz. Maximum efficiency was obtained at 30 kHz, giving 26% conversion. They note that at low power inputs, that lower frequencies give the highest conversions. Wang et al, who observed the highest efficiency of CO_2 reduction (9.3%), found that for equal conversion of CO_2 to be obtained, then high frequencies give higher efficiencies, although generally speaking, the highest efficiencies can be achieved at the lowest frequencies. Wang et al [55] believe that the reduced impedance of their reactors at higher frequencies could be the cause of this behavior, resulting in less heating and consequently less energy consumption. Interestingly, Ramakers et al [58] tested a range of frequencies from 6 – 75 kHz and found no significant effect on conversion or efficiency, although they do note that the discharge appeared to be more filamentary at 75 kHz.

For CO_2 reduction in a DBD, the optimum operating frequencies are yet to be identified. The challenge in determining optimum operating frequencies for the reduction reaction will be to isolate the reaction mechanism from changes in impedance of the reactor and experimental equipment. Modelling of the system may be useful in isolating some of the effects that frequency has on reaction kinetics [68]. Impedance spectroscopy, a technique that has been used

to great effect by the electrochemistry community, and has recently been successfully applied to plasma electrochemical reactions [69], may help to unravel the complex problem of the effects of frequency in DBD plasma discharges.

Wang et al [55] also tested the effect of using different transition metal coatings on the internal electrode of their reactor. As the discharge gap between the quartz tube dielectric and the inner coated electrode was just 1 mm, the proximity of both walls to the flow of gas would increase the dominance of surface reactions compared to a larger discharge gap. Of the transition metals tested, they found that the order of activity of the metals (given by their elemental symbols) was as follows: Cu > Au > Rh > Fe ≈ Pt ≈ Pd. They found that the difference in conversion was as much as 6.5% when comparing the copper electrode (19.4% conversion) with the palladium electrode (12.9% conversion) at an input voltage of 6 kV. The authors state that these differences are not due to electric properties of the metals (i.e. conductivity), but likely a combination of other physical or chemical properties. This could be due to the formation of oxidised metal species, or perhaps the electron emission properties of the metals. Addionally, the thin layer of gold that was applied to the electrode was observed to have been sputtered over long periods of operation. This suggests the possibility that sputtered gold ions may be participating in reactions with CO_2, leading to transfer of energy in a Penning type mechanism and artificially enhancing the conversion. However, not enough information is provided to make any conclusions about the processes that are actually occurring.

Brock et al [56] also tested Pt, Pd, Rh, Cu and Au metal oxide coatings (Au was the only non oxidized metal used) in a "fan type" AC glow discharge reactor using 2.5% CO_2 in helium. A voltage of 400 - 900 V was applied across a gap of 0.3mm, with the stator and rotor acting as electrodes, where the blades of the fan are coated with the metal. The maximum conversion obtained is 30.5% using the rhodium electrode, at an efficiency of 3.5%. The activity of the electrodes to maximize conversion, in decreasing order, was found to be Rh > Pt ≈ Cu > Pd > Au/Rh ≈ Au. This result differs quite significantly from those of Wang et al, with regards to the efficacy of certain electrode materials. Using optical emission spectroscopy, Brock et al determined a strong inverse relationship between excitation temperature and CO_2 conversion in their reactor. They state that no link is found between material work function, a parameter that has been suggest by other authors. They suggest that the observed changes may be due to sticking coefficient, specific heat, or ionization potential. Also, in this case no sputtering of gold ions was observed.

Despite the similarities in choice of material between the experiments of Brock et al [56], and Wang et al [55], there are no similar identifiable trends between the two sets of experiments.

This highlights the challenges in determining the cause of an observed trend in a plasma-catalytic system.

As stated in section 2.3.2, the dielectric constant of the barrier material is believed to have a significant effect on the nature of the plasma discharge. Li et al [70, 71] have investigated the effect of different dielectric materials on conversion of 10% CO_2 balanced with N2 in a planar DBD at frequencies from 2 – 12 kHz. The highest conversion (15.6%) was observed using a $Ca_{0.7}Sr_{0.3}TiO_3$ dielectric, where $\varepsilon \approx 240$ at 20 °C and AC frequency of 10 kHz. 0.5 wt% $Li_2Si_2O_5$ was added as a sintering additive to increase density, improving the electronic and mechanical properties when processing the $Ca_{0.7}Sr_{0.3}TiO_3$. The other dielectric materials used were Al_2O_3 and SiO_2 ($5 < \varepsilon < 10$), and the maximum conversion for each material was approximately 5%. The intensity, and number of microdischarges in the $Ca_{0.7}Sr_{0.3}TiO_3$ dielectric reactor are much greater compared to the alumina and quartz dielectrics. A property that is attributed to the dielectric permittivity of the material. This suggests that high dielectric constant materials are beneficial to improve the conversion of CO_2 in a DBD.

Current research into CO_2 conversion using DBD plasmas has demonstrated the potential for moderate conversion, higher than those found in corona discharges, at the expense of efficiency, which has not yet exceeded 9.3%. Similarly to corona discharge reactors, the inclusion of catalytic materials in the discharge area is beneficial, although it is currently poorly researched.

3.1.3 Packed bed and catalytic reactors

Similar reactors to the DBD are the packed bed reactors, as discussed in section 2.3.3. The possibility to incorporate combinations of catalysts, ferroelectric ceramics or other packings offers an opportunity to overcome the limitations that are imposed by plasma generation on its own. Sections 3.1.1 and 3.1.2 mentioned that the addition of catalysts to corona and DBD plasmas has been shown to greatly improve the conversion and efficiency of CO_2 reduction.

There are numerous publications that investigate packed bed or catalytic reactors solely for reduction of CO_2 [34, 55, 56, 65, 66, 71-77]. Two approaches to improving CO_2 reduction are documented, one being the application of high dielectric constant materials (E.g. $BaTiO_3$ [72, 75, 76], or other high ε ceramics [71, 73]), the other being the use of potentially catalytic materials (e.g. Transition metal [34, 55, 56, 74], Al_2O_3 based [65, 73, 74, 77] or other [66, 77] catalysts). These packing materials are often compared with an unpacked reactor [65, 72, 77], or a material that is perceived as being relatively "inert" (e.g. glass [65, 72, 77], silica [71, 73, 77], non-catalytic phases of Al_2O_3 [65, 71]).

The first investigations into the reduction of CO_2 in a packed bed plasma reactor were by Jogan et al [75], using $BaTiO_3$. $BaTiO_3$ packing pellets with two different dielectric constants, 660 and

10,000, were tested for the reduction of CO_2 from a simulated flue gas mixture composed of $N_2:O_2:CO_2$ = 0.75:0.15:0.1. Maximum CO_2 conversion of 18% at an efficiency of 108 g CO_2/kWh (~19.3% efficiency) was achieved using the ε = 660 $BaTiO_3$ packing. It is worth noting that the ε = 10,000 $BaTiO_3$ packing was limited in its maximum applied potential difference caused by the tendency towards arcing and sparking, this is likely to be due to the lack of dielectric barrier in the reactor.

Similarly, Mei et al [72], compared using $BaTiO_3$, glass, and an unpacked reactor for reduction of CO_2 from an undiluted gas stream. Maximum CO_2 conversion of ~28% is obtained at an input power of 50 W using the $BaTiO_3$ packed reactor. Compared with an unpacked reactor, the addition of $BaTiO_3$ or glass packing increases CO_2 conversion by 75% and 35% respectively, despite the gas residence time being reduced by 3.5 times. The increase in conversion is not attributed directly to dielectric constant, but rather to changes in discharge characteristics such as average electric field strength and mean electron energy. The authors also mention the possible adsorption of CO_2 to the surface of $BaTiO_3$ and the possibility of photocatalytic reactions occurring on the surface of $BaTiO_3$ due to UV light generated by the discharge [78], although $BaTiO_3$ typically has a very low porosity, so this is not likely to be a significant contributing effect to CO_2 conversion.

Wen & Jiang [65] were the first to investigate the use of γ-Al_2O_3 for reduction of CO_2 in plasmas, using a pulsed corona discharge, as mentioned in section 3.1.1. CO_2 conversions up to 23% at efficiencies up to 318.7 gCO_2 / kWh (~57%) were achieved. The reactor was compared using different surface area (SA) materials with a similar dielectric constant, γ-Al_2O_3 (SA = 171.7 m^2/g), α-Al_2O_3-I (20.5 m^2/g), α-Al_2O_3-II (94.4 m^2/g), glass and without packing. The yield of CO achieved, from highest to lowest, are γ-Al_2O_3 (~13%)> α-Al_2O_3-II (~6%)> α-Al_2O_3-I (~4.5%) > glass (~3.5%). The dielectric constants of each alumina packing are approximately the same, so the materials can be compared purely on the basis of their surface area or the properties of their crystalline structure. It is clear from their results that the increase in surface area of the materials leads to an increase in CO_2 conversion, which suggests that surface reactions contribute significantly to the dissociation mechanism. The authors cross-reference an article [79] showing the interaction mechanisms between CO_2 and γ-Al_2O_3 under non-plasma conditions, these are: 1) formation of a very strongly held surface carbonate, 2) surface bi-carbonate from reactions with hydroxyl groups that slowly form carbonate, and 3) weakly bonded CO_2. Additionally, the preferential adsorption of CO_2 over CO [80] is also suggested as an important contributing factor in the enhanced CO yield observed using γ-Al_2O_3.

More recently, Roland et al [81, 82], observed synergistic effects between plasma and γ-Al_2O_3 packed DBD plasmas for oxidation of hydrocarbons [82]. They subsequently demonstrated [81],

using electron paramagnetic resonance (EPR), the existence of a semi-stable (lifetime up to 14 days), paramagnetic species in γ-Al_2O_3 that occurs only after the material has been subjected to a non-thermal plasma discharge. They demonstrate that this is probably related to an $Al-O-O\bullet$ aluminium peroxyl group. The concentration of the paramagnetic species were found to be at a maximum when they were subjected to an applied voltage of 15 kV, this is believed to be due to the reactor temperature exceeding ~100°C above these potential differences which limits their formation. Additionally, the presence of water in the sample almost entirely destroyed the characteristic paramagnetic signal from the EPR, this is attributed to a reduction in electric field strength caused by thin films of water, and water preventing formation of a paramagnetic centre. Roland et al found that ozone decomposition on the active sites in $\gamma-Al_2O_3$ is competitively inhibited (poisoned) by CO_2, suggesting that the interaction with these active sites and CO_2 is strong and may explain the enhanced CO_2 decomposition observed by Wen and Jiang [65]. These studies demonstrate a synergistic plasma – catalyst relationship, showing that enhanced CO_2 decomposition in plasma over γ-Al_2O_3 is primarily due to enhanced surface chemistry, with the contribution to CO_2 decomposition from other discharge enhancements (e.g. localised strengthening of the electric field) being a secondary effect. However, in order to ascertain whether or not γ-Al_2O_3 does act as a catalyst for the reduction of CO_2 by enhancing surface chemistry would require a more targeted investigation, perhaps using a technique such as diffuse reflectance infrared spectroscopy – mass spectrometry (DRIFTS – MS) that has recently been demonstrated by Stere et al [83].

An interesting study by Duan et al [77] has investigated the use of a range of materials (CaO, MgO, γ-Al_2O_3, SiO_2 wool, and SiO_2 sand) in a packed bed microplasma reactor. In comparison to other studies, the particle size used is relatively small (180 – 420 μm) compared to many other studies where particle sizes tend to be in excess of 500 μm. Using a pure CO_2 stream, a maximum conversion of 41.9%, at an efficiency of 7.1% was achieved using a CaO packing material. From highest CO_2 conversion to lowest, the order of activity was found to be: CaO > SiO_2 wool > MgO > γ-Al_2O_3 > SiO_2 sand. All of the materials have similar dielectric constants (ε = 4.6 for SiO2, and ε = 9.3 – 11.8 for the rest), so the effect of dielectric constant is insufficient to explain the range of conversions observed. Activity is attributed predominantly to basicity, with CaO, and MgO being most basic, γ-Al_2O_3 being amphoteric, and SiO_2 being acidic. Both CaO and MgO are likely to chemisorb, and possibly react to form carbonates with CO_2, as opposed to a physisorption mechanism that the authors associate with γ-Al_2O_3. Surprisingly, the authors describe, in passing, the effects of secondary electron emission leading to surface discharges with CaO, citing a previous article of theirs that seemingly does not discuss this effect. Despite not exploring this further, an additional possible explanation may be due to the lower work function (and hence higher secondary electron emission) of their chosen materials, with work

functions order from low to high: CaO < MgO < γ-Al$_2$O$_3$. Given that the particle sizes used in this experiment are relatively small, and consequently electron-wall collisions become an important loss mechanism, the use of low work function materials may assist in CO_2 conversion by maintaining a high electron density via the possible mechanisms described in section 2.3.3. The previously discussed study by Duan et al [77] used the smallest particle sizes of any of the mentioned studies, and achieves the highest CO_2 conversion, which highlights the importance of particle size in packed bed reactors.

In order to be of maximum benefit, a heterogeneous catalyst would have to have a high surface area to volume ratio. This would mean either the inclusion of a porous ceramic monolith, a pelletised packing material, or alternatively some form of fluidized bed. These options require some atypical additional considerations for the geometric properties of the catalyst; a ceramic monolith would have to feature sufficiently large void spaces for electrical breakdowns to occur within them [84, 85]; a packed bed reactor would require the pellet size and shape to be optimised [38]. To date, there are a small number of studies [86-89] that demonstrate that particle size and shape have an effect in plasma discharges, but further investigation is necessary in order to elucidate the relationship between experimental parameters. The effects of particle size in packed bed reactors is a regularly disregarded consideration that requires further attention, with numerous examples in literature where the effects have not been considered at all [36, 88]. This gap in the literature has also been highlighted by some reviews as an area that needs to be addressed [38].

3.2 Electrical Characterisation

Some of the physical properties of DBDs and PBRs can be determined by analysis of their electrical characteristics. There are a number of different methods that can be used to study the behavior of the plasma discharge, such as current and voltage signals [36, 72, 90-92], Q-V plots [36, 72, 90-95], or fast fourier transforms [36] of current pulses.

The first in depth investigation into the electrical characteristics of plasma discharges was by T. C. Manley in 1943 [92] through oscillographic studies of industrial ozone generators for water treatment. Based on these studies he observed the intermittent nature of the DBD, identifying the discharge phase and the capacitive phase of DBD plasma breakdown, as well as the discharge potential, and a method to calculate plasma power consumption based on Q-V plots. Since this initial discovery, there has been further development of the oscillographic methods used by Manley, often alongside equivalent electrical models that represent the DBD as a modular system of more simple electrical components, typically capacitors and resistors.
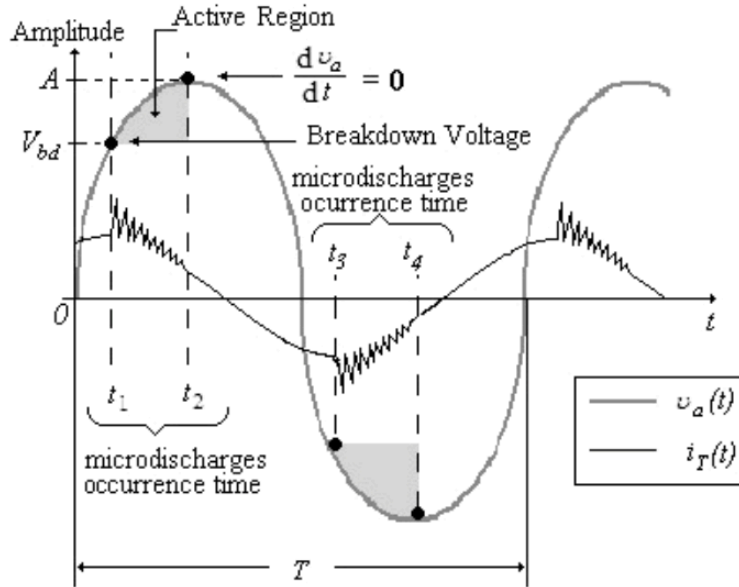
Figure 20: Characteristic waveform of DBD applied voltage and current [90]

Figure 20 shows a characteristic current and voltage waveform of a DBD with the applied potential difference being a sine wave, and the resultant total current being a displacement current (approximately a sine wave) with a number of microdischarges (superimposed pulses). The total current and applied voltage are out of phase, with the current leading the potential difference, this is indicative of a capacitive – resistive circuit [96]. If the current leads the voltage by ¼ of a cycle (I.e. 90°) this indicates an ideal capacitor with no resistance. If the voltage and current are in phase, this indicates an ideal resistor. If the current leads the voltage by anything less than 90°, but greater than 0°, this indicates combined resistive and capacitive behavior.
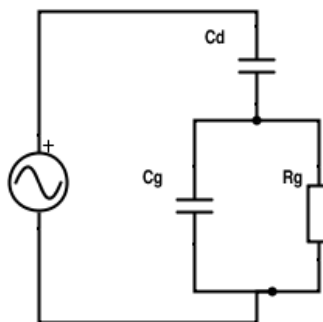
Figure 21: Simplest equivalent electrical circuit of a DBD

The circuit shown in Figure 21 shows the simplest equivalent circuit that can be used to model a DBD [94]. Consisting of an AC source, a capacitor (C_g) and a variable resistor (R_{gap}) in parallel, connected to a second capacitor in series (C_d). The dielectric layers of the reactor are treated as an ideal capacitor, represented by C_d. The gas gap, i.e. the space in which the plasma is generated, is treated as the capacitor, C_g, and the variable resistor, R_g. In a single AC cycle, as the

applied potential difference rises such that the gas gap voltage exceeds the gas breakdown voltage, i.e. $V_g > V_{bd}$, the resistance of R_g falls and charge transfer through the gas gap begins. As the applied voltage decreases, and $V_g < V_{bd}$, the resistance of R1 tends to infinity and no charge is transferred through the gas gap.

The capacitance of C_d can be approximated using Equation 11 [90]:

$$C_d = \frac{2\pi\varepsilon_0\varepsilon_q l}{\ln\left(\dfrac{d + x}{d}\right)}$$

Equation 11

where ε_0 = 8.854 x 10^{-12} F m^{-1} is the permittivity of a vacuum, ε_q = 3.8 is the relative permativity of quartz glass. Reactor dimensions are incorporated by l (length), d (internal radius to the the dielectric material), and x (wall thickness).

Figure 20 also shows the "discharge phase", also originally described by Manley. The discharge phase is characterised by a number of microdischarges, observed as current pulses, that typically terminate at the point where the applied potential difference to the reactor is beginning to either decrease or increase (dependent on phase) I.e. $\frac{dv}{dt} = 0$. These microdischarges initate at a breakdown voltage, V_{bd}, which will vary dependent upon the properties of the reactor (e.g. gas composition, particle size, etc).

From the voltage and current waveforms it is possible to determine:

> **From the applied potential waveform** - Wave shape, frequency, amplitude
> **From the current waveform** – Pulse magnitude, pulse duration, frequency, and discharge phase duration of microdischarges
> **Combined voltage and current** – breakdown voltage, capacitance

As it is shown in Figure 20 the voltage waveform is a relatively smooth and continuous shape that is easy to obtain accurate measurement of. The current waveform, however, features very fast, dynamic pulses that are difficult to measure and resolve accurately. This problem makes numeric determination of reactor electrical characteristics a more complex challenge than it might seem. This problem is illustrated by the wide discrepancies in literature over obtained values for DBD power consumption and capacitance via a range of methods [97], however a comparative study between the different method by Ashpis et al [98] shows that a "monitor capacitor" used to calculate power consumption via a Q-V plot yields the most accurate results.

The "monitor capacitor" is a capacitor inserted in series with the DBD between the reactor and the ground, with the potential difference (V_m) measured across it. The capacitance of the monitor capacitor (C_m) is chosen to be much larger than that of the reactor (C_{cell}), i.e. $C_m \gg C_{cell}$ [97, 98].

The instantaneous charge (Q_m) on the capacitor (With an assumed constant capacitance of C_m) is determined using Equation 12:

$$Q_m(t) = C_m V_m(t)$$

Equation 12

where the current (I_m) through the capacitor is obtained with Equation 13:

$$I_m(t) = C_m \frac{dV_m(t)}{dt}$$

Equation 13

As they are in series with each other, the current through the capacitor must be equal to the current through the DBD (I_{cell}), i.e. $I_m = I_{cell}$. The instantaneous power of the reactor is therefore determined using Equation 14:

$$P(t) = V_{cell}(t) \cdot I_{cell}(t) = V_r(t) \cdot C_m \frac{dV_m(t)}{dt}$$

Equation 14

where V_r is the potential difference across the reactor. The average power, $\bar{P}$, over one cycle period (T) is therefore determined with Equation 15:

$$\bar{P} = f \int_0^T V_r(t) \cdot C_m \frac{dV_m(t)}{dt} dt = f \int V_r \cdot C_m dv_m = f \oint V_r dQ_m$$

Equation 15

where f is the applied frequency, i.e. $1/T$. The Q – V plot of the instantaneous charge on the monitor capacitor, against the instantaneous voltage across the DBD generates a hysteresis loop known as a Lissajous figure. Equation 15 shows that the area enclosed by the Lissajous figure is equal to the energy consumed per cycle, therefore when multiplied by the frequency it gives the reactor operating power.

An example Lissajous figure generated using experimental data is shown Figure 22. The diagram also shows additional, important electrical characteristic data that can be obtained from the Lissajous figure, such as the burning voltage (U_b) of the reactor, as well as charge transferred in the plasma, and capacitances of the dielectric layer (C_{diel}), the gap (C_g) and the overall cell (C_{cell}). Different parts of the lissajous figure correspond to different phases in the discharge cycle of the DBD. Taken from Figure 22, lines AB and CD correspond to the "discharge off" phase, when there is no plasma formation in the gap and the gradient of the line is equal to C_{cell} [94]. Where C_{cell} is composed from the gap capacitance (C_g), and the dielectric capacitance (C_{diel}), applying Kirchoff's law this is expressed by Equation 16.

$$\frac{1}{C_{cell}} = \frac{1}{C_{diel}} + \frac{1}{C_g}$$

Equation 16

Lines *BC* and *DA* are the "active phase" of the discharge, when a plasma breakdown occurs. The gradient of these lines should, theoretically, be equal to the capacitance of the dielectric (C_{diel}) for a "fully bridged gap" [99].
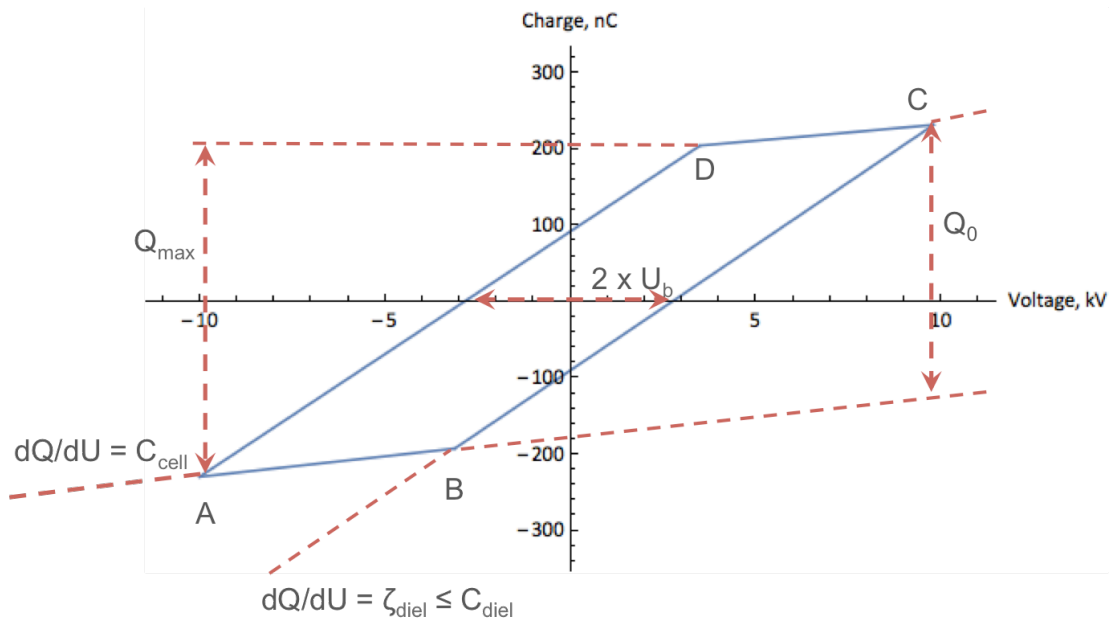
Figure 22: Lissajous figure generated from sampling potential difference over a monitor capacitor, and potential difference over a DBD plasma reactor. Red dots indicate sample points of experimental data, and blue lines show linear models fitted to the data using a least squares method.

The dielectric capacitance is determined entirely by the geometry of the DBD, which in the case of a typical, unpacked, coaxial DBD can be calculated using Equation 11. If the gap is not "fully bridged", i.e. not all of the charge accumulated on the dielectric layer is transferred during the plasma discharge phase, the capacitance measured from the gradient of the lines *BC* and *DA* is less than C_d. This occurs due to some areas of the electrode not becoming saturated with microdischarges [95, 100]. Saturation of the electrodes, and consequent full charge bridging of the gap tends to happen through the application of voltages that greatly exceed the breakdown voltage [100] or through the usage of packing materials [72].

Peeters & Van De Sanden [95] have developed an alternative equivalent electrical circuit and accompanying numerical model based on the geometry of the Lissajous figure, that can be used for instances where the DBD is only partially discharging. This alternative equivalent geometry, shown in Figure 23, splits the circuit into a non-discharging (α) fraction, and a discharging fraction (β).
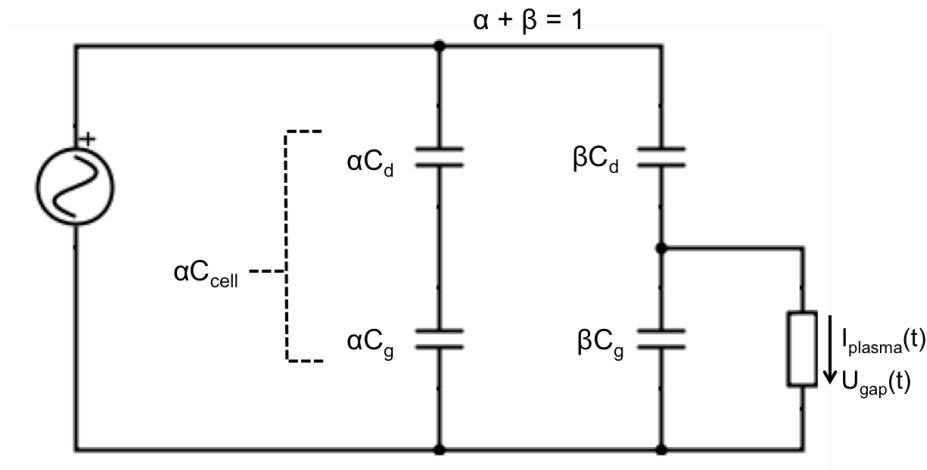
Figure 23: Alternative equivalent circuit of a partially discharging DBD, presented by Peeters & van de Sanden [95]

This alternative equivalent electrical circuit and accompanying mathematical treatment, addresses the problem of the calculated (a.k.a. effective) dielectric capacitance from the Lissajous figure (ζ_{diel}) (calculated from the gradient of lines *BC* and *DA* in Figure 22), being less than the actual dielectric capacitance of the reactor, C_{diel}. However, in order to apply this alternative mathematical treatment of the DBD reactor requires the value of C_{diel} to be well defined.

In a packed bed reactor, the capacitance of the packing material should also be taken into account. Mei et al [72] have proposed a simple model where the gap capacitance, C_{gap}, is treated as the capacitance of the gas (c_g) and packing material (c_p) as though they were two parallel plate capacitors. This is a simplified relationship, and although the actual capacitive behavior of the packed bed is more complex than this simplified model, it cannot be easily described by a simple mathematical relationship. In reality, each packing particle would act as an individual capacitor of unknown capacitance. However, this approach to equivalent circuit modeling would be very difficult to apply an actually packed bed DBD, hence the model proposed by Mei et al [72] is currently the best approach to mathematical representation of packed bed DBDs.

4 Experimental Design

In order to investigate the effect of packing materials in a packed bed plasma reactor, the experimental rig has a requirement of some minimum capabilities. These are:

1. An appropriate reactor in which a range of packing materials can be tested
2. The means to safely deliver known concentrations of reactant gases to the reactor, and to deliver the product gases from the reactor to the analytical equipment
3. A power supply to drive the reactor that is suitably matched to its electrical requirements, that can be controlled in a methodical and repeatable way
4. Electrical characterization techniques that allow the calculation of essential parameters, e.g. Power consumption
5. Gas analysis techniques that perform stably and reliably, and allow a complete mass balance of the gases over the reactor

This chapter focuses on these minimum requirements, and in some cases additional capabilities of the experimental rig are also discussed.

4.1 Introduction

As with any new project, the approach to experimentation evolves over time as new challenges arise. This introduction to the experimental design chapter offers an insight into the timeline of the project, and shows how and why the experimental plan has evolved in response to the challenges that presented.

The original experimental plan was to replicate the experiments of Futamura & Kabashima [76], where CO_2 and H_2O diluted with 97% N_2, are co-reduced to generate syngas in a $BaTiO_3$ packed bed reactor. The authors describe CO_2 conversions up to 12.3%, H_2 and CO yields of 12.4% and 11.8% respectively, which they report as being approximately 20 times higher than a dielectric barrier discharge reactor that they were using as a comparator. The reactor design, described in [101], is a co-axial geometry with an inner electrode diameter of 16.6 mm, outer diameter of 47.3 mm, gap distance of 15.4 mm, and a length of 127 mm. The reactor is driven by an 8kV, 50 Hz AC power supply. The authors do not describe the presence of a dielectric layer, or the materials from which the electrodes are constructed. The results reported by Futumura & Kabashima demonstrated promise, and the intention was to develop their reactor and test it at higher frequencies (from 10 – 60 kHz).

The 1ˢᵗ generation reactor design was a Perspex and stainless steel construction, with similar dimensions to the reactor used by Futamura & Kabashima. The reactor is a coaxial geometry with a central stainless steel live electrode, external stainless steel ground and a Perspex dielectric layer on the inside of the ground. A diagram and an image of the 1ˢᵗ generation reactor are shown in figure:
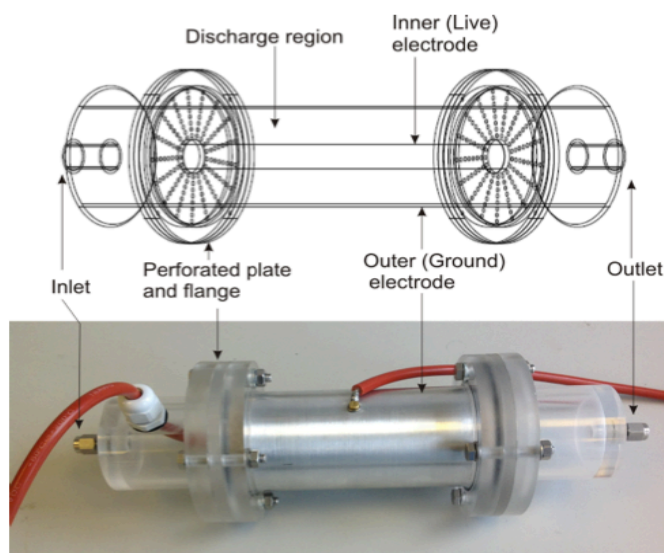
Figure 24: 1st Generation reactor. No longer used for experiments due to very large power requirement, as well as problems with arcing due to construction materials.

A private supplier was found to make the 1ˢᵗ generation power supply, with the following specification, Power output – 500W, Frequency range – 10 – 60 kHz, Voltage output – 10 kV (20 kV peak to peak). Unfortunately, there were a number of problems with these specifications, which were not foreseen, primarily due to inexperience. Firstly, Perspex is a very poor dielectric material as it has a low melting point, and a low dielectric strength leading to failure at low applied voltages. Secondly, due to the electrode spacing of the reactor the potential difference required to drive the reactor with a pure CO_2 gas stream would be greater than 10 kV. Thirdly, due to the volume of the reaction chamber the power required to effectively drive the reactor would be very high, particularly with a pure CO_2 stream. Finally, the specifications for the power supply are extremely demanding, especially considering it was to be designed and constructed by an amateur in a short space of time.

The power supply never operated as it was specified to do so. The highest stable output voltage never exceeded 3.5 kV, as shown in Figure 25. If the voltage was increased beyond 3.5 kV, the output signal became very unstable over all frequencies, as shown in Figure 26. Unfortunately, although the high voltage output was insufficient to generate a stable plasma, through its instability it did cause an arc through the Perspex dielectric of the reactor, destroying it in the process.
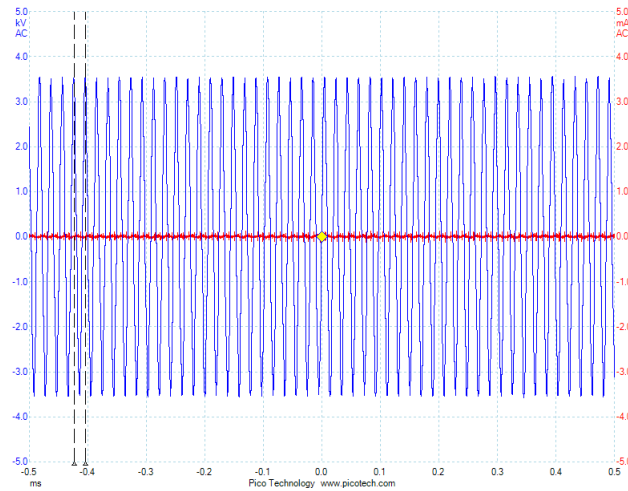
Figure 25: Stable output at 3.5 kV from the 1st generation power supply
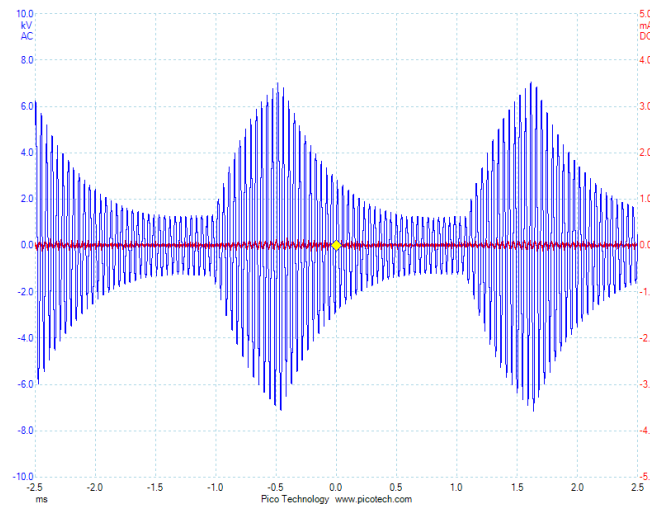
Figure 26: Unstable output of the 1st generation power supply

Both the 1st generation reactor and power supply were subsequently scrapped.

The 2nd generation of power supply was a second hand Trek 10/10B high voltage amplifier. The 2nd and 3rd generation reactor evolved from the necessity to progress quickly, which meant avoiding unnecessary delays in manufacturing. It was produced by the University glass blower from Borosilicate glass. The 2nd generation power supply and reactor operated relatively well together, but early experimentation showed very low CO_2 conversions due to the limited power densities that could be applied using the 2nd generation power supply. A 3rd generation power supply, a Trek 10/40a-HS, was ordered and it effectively addressed the problems of having insufficient power. However, the high power of the 3rd generation of reactor caused failure of the 2nd and 3rd generation reactors due to arcing over long periods of operation. Finally, a 4th generation of reactor was designed, with the main reactor body constructed from quartz glass, a material with a much higher dielectric strength and stability in a strong AC electric field than borosilicate glass. The details of this reactor are described in section 4.3.

4.2 Experimental Set-up Overview

A schematic showing a block diagram of the experimental set-up is shown in Figure 27.
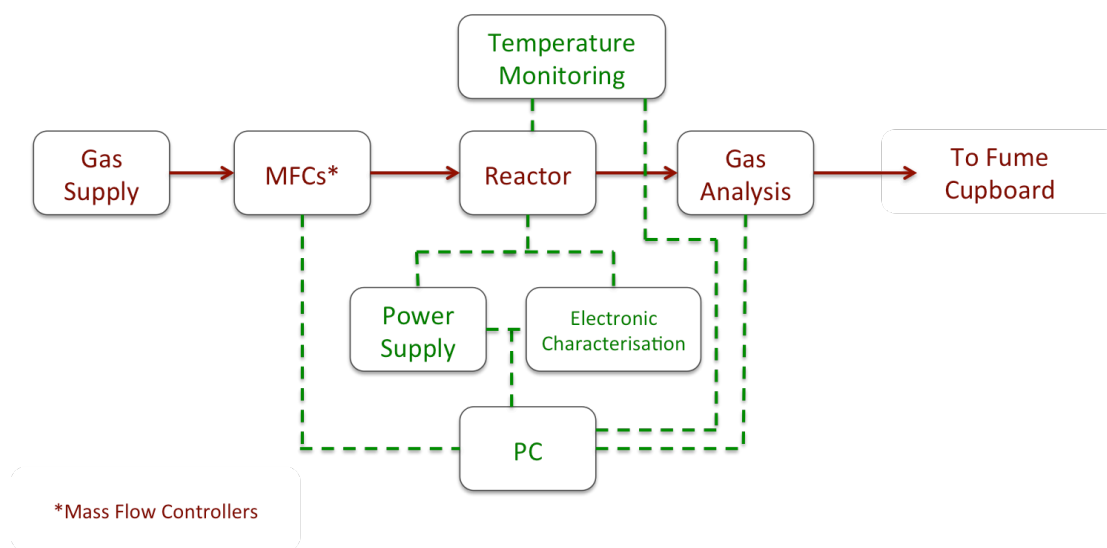
Figure 27: Block diagram showing an overview of the experimental set-up

Each component of the block diagram is described briefly below, with a more in depth discussion provided in the section indicated in brackets.

The reactor used is a quartz glass coaxial DBD (Section 4.3) that can support approximately 3.5 cm^3 of packing material in the space between its electrodes, having an electrode spacing of 6 mm. The range of gases used in the reactor are argon (CP grade), CO_2 (CP grade), CO (research grade) and O_2 (Research Grade) (all Supplied by BOC), at flowrates up to 200 ml/min each, controlled by Bronkhorst EL-Flow mass flow controllers (MFCs). The reactor is driven by a high voltage amplifier (Trek 10/40B-HS) (Section 4.4) with signal amplitudes up to 10 kV, at frequencies up to 10 kHz with a range of possible applied voltage waveforms generated by the analogue output of a Labview controlled data acquisition device (Section 4.4.2). Characterisation of the electrical properties of the reactor is achieved by sampling 3 signals (Section 4.4.3): voltage applied to the reactor, instantaneous current measured by a Rogowski coil, and the charge transferred in the reactor measured using a "monitor capacitor". The reactor external wall temperature is monitored using an Omega USB IR temperature sensor. Product gas analysis is carried out using Fourier Transform Infrared (FTIR) Spectroscopy (Section 4.5.2) and Mass Spectrometry (MS) (Section 4.5.3).

4.3 Reactor Design

The reactor is a coaxial type dielectric barrier discharge, fabricated from quartz glass. Packing materials are supported on an internal quartz glass support plate. The packing is fed into the reactor via a 3/8 inch, gas sealed, screw cap that sits opposite the gas inlet. The gas inlet and outlet are ¼ inch in external diameter in order to be used with plastic, ¼ inch push fit gas connectors. The reactor also features a small weir at the base in which any dust from packing materials collects, as well as any liquid that is condensing. This is particularly important when using hygroscopic packing materials (e.g. Alumina) as any water absorbed by the material collects here, rather than going to the analytical equipment. The condensed liquid can then be easily evaporated using a heat gun, this is typically carried out prior to carrying out an experiment in order to make sure the reactor contains minimal water vapour.

The central, live electrode is an uncoated stainless steel rod, that is fixed in a central position from either end. The live end of the live electrode passes through a porous quartz glass packing support plate, with a 3mm hole drilled out of its centre. The floating end of the electrode is rounded and smoothed in order to reduce the formation of corona discharges on the tip of the electrode. The terminated end of the live electrode passes through a gas sealed, plastic screw cap, with the end of the electrode threaded into a male Genvolt 30 kV high voltage connector.

The ground electrode is created using silver paint painted onto the exterior of the reactor body, with this connected to the ground cable using a tightly connected copper strip and a crocodile clip. Silver paint is used for the ground material as the electrode sits directly on the surface of the dielectric, with no space for a gap in which an air plasma can form between the electrode and the dieletric material, potentially affecting the outcome of the electrical measurements made. Silicone sealant is applied to the edges of the painted ground electrode in order to prevent plasma discharges that over time are found to corrode the silver paint electrode.

An overview of the reactor, showing the key features, is shown in Figure 28.
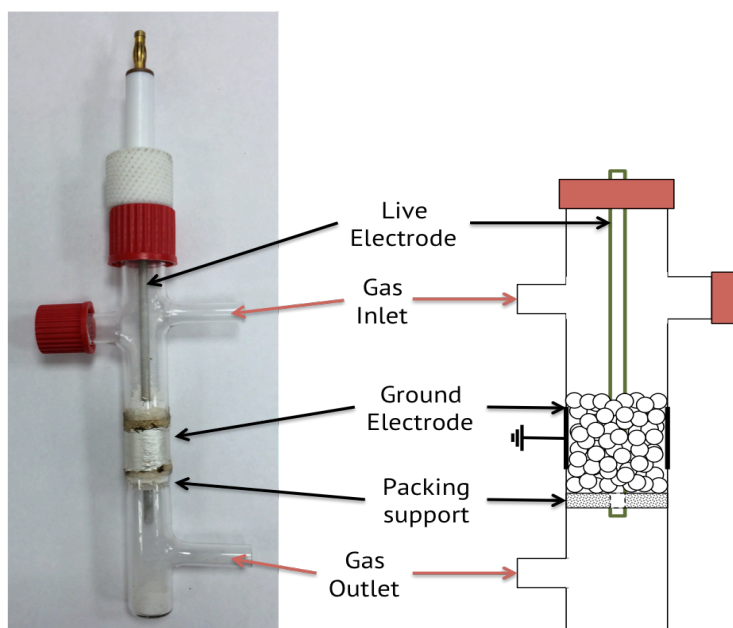
Figure 28: Annotated reactor image and diagram

The reactor dimensions of the active plasma region are shown in Table 4:

Table 4: Reactor dimensions in which plasma generation occurs

Parameter	Dimension
Outer Diameter	15 mm
Internal Diameter	13 mm
Wall Thickness	1 mm
Live Electrode Diameter	3 mm
Ground Electrode Length	18 mm
Inter Electrode spacing	6 mm
Volume between electrodes	2.3 cm^3
Packed Bed Volume	3.5 cm^3

4.4 Power supply operation & electrical characterisation

4.4.1 Overview

In order to generate plasma in the reactor, and to collect data to characterise its behavior a range of experimental equipment is required. A diagram showing the equipment used, and the direction and type of electronic signal transmission is shown in Figure 29.
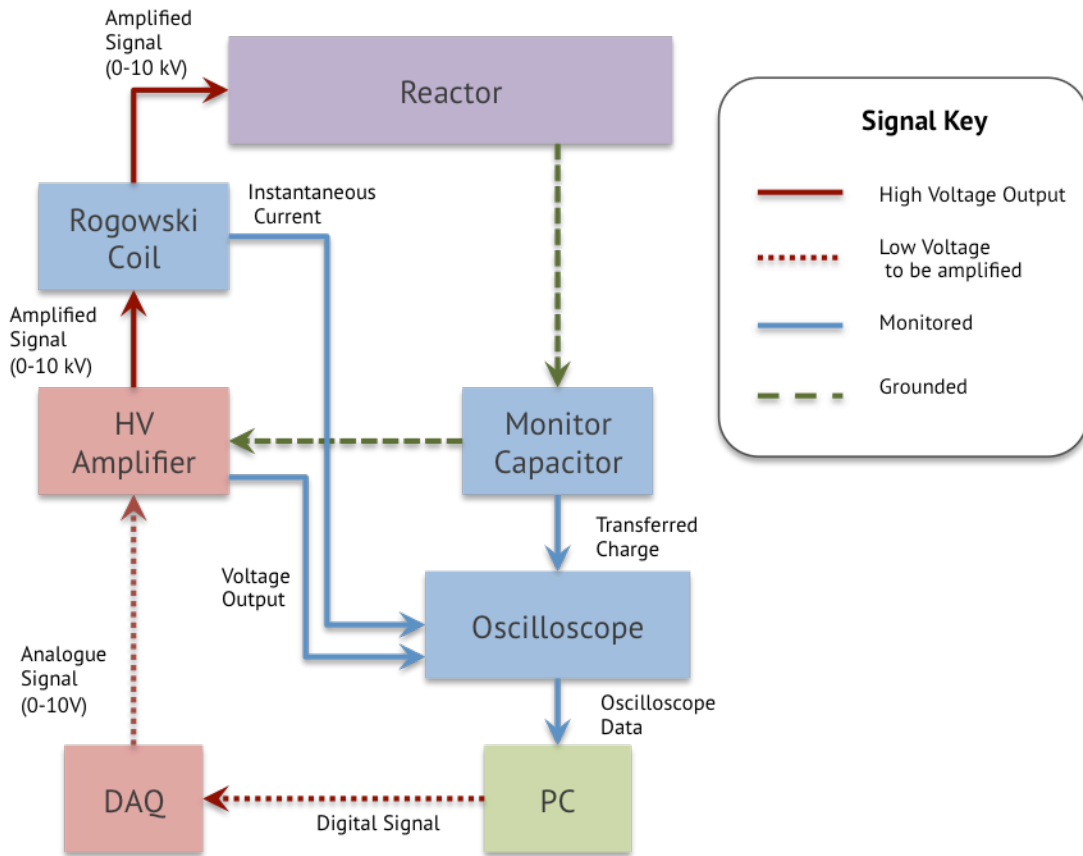
Figure 29: Experimental setup used for plasma generation and characterization. Showing type and direction of the electronic signals transmitted.

A high voltage amplifier (Trek 10/40a-HS) is used to drive the reactor, the properties of which are given in Table 5. The high voltage (HV) output signal is applied to the central, live electrode of the reactor. The HV output is monitored using an oscilloscope (Picoscope 6404c) using the amplifiers built in HV monitor (Signal verified using Tektronix P6015A High Voltage probe). The high voltage cable that is used to carry the HV signal passes through a wide band current monitor (Pearson Electronics 4100 - Rogowski coil) connected to the oscilliscope that is used to monitor instantaneous current. The ground cable from the reactor is connected back to the HV amplifier, via a 47 nF (±10%), polyester layer capacitor connected in series with the reactor. This capacitor is used to measure total charge transferred during a plasma discharge cycle in the reactor by measuring the potential difference across it, a method discussed in section 3.2. This potential difference across the capacitor is measured using a 10:1 passive oscilloscope probe (Picoscope TA133) connected to the oscilloscope. The HV output signal generated by the amplifier is controlled by a Labview operated National Instruments USB–6211, a data acquisition device (DAQ) that is used to generate analogue signals, i.e. it operates as a function generator. Depending on the experiment being carried out, data from the oscilloscope is either, collected and analysed in real time using Labview, or collected using the Picoscope software for subsequent export to a Mathematica based analysis program.

Description	Specification
Output Voltage Range	0 to ±10 kV DC or peak AC
Output Current Range	0 to ±40 mA DC or AC rms, Peak = ±120 mA for 1 ms
Slew Rate	900 V/ µs
Large Signal Bandwidth	DC to greater than 9 kHz (The unit will trip when the maximum bandwidth is reached)
Internal Capacitance	133 pF

4.4.2 High Voltage Signal Generation Performance

For a plasma generation system, the power supply must be matched to the reactor. The output signal voltage, frequency, and current capacity must be similar to the requirements of the reactor. Also, as the reactor behaves as a resistive-capacitive load, the power supply should be able to act as both a sink and a source of current. It is important to understand the limitations of the equipment available, and although to a certain extent matching of reactor with power supply can be a trial and error process, there are guidelines and estimations that can be used to inform decisions regarding the power source.

Trek recommends using the formula given in Equation 17 to calculate the peak current (I_{peak}) required of the power supply for generating a Sine output signal.

$$I_{peak} = (C_{load} + C_{int}) \bullet \pi \bullet f \bullet V_{p\text{-}p}$$

Equation 17

where C_{load} is the load capacitance, C_{int} is the power supply internal capacitance (133 pF), f is the AC frequency to be used, and $V_{p\text{-}p}$ is the peak-to-peak voltage (20 kV) to be applied. Using Equation 11, it is possible to calculate an estimate for the maximum reactor capacitance (C_{load}) of the empty reactor as approximately 50 pF [2]. Equation 17 can be rearranged to solve for maximum operating frequency, substituting in known values and taking peak current (From Table 5) as 120 mA, *f* can be calculated as 10,360 Hz.

Experimental determination of the performance of power supply for driving the reactor shows that the possible operating frequency ranges from DC to approximately 11 kHz (with a 10 kV

---

[2] $C_d = \frac{2\pi\varepsilon_0\varepsilon_q l}{\ln\left(\frac{d+x}{d}\right)}$ Max reactor capacitance occurs during the discharge on phase, i.e. C_{tot} = C_d. Using reactor dimensions and properties for quartz glass: ε_0 = 8.854E-12, ε_q = 3.8, l = 0.018, d = 0.0065, x = 0.0005. ∴ C_d = 51.3 pF

Sine wave) before the power supply trips (i.e. Peak current > 120 mA), using an empty reactor in pure CO_2. This agrees very well with the calculated limit to operating frequency, and consequently gives a limit of 10 kHz to the frequency range that can be used in this experimental work.

In this work, the DAQ is used to generate a low voltage signal, which is amplified 1,000 times by the amplifier in order to drive the reactor. The sample rate limit to the analogue output of the DAQ is 250,000 samples per second. Given that the maximum signal output frequency of the HV amplifier can be taken as ~10 kHz, a signal generated by the DAQ at this frequency with a sample rate of 250 kHz would generate a signal with 25 samples per cycle. This sample rate would not be a problem for generating sine waves from the amplifier, but it may be problematic for signals that inherently require a fast rise time, e.g. square waves. The effect of the sampling rate of 25 samples per cycle on the signal output of a square wave is shown in Figure 30.
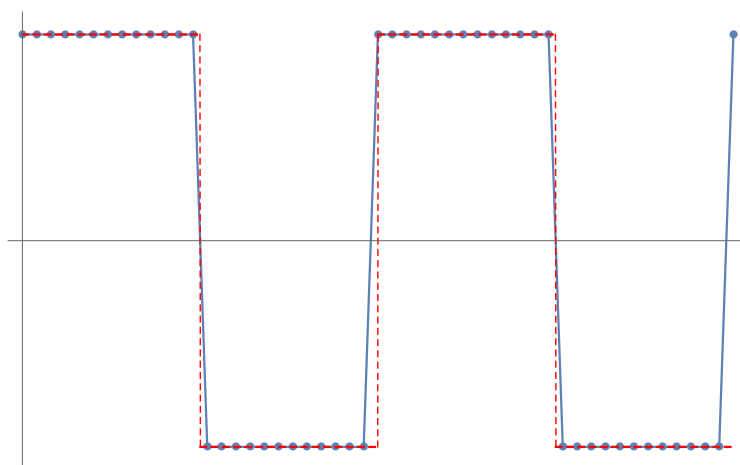
Figure 30: Effects of sample rate on generation of a square wave. Sample frequency shown is 25 samples per cycle. The dashed red line shows the input signal to the sample generator, whilst the blue signal shows the output with points indications sample locations.

Although the output signal is clearly affected by the sample rate, causing the square wave to become distorted, it is only a problem if the output signal rise time from the DAQ is longer than the HV amplifier output signal rise time. Figure 31 compares the signal from the DAQ (blue) with the HV amplifier (red). The reported rise rate (slew rate) of the signal from the HV amplifier is 900 V/μs. Using an oscilloscope, the measured rise rate of the signal from the DAQ is 4,016 V/μs, which gives a HV output signal rise rate of 854 V/μs. Using the square wave input from a dedicated function generator the measured rise time of the output high voltage square wave is 861 V/μs. This gives less than 1% reduction in rise time using the DAQ compared with a function generator.
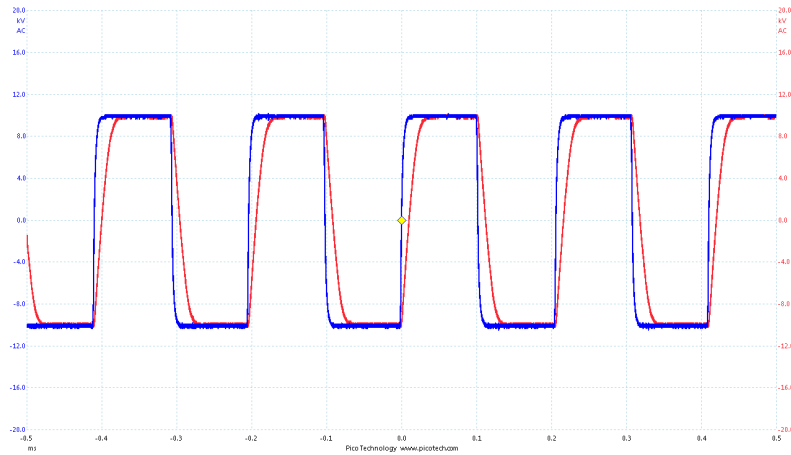
Figure 31: NI USB-6211 analogue signal output (Blue), and HV amplifier signal output (Red) compared for a square wave at 5 kHz and 10 V / 10 kV. Data collected using Picoscope software.

4.4.3 Electrical Characterisation

As shown in Figure 29, there are 3 electrical signals that are monitored using the oscilloscope that are collected in order to characterise the behavior of the reactor:

1. High voltage output from the amplifier
2. Instantaneous current measured using a wideband current monitor
3. Reactor charge transferred, measured from the potential difference over a capacitor in series after the reactor

Figure 32 shows a sample oscilloscope trace of all 3 of these (unprocessed) signals, with 3 different time scales shown. The time scale for the top image is 100 µs/div, and the middle and lower images are sections from the original oscilloscope data magnified by 8x and 2,048x respectively.
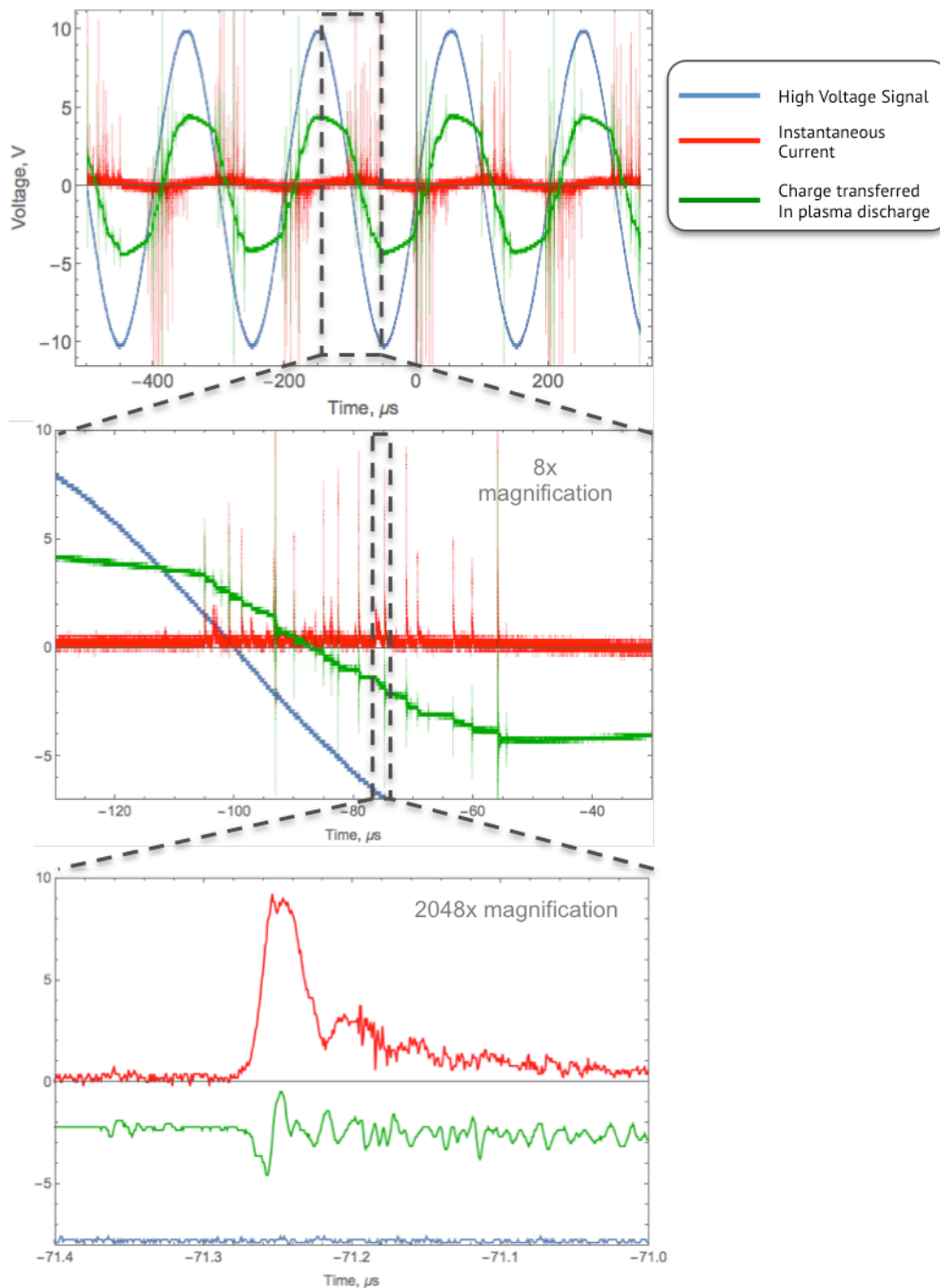
Figure 32: Sample oscilloscope trace showing unprocessed signals of voltage, instanenous current and charge transferred in the plasma. Data is obtained using $300 - 500$ μm Al_2O_3 particles, with a 5 kHz, 10 kV, Sine wave in 50% $CO_2 - 50\%$ Ar. Oscilloscope set-up: Sample Interval - 800 picoseconds, 100 μs/division. Image generated using Mathematica.

From the graphs shown in Figure 32 it is possible to see that processes that can be observed with the oscilloscope happen over a wide range of timescales. The applied voltage (blue) in this example is sinusoidal with an amplitude of 10 kV, at a frequency of 5 kHz. The instantaneous current signal (red) in the image shows a number of very fast, high amplitude pulses occurring, this is indicative of plasma micro discharges. Although the oscilloscope is sufficiently fast to accurately resolve these events (800 ps sample interval), the minimum usable rise time of the current monitor is limited to 10 ns. This limits the quantitative application of this device for very

short duration events. For an insight into the timescales of microdiscarges, the duration of the pulse shown in Figure 32 is approximately 150 ns, although it is expected in high CO_2 concentrations this value will significantly decrease. Falkenstein & Coogan [93] report individual microdischarge pulse durations in DBDs ranging from 15 to 200 ns in mixtures of N_2 and O_2, with increased concentrations of more electronegative O_2 causing a significant decrease in pulse duration.

If a QV plot (shown in Figure 33) of the scaled and processed signals from Figure 32 is made, i.e. charge measured by the monitor capacitor (green) plotted against applied voltage, the burning voltage of the reactor can be easily measured. As described in section 3.2, the x-intercepts of the Lissajous figure correspond to the burning voltage of the reactor. In this example, Figure 33, shows that the burning voltage is between approximately 4 – 4.8 kV and -3.7 – -4.3 kV on the two opposing parts of the cycle.
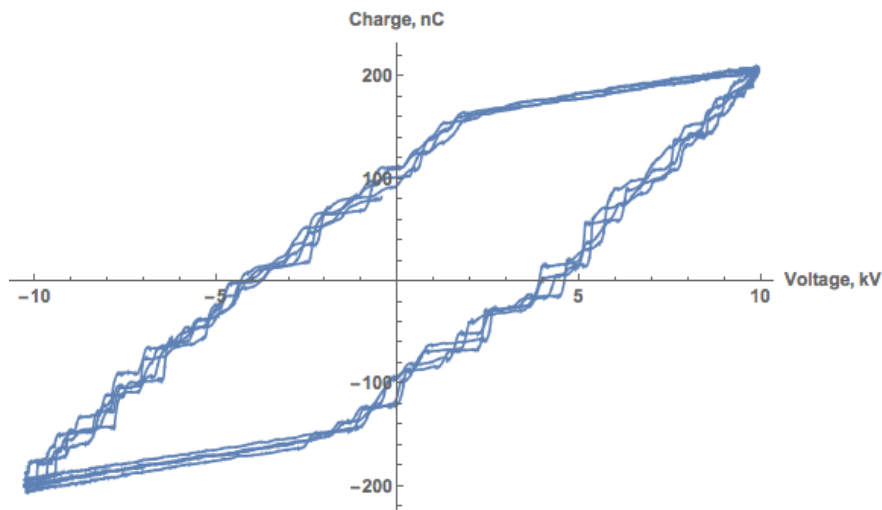
Figure 33: Example Lissajous plot

The data used to plot Figure 33 is based on 3 ½ cycles of the applied AC signal. The data presented in Figure 33 appears to be noisey during the plasma discharging phase of the Lissajous figure as multiple steps appear in the data. This is actually due to microdischarge pulses transferring large amounts of charge during individual current pulses. This can be confirmed by carefully examining the middle graph in Figure 32, the high amplitude, long duration pulses shown by the red line (instantaneous current), correspond with large step changes in the green line (charge transferred). The magnitude and duration of these pulses is clearly of academic interest, so further data smoothing techniques should not be applied to eliminate these features in order to obtain, for example, more easily readable breakdown voltages. Alternatively, collecting large sample sizes and applying linear regression techniques to automatically fit models to the data is preferable. This allows the integrity of the information contained within the data to be maintained, whilst allowing the possibility to analyse a range of

data sets quickly, with the possibility of easy retrospective analysis of data sets that are of particular interest.

Electrical signals are analysed using two different software packages, both of which are based on the methods described in section 3.2:

1. A Labview method for live calculation of reactor power consumption. This uses the Q-V plot Lissajous method to calculate the area confined by the hysteresis loop multiplied by the applied frequency, and subsequently averaged out over 200 discharge cycles. The Labview program is shown in the appendix in section 9.1.

2. A Mathematica based method where a range of electrical characteristics are obtained from the Q-V Lissajous plot. This includes reactor capacitances, charge transferred during a discharge cycle, breakdown voltage, and power. The sample method is user controlled, with data collected using the Picoscope software and exported as "comma separated values". Up to 200 discharge cycles are used, at sample intervals equating to 6.4 ns, typically giving approximately 12.5 million samples. The Mathematica program is shown in the appendix in section 9.2

The Labview program is used to generate the power consumption data used in chapter 6, whilst the Mathematica program is used for analysis of the data in chapter 7.

The Mathematica program consist of 8 steps:

1. Importing and preparing data.
2. Smoothing of data. This uses the Savitzky-Golay method [102] of data smoothing, which is a well documented technique to minimise signal distortion whilst improving the signal-to-noise ratio.
3. Removing invalid data points (e.g. infinite values).
4. Generating a Q-V Lissajous plot.
5. Finding approximate maxima, minima and intercepts of the plot.
6. Using arbitrary relationships based on these intercepts and extrema to define 4 separate regions corresponding to the 4 different phases of the hysteresis loop.
7. Using a least squares method to fit 4 separate linear models to this data
8. Extracting useful data from the linear models.

A sample of the Q-V Lissajous plot generated using this program featuring the 4 linear models and the input raw data is shown in Figure 34.
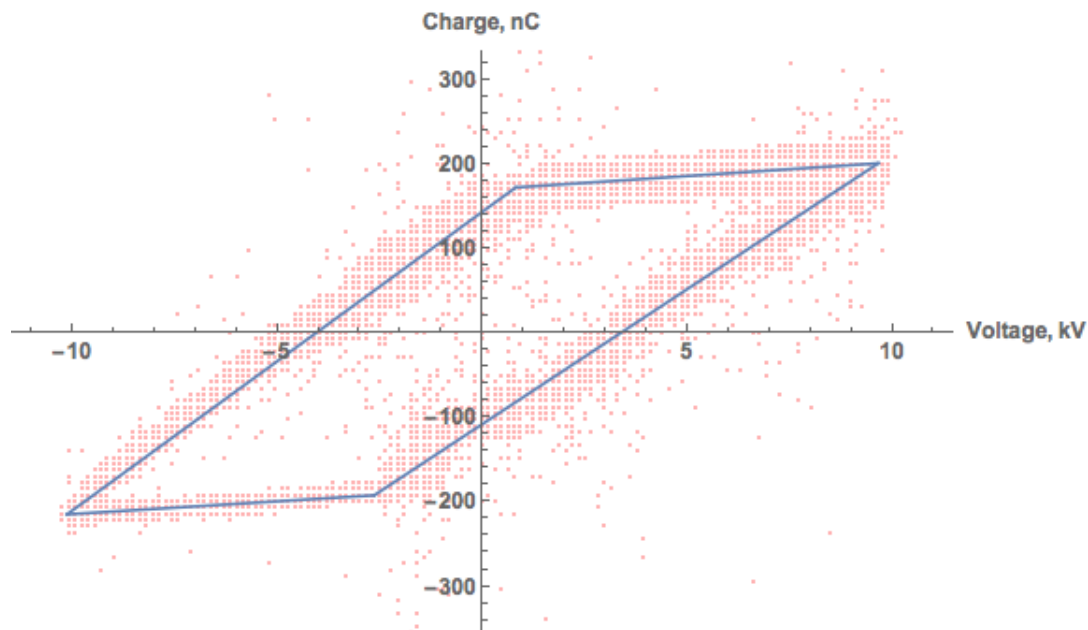
Figure 34: Lissajous figure with 4 independent linear models corresponding to different phases of the plasma discharge cycle.

4.5 Product Gas Analysis

4.5.1 Introduction

The product gases from the reactor are analysed by one of two methods, either Fourier transform infrared spectroscopy (FTIR), or mass spectrometry (MS). Initially, gas analysis was attempted using gas chromatography (GC) with a thermal conductivity detector (TCD). However, it was found that over a period of about month that the calibration of the GC was drifting, with the measured concentration of gases appearing to increase. Prior to each experimental run, a stream of 100% CO_2 was sent to the GC to check the calibration. At the point at which the GC method was no longer used, the CO_2 concentration from this pure stream of CO_2 was measured as 130%. The GC manufacturers (Agilent) state that corrosive gases can damage the TCD. The TCD consists of a wire heated to 250°C with a coating to prevent oxidative damage to it. Highly corrosive gases can damage this coating, and so damage to it would appear initially as increase in the sensitivity of the GC, consistent with the effects that were being observed with the laboratory GC. One of the possible product gases from plasma initiated CO_2 reduction is O_3 [103], and this was not being detected in the GC. It is also known that in DBD reactors that O_3 production is inhibited by high temperature due to rapid degradation of the molecule leading to formation of O_2 and atomic oxygen, a very powerful oxidizing agent [104]. The possible cause for the degradation of the TCD could have been temperature induced decomposition ozone leading to formation of atomic oxygen, which in turn would degrade the protective coating of the TCD.

Alternative analysis methods to GC were sought, and FTIR was deemed an appropriate alternative as it is able to detect CO_2, CO and O_3. Initial tests using FTIR demonstrated the presence of O_3 in the product gas, providing evidence for the cause of the change in behavior of the GC. In addition to FTIR, mass spectrometry was additionally utilised as an analytical technique as it allows real time observation and analysis of the product gases. A full description of the method development used for the FTIR and MS are given in sections 4.5.2 and 4.5.3.

4.5.2 Fourier Transform Infrared Spectroscopy

Fourier Transform Infrared spectroscopy (FTIR) is an optical technique where infrared light over a range of wavelengths is passed through a sample of a specimen of interest. This sample will then absorb some of the light in a characteristic wavelength dependant upon its composition. A detector on the opposite side of the specimen sampling system will quantify the subsequent change in light intensity relative to a reference cell. The Beer-Lambert law, given by Equation 18, is used to determine the concentration of a species based on this change in light intensity. I_0 is defined as the light intensity passing through the reference (background) cell, I is the light intensity passing the through the sample of interest, ε is the molar absorptivity of the species of interest (N.B. This parameter varies dependent upon wavelength of the light applied), l is the path length of light through the sample, and c is the species concentration.

<div align="center">Equation 18</div>

$$\log \frac{I}{I_0} = \varepsilon l c$$

FTIR is a technique that can be applied for solid, liquid or gaseous samples. The FTIR is used to quantify the concentration of CO_2, CO and O_3 from the outlet of the reactor. FTIR can only be used to detect and quantify molecules that are "IR active". Molecules are IR active if a molecular vibration (See section 2.2.2 for more information on vibrational excitation) causes a change in the dipole moment of a molecule. Consequently a number of gases that are used and produced in this experimental work cannot be detected, for example O_2 and Ar. In order to be able to carry out a complete mass balance additional gas analysis techniques are required, hence mass spectrometry is used in addition to FTIR.

The general procedure for using an FTIR consists of two steps. The first step is to take a background measurement, and the second step is to take a sample measurement. The background is the scan against which all subsequent scans are measured, i.e. it is the equivalent of zeroing the instrument. The sample is the scan that is used to obtain experimental concentration data. The choice of gas composition used for a background scan has an impact on the outcome of the subsequent measurements. There are two options for choice of background

gas composition; either to use an IR inert gas such as argon or nitrogen, or to use the gas composition that is being used as the experimental feed to the reactor (e.g. 90% Ar and 10% CO_2). If the former option is chosen, then all peaks in sample scans will appear as positive peaks on the y-axis. The disadvantage to this method is that it is difficult for a user to observe small changes in gas composition, as well as it being difficult to tell when the FTIR is taking poor quality samples. This is due to the fact that the CO_2 peak will always appear relatively much larger than any other peaks in the spectrum. The latter method is beneficial, as increase in the concentration of a gas appear as positive peaks, and decreases in the concentration of a gas are observed as negative peaks. It is also much easier for an FTIR user to observe when the FTIR is taking poor quality samples. The disadvantage to this method is that it may be less effective at measuring very small changes in CO_2 concentration; this is due an overlap in the IR spectra of CO_2 and water vapour. This is explained in more detail later. The choice of gas composition for the background in this work is gas with the experimental gas feed composition, i.e. the latter option.

Before using an FTIR there are a number of important considerations that need to be taken into account, the first is to make sure that the accessories being used with the FTIR are appropriate for the application. The gases that are being detected, CO_2, CO and O_3, show absorbance peaks in the regions from approximately 500 to 4000 cm^{-1} wavenumbers. A table summarising the FTIR accessories and the reason for their selection is summarised in Table 6. The FTIR itself is a Varian 660-IR.

Table 6: A summary of FTIR accessories and fittings used, and their properties that are critical in their selection

Accessory	Specification	Properties	Manufacturer
IR Source			
Detector	Mercury Cadmium Telluride (MCT)	High sensitivity, and operable range from 650 – 8,000 cm^{-1} wavenumbers	Varian
Beam Splitter			
Gas cell window material	Germanium	Transmission range from 830 - 5,000 cm^{-1} wavenumbers. Not soluble in water, non-toxic. Durable.	Kromatek
Gas Cell Path Length	5 or 10 cm	2 different gas cells, allows option of a long path length for high sensitivity to trace gases, as well as small volume allowing for faster and more sensitive performance with very low flow rates	

4.5.2.1 FTIR Calibration – Peak selection

In order to use the FTIR for quantitative analysis of the product gases, it must first be calibrated. Any IR active species will have a number of characteristic peaks. The area under a peak is proportional to the concentration of the species, as defined by the Beer-Lambert law. The process of calibration therefore involves passing the gases of interest through the FTIR gas cell over a range of concentrations, and measuring the change in the area of the peaks. In order to find the area of the peaks, the peaks themselves need defining. There are 5 points required to define one peak, the centre point, the left and right edges, and the left and right baselines. The centre point has no impact on the area calculation; it is used simply to define the name of the peak by the software. The left and right edges constrain the integration to an interval on the x-axis. The left and right baseline points are used to define the region within which the baseline is "flat". The left and right baseline points are connected by a straight line, this acts as the boundary above which the area of the peak is calculated. Each peak must be defined in such a way that the peaks of other components will have minimal effect on the integration calculation that corresponds to the species concentration.

Calibration of the FTIR requires careful consideration of the spectrum of each IR active species that may be present. These species are CO_2, CO and O_3 from the reactor, as well as H_2O in both gaseous and liquid forms that can originate from absorbed water in the packing material, as well as atmospheric water vapour. The characteristic spectra for each species of interest are shown in Figure 35 to Figure 39.
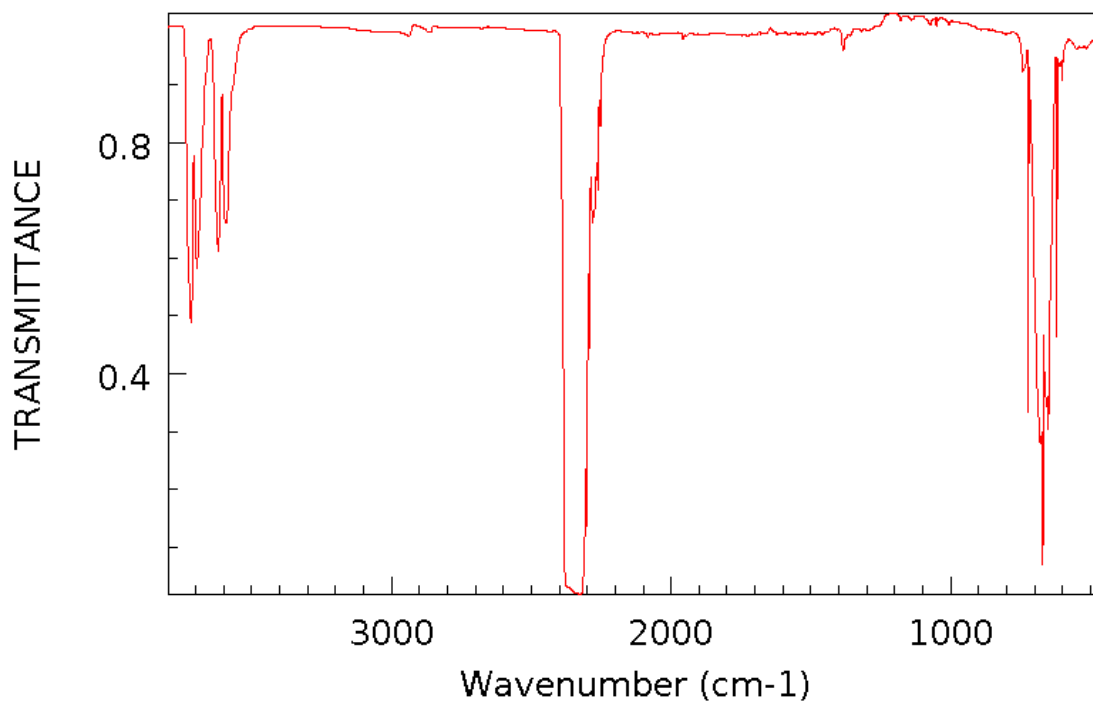
Figure 35: IR transmission spectrum of carbon dioxide. CO_2 at 26.7 kPa, diluted with N_2 to a total pressure of 80 kPa. Path Length – 10 cm, resolution 4 cm^{-1}, instrument – Dow KBr foreprism. [105]
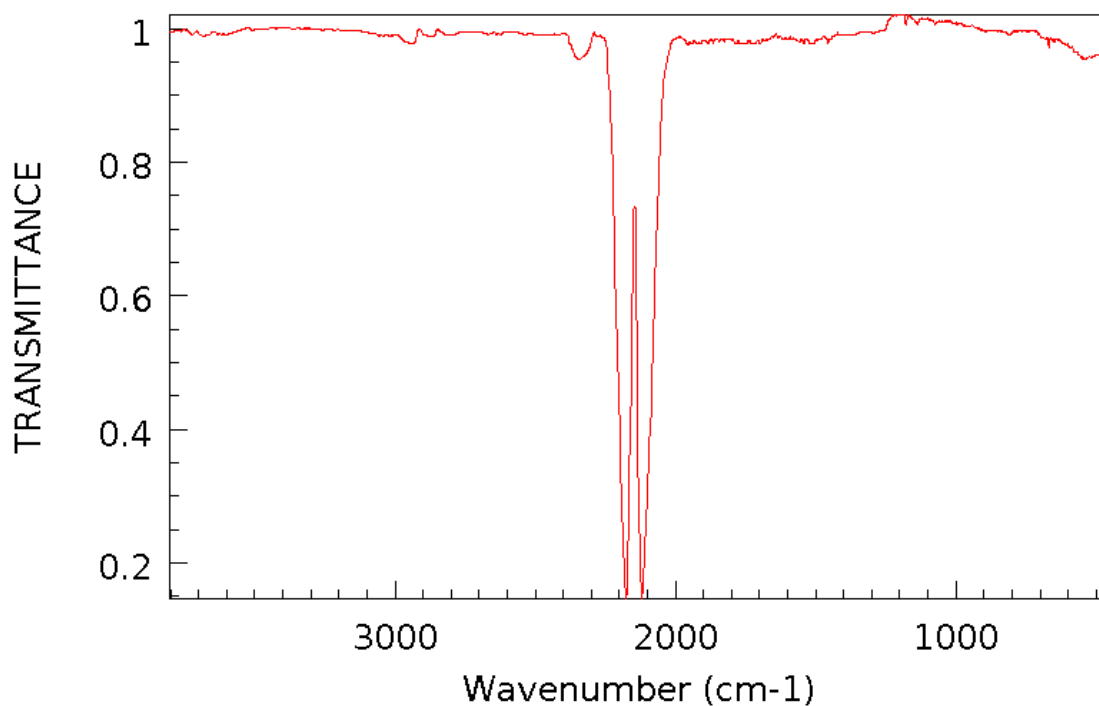
Figure 36: IR transmission spectrum of carbon monoxide. Note that rotational lines in the region 2000 - 2250 cm^{-1} wavenumbers are smoothed in this spectrum. An experimental spectrum of carbon monoxide would show peaks in the same region, and general shape but would consist of a large number of narrower peaks. Carbon monoxide at 53 kPa diluted with N_2 to 80 kPa. Path Length – 10 cm, resolution 4 cm^{-1}, instrument – Dow KBr foreprism. [106]
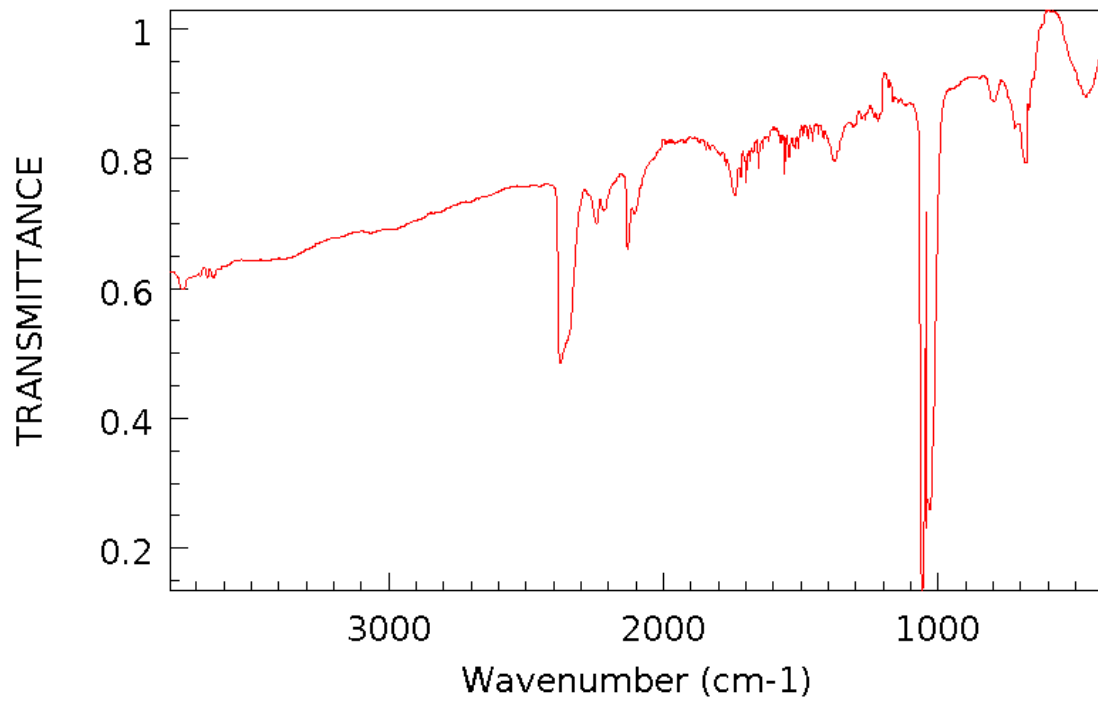
Figure 37: IR transmission spectrum of ozone. The main peaks corresponding to ozone absorbance occur at approximately 1000 – 1100 cm^{-1} wavenumbers. The concentration of ozone is estimated to be 40 ppm. There is absorption due to two unknown species, at 2244 and 2215 cm^{-1} wavenumbers, as well as absorption due to CO_2 at 2376 cm^{-1}. Path length – 1000 cm, resolution 2 cm^{-1}, instrument – Beckman IR9. [107]
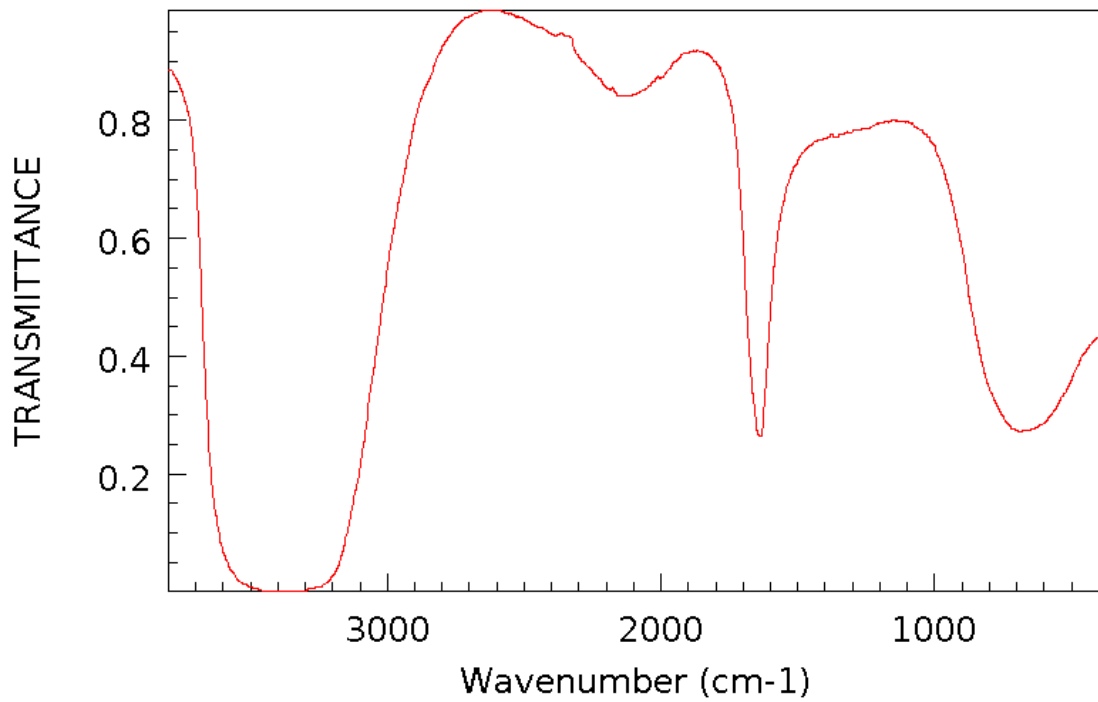
Figure 38: Liquid water IR transmission spectrum. Pure liquid water. Path Length – capillary, AgCl plates. Resolution 4 cm^{-1}. Instrument – Dow KBr foreprism. [108]
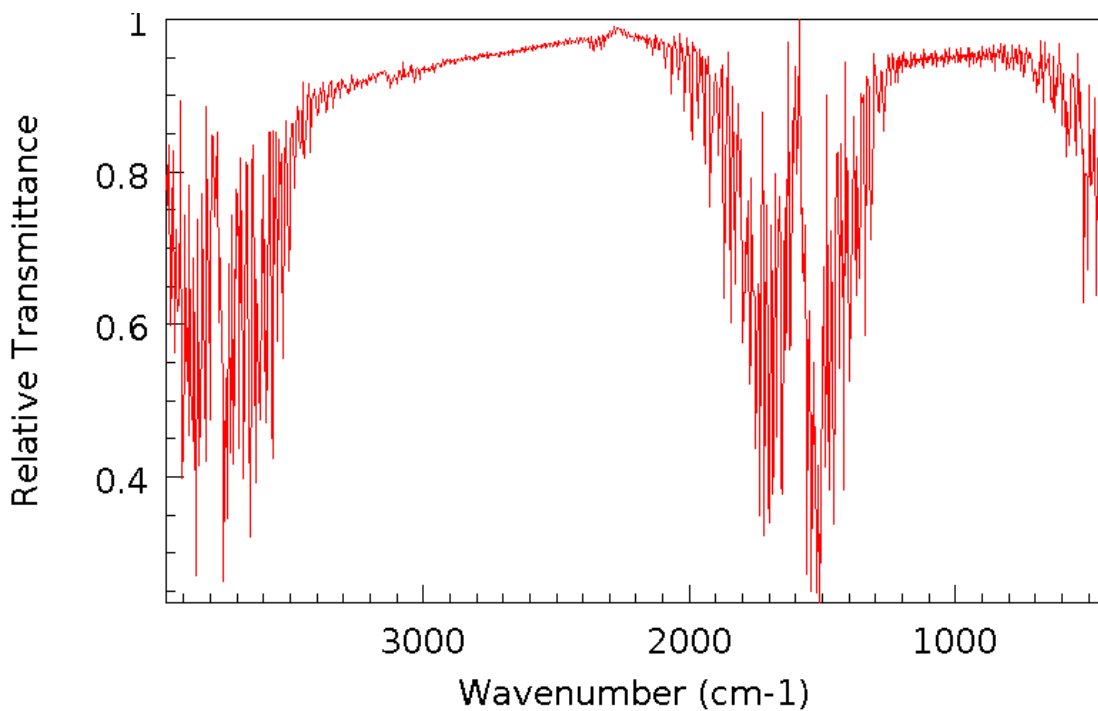
Figure 39: Gaseous water IR transmission spectrum. Species concentration, instrument, resolution and path length not specified. [109]

An ideal experimental FTIR spectrum is shown in Figure 40. Please note that in this figure, a positive value for absorbance indicates an increase in a species concentration, and conversely a negative value indicates a decrease in a species concentration, the reason for this is discussed in further detail in section. With reference to figures Figure 35 Figure 37, it can clearly be seen that there is an increase in the concentration of CO and O_3, and a decrease in CO_2 concentration.
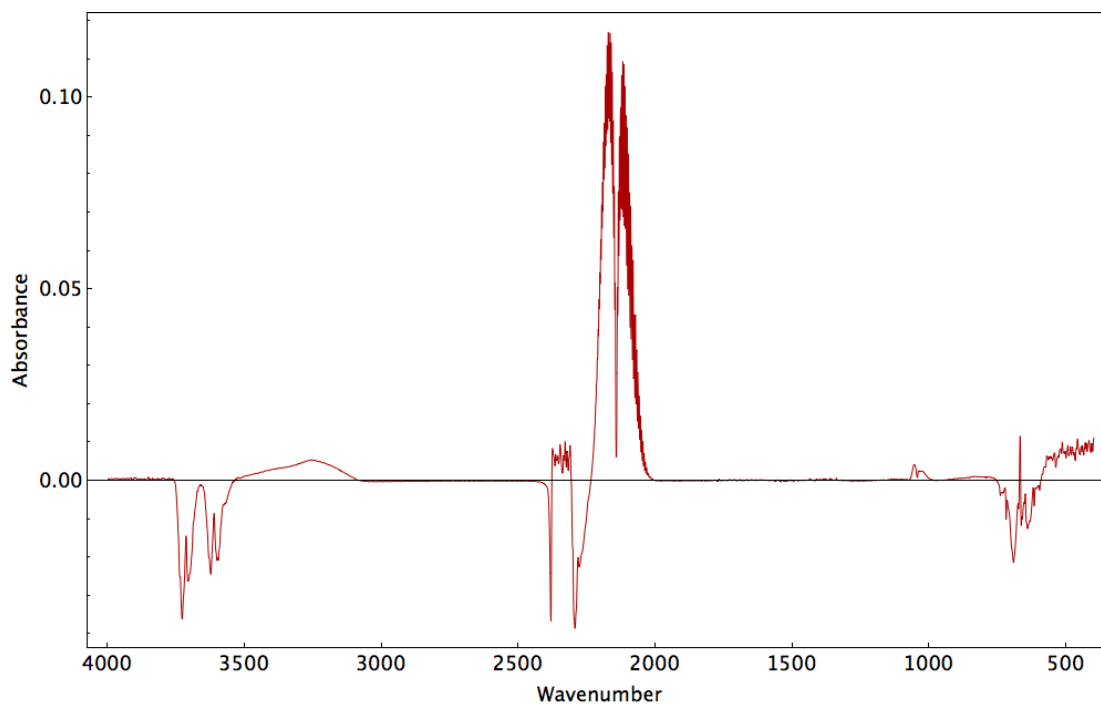
Figure 40: Typical FTIR spectra obtained experimentally for the reduction of CO_2. This data is taken from an experimental run using 50 ml/min CO_2, 50 ml/min Ar, with 500-850 μm Al_2O_3 particles in plasma generated at 10 kV, with a 5 kHz square wave.

A positive carbon monoxide peak is seen clearly at the $2,000 - 2,300$ cm^{-1}, as well as a small but positive ozone peak at $1,000 - 1,100$ cm^{-1}. Peaks corresponding to a decrease in CO_2 concentration can be seen at $600 - 800$ cm^{-1}, $2300 - 2400$ cm^{-1}, and at $3500 - 3800$ cm^{-1}.

The CO_2 peak at $2,300 - 2,400$ cm^{-1} is poorly defined in Figure 40, this is due to the IR absorbance of this particular CO_2 peak being sufficiently strong to absorb most of the infrared light passing through it, even at low CO_2 concentrations. This can be illustrated by examining a background scan that was taken prior to this sample, shown in Figure 41. It can be seen that the peak at $2,300 - 2,400$ cm^{-1} has a response of zero, indicating that all IR in this region is being absorbed by the sample. Consequently, although there is a strong absorbance peak in this region, it can only be used as an indicator of CO_2 concentration when CO_2 is at an initial concentration of less than approximately 3 mol%. Therefore an alternative peak must be used for the calibration. The CO2 peak at $600 - 800$ cm^{-1} is too close to the limit of the spectral range of the current FTIR set-up to give accurate data, this can also be seen in Figure 41.
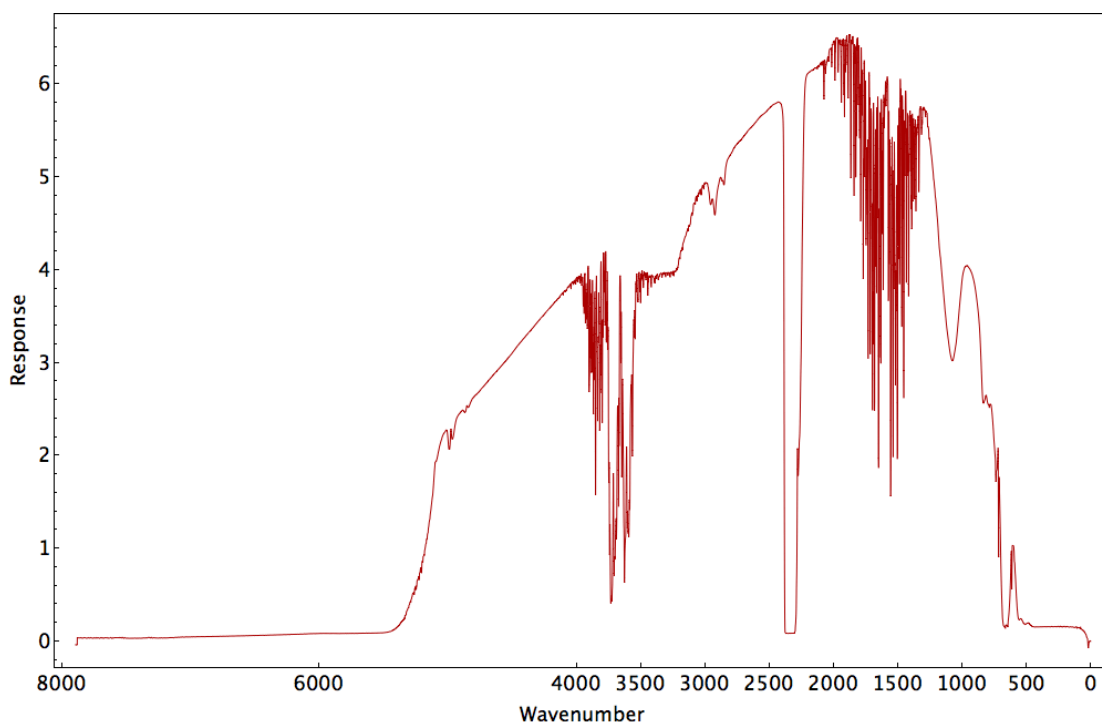
Figure 41: Background spectrum for a 50-50 mix of argon with CO_2

Therefore the peak that must be used for calibration of the FTIR for CO_2 is in the spectral region from 3500 – 3800 cm^{-1} wavenumbers. This peak, however, is also not without its limitations. A comparison between Figure 39 and Figure 35 shows a significant overlap in the absorbance peaks for water vapour and CO_2 in this region. This can also be seen in Figure 41, where in the region from 3500 – 4000 cm^{-1} there are clearly two strong negative peaks from CO, as well as the characteristic "spikey" peaks from water vapour. This overlap in FTIR signature is not a problem if the gases exiting the reactor are dry, and the changes in CO_2 concentration are sufficiently large that the relative effect of water vapour is insignificant. The graph in Figure 42 shows a poor quality FTIR spectrum, with the clarity of the CO_2 peak suffering as a consequence of it's overlapping spectral region with water vapour. Such results are problematic, as it becomes very difficult to take an accurate measurement of CO_2 concentration when the noise caused by water becomes excessive.

Fortunately, measurement of carbon monoxide concentration is much simpler, and does not have quite the same problems as CO_2. There is only one pair of peaks for carbon monoxide, as shown in Figure 36, that absorb in the region from 2000 – 2300 cm^{-1}. The adjacent CO_2 peak at 2300 – 2400 cm^{-1} has an effect of "pulling" the left edge of the CO peak down. This effect can cause errors in the measurement of carbon monoxide concentration. In order to avoid this problem, the CO peak can be split into two separate peaks, at approximately 2000 – 2150 cm^{-1}, and 2150 - 2300 cm^{-1}. If just the peak at 2000 - 2150 cm^{-1} is used as the calibration area, then

the measured concentrations of CO are not affected by change in CO_2 concentration, and are therefore more accurate.
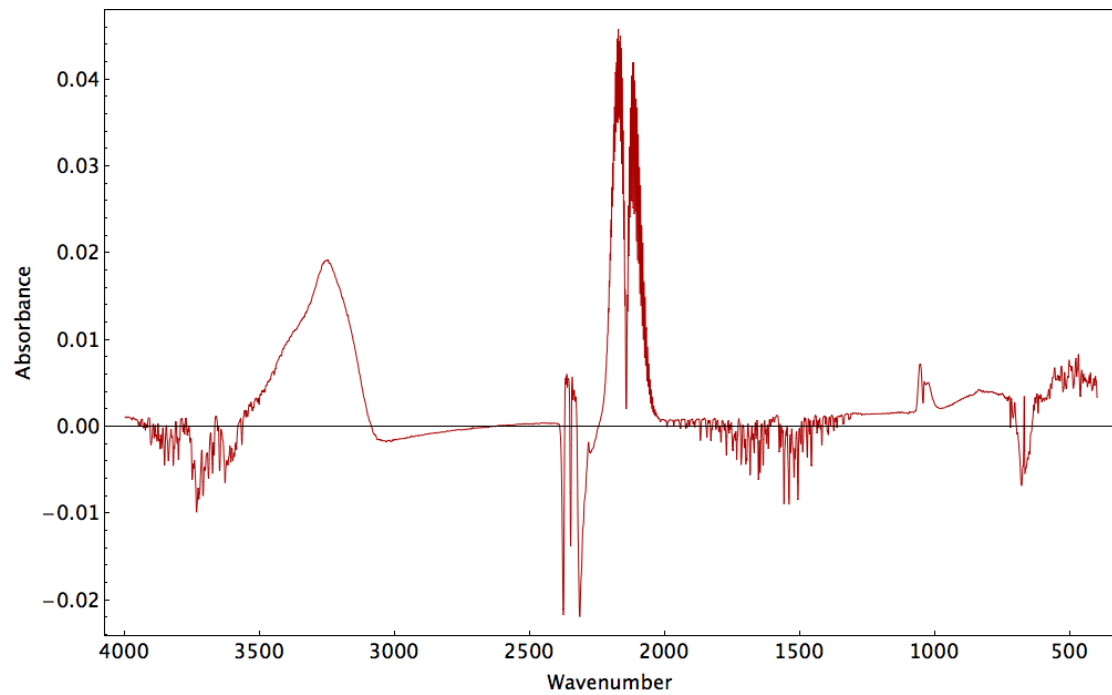
Figure 42: A poor quality FTIR spectrum. The species shown in this graph, their corresponding wavenumbers, and their relative change in concentration are: Decrease in CO_2 at $600 - 800$ cm^{-1}, $2300 - 2400$ cm^{-1}, and at $3500 - 3800$ cm^{-1}. Decrease in water vapour, $1200 - 2000$ cm^{-1}, and $3500 - 4000$. Increase in liquid water (Possibly some minor condensation), at $3000 - 3500$ cm^{-1}. Increase in CO, $2000 - 2300$ cm^{-1}. Increase in ozone, $1000 - 1100$ cm^{-1}.
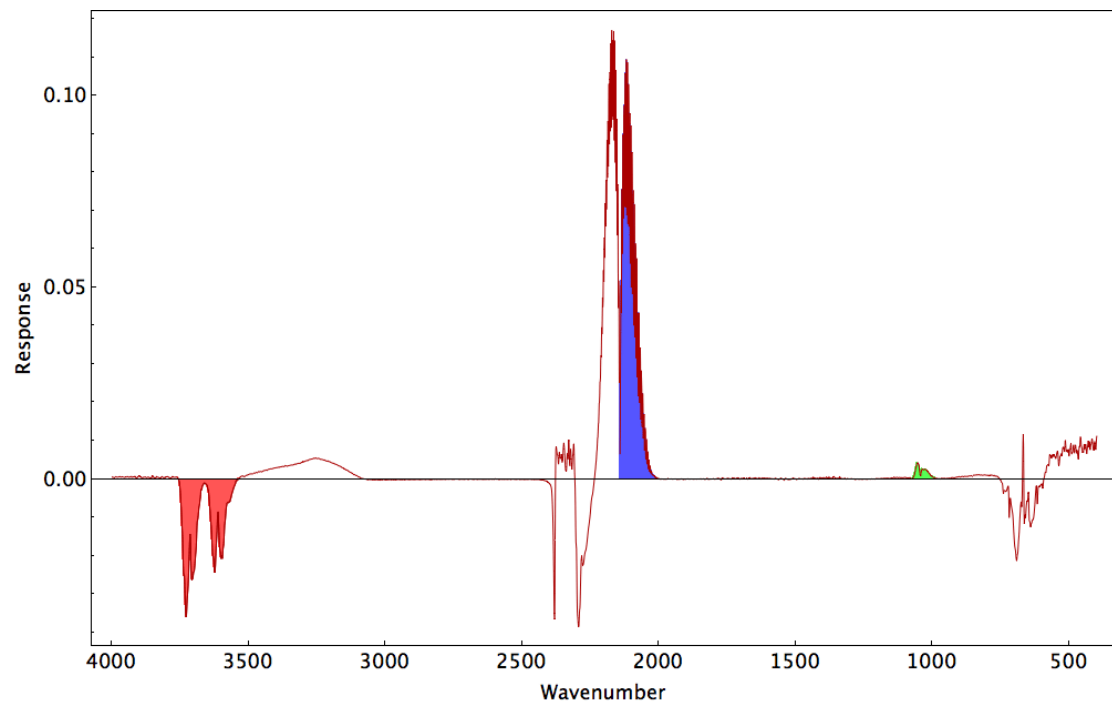
Figure 43: A summary of spectral regions used for the calibration of the FTIR. CO_2 (Red) – $3772 - 3510$ cm^{-1}. CO (Blue) $2143 - 2003$ cm^{-1}. O_3 (Green) $1077 - 990$ cm^{-1}.

Selecting the appropriate spectral region to determine ozone concentration is relatively straightforward, as there is no other species in the gas mixture that has an adjacent or overlapping peak. The peak in the region from 1000 – 1100 cm^{-1} is used to define the calibration area for ozone. A summary of the spectral regions used to calibrate the FTIR is shown in Figure 43, note that the numbers stated are the exact values used in the calibration files for the FTIR.

4.5.2.2 Method of FTIR Calibration – CO_2 and CO

In order to calibrate the FTIR for CO_2 and CO, the experimental rig must undergo some minor alterations. A diagram showing a schematic for the CO and CO_2 FTIR calibration rig is shown in Figure 44.
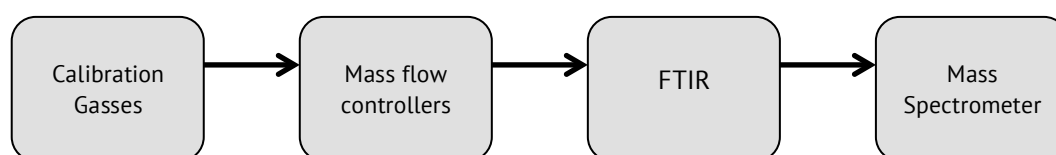
Figure 44: Modified schematic for calibration of the FTIR with the gasses CO and CO_2

The primary difference between the typical experimental schematic, and that shown in Figure 44 is the absence of the plasma reactor, and also the positioning of the mass spectrometer after, rather than before the FTIR. The mass spectrometer in this position can be used to determine when gas composition inside the FTIR sample cell is stable, allowing for a greater confidence in the accuracy of the calibration procedure.

It is important to ensure that the conditions under which the FTIR is calibrated are as similar as possible to the typical experimental conditions. I.e. The FTIR set-up accessories and sample collection method (E.g. FTIR resolution) must be identical, gas flowrates and mixture compositions used should be similar.

Although the Beer-Lambert law states that the relationship between species concentration and absorption is linear, under some circumstances, such as very high or low gas concentrations, a quadratic relationship is actually more appropriate. The FTIR is calibrated for CO concentrations ranging from 0 – 5 mol%, CO_2 concentrations ranging from 95 – 100 mol%, and O_3 concentrations up to 1 ppm using a quadratic relationship.

Method of FTIR Calibration - Ozone

The FTIR calibration for ozone requires a different method to CO and CO_2. As ozone is a relatively unstable molecule, it is not possible to buy it commercially as it would very quickly degrade to oxygen in storage. Therefore, the only way viable way to produce ozone is in the plasma reactor. To produce ozone, a feed stream of pure oxygen is connected to the reactor and

the electrical properties being applied to the reactor, such as voltage and frequency, are varied in order to try to produce a range of ozone gas concentrations. The product gases are passed from the reactor and through the FTIR gas cell, the concentration of the ozone is then determined using a simple chemical test based on the discolouration of a dye, indigo trisulphonate. This is based on a method originally developed by Bader and Hoigné [110]. In order to carry out this calibration the experimental setup must be modified again, a schematic of this setup is shown in Figure 45.
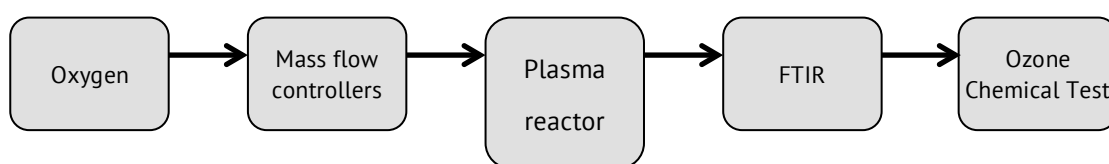
Figure 45: Modified schematic for calibration of the FTIR with Ozone

4.5.3 Mass spectrometry

Mass spectrometry (MS) is a highly sensitive analytical technique used to determine the chemical composition of a substance. It can be used for volatile liquids and gases and can be used for time resolved qualitative and quantitative analysis. In the mass spectrometer an ionised species is detected based on its mass to charge ratio, *m/z*. A mass spectrometer consists of 3 sections, 1) an ion source, 2) mass separation, and 3) species detection. The mass spectrometer used in this thesis is a Hiden Quantitative Gas Analyser (QGA), which is a type of quadrupole mass spectrometer. An image of the 3 mass spectrometer components that are essential for species detection in the QGA are shown in figure Figure 46.
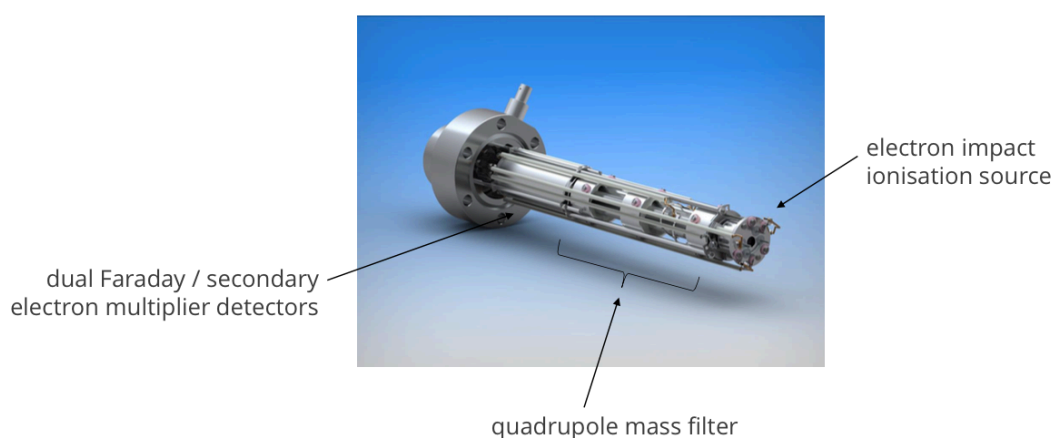
Figure 46: Mass spectrometer components used for species detection found within the Hiden QGA (Image taken from [111])

The mass spectrometer generates a constant stream of charged particles with an ion source, by electron impact ionsation, at the gas inlet to the MS. The ionised particles pass into a quadropole, which consists of 4 long, parallel, cylindrical rods to which a radiofrequency (RF) with a superimposed DC electric field is applied. The direction of motion of the ionised particles is affected by the applied field. By tuning the voltage applied to the quadropole, ions with a specific mass to charge ratio can be allowed to pass to the detector. In the QGA, two different detectors are available, a Faraday detector and a multiplier detector. In each type of detector, when an ion hits the detector it generates a current which is detected by an amplifier. The magnitude of the current is directly proportional to the number of ions striking the detector. In a multiplier detector, the ions striking the detector initiate electron avalanches that effectively magnify the amplitude of the current generated in the detector per incoming ion.

The mass spectrometer operates at a reduced pressure, 3×10^{-6} torr, in order for ionised species entering the MS to have a sufficiently long mean free path to not collide with another molecule before reaching the detector. However, due to natural variation in atmospheric pressure, temperature, and cycling of the external pump, the operating pressure of the MS is prone to fluctuation. The concentration of a detected species, determined by its mass to charge ratio, is expressed in terms of partial pressure relative to the QGA operating pressure. Consequently, in order to quantitatively use the mass spectrometer, the concentration of the species of interest must be measured relative to a species with a fixed concentration, i.e. the use of an internal standard is essential. It is desirable for the internal standard used in an MS experiment to have three properties, 1) for it to be monatomic, 2) for its principal ion to have a mass to charge ratio within the same order of magnitude of the species of interest, and 3) for its characteristic m/z signal to not overlap with the species of interest. The carrier gas used in this thesis is Argon, as it fulfills these 3 criteria. The reasons for these criteria is because the *m/z* peaks detected in a mass spectrometer can appear to be very complex, even in a system with very components. The fragmentation pattern obtained from argon is shown in Figure 47.
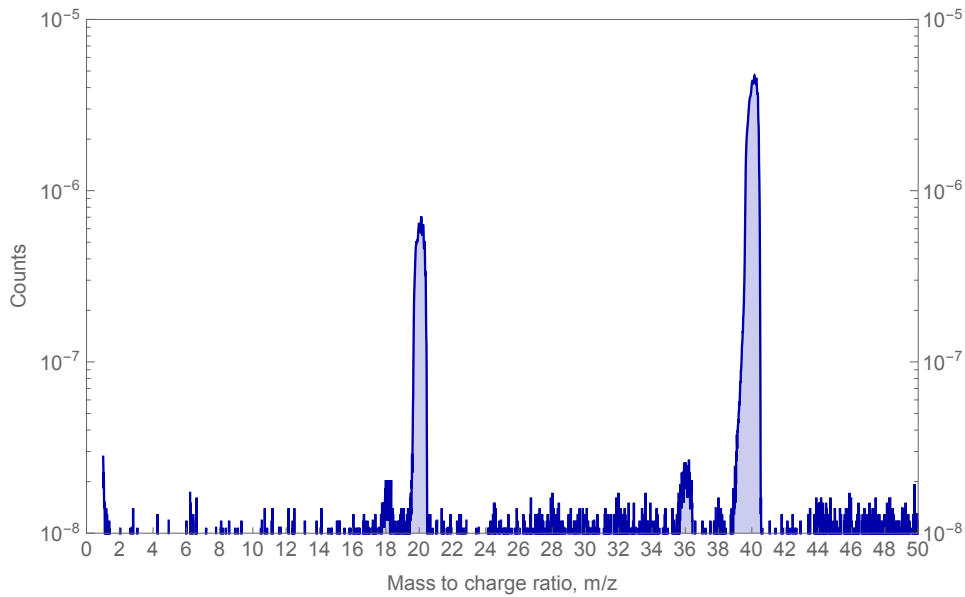
Figure 47: Argon QGA fragmentation pattern. Instrument settings used: Electron energy – 70 eV, Emission - 250 µA, Focus – 90 V. Peaks occur at m/z = 40, 36, 20 and 18 due to the 2 most common isotopes, ^{40}Ar and ^{36}Ar, and the respective single and double ionised forms.

Consider the species that are expected from the experiment, CO, CO_2, Ar, O_2 and O_3. Also consider that due to the high sensitivity of the mass spectrometer, and the difficulty in completely isolating external gas leaks into the system, that the MS will also detect small concentrations of N_2 and water vapour from atmospheric sources. If we include only the possibility of single ionisation events, with only the most common isotopes considered, we would have 7 different species with 6 independent m/z peaks. This number is reduced to 6 different species with 5 independent peaks, as O_3 (which would be found at *m/z* = 48) cannot be detected due to its instability. The overlapping peaks are due to CO and N_2 sharing a peak at m/z = 28. This result is already problematic, as CO is the species that we are most interested in detecting. However, this problem is further compounded when we consider the possibility of species cracking, double ionisation events and isotopes. Taking CO_2 as an example, the following cracking reactions are possible:

$$^{12}C^{16}O_2 + e^- \quad \rightarrow \quad \mathbf{^{12}C^{16}O_2^+} + 2e- \quad \text{(Peak at m/z = 44)}$$

$$^{12}C^{16}O_2 + e^- \quad \rightarrow \quad \mathbf{^{12}C^{16}O^+} + O + 2e^- \quad \text{(Peak at m/z = 28, and formation of unstable O)}$$

$$^{12}C^{16}O_2 + e^- \quad \rightarrow \quad ^{12}C^{16}O + \mathbf{O^+} + 2e^- \quad \text{(Peak at m/z = 16, and formation of unstable ionised O)}$$
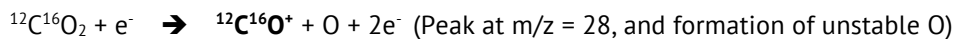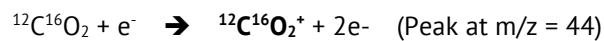
This can also lead to recombination reactions of unstable species:

$$^{16}O + {}^{16}O^+ \quad \rightarrow \quad \mathbf{^{16}O_2^+} \quad \text{(Peak at m/z = 32)}$$
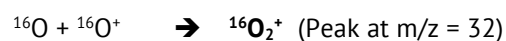
and considering the isotope ^{13}C:

$$^{13}C^{16}O_2 + e^- \quad \rightarrow \quad \mathbf{^{13}C^{16}O_2^+} + 2e- \quad \text{(Peak at m/z = 45)}$$
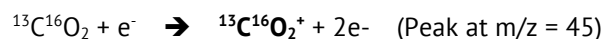
or for the possibility of single or double ionisation events, using Ar as an example:

$$^{40}\text{Ar} + e^- \quad \rightarrow \quad ^{40}\textbf{Ar}^+ + 2e^- \qquad \text{(Peak at m/z = 40)}$$

$$^{40}\text{Ar} + e^- \quad \rightarrow \quad ^{40}\textbf{Ar}^{2+} + 3e^- \qquad \text{(Peak at m/z = 20)}$$
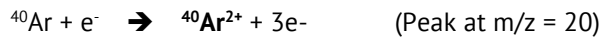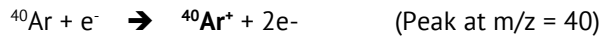
These examples show how a single species can create multiple peaks. Taking a closer look at the CO_2 example, and comparing to the species that we are interested in detecting, CO_2 not only generates a peak at *m/z* = 44, but also at *m/z* = 28 and 32, the expected characteristic peaks for nitrogen and carbon monoxide (*m/z* = 28), and oxygen (*m/z* = 32) respectively. Although this overlap appears to be a significant problem, in most cases it can be compensated for by considering the relative contribution to any m/z peak for each non-ionised species that is present. Peaks caused by cracking of molecules, double ionization events and isotopes are typically relatively much smaller than the main peak, with their amplitude proportional to the main peak, and therefore predictable. Shown in Figure 48 is the cracking pattern for pure CO_2 generated in the QGA, with the electron energy at the ion source set to 70 eV. The possible ions that are causing each peak are labeled.
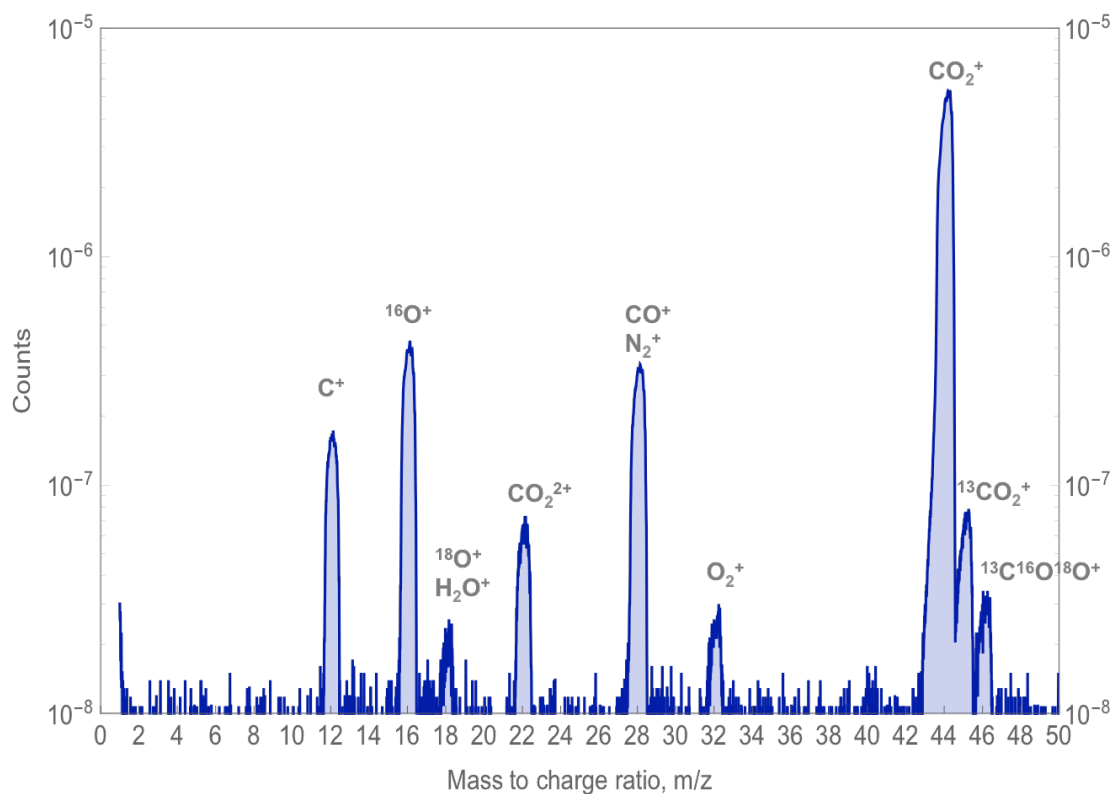
Figure 48: Pure CO_2 cracking pattern obtained from the Hiden QGA. Instrument settings used: Electron energy – 70 eV, Emission - 250 μA, Focus – 90 V.

The height of each peak is directly proportional to the concentration of ions generated by the fragmentation of CO_2 as it passes through the ion source. As expected, CO_2^+ ions generate the largest peak (5.30×10^{-6}), with $^{16}O^+$ (4.27×10^{-7}) and CO^+ (3.36×10^{-7}) ions 2nd and 3rd largest peaks respectively. This indicates that for an ion source electron energy of 70 eV, using a pure CO_2 stream, that the peak height at *m/z* = 16 and 28 will be 8.0% and 6.3% of the peak height at

m/z = 44 respectively. Also worth noting is that the peak at m/z = 32, the same expected peak as oxygen, has a height of 3.00×10^{-8}, which equates to 0.57% of the peak height at m/z = 44. The contribution of CO_2 to these peaks could theoretically be accounted for in the mass spectrometer calibration methodology, as no other species in the gas mixture would have a peak at m/z = 44, which would make removal of secondary CO_2 peaks relatively straightforward.

However, the relationship between fragmentation pattern characteristic peak heights of any given compound is non-linear in the presence of other compounds, particularly noble gases. This can be explained by considering that the ion source to the QGA is a non-equilibrium plasma, and therefore similar non-linear behavior that is observed with different gas mixtures in the laboratory plasma also occur in the ion source. In experiments where the gas concentration of noble gases is kept relatively constant, it is reasonable to approximate that the relationship between the heights of the secondary m/z peaks relative to the primary peak is constant. This allows the contribution of the secondary peaks to be accounted for, as in most cases the variation in relative secondary peak height is insignificant compared with the height of a primary peak found at the same m/z.

There are two potential methods to compensate for these problems in non-linearity in the method of measurement:

1. Measure fragmentation patterns of different compounds to be detected for a range of different gas compositions that are similar to those that are expected to be found experimentally. Identify overlapping peaks, and mathematically account for the relative contributions of secondary fragments to primary peaks in order to determine species concentration. This method requires extensive preparation prior to experimental work.

2. Prior to an experimental run, feed two different gas compositions through the reactor to the mass spectrometer. One with a gas composition consisting of just expected product gases (CO and O_2), and carrier gas (Ar) at concentrations close to those expected limit of the experiment, and the other at the feed composition of gas that is to be used in the experiment, i.e. CO_2 and Ar. The concentrations of the compounds of interest obtained experimentally can then be found by linear interpolation between the measured values at each m/z peak height value. This method is easier to implement, but requires more time spent on post experimental analysis.

As mentioned earlier in this section, O_3 concentration cannot be measured using mass spectrometry due to its instability. Results from FTIR indicate the O_3 concentration is typically very low, and does not exceed 100 ppm during these experiments. The selectivity of CO, compared to other possible products, C and O_3, is sufficiently high that it is possible to carry out a reactor mass balance using data from either the MS, or the FTIR, without

depending on the other instrument for supporting data. Therefore, for the experiments carried out in this thesis, the 2nd method (i.e. linear interpolation) described above is used to calculate CO_2 conversion in the reactor.

4.6 Materials Characterisation

Two different packing materials are tested in this thesis, barium titanate ($BaTiO_3$) (Supplied by Catal UK ltd) and alumina (Al_2O_3) (Sigma Aldrich). In order to understand the behavior of the plasma discharge when these materials are packed into the reactor, it is important to try to understand the properties of the packed bed as well as the materials themselves. The material properties that are considered to be of most interest for this work are the composition, the dielectric properties, and the catalytic activity of the materials. As received, both the Al_2O_3 and $BaTiO_3$ are in the form of 3 mm, approximately spherical pellets. The particles in the size ranges from 180 – 300, 300 – 500, 500 – 850, 850 – 1400, and 1400 – 2000 µm are created by repeatedly using a pellet crusher to break up the 3 mm pellets into smaller pieces. The mixed, crushed pellets are then sieved using Retsch test sieves with a vibratory sieve shaker (Retsch AS 300 Control), with the mesh sizes corresponding to the desired particle sizes. Sorting particles by this method is known to separate them by their second largest dimension; hence further particle size characterization should be undertaken.

4.6.1 Packed bed characterisation

In order to determine gas residence time in the reactor, it is required to determine the properties of the packed bed. In order to achieve this the reactor is filled with a known mass of the different sizes of particles (2g of $BaTiO_3$, or 5g of Al_2O_3 due to differences in density), and the length of the packed bed is measured.

As alumina is hygroscopic and is very difficult to completely dry, the packing material is stored for a week in identical atmospheres in open containers before being tested. This is assumed to equilibrate the mass fraction of atmospheric water in the Al_2O_3 in each sample. Density of the material tested is approximated by measuring the mass of 30 spheres, then dividing the total mass by the approximated total volume occupied by the spheres. The total volume occupied by the spheres is determined by measuring the diameter of each individual sphere using a caliper, calculating the volume of each sphere, then summing the values to obtain a total volume.

Void fraction of the packed bed is determined by calculating the total bed volume occupied by the spheres plus the voids, calculating an equivalent mass of the bed volume if it was to be fully packed with spheres, and then subtracting the difference between the hypothetical equivalent mass of the bed volume occupied, and the actual mass of the bed.

Measured void fraction results for $BaTiO_3$ are shown in Figure 49.
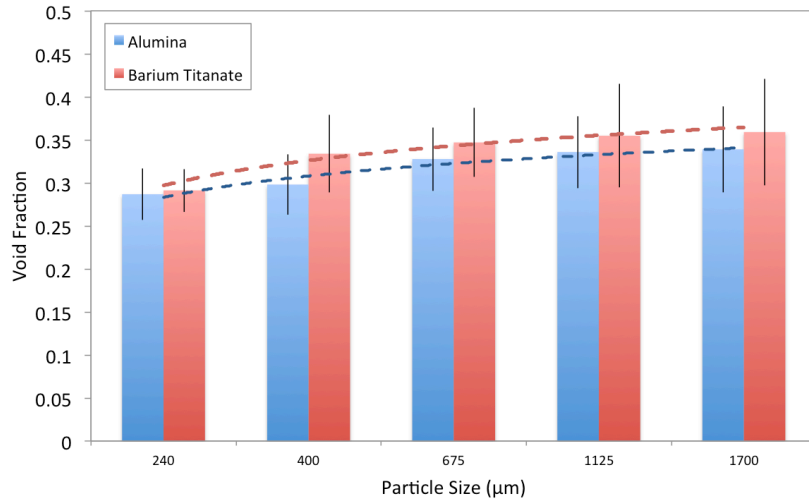
Figure 49: Void fraction measured for different particle sizes for $BaTiO_3$ and Al_2O_3 in the packed bed reactor

4.6.2 Method of materials electronic characterisation

The electronic properties of a material are determined using 2 different analytical methods, Inductance – Capacitance – Resistance (LCR) testing and ferroelectric testing. Both of these testing methods require the material to be characterised to be in the form of a cylindrical pellet with an approximately constant thickness, and uniform surface area on either face. In order to do this the sample to be tested is carefully polished from a spherical shape, to a pellet shape. A diagram illustrating this process is shown in Figure 50.
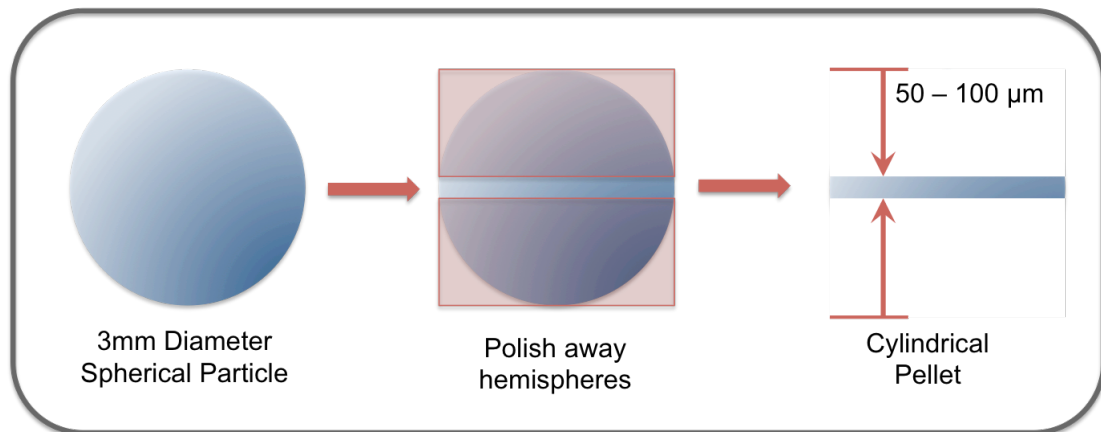
Figure 50: The process of preparing spherical samples for electronic characterisation

Characterisation of the electronic properties of a material is typically carried out using 2cm, cylindrical pellets with a thickness of approximately 50 µm for ferroelectric testing, and 100 µm for dielectric testing. In order to prepare the samples by the process shown in Figure 50, the spherical particles are fixed to an SEM pellet stub with beeswax, then using clean, unused sandpaper polished down until the approximate desired thickness is achieved. The sample is then cleaned by submersing it in acetone in a sealed 5 ml vial, then placing it in an ultrasonic

87

bath. After cleaning, the sample thickness is measured using calipers at a number of points to ensure uniformity. If the sample is at the desired thickness, it is stored for testing. If not, either the process of polishing is repeated until the desired thickness is achieved, or if the sample is too thin, it is discarded. Stored samples are prepared for testing by carefully applying a gold paste to either side of the pellet that acts as an electrode, taking care to avoid applying the paste to the perimeter of the sample, then firing for 1 hour at 200 °C. The samples are then polished around the perimeter using P1000 (Super fine) sandpaper in order to remove any residual gold paste that may be present.

The dielectric constant of the material is measured using a Labview operated LCR meter (HP 4284A Precision LCR meter), with a custom built sample holder contained within a tube furnace. This allows the temperature, and frequency dependence of the dielectric constant to be measured. In order to confirm that the $BaTiO_3$ sample behaves a ferroelectric, and displays the characteristic ferroelectric hysteresis loop, the sample is tested in a Radiant Technologies rt-66a standardized ferroelectric test system. Additionally, in order to test the composition of the material, the $BaTIO_3$ samples are tested scanning electron microscopy with energy dispersive x-ray spectroscopy (SEM-EDS). Due to the high porosity of the Al_2O_3 samples, electrodes applied to the pellets migrate into the pores and cause short-circuiting when trying to measured dielectric constant. Therefore, the value for the dielectric constant used for Al_2O_3 is assumed to be $\varepsilon = 9$.

4.6.3 Results of BaTiO$_3$ testing

The result for the measured dielectric constant from the LCR test at 1,000 Hz is shown in Figure 51.
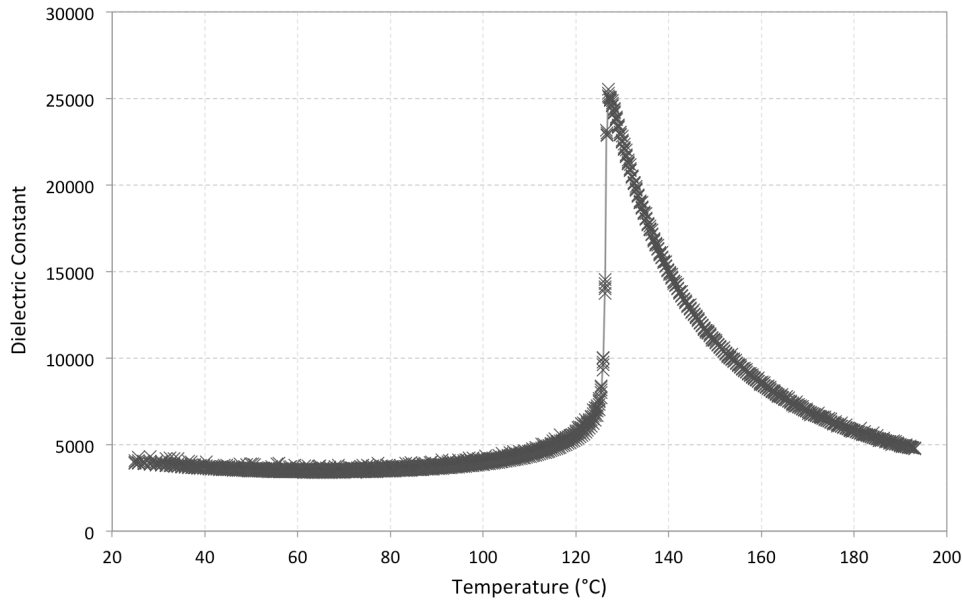
Figure 51: Results of LCR testing of BaTiO₃. The Curie point is observed at 127 °C, and dielectric constant is found to be approximately 4,000 at 25 °C, at a frequency of 1,000 Hz.

The data indicates that the curie point of the material is at 127 °C, whilst the dielectric constant measured in the region from 25 – 100 °C is approximately 4,000. The measured values for dielectric constant and curie point are comparable with those reported in literature [112]. As stated in section 2.3.3, BaTiO₃ behaves as a ferroelectric material below its curie point. When the temperature increases through the curie point, the structure of material changes from being tetragonal to cubic and the material loses its characteristic ferroelectricity. The results of the ferroelectric test (shown in Figure 52) demonstrate that the BaTiO₃ sample used in the experiments behaves as a ferroelectric material.
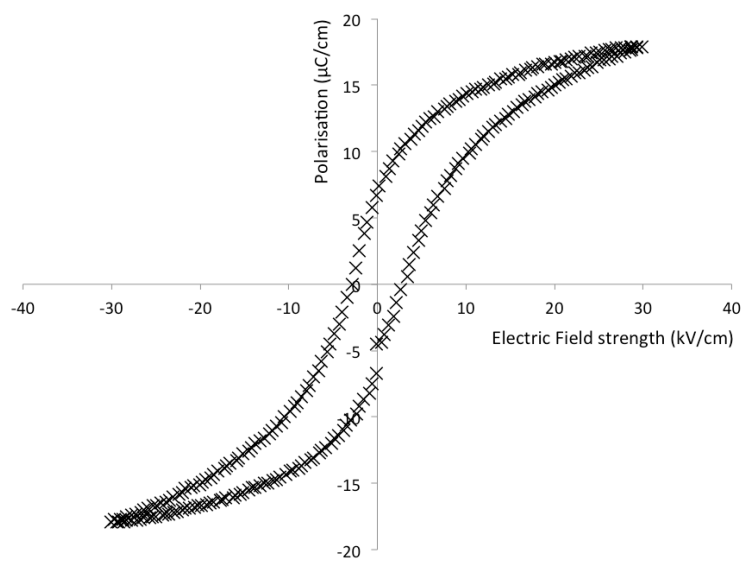
Figure 52: Ferroelectric test of BaTiO₃, showing the characteristic hysteresis loop of a ferroelectric material

In order to determine the composition, and to observe the microstructure of the samples SEM-EDS is used. Shown in Figure 53 and Figure 54, are two representative SEM-EDS images, and accompanying compositional data, of the BaTiO$_3$ samples. The EDS data in Figure 53, shown below the SEM image, indicates an approximately equimolar presence of the elements barium and titanium in the pellets, which, combined with the ferroelectric test data, and the dielectric testing, is consistent with the sample being predominantly made from BaTiO$_3$. The EDS data in Figure 54, which is representative of the small dark patches that are found randomly, but uniformly, distributed throughout the samples indicates the presence of ~ 10 mol% aluminium in these regions. This is likely to be due to contamination in these regions with an alumina species. Overall, the concentration throughout the material is very low. From the SEM image, the density of this region is very high, so the alumina is likely to have very little catalytic effect in the plasma reactor due to having a very low surface area, regardless of crystalline phase. Additionally, the effect on electric field in the plasma reactor is likely to be insignificant.
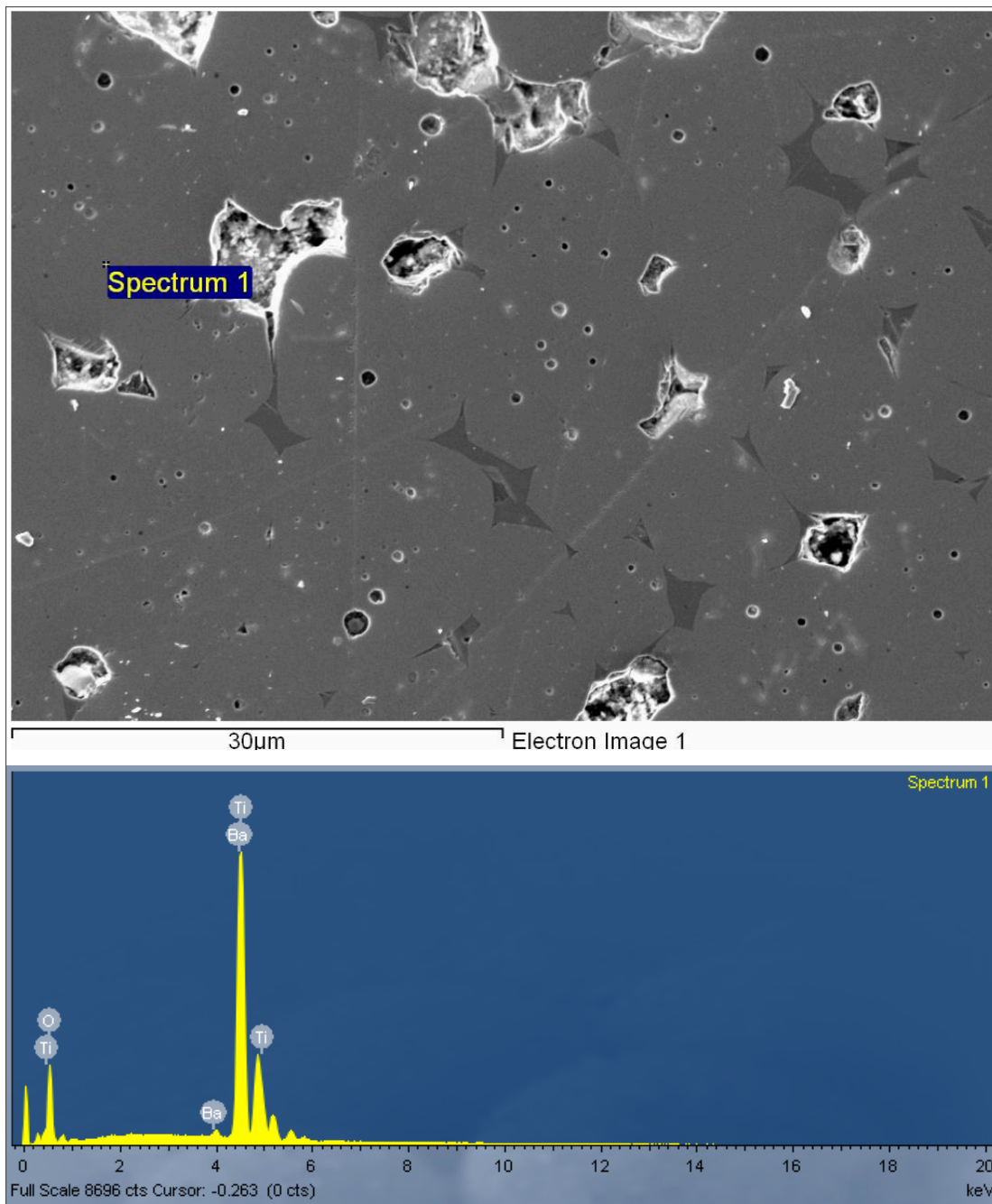
Figure 53: SEM image and EDS analysis of "Spectrum 1", a sample area of the surface of one of the Barium Titanate pellets. Spectrum 1 and its EDS is representative of the light grey area observed in the SEM that forms the majority of the composition of the pellet.
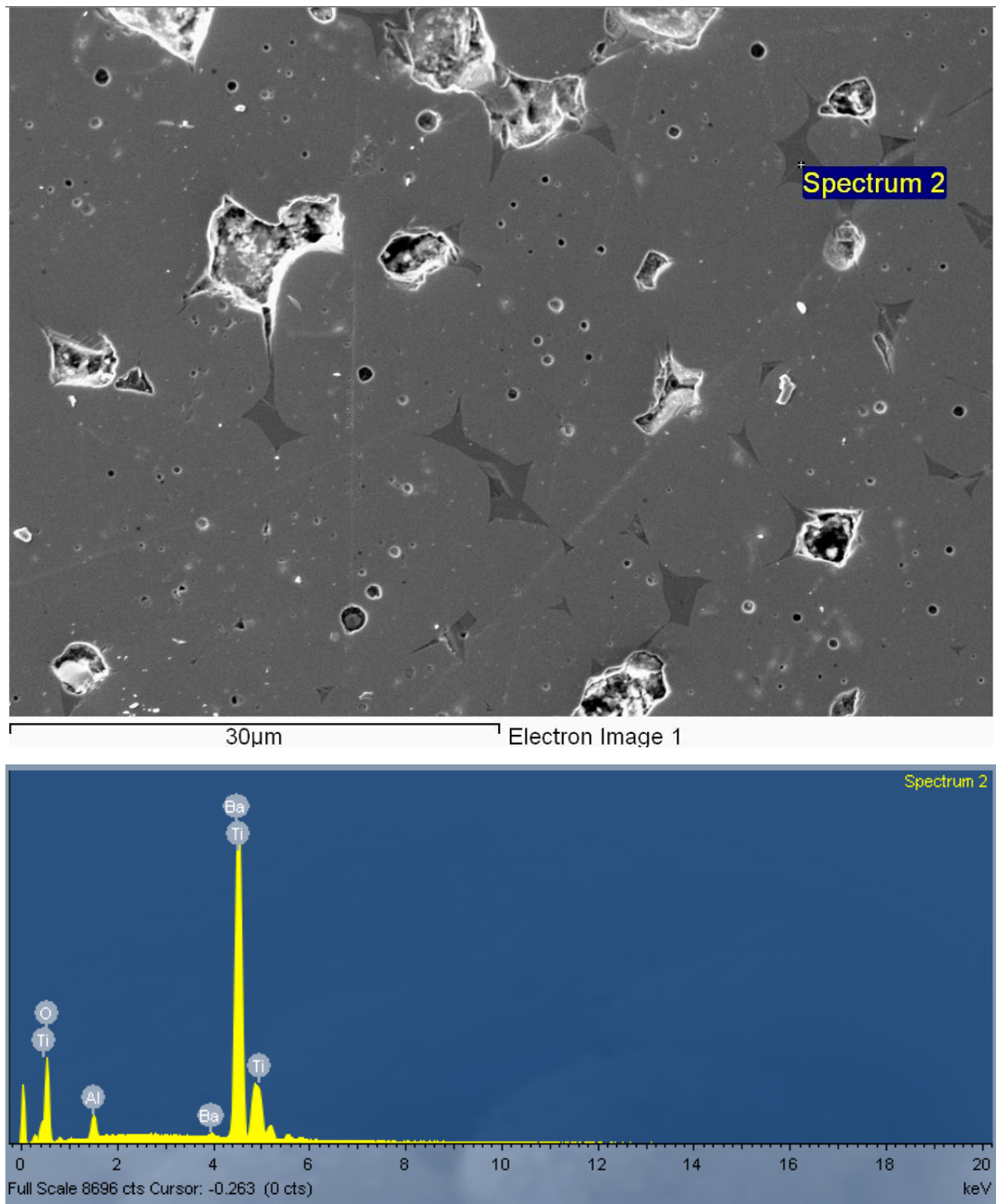
Figure 54: SEM image and EDS analysis of "Spectrum 2", a sample area of the surface of one of the BaTiO$_3$ pellets. Spectrum 2 and its EDS data is representative of the dark grey area observed in the SEM that appears as a randomly, but evenly distributed impurity through the pellets.

4.7 Experimental method

Two novel sets of experiments have been carried out, both of which investigate the use of packed bed DBDs in mixed atmospheres of argon and CO_2. Two packing materials are used, $BaTiO_3$ and Al_2O_3, with 6 different particle sizes ranging from 180 – 2000 μm, using the reactor, equipment and analytical techniques described in chapter 4. The purpose of this chapter is to succinctly describe the procedure that was used during each experiment.

4.7.1 Experiment 1: Effect of particle size on CO_2 conversion in a packed bed DBD

The aim of this experiment is to determine the effect that changing packing particle size, material, and gas composition has on the conversion of CO_2 in the reactor, and the overall efficiency of the process. The results of this experiment are given in section 5.1.1 to 5.1.3.

For this experiment, 3 different gas compostions are used: 90% Ar – 10 % CO_2, 50% Ar - 50% CO_2, and 100% CO_2. Total gas flow rate is used at a fixed value fixed of 100 ml / min in order to keep the residence time of gas in the reactor constant at each particle size. The voltage applied to the reactor is in the range from 5 – 10 kV, with the waveform being applied to the reactor being a squarewave at a frequency of 5 kHz.

Monitoring of voltage applied to the reactor, power consumption and frequency is carried out using the LabView based method described on page 68. Gas analysis is carried out using either FTIR or MS, with experimental repeats being carried out using both instruments on independent runs. The quantity of packing material charged in the reactor is done on a volumetric basis such that the reactor is packed to 5 mm above the top edge of the ground electrode, i.e. the volume of packing material used in the reactor is 3.5 cm^3. Prior to running an experiment, the reactor is purged with pure argon for 20 minutes, and a 10 kV, 10 kHz square wave argon plasma is used to dry the packing material, with a heat gun used to dry the reactor.

After the reactor is well dried, the feed gas composition is applied to the reactor. Dependent upon whether FTIR or MS is used, this procedure varies slightly. If FTIR is being used, the gas is fed at the feed composition to the reactor for 60 minutes before an experiment is started. If MS is used, 2 different gas compositions are used, an intial composition for a duration of 30 minutes before switching to the feed composition, again for a duration of 30 minutes prior to beginning an experiment. Both of these timings are to allow the gas concentration to become stable, as Al_2O_3 is found to absorb gases, particularly CO_2, in the reactor, additionally, when using the FTIR

the volume of the gas cell must be displaced a number of times before the measured concentration becomes stable. The timings and gas flowrates are controlled via the Bronckhorst Flowplot Software. The 2 different compositions are used so that experimental gas concentrations can be interpolated from mass spectrometer data.

Table 7

Composition Number	Initial Composition	Feed Composition
1	90% Ar – 5% CO – 5% O_2	90% Ar – 10% CO_2
2	50% Ar – 25% CO – 25% O_2	50% Ar – 50% CO_2
3	50% CO – 50% O_2	100% CO_2

As described in section 4.4.2, the power supply is controlled by a Labview operated PC, with a National Instrument DAQ with an analogue output. For this experiment, the voltage applied to the reactor is initialised at 10 kV peak (20 kV peak to peak), and goes through stepwise 1 kV decreases (2 kV peak to peak) every 20 minutes until it reaches 5 kV (10 kV peak to peak), where it continues for a further 20 minutes before switching off the HV power source. At this point data is collected for a further 30 minutes and then the experiment is switched off.

4.7.2 Experiment 2: Effect of particle size on reactor electrical characteristics in a packed bed DBD

The aim of this experiment is to try to understand the cause of the change in CO_2 conversion observed in experiment 1. The results of this experiment are given in section 6.

For this experiment, 11 different gas compositions are used, from 100% Ar to 100% CO_2 in 10% concentration increments (e.g. 90% Ar – 10% CO2, 80% Ar – 20% CO_2, etc…). Gas composition is monitored using the mass spectrometer in order to determine the stability in the behavior of the reactor, but MS data is not recorded as concentration data could not be calculated from the data that is generated by this method. The power supply is again controlled using the Labview operated PC, with NI DAQ. In this case, applied electrical properties are changed with a number of different settings and are discussed on a case-by-case basis. Frequency is applied in the range from 1 – 10 kHz, with square or sine waves, at voltages from 5 – 10 kV. Determination of reactor electrical characteristics is done using the Picoscope – Mathematica based method described in 4.4.3, with details given in the appendix in section 9.2.

5 Experimental Results

5.1.1 CO_2 conversion in Al_2O_3 packed beds

Shown in Figure 55, Figure 57, and Figure 58 are CO_2 conversion plotted against plasma input power in an Al_2O_3 packed bed at CO_2 inlet concentrations (balanced with Ar) of 10%, 50%, and 100% CO_2 respectively.
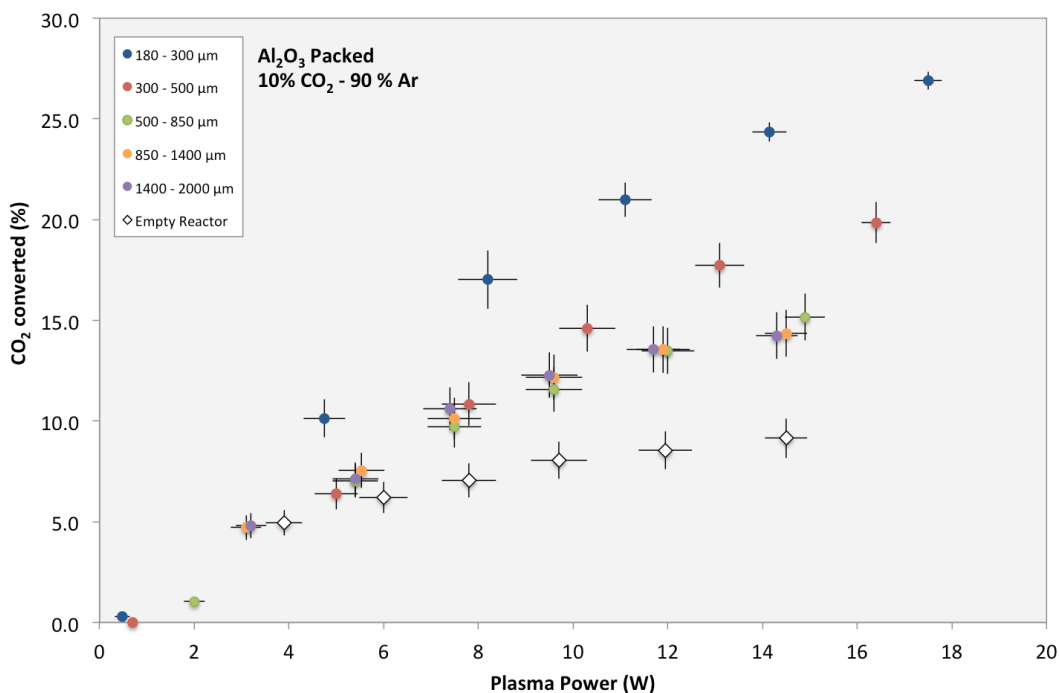
Figure 55: CO_2 conversion plotted against plasma power in an Al_2O_3 packed reactor. Inlet gas composition is 10% CO_2, 90% Ar with a total flowrate of 100 ml/ min. Reactor is driven by a 5 kHz Square wave, with voltage stepped between 5 – 10 kV. Error for 180 – 300 μm particles is based on 5 repeats, with error bars indicating one standard deviation. Other particle sizes and the empty reactor data are based on two repeats with standard deviation estimated from 180 – 300 μm particle sizes.

Figure 55 shows that in all cases, for any applied power that the smallest particles (180 – 300 μm) size range, give the highest conversion (26.9%) in 90% Ar – 10% CO_2 mixtures. A similar trend is observed with the next smallest particle size (300 – 500 μm, max conversion = 19.9%), although the effect is less pronounced. Particle sizes from 500 μm to 2000 μm give very similar CO_2 conversions to each other for any given applied power. For example, at an input power of ~ 14 W, 500 – 850, 850 – 1400, and 1400 – 2000 μm particles all give a CO_2 conversion of between 14.3 – 15.1 %, whilst 180 – 300 μm particles give conversions of 24.3 %, and 300 – 500 μm predicted conversion is ~ 18.3%. These are increases of up to 70% and 28% respectively for the same plasma power. With decreasing powers, these large differences in CO_2 conversion tend to become less significant, for example, at powers lower than 10 W, the CO_2 conversion for 300 – 500 μm Al_2O_3 is approximately equal to those obtained with larger particles. Also, the

95

relative difference between the conversion obtained with the 180 – 300 μm particles, compared to larger particle sizes decreases. Comparing the empty reactor with the Al_2O_3 packed reactor, it is clear that the Al_2O_3 packing is beneficial for CO_2 conversion, with conversion being at least 80% higher at input power > 14 W with the unpacked reactor. It must also be taken into account that the residence time in the unpacked reactor is ~ 1.35 seconds as opposed to ~ 0.46 seconds with the largest particle sizes. With previous studies typically showing that lower gas flow rates, and therefore increased residence time tends to increase CO_2 conversion [67, 75].
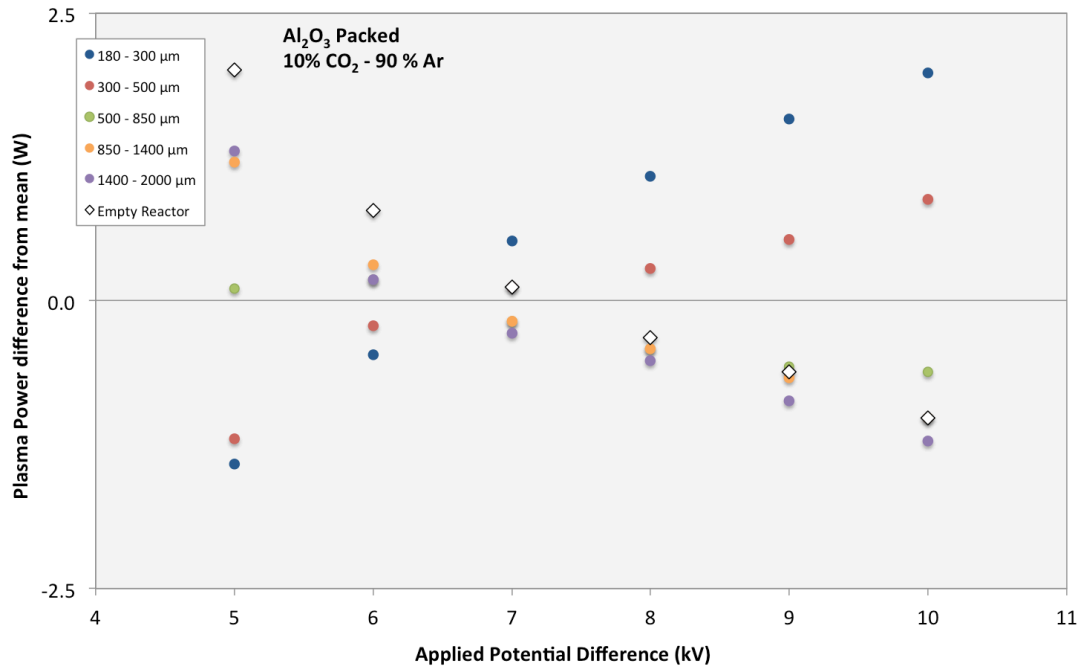
Figure 56: Measure of plasma power difference from mean for each applied potential difference for an Al_2O_3 packed reactor with 10% CO_2 – 90% Ar. Values above the line at $\Delta P = 0$ indicate an above average power consumption. Error bars are not included as the graph becomes too difficult to easily read.

In addition to this, and illustrated by Figure 56, when the voltage applied to the reactor is 7 kV or greater and the reactor is packed with particles smaller than 500 μm, the power drawn by the reactor at any given applied voltage significantly exceeds the mean power of all particle sizes in the reactor. Conversely, at voltages less than 6 kV, the opposite trend is observed, smaller particles sizes draw less power for any given applied voltage. There appears to be a strong relationship between particle size, and power drawn by the reactor, as all particle sizes have an influence on reactor power consumed. Interestingly, the unpacked reactor draws similar amounts of power to the reactor packed with the largest particle sizes at voltages of 8 kV and greater, whilst at lower voltages it draws more power than the packed reactor with any particle size of Al_2O_3.

This result also indicates that the behaviour of the plasma discharge (at these gas concentrations) must be significantly different with the 2 smallest particle sizes compared to the

larger ones, as the average current drawn by the reactor is much larger at high voltages. It is not clear, however, whether the significant increase in CO_2 conversion is due to a catalytic effect as a result of the increased surface area available for reactions, or due to the difference in the behavior of the plasma discharge itself, or even a combination of both effects.

Figure 57: CO_2 conversion plotted against plasma power in an Al_2O_3 packed reactor. Inlet gas composition is 50% CO_2, 50% Ar with a total flowrate of 100 ml/ min. Reactor is driven by a 5 kHz Square wave, with voltage stepped between 5 − 10 kV.

Figure 57 shows CO_2 conversion in 50% Ar − 50% CO_2 mixtures. Please note that the max value of conversion is significantly reduced between Figure 58 and Figure 57, from 26% to just 5%. This is due to the total flowrate (100 ml /min) being kept constant in order to keep reactor residence time approximately constant between experiments. Presenting data for CO_2 conversion as absolute values, (e.g. in ml of CO_2 converted per minute) allows comparison of CO_2 conversion between different gas compositions, an example of this is shown in Figure 59 and Figure 60.

Similarly to Figure 55, Figure 57 shows that with high input powers that the smallest particles show the highest conversions. For an input power of 15W, the particles with the highest conversion of CO_2 are the 180 − 300 μm particles, with decreasing conversion for each incrementally increasing particle size. The difference between the highest and lowest values for CO_2 conversion at high input powers is less significant compared with the results presented in Figure 55, e.g. at 15 W the CO_2 conversion with 180 − 300 μm particles is 54% higher than those obtained with 1400 − 2000 μm particles (Compared with the 70% difference obtained at 14 W with the 90% Ar − 10% CO_2 mix). Again, CO_2 conversion in the unpacked reactor is lower than for

the Al_2O_3 packed reactor, although the relative change of CO_2 reduction is reduced compared to the higher 90% Ar concentration reactor.

However, as input power decreases, similarly to Figure 55, these differences in conversion rapidly become less pronounced. Moreover, comparing small and large particles, the power of the plasma is much lower with small particle sizes at the same applied voltage. Take, for example, the cluster of points that occurs at about 8 – 9 W, these represent an applied voltage of 8kV with particle sizes from 500 – 2000 µm particles. However, for 180 – 300 µm particles at an applied voltage of 8 kV, the plasma power is just 5 W. For the same applied voltage, the power decreases by 40% when comparing the smallest with the largest particles. This decrease in power is likely to be due to the discharge not occurring in all of the void spaces of the packed bed, this consequently leads to a related drop in conversion due to decreased gas – plasma contacting. It should be noted that in the reactor with this gas composition, that at voltages of 6 kV or lower in both the Al_2O_3 packed and unpacked reactors the potential difference applied to the reactor is insufficient to maintain a plasma discharge.
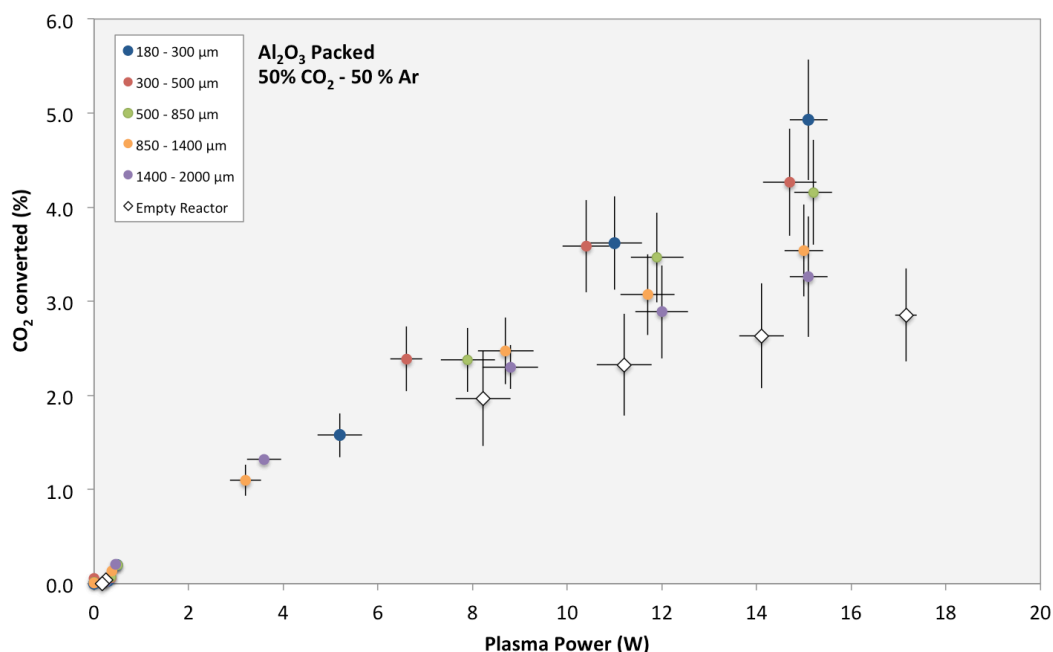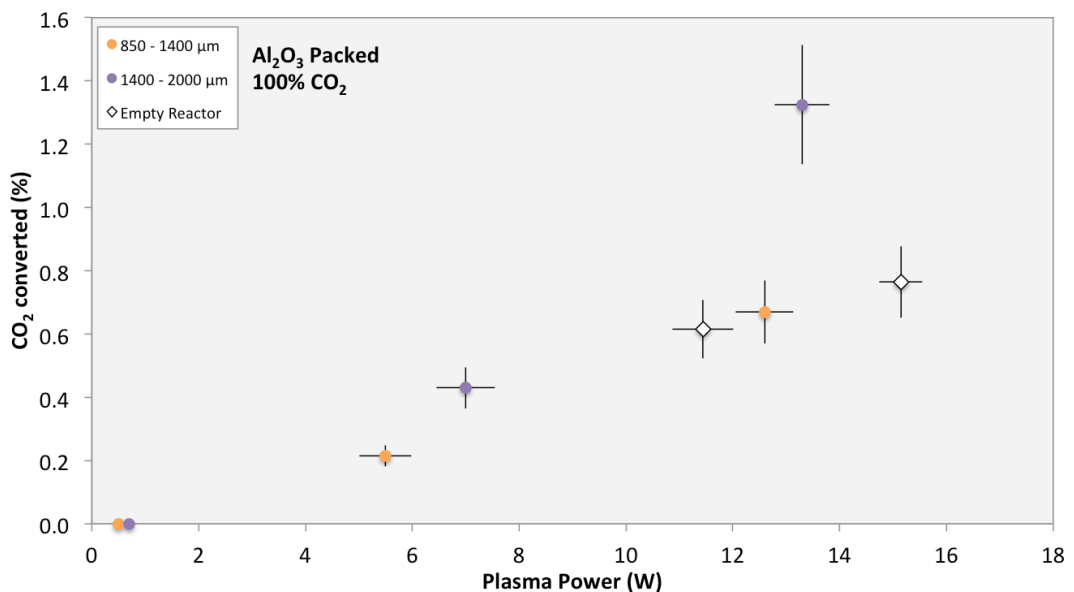

Figure 58: CO_2 conversion plotted against plasma power in an Al_2O_3 packed reactor. Inlet gas composition is 100% CO_2 at a flowrate of 100 ml/ min. Reactor is driven by a 5 kHz Square wave, with voltage stepped between 5 – 10 kV. Data for particle sizes from 180 – 850 µm as no CO_2 conversion occurs at any applied voltage.

Figure 58 shows CO_2 conversions obtained in 100% CO_2, only the data for the largest particle sizes (850 – 1400, and 1400 – 2000 µm) at 8 - 10 kV is included. No CO_2 conversion occurs with particle sizes less than 850 µm, this is due to no plasma discharge occurring in the void spaces of particles of this size. With a pure CO_2 feed, the largest particle size gives the highest CO_2 conversion, and any benefits from having smaller particle sizes are eliminated.

This result does not necessarily indicate that with pure CO_2 feeds that plasma discharges cannot occur in beds with small particle sizes, but rather than much higher electric field strengths are required for larger electrode spacings.
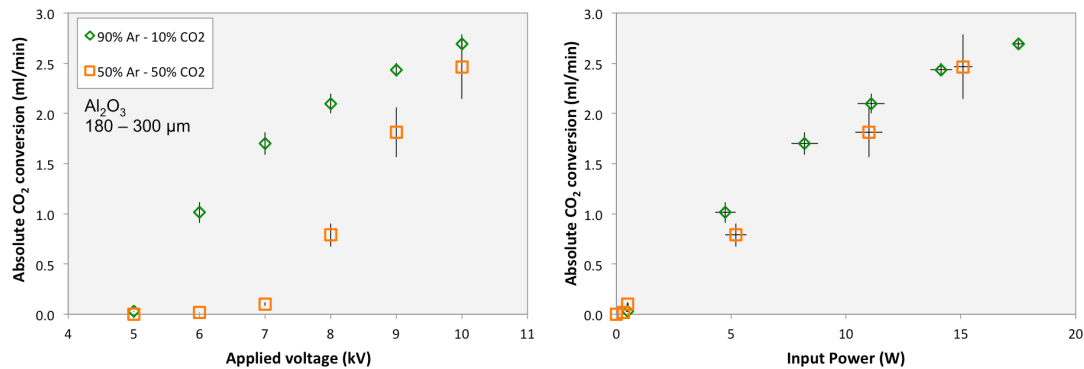
Figure 59: Applied voltage (left) and plasma power (right) plotted against absolute CO_2 conversion (in ml of CO_2 converted per minute) in for 180 – 300 µm Al_2O_3 particles with 50% Ar – 50% CO_2 and 90% Ar – 10% CO_2 gas mixtures.

Figure 59 shows absolute values for CO_2 conversion measured in ml/min of CO_2 converted for 180 – 300 µm particles of Al_2O_3. The right hand graph, showing input power vs absolute conversion, indicates that a similar amount of CO_2 is converted for any similar input powers, with the 90% Ar concentration reactor being able to convert slightly more CO_2 per watt of power. The left hand graph shows CO_2 conversion as a function of applied voltage. At any applied voltage, conversion of CO_2 in the 90% Ar reactor is significantly higher. Although at high input voltages these differences in CO_2 conversion tend to decrease.
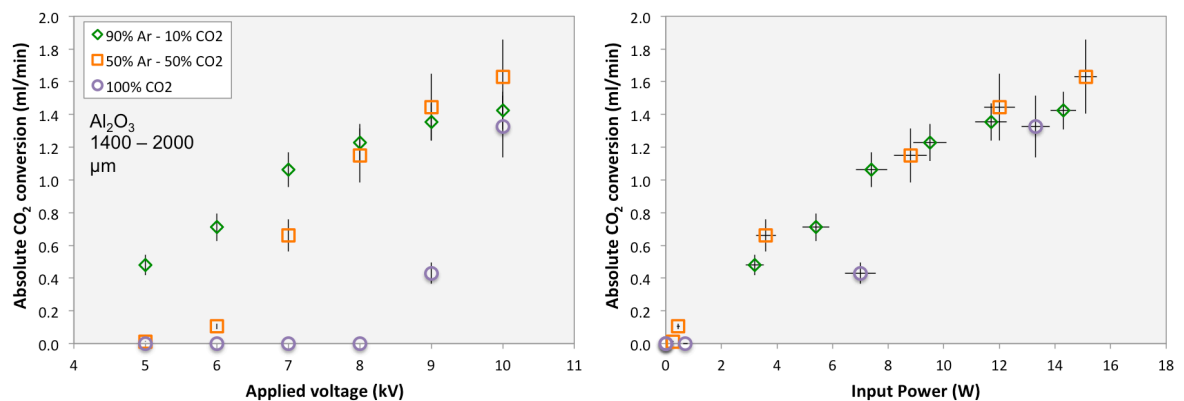
Figure 60: Applied voltage (left) and plasma power (right) plotted against absolute CO_2 conversion (in ml of CO_2 converted per minute) in for 1400 – 2000 µm Al_2O_3 particles with 100% CO_2, 50% Ar – 50% CO_2 and 90% Ar – 10% CO_2 gas mixtures.

Figure 60 shows absolute values of CO_2 converted for 1400 – 2000 µm Al_2O_3 particles under different gas feed conditions. Similarly to Figure 59, Figure 60 shows that per watt of input power, similar quantities of CO_2 are converted in the packed bed, although very high concentrations of CO_2 do lead to lower absolute values of conversion. Similarly again, if these results are compared on the basis of the applied voltage, with increasing CO_2 concentration in

the gas less CO_2 is converted per volt applied, until voltages of 9 – 10 kV are applied at which point the absolute CO_2 conversion figures become similar to each other.

With Figure 59 and Figure 60 it must be noted that although absolute values of CO_2 conversion can be used to make some comparisons between gas compositions, this comparison is not used to suggest that reactor operating conditions are equivalent. Gas plasma contacting is likely to be non-ideal, i.e. gas treatment is not uniform, therefore each plasma discharge in the 50% CO_2 – 50% Ar contains 5 times more CO_2 than the 10% CO_2 – 90 % Ar mix, meaning that in absolute terms more CO_2 is available to be converted.

5.1.2 CO_2 conversion in $BaTiO_3$ packed beds

Similarly to the results presented for Al_2O_3, the data for the $BaTiO_3$ packed bed is presented in Figure 61 to Figure 64 as CO_2 conversion plotted against power for gas compositions of 90% Ar – 10% CO_2, 50% Ar – 50% CO_2, and 100% CO_2.

Figure 61: CO_2 conversion plotted against plasma power in a $BaTiO_3$ packed reactor. Inlet gas composition is 10% CO_2, 90% Ar with a total flowrate of 100 ml/ min. Reactor is driven by a 5 kHz Square wave, with voltage stepped between 5 – 10 kV. Error for 180 – 300 μm particles is based on 3 repeats, with error bars indicating one standard deviation. Other particle sizes are based on two repeats with standard deviation estimated from 180 – 300 μm particle sizes.

The most interesting feature of the data presented in Figure 61 is the 180 – 300 μm particle size yielding the highest conversion of CO_2 at input powers greater than ~9 W, corresponding to an applied voltage of 9 kV or greater. All other particle sizes, with the exception of the 300 – 500 μm particles, give remarkably similar results to each other. They draw similar powers for any given applied voltage, and convert similar amounts of CO_2. The 300 – 500 μm particles follow a

different trend, having the lowest conversion of CO_2 for each applied power. In addition to this, these 300 – 500 μm particles also draw the lowest power for each applied voltage, particularly at low applied potential differences. However, given the relative magnitude of the error in CO_2 conversion and power consumption, it would be unreasonable to make any conclusions about the nature of the plasma in the 300 – 500 μm packed bed based on this data set. On the other hand, and similarly to the case of Al_2O_3, it is reasonable to state that the nature of the plasma discharge in the 180 – 300 μm particle sizes at voltages of 9 kV or greater must be different to the plasma discharge in particles with sizes greater than 300 μm. If the effect was due solely to increased surface area enhancing CO_2 reduction by a surface reaction mechanism, then it would be expected that the 300 – 500 μm particles would yield the second highest CO_2 conversions, rather than the lowest. Comparing the $BaTiO_3$ packed reactor with the unpacked reactor, the unpacked reactor appears to yield a higher CO_2 conversion. Although it should be noted that these data sets are not directly comparable as the residence time in the unpacked reactor is approximately ~1.36 seconds, as opposed to 0.4 – 0.5 seconds in the packed reactor. However, this is still an unusual result as the Al_2O_3 packed reactor yields a significantly higher CO_2 conversion, particularly at high power inputs. Also, $BaTiO_3$ has been reported to enhance conversion of CO_2 in a packed bed reactor compared with an unpacked reactor, regardless of the reduction in residence time that is induced by adding packing material into reactor [72].

Figure 62: CO_2 conversion plotted against plasma power in a $BaTiO_3$ packed reactor. Inlet gas composition is 50% CO_2, 50% Ar with a total flowrate of 100 ml/ min. Reactor is driven by a 5 kHz Square wave, with voltage stepped between 5 – 10 kV. Error is based on two repeats of each experiment.

Figure 62 shows CO_2 conversion in $BaTiO_3$ packed reactors, where the feed composition is 50% Ar – 50% CO_2. The 180 – 300 μm particles show the lowest CO_2 conversion for any applied

power. 300 – 500 μm particles then show the 2nd lowest conversion for any applied power, except for at input powers > 10 W, where it appears that the CO_2 conversion exceeds that obtained with larger particle sizes. However, this trend does not fall within the margins of the error bars so no conclusions can be made regarding this behaviour. The 3 largest particle sizes, again, show very similar trends to each other, with very little discernible difference between the CO_2 conversions obtained at each applied power. This implies that there is no difference in the behavior between the 3 different sizes of particles. Interestingly the relationship between applied power and CO_2 conversion with the smallest particle sizes (<500 μm) follows a very different trend to the larger particle sizes (>500 μm), with the curves being a concave, rather than a convex shape. The cause of this change in shape of these trends is not clear, although it may be related to the distribution of the sizes of void spaces in tightly packed reactors.

By examining the relationship between applied voltage and difference from the mean power, as shown in Figure 63, it becomes clear that with applied voltages of 8 kV or less, there is a difference in the behavior of the reactor, with incrementally decreasing sizes of particle, the power consumption per applied voltage decreases. This is likely to be due to the reactor only partially discharging with these gas conditions, with the volume of the packed bed discharging being reduced with decreasing particle size. I.e. for the same applied voltage, less power is drawn by the reactor with smaller particle sizes, which is likely to be due to the reactor only partially discharging.
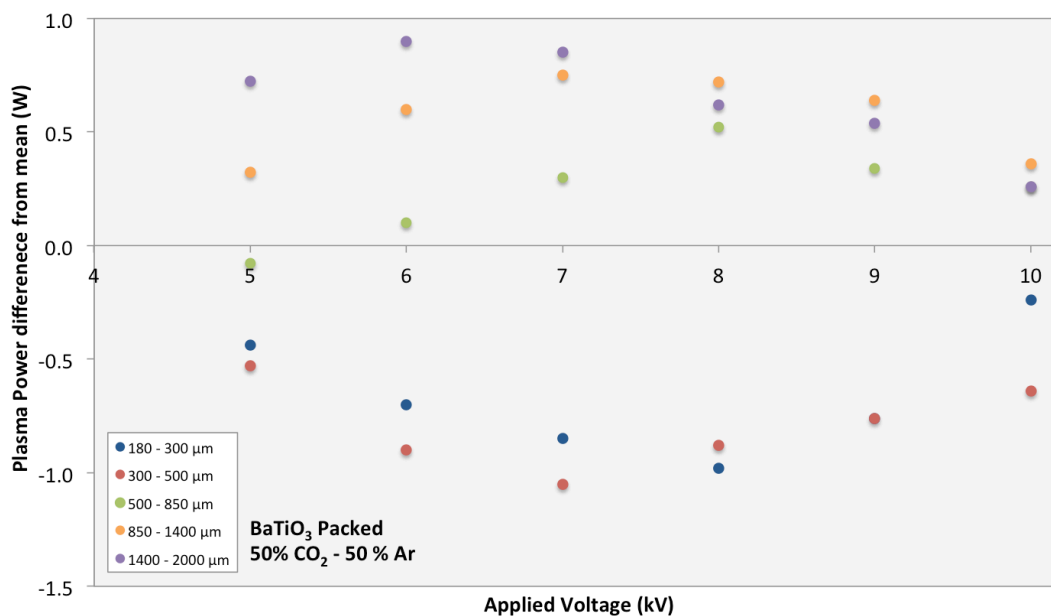
Figure 63: Measure of plasma power difference from mean for each applied potential difference using a BaTiO₃ packed reactor at a gas composition of 50% CO₂ – 50% Ar. Values above the line at ΔP = 0 indicate an above average power consumption. Error bars are not included as the graph becomes too difficult to easily read.
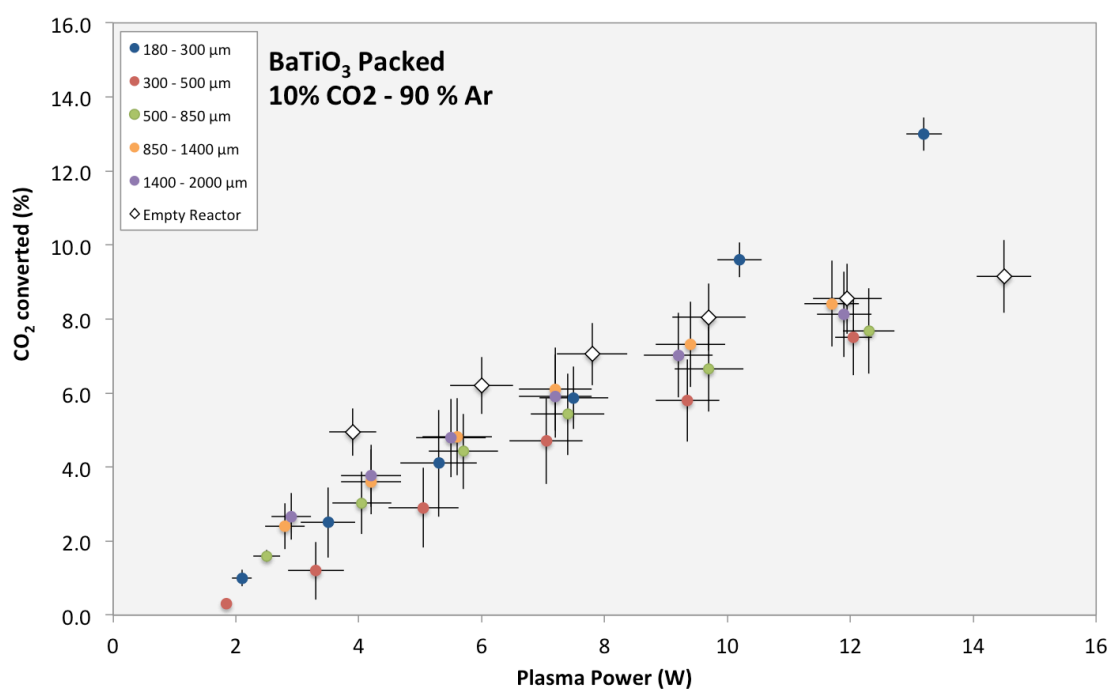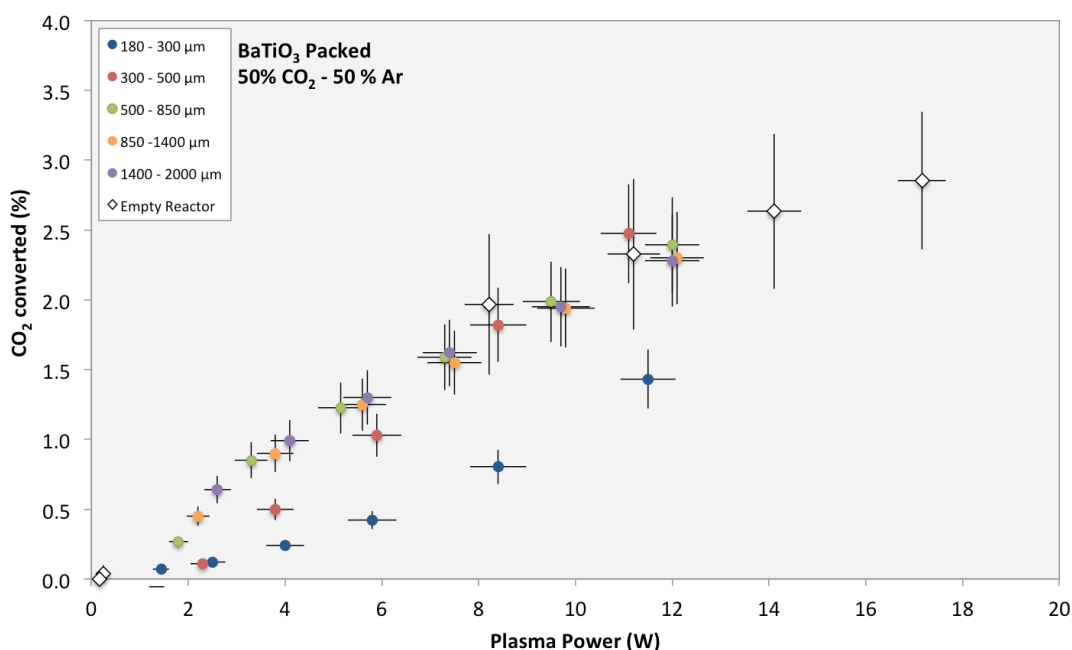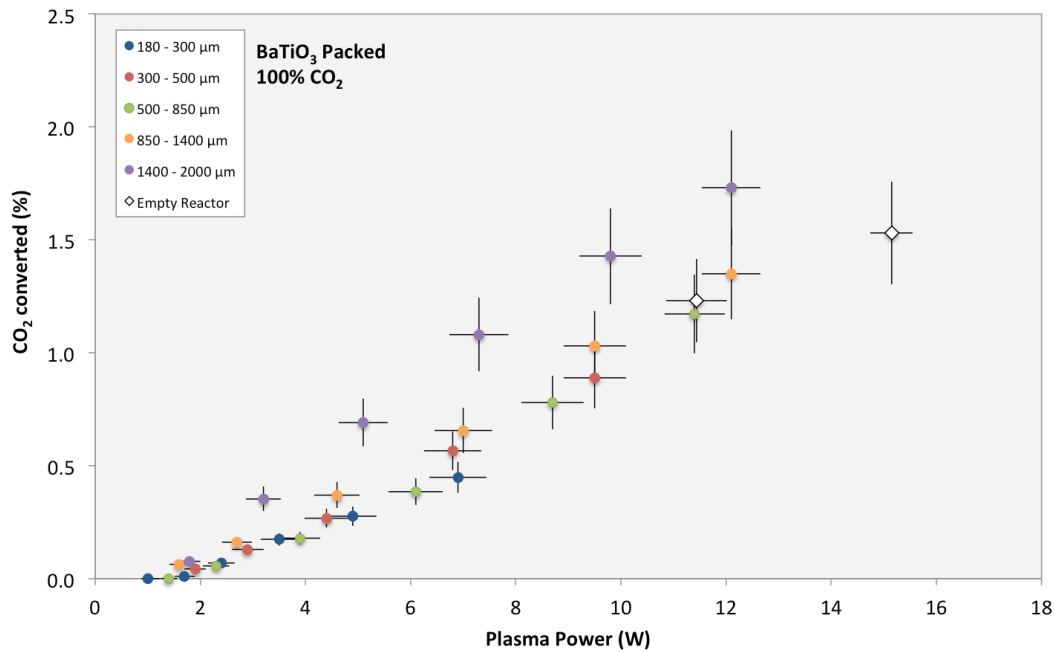
Figure 64 CO$_2$ conversion plotted against plasma power in a BaTiO$_3$ packed reactor. Inlet gas composition is 100% CO$_2$ with a flowrate of 100 ml/ min. Reactor is driven by a 5 kHz Square wave, with voltage stepped between 5 – 10 kV. Error is based on two repeats of each experiment.

Figure 62 shows the use of a BaTiO$_3$ packed bed for CO$_2$ reduction in 100% CO$_2$ streams. In this experiment, the highest CO$_2$ conversion occurs with the largest particle sizes. CO$_2$ conversion decreases incrementally with each decreasing particle size. CO$_2$ conversion occurs at every applied voltage with almost all particle sizes. This is a stark contrast to the Al$_2$O$_3$ and unpacked reactors, and can only be justified by stating that BaTiO$_3$ reduces the breakdown voltage of the reactor, even with the smallest particle sizes. This is most likely due to the ferroelectric nature of the material giving it a high dielectric constant, and potentially electron emission properties that might not otherwise occur.

Unlike the 50% CO2 – 50 % Ar case with the BaTiO$_3$ packed reactor, the trends in the data with particle sizes < 1400 μm can be described as concave, where as with the 1400 – 2000 μm particles the relationship is convex, but almost linear. The data supports the hypothesis that this concave trend is related to the distribution of void spaces between particles, as an increase in CO$_2$ concentration should theoretically increase breakdown voltage. Hence this effect would begin to apply to larger particle sizes, as longer void spaces would be required in order to accelerate electrons to have sufficient energy to initiate a discharge.

5.1.3 Efficiency of CO$_2$ conversion

Although the experiment has not been designed for optimum efficiency of conversion of CO$_2$, process efficiency will be one of the most important factors in determining the viability of a plasma based method for carbon dioxide utilisation. In addition to this, in some circumstances the efficiency data can provide an insight into reaction mechanism, as some mechanisms inherently limit efficiency. Many of the trends related to applied voltage, input power and gas composition are well documented, and so they are not covered extensively here. Efficiency is calculated using Equation 8, given on page 42.
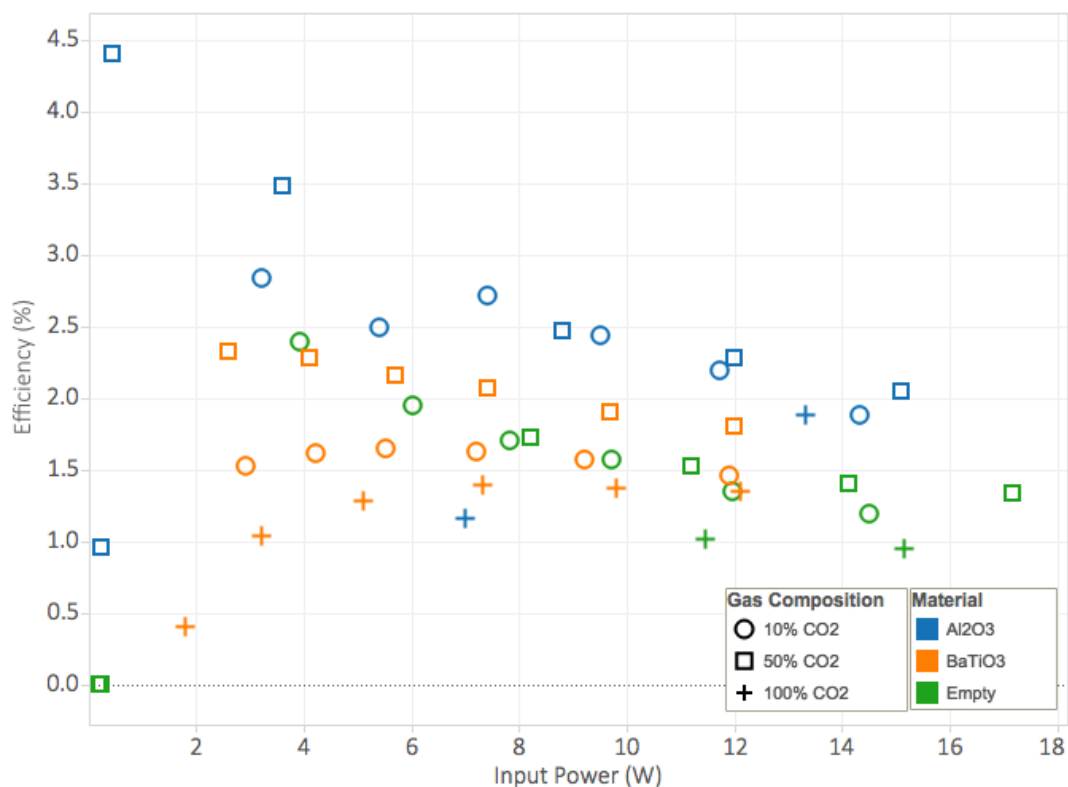
Figure 65: Efficiency plotted against reactor input power for all different packing materials and gas compositions tested. Particle size is 1400 – 2000 μm in cases where particles are used.

Figure 65 shows efficiency as a function of reactor input power for BaTiO$_3$, Al$_2$O$_3$ and with an unpacked reactor at 90% Ar – 10% CO$_2$, 50% Ar – 50% CO$_2$, and 100% CO$_2$. Where packing material is used, the size is 1400 – 2000 μm.

The data in this graph shows that for 10% CO$_2$ and 50% CO$_2$ gas mixtures, that as reactor input power decreases, the efficiency of conversion tends to increase with Al$_2$O$_3$, BaTiO$_3$ and the unpacked reactor. This trend is strongest with the empty and Al$_2$O$_3$ packed reactor, compared with the BaTiO$_3$ packed reactor, and is in good agreement with observations relating power and efficiency made by other research groups. When the highest input CO$_2$ concentration is used, the efficiency of the reactor tends to decrease as input power decreases, a result that is not

104

commonly observed and may be indicative of the reactor partially discharging. Although, it must be remembered that only $BaTiO_3$ yields any conversion of CO_2 at input voltages of 8 kV or lower in 100% CO_2.

Comparing gas compositions with each other, 10% and 50% CO_2 mixtures give similar efficiencies in Al_2O_3 packed beds and the empty reactor at all applied powers. Other groups have reported that efficiency tends to increase with increasing CO_2 concentration [58].

Efficiency of conversion is highest in the Al_2O_3 packed reactor, with the $BaTiO_3$ packed and empty reactors having similar efficiencies under this condition.
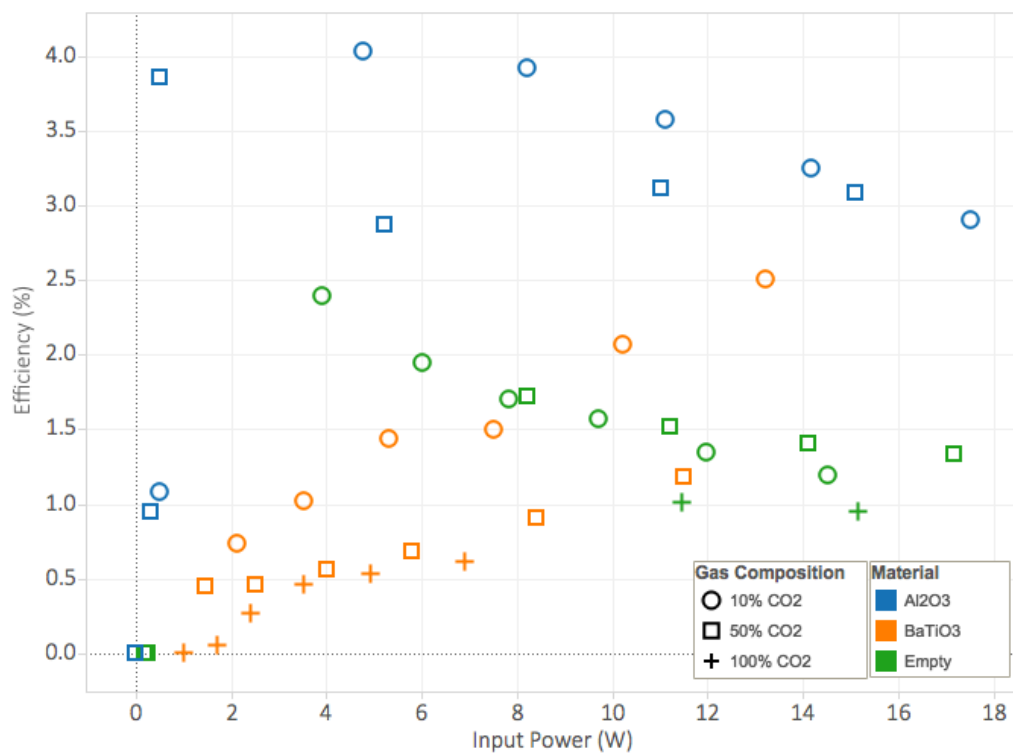
Figure 66: Efficiency plotted against reactor input power for all different packing materials and gas compositions tested. Particle size is $180 - 300$ μm in cases where particles are used.

Figure 66 shows efficiency as a function of reactor input power for all $180 - 300$ μm packing materials and gas compositions tested. In order to understand the change in reactor behavior, the identified trends in Figure 65 (Large particles) are compared with Figure 66 (Small particles). The data used for the empty reactor is identical in both graphs.

Examining the case of Al_2O_3 packing, it is found that with the 10% CO_2 feed, that similarly to Figure 65, efficiency increases with decreasing power. However, with a 50% CO_2 feed, the efficiency is seen to decrease with decreasing input power, this behavior is different to the trend identified in Figure 65. This same trend, decreasing power correlated with decreasing efficiency, is observed for all gas compositions in the $BaTiO_3$ packed reactor. As stated previously, this may

indicate that the reactor is partially discharging in cases where this occurs. This trend of efficiency decreasing with applied power is more pronounced with smaller particle sizes, or higher CO_2 concentrations.

In the case of the smallest particle sizes, Al_2O_3 again shows the highest efficiency, followed by the unpacked reactor, with the $BaTiO_3$ having the lowest (excluding two cases in 10% CO_2 at high input powers).

The highest efficiency obtained from all cases is ~ 4.5%. This is relatively low for a packed bed reactor, and is a reflection of the operating conditions not being optimized for this reactor.

5.1.4 Relationships between measured outer wall temperature and observed changes in reactor behaviour
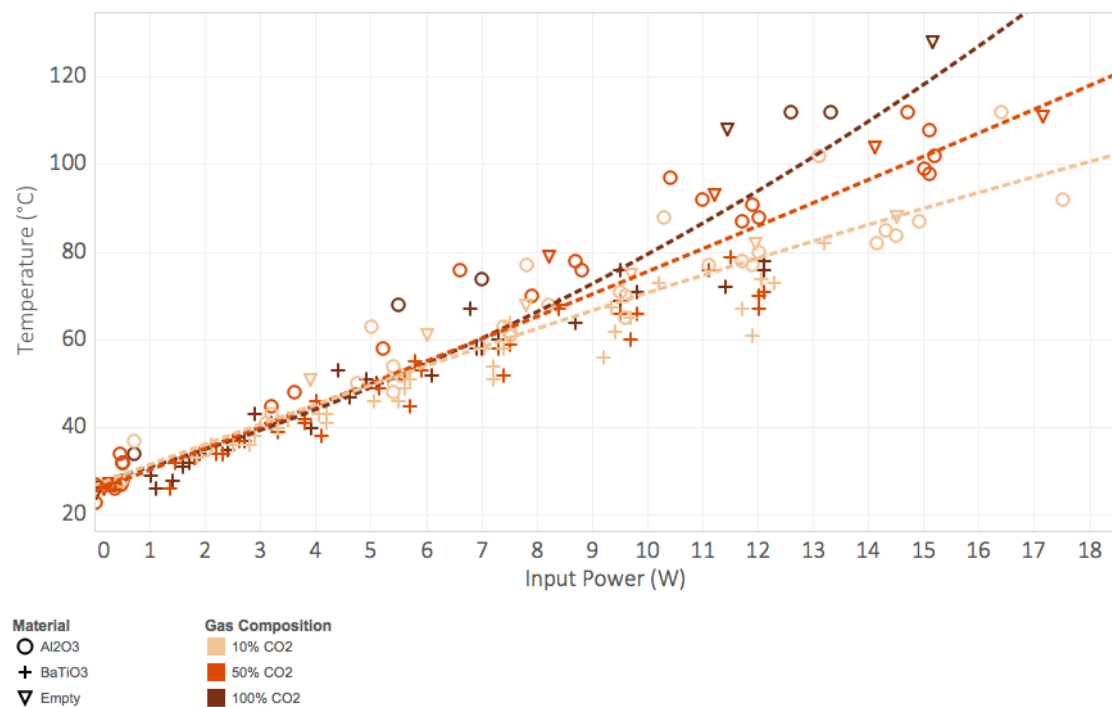
Figure 67: Measured outer wall temperature as a function of reactor input power. Please note that the wall temperature is measured from a point on the outside of the wall, and the values shown here are therefore representative of the minimum average temperature that is found inside the reactor. Dashed line indicates a 2nd order polynomial best fit line applied to each different gas composition.

Shown in Figure 67 is the measured outer reactor wall temperature as a function of reactor input power. A strong positive relationship between reactor input power and measured outer wall temperature is observed, with gas composition as well as reactor packing material also affecting the measured temperature. The measured wall temperature at a given power input is linked to packing material as follows, from lowest measured temperature to highest: $BaTiO_3$ < Al_2O_3 </≈ unpacked reactor. Gas composition is also seen to have an effect on the reactor wall temperature, with higher CO_2 concentrations correlating with higher wall temperatures at high

input powers. The relationship between reactor temperature, gas composition, and packing material becomes more clear upon examining each power vs. temperature plot dependent upon the packing material used. Shown in Figure 68 is the data from Figure 67 separated by the packing material used.
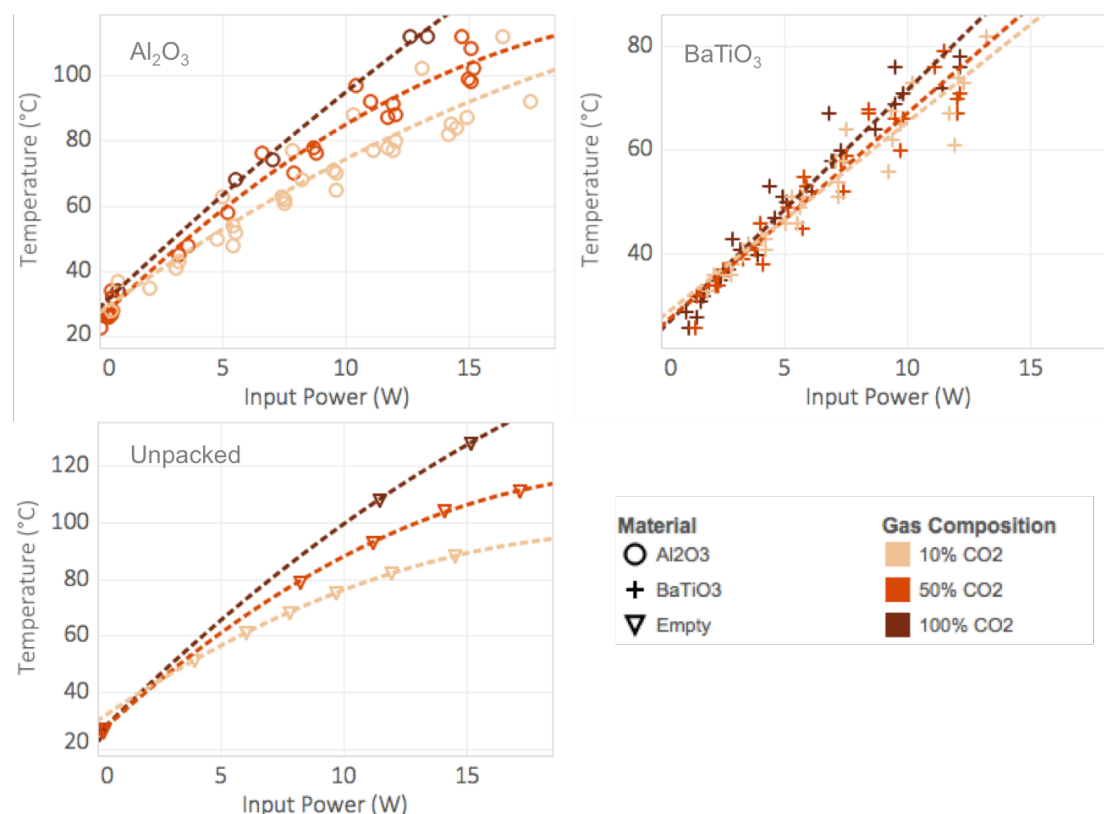
Figure 68: Measured outer wall temperature as a function of reactor input power. Please note that the wall temperature is measured from a point on the outside of the wall, and the values shown here are therefore representative of the minimum average temperature that is found inside the reactor.

The reactor temperature is found to be correlated with CO_2 conversion, but this is most likely due to CO_2 conversion and temperature both being a function of reactor power. CO_2 reduction to CO is likely to be limited at high temperatures due to fast, exothermic, reverse reactions of CO and oxygen containing species occurring (I.e. combustion).

Brehmer et al [103] have demonstrated a relationship between reactor temperature and ozone production, with high temperatures appearing to inhibit either the generation or the stability of high concentrations of ozone. Ozone concentration was monitored solely with the 90% Ar – 10% CO_2 set of experiments. However, the data collected, despite numerous repeats, was not always consistent due to changes in gas temperature, humidity, and the ozone concentrations being generated being, in some cases, at the detection limit of the FTIR with the set-up that was being used. The ozone concentration data is therefore presented as a fraction of the highest stable ozone concentration measured, 428 ppm. No significant trend was found that relates particle size to ozone concentration, however this may be due to insufficient good quality data being

collected in order to observe a trend. The strongest relationship with ozone concentration is found between packing material, input power, and measured outer wall temperature.
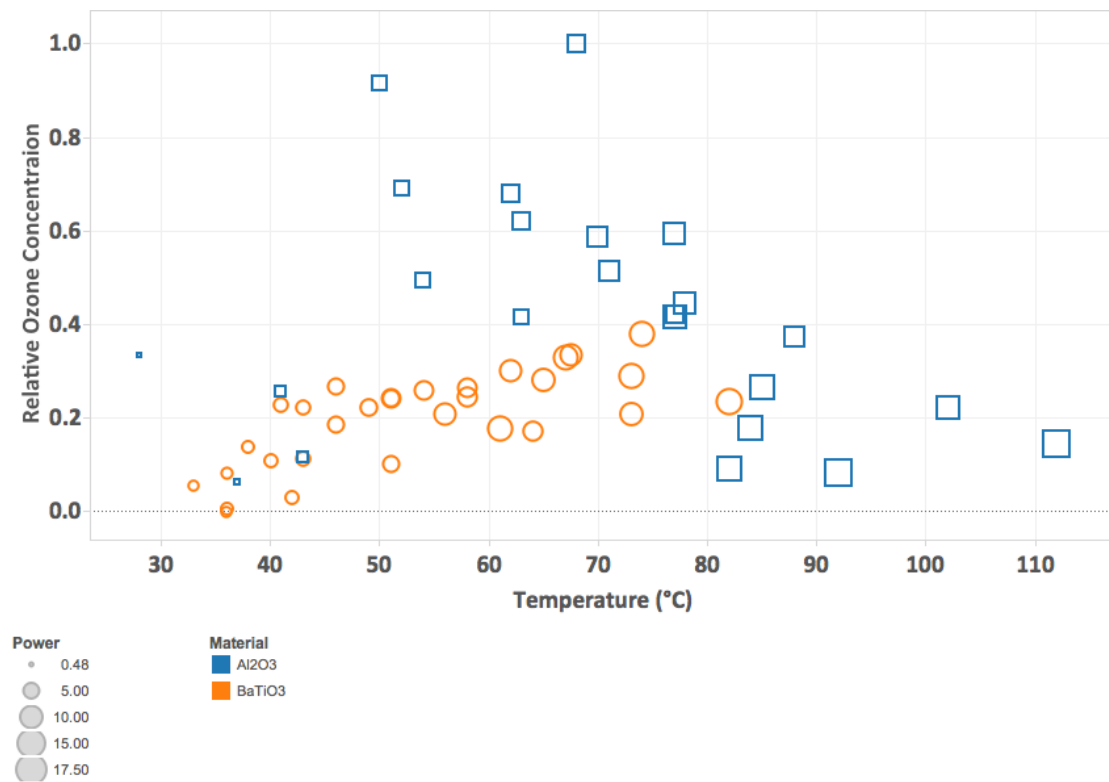
Figure 69: Relationship between reactor temperature and ozone concentration for Al_2O_3 and $BaTiO_3$ at a feed gas composition of 90% Ar – 10% CO_2. The plot markers are scaled to indicate reactor power, with larger markers indicating a higher power. Ozone concentration is measured relative to the highest measured stable ozone concentration, 428 ppm. Which occurs at 72 °C with 8.2 W input power in 180 – 300 µm Al_2O_3 packing.

The relationship between reactor temperature and ozone concentration is shown by Figure 69. The data for $BaTiO_3$ shows that with increasing reactor power the ozone concentration increases almost linearly, with seemingly no effect of temperature limiting ozone concentration. Al_2O_3, which generates much higher concentrations of ozone, shows that moderate powers tend to have the highest ozone concentrations. Higher input powers, where measured wall temperature is also highest, have much lower ozone concentrations. This data is not sufficient to state that there is a relationship between ozone concentration and temperature, although O_3 is known to decay very rapidly at high temperatures.

Figure 70, however, shows ozone concentration plotted as a function of FTIR scan number. FTIR scan number can in this case be considered as time. The reactor is turned on at 10 kV shortly before scan 1 occurs. Immediately afterwards, ozone concentration is seen to be at a maximum, with measured concentrations being between 650 – 750 ppm immediately after the reactor is switched on. Shortly after this peak, the ozone concentration rapidly decreases to its 2nd lowest point on the graph, whilst still being at the same applied voltage (and similar corresponding

power) at 10 kV. This decrease in ozone concentration corresponds with an increase in the reactor temperature, at this point reactor temperature is at its stable high point, with a measured outer wall temperature of 110 °C. From here, ozone concentration steadily increases with each decreasing applied voltage down to 7 kV. With each step decrease in voltage, the ozone concentration can be seen to slowly increase over the duration of the applied voltage. This could possibly be attributed to the reactor cooling down between each step change in applied potential difference.
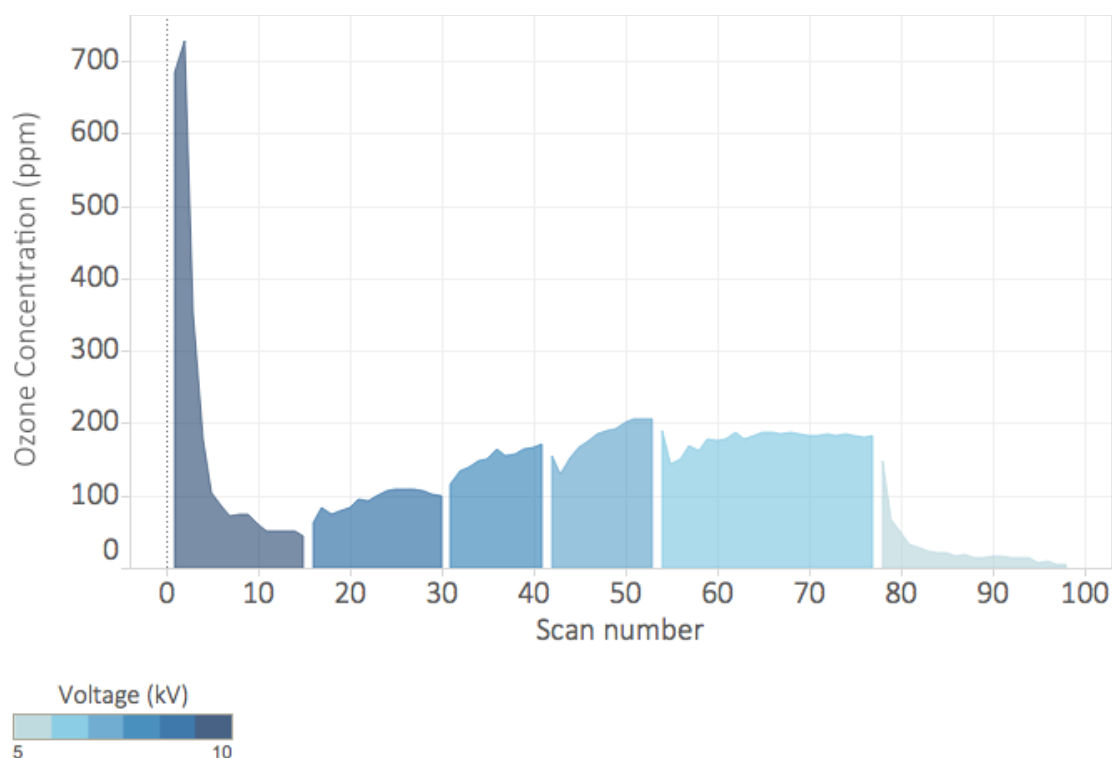
Figure 70: Ozone concentration plotted as a function of FTIR scan number in 300 − 500 µm Al_2O_3 particles with 90% Ar − 10% CO_2 feed gas composition. Increasing scan number is equivalent to increasing time. Darker shades of blue represent a higher voltage. As stated in the experimental method, initial applied voltage is 10 kV, and this decreases by 1 kV steps until it reaches 5 kV.

Figure 70 provides compelling evidence that ozone concentration is limited by reactor temperature, rather than by some change in a reaction mechanism occurring at different applied potential differences. As the high input power immediately leads to a high ozone concentration that immediately is seen to decrease as the reactor heats up.

5.1.5 Summary - CO_2 conversion data

The data shows that there is a strong relationship between particle size, gas composition, materials properties and applied electric field strength and the resultant CO_2 conversion that can be achieved. Increasing argon concentration allows the possibility of operation of the reactor with smaller particles. Smaller particles are more effective in both the cases of $BaTiO_3$ and γ-

Al_2O_3 for achieving the highest conversions of CO_2. However, it appears that plasma discharges can only be ignited in the smallest particles if a sufficiently high electric field gradient can be applied. The ability to apply this high field gradient is dependent upon electrode spacing, as well as the potential difference that can be generated by the power source.

Some other important observations are summarized below:

- Al_2O_3 can significantly increase conversion and efficiency of CO_2 reduction compared with both an unpacked reactor, and a $BaTiO_3$ packed reactor.
- The smallest particle sizes (180 – 300 μm) of Al_2O_3 increase CO_2 conversion by up to 70% compared with particle sizes of 500 μm and above, provided that argon concentration and electric field strength are sufficiently high. The mechanism that causes the enhancement to CO_2 conversion in the particle sizes from 180 – 500 μm is likely to be different to that causing enhancement in particles greater than 500 μm in size.
- Small Al_2O_3 particles (< 500 μm) and $BaTiO_3$ particles (< 300 μm) draw high powers at high voltages (particularly in high Ar concentrations) compared with larger particle sizes
- Conversely, using small particles at low applied voltages, less power tends to be drawn by the reactor compared with larger particle sizes
- $BaTiO_3$ significantly decreases breakdown voltage. In a 100% CO_2 feed reactor, conversion is found to occur at 6 - 7 kV with the smallest particle sizes. With both the Al_2O_3 packed and empty reactors, no plasma discharge is found to occur under these conditions with any particle size.
- $BaTiO_3$ packing does not, in the majority of cases, increase CO_2 conversion for the applied powers and voltages tested in this experiment compared with an empty reactor. However, reactor residence time is reduced by up to 3 times in a packed bed compared with an unpacked reactor that may account for this decrease in conversion.

The data presented here, along with these summarized trends lead to a number of research questions. Some of these questions are more general, relating to the overall behavior of packed bed reactors, whilst some of the questions concern observations made specifically about the data presented.

Perhaps the most critical question would be, what is the relationship between breakdown voltage, applied voltage, particle size (and shape), gas composition and choice of packing material? The trends from the data demonstrate that there are potentially significant benefits to using small particles, as CO_2 conversion can be increased significantly under some conditions by using small particle sizes. To be able to elucidate the relationship between these parameters

and obtain a general empirical relationship that could be used to inform reactor design would be very beneficial.

Another question raised would therefore be, can the benefits of small particle sizes be realised in all packed bed plasma reactors? If so, how? Is it possible to ignite a plasma discharge in small particle sizes when a noble gas is not present? Why does the trend amongst publications on packed bed reactors tend toward using larger particle sizes?

Relating the last question to this experiment, why do the particle sizes and material properties tested cause an increase or decrease in observed CO_2 conversion?

6 Reactor electrical characterisation – Results and Discussion

The aim of this section is to try to answer the questions posed at the end of section 5.1.5:

1. What is the relationship between burning voltage, applied voltage, particle size (and shape), gas composition and choice of packing material?
2. Can the benefits of small particle size be realised in all packed bed plasma reactors?
3. Why do the particle sizes and material properties tested cause an increase or decrease in observed CO_2 conversion?

In order to try to understand the behavior of the plasma discharge, the electrical properties of the reactor can be characterised. Based on the previous work of other research groups, described in section 3.2, and using the methodologies described in section 4.4.3, characteristics such as the burning voltage and the reactor capacitances (eg. dielectric, plasma, gap, and effective dielectric capacitances) can be obtained from Q-V Lissajous plots. In this section data obtained from using Mathematica to generate Lissajous plots and subsequently extract data from them is presented. For reference, Figure 71 shows a Lissajous figure, and the values relating to electrical characteristics that can be obtained from its geometry.
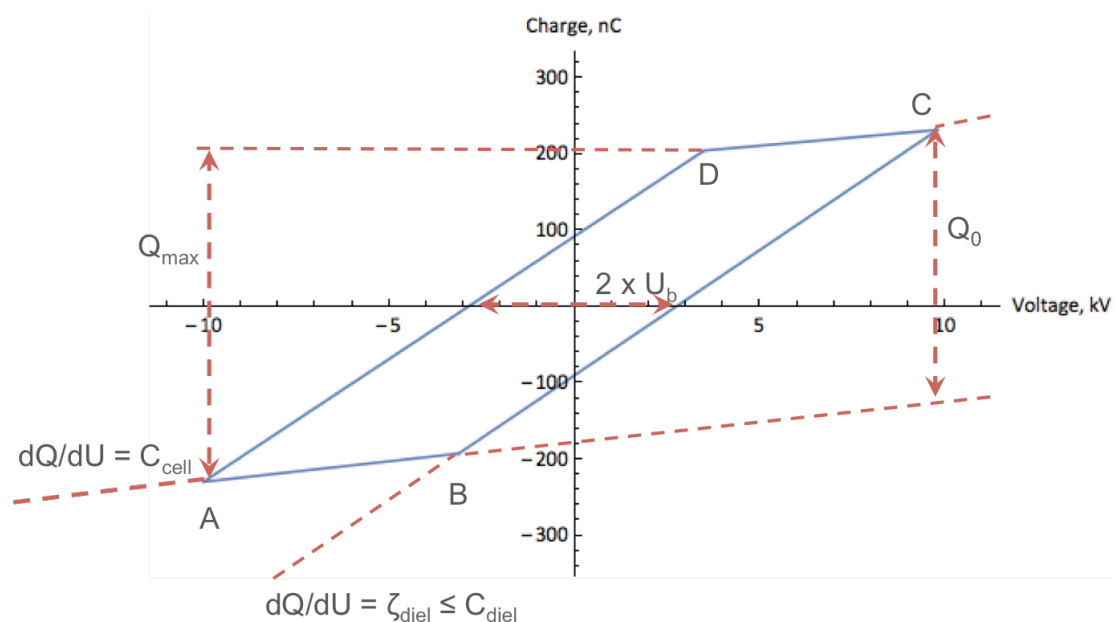
Figure 71: Annotated Lissajous figure, featuring data that can be obtained from its geometry

Before attempting to answer these questions, a concept that must be explored first and in greater depth is the "partial discharging" of the reactor that is mentioned throughout the

presentation of the results in section 5.1.1 and 5.1.2. As described in section 3.2, the Lissajous figure is represented by a parallelogram shaped figure. The gradients of the lines that make up the parallelogram correspond to capacitances of the plasma reactor. C_{cell} is the capacitance of the reactor during the "discharge off" phase, and is related to the capacitances of the quartz glass dielectric layer, the packing material and the gas capacitance by the sum of their reciprocals, represented by Equation 19:

$$\frac{1}{C_{cell}} = \frac{1}{C_{diel}} + \frac{1}{C_{packing}} + \frac{1}{C_{gas}}$$

Equation 19

C_{cell} therefore corresponds to the minimum value that can be obtained for capacitance from the gradient of the lines in the Lissajous figure. In the packed bed reactor used in these experiments, 2 different packing materials are used in 5 different particle sizes, with a range of different gas compositions. C_{gas} and $C_{packing}$ will therefore be different every time the reactor has a different particle size, packing material or different gas composition.

In the reactor discharging phase, the gas becomes conductive and the C_{gas} and $C_{packing}$ terms of Equation 19 are negated. Therefore during the discharging phase the capacitance measured by the gradient of the line, BC and DA, is equal to the value of the capacitance of the dielectric layer. Provided that the reactor is fully discharging, the value of C_{diel} is the maximum value obtained for capacitance measured from the Lissajous figure. C_{diel} is a product of the geometry of the reactor, and should therefore theoretically have a fixed value. In reality, the value of this capacitance will have some dependence on applied frequency and temperature.

When the reactor is partially discharging, the gradient of the line BC / DA is less than the value of the dielectric capacitance, C_{diel}, but greater than the value of the cell capacitance, C_{cell}. This has been termed the effective dielectric capacitance, and is represented by ζ_{diel}. Under conditions when the reactor is partially discharging the parallelogram becomes misshapen as the gradient of the line representing C_{diel} approaches the gradient of C_{cell}. Consequently the parameters that are measured from the Lissajous figure must be corrected in order to obtain figures that are an accurate reflection of the behavior that is actually occurring. As demonstrated by Peeters & van de Sanden [95], ζ_{diel}, can be used to correct the measured parameters from the Lissajous figure. The relationships derived in their work, based upon ζ_{diel}, are used throughout this section, and are described in further detail as required.

6.1.1 Determination of reactor capacitances, C_{diel} and C_{cell}

In order to determine partially discharging reactor behavior, a value for dielectric capacitance must first be obtained. Shown in Figure 72 is the gradient of the Lissajous figure lines BC and

DA, corresponding to C_{diel}, in an unpacked reactor driven by a 10 kV, 5 kHz sine wave using a feed gas of Argon balanced with CO_2 with concentrations ranging from 0 – 100%. The graph indicates that the two measured gradients are not identical, so a mean gradient is used to determine a value for C_{diel}. In high argon concentrations (90 – 100% Ar) the mean value for capacitance reaches a maximum of ~ 35 pF, +/- ~ 1 pF. Although this only provides an estimate for dielectric capacitance, it is difficult to determine a more accurate measurement, therefore this is the value used for the dielectric capacitance of the reactor henceforth. Its suitability as a value for C_{diel} is reflected in the observed saturation of reactor capacitances with other packing materials that is presented in later results.
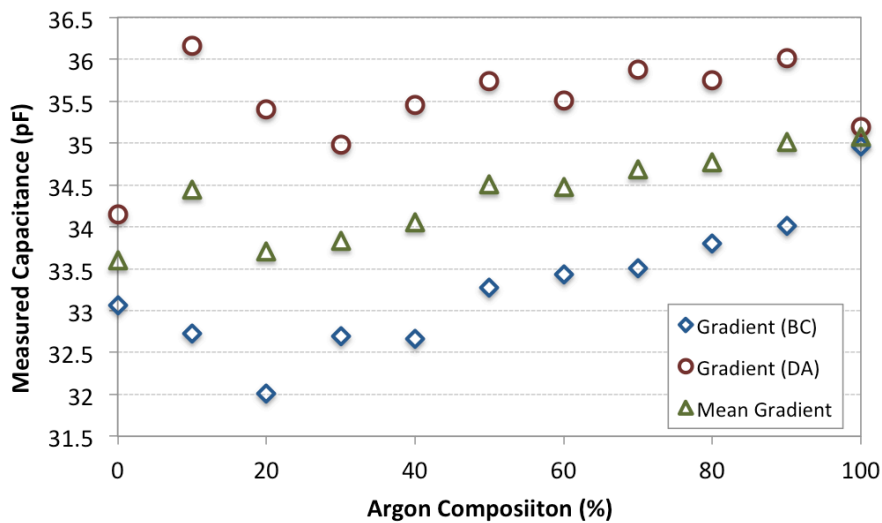
Figure 72: Measurements of C_{diel} based on the gradient of Lissajous figure lines BC and DA. The argon concentration is balanced with CO_2. The reactor is driven by a Sine wave at a frequency of 5 kHz.

A value for C_{cell} for each reactor set-up must also be known. However, as stated previously C_{cell} is dependent upon C_{gas} and $C_{packing}$, which in turn are dependent upon gas composition, material dielectric constant, size, shape, and packing density, all of which are variables in this experiment.

In order to decide upon a value that should be used for C_{cell} the relationship between gas composition, particle size and packing material should be examined. Figure 73 - Figure 75 show measured mean values for C_{cell} as a function of the reactor argon concentration, with particle size also indicated for Al_2O_3, $BaTiO_3$ and an unpacked reactor respectively.
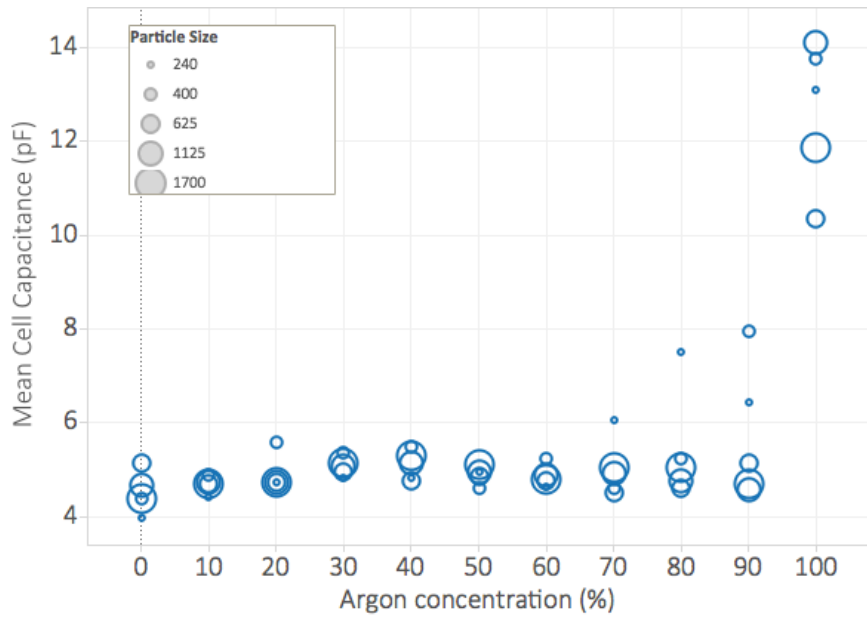
Figure 73: C_{cell} as a function of argon concentration balanced with CO_2 for different sizes of Al_2O_3 particles. Measured using a 10 kV, 5 kHz sine wave.
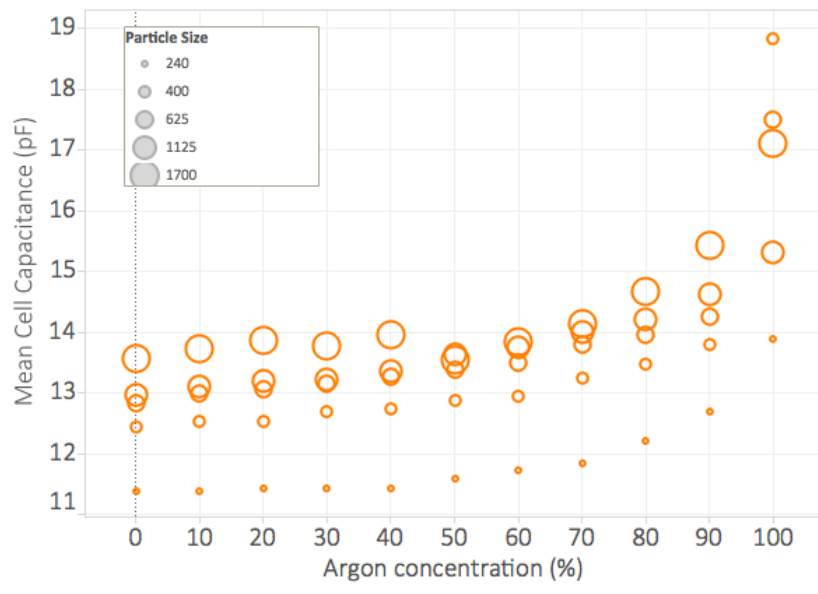
Figure 74: C_{cell} as a function of argon concentration balanced with CO_2 for different sizes of $BaTiO_3$ particles. Measured using a 10 kV, 5 kHz sine wave.
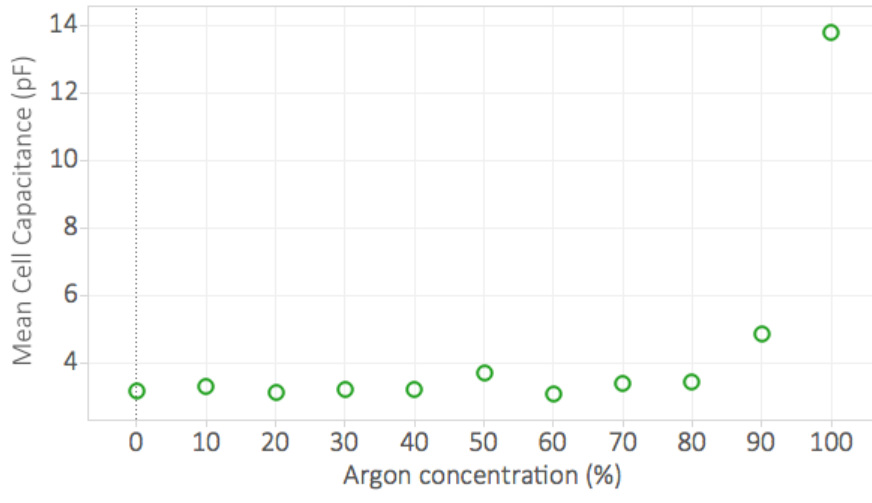
Figure 75: C_{cell} as a function of argon concentration balanced with CO_2 for an unpacked reactor. Measured using a 10 kV, 5 kHz sine wave.

Comparing Figure 73 and Figure 75 with each other, with respect to the change in the measured cell capacitance as a function of argon concentration, they all show similar trends to each other. With the highest cell capacitance measured in 100% argon, and this value rapidly decreasing with increasing CO_2 concentration, to a plateau that occurs between approximately 0% and 60% Ar concentration. The greatest decrease in value occurrs between 90% and 100% Ar. The highest value of C_{cell} occurs in the BaTiO$_3$ packed bed, followed by Al$_2$O$_3$, and the unpacked reactor. In the Al$_2$O$_3$ packed reactor, there does not appear to be a strong relationship between packing particle size and cell capacitance. In the BaTiO$_3$ packed bed, there is a correlation between particle size and measured cell capacitance. In this instance, the packed bed with the largest particles has the highest capacitance, descending sequentially to the smallest particles having the lowest capacitance. These graphs show that to find an appropriate value to use for cell capacitance, there are a number of different scenarios that can be justified:

- Mean value of C_{cell} for all particle sizes of Al$_2$O$_3$ and the unpacked reactor at Ar concentrations <90%
- Mean value of C_{cell} for all particle sizes of Al$_2$O$_3$, and the unpacked reactor, at Ar concentration = 100%
- Mean values of C_{cell} for separate sizes of BaTiO$_3$ at Ar concentrations <70%
- Independent values of C_{cell} for separate sizes of BaTiO3 at each Ar concentration of 80% and above

6.1.2 Partial discharging reactor correction

With the values of C_{cell} and C_{diel} defined, cases where $\zeta_{diel} < C_{diel}$ can be examined. Shown in Figure 76 is the measured mean value for effective capacitance for 180 – 300 µm, and 300 –

116

500 μm BaTiO$_3$ particles, in a 90% Ar – 10% CO$_2$ reactor driven by a 5 kHz square wave, with voltages ranging from 5 – 10 kV.
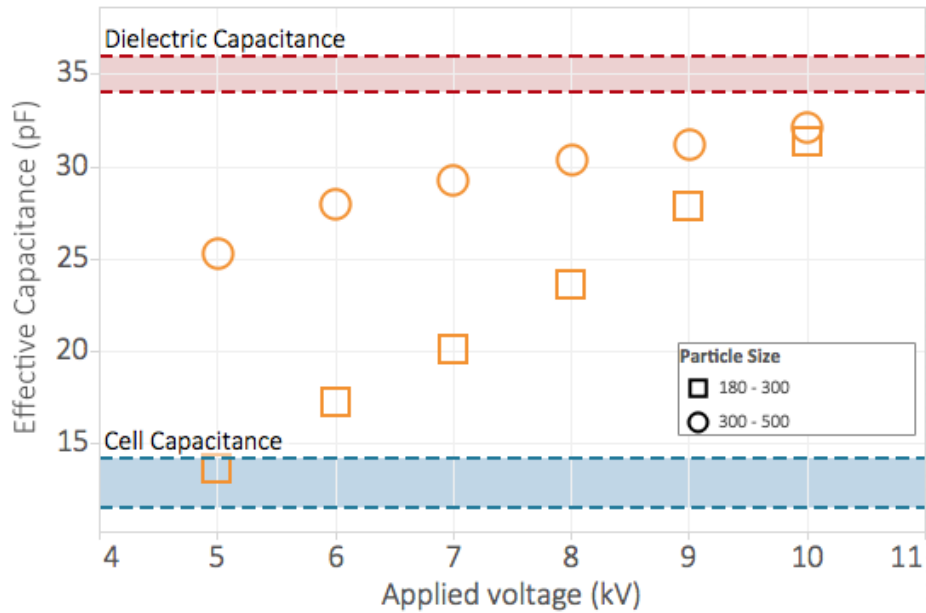
Figure 76: Measured mean effective capacitance of a 180 – 300 μm BaTiO$_3$ packed reactor in 90% Ar – 10% CO$_2$ at a range of applied voltages.

Figure 76 shows that with the 180 – 300 μm particles that the measured value for effective capacitance decreases with decreasing applied voltage almost linearly, from the point at 10 kV, where ζ_{diel} is at ~32 pF, approximately ~ 3 pF less than C_{diel}, to the point at 5 kV where ζ_{diel} is almost equal to C_{cell}. This indicates a transition from almost full discharging of the reactor, with complete charge transfer from one electrode to the to other, to almost no discharge occurring. For comparison, the 300 – 500 μm BaTiO$_3$ particles show ζ_{diel} decreasing with applied voltage, however in this case the minimum value is ~25.3 pF at 5kV, indicating that a significant proportion of charge is transferred from electrode to the other.

There are limitations to the Mathematica program that is used to analyse the data generated from the oscilloscope, namely that it is not able to determine all capacitances of the reactor when the reactor is partially discharging if the data obtained has a high level of noise (or is highly irregular in shape), even after data smoothing has been applied. The noisiest data happens to occur when Al$_2$O$_3$ is packed into the reactor, particularly with small particles. The source of the noise is a point of discussion in itself, and its origins are discussed in section 6.1.5. Therefore, it is not possible with the current program to use this step decrease in voltage method to determine effective reactor capacitances at each different gas composition tested.

However, the purpose of trying to determine effective capacitance is to correct the data obtained from the Lissajous figures, namely the burning voltage of the reactor. Theoretically, burning voltage for any individual void space in which a discharge can occur should be constant,

regardless of applied voltage. Once the applied voltage reaches a threshold voltage, an electrical breakdown will begin to occur in the void of the particle. Peeters and van de Sanden demonstrated that the burning voltage is almost constant as a function of applied voltage amplitude in a fixed geometry DBD plasma jet [95]. The reactor burning voltage of a packed bed reactor, being composed of a number of voids with a range of sizes, is likely to have an applied voltage dependent burning voltage. Before testing this hypothesis, the voltage dependent burning voltage of the unpacked reactor should be measured. The equation derived by Peeters and van de Sanden to determine burning voltage (U_b) based on the geometrically determined ΔU is given by Equation 20:

$$U_b = \frac{1 - C_{cell}/C_{diel}}{1 - C_{cell}/\zeta_{diel}} \Delta U$$

<div align="center">Equation 20</div>

Using this equation, with C_{diel} = 35 pF, and C_{cell} = 2.57 pF, the burning voltage of the empty reactor is determind for 90% Ar − 10% CO_2 with a total flowrate of 100 ml/min, driven by a 5kHz sine wave at voltages ranging from 5 − 10 kV, with the results presented in Figure 77.
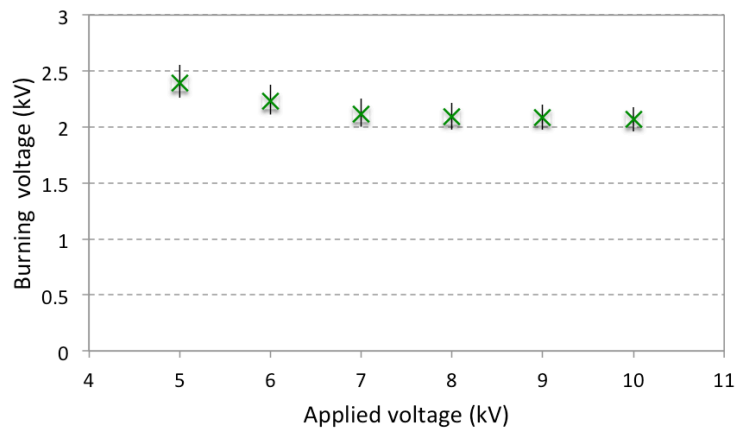
Figure 77: Burning voltage of the empty reactor with a gas composition of 90% Ar − 10% CO_2 at a total flowrate of 100 ml/min. Reactor is driven by a 5 kHz sine wave with voltages ranging between 5- 10 kV.

Figure 77 shows that as applied voltage decreases, that burning voltage increases. The burning voltage is seen to plateau with increasing applied voltage, up to 10 kV where it has a value of 2.07 kV +/- 0.1. This result contradicts that of Peeters and van de Sanden [95], who found the opposite trend to be true, i.e. burning voltage increases with applied voltage. A possible cause of this result is that with increasing applied voltage the reactor temperature increases up to 110 − 130 °C (as shown by Figure 68). An increase in temperature is known to decrease the breakdown strength of gases [113]. Using a 300 − 500 μm $BaTiO_3$ packing material as an example the change in burning voltage measured as a function of applied voltage to the reactor is presented in Figure 78.
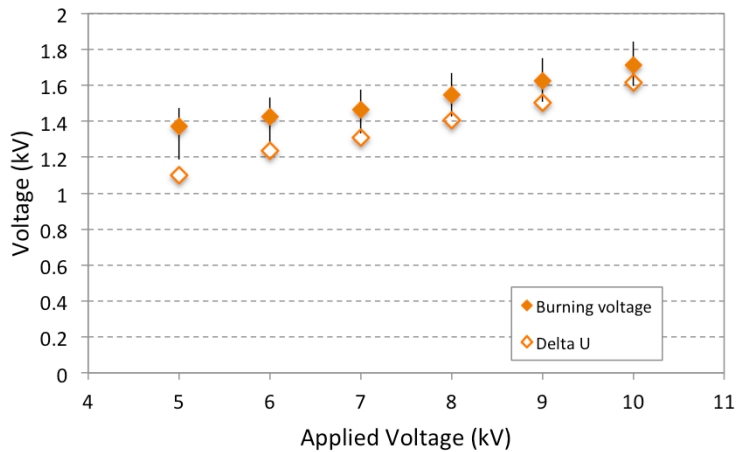
Figure 78: Burning voltage and ΔU measured as a function of applied voltage for 300 – 500 µm BaTiO₃ particles in 90 Ar − 10% CO₂ driven by a 5kHz sine wave.

Figure 78 shows that with increasing applied voltage the burning voltage increases. As stated previously, this may be due to higher applied voltages causing localized electric field strengths to exceed the threshold field strength required to initiate an electrical breakdown in void spaces that happen to have a higher breakdown strength. This increased breakdown strength may be due to either the size of the void, or the shape of the particle on which it forms. This in turn raises the average burning voltage of the reactor, and consequently the measured burning voltage increases. Further studies of this burning voltage data at different applied voltages with a range of particle sizes and materials would be of interest, although the limitations of the Mathematica program prevent the ability to analyse all of the generated data with sufficient accuracy.

Determination of minimum burning voltage would be of academic interest, however this is very difficult to accurately measure. Optimal reactor performance from the perspective of CO_2 conversion is obtained at the highest applied voltages. Therefore, measurements of reactor burning voltages are determined from the perspective of the highest possible applied voltage amplitude than can be generated by the HV amplifier, 10 kV.

An additional comparison that can be made is to determine whether wave shape has an effect on reactor burning voltage. Although the CO_2 conversion experiments were performed using square waves for the driving voltage, the majority of electrical analysis is carried out using sine waves, as the Lissajous figure analysis is derived for the diagnostics of sinusoidally driven reactors. The Lissajous figure derived from square waves can still effectively be applied for measurement of reactor burning voltages, however for determination of reactor capacitances the obtained values may differ; the problem of electrical diagnostics of square waves is beyond the scope of this thesis.

119
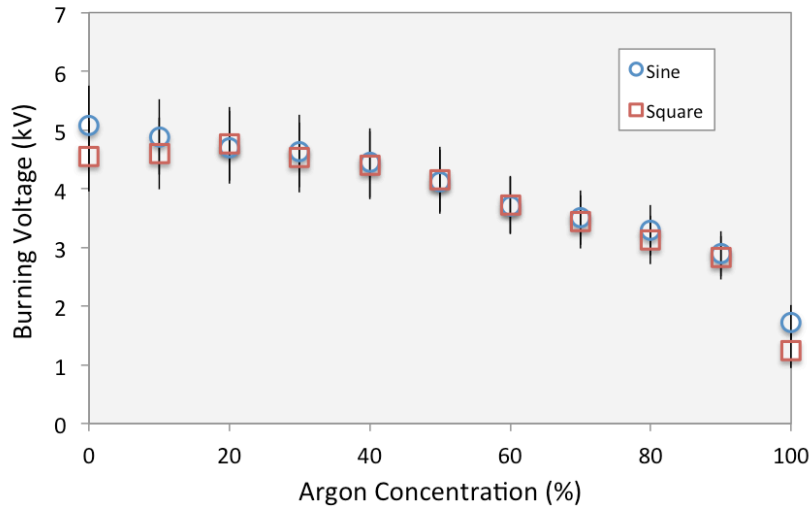
Figure 79: Reactor burning voltage in a 180 - 300 μm Al_2O_3 packed reactor with different applied voltage wave shapes at 10 kV and 5 kHz.

Figure 79 shows that for both sine and square waves that the reactor burning voltage under the conditions tested is, within the margins of error, the same. This relationship has been tested with $BaTiO_3$ packing as well as the unpacked reactor, and no change is observed when the applied wave shape is changed.

6.1.3 Reactor burning voltage relationship

In section 5.1.5, the first question posed was, "what is the relationship between burning voltage, applied voltage, particle size (and shape), gas composition and choice of packing material?" The purpose of this section aims to determine what this relationship might be.

Presented in Figure 80 is reactor burning voltage data for Al_2O_3, $BaTiO_3$ and an unpacked reactor at Argon – CO_2 concentrations ranging from 0 – 100%, with the reactor driven by a 10 kV, 5 kHz sine wave.
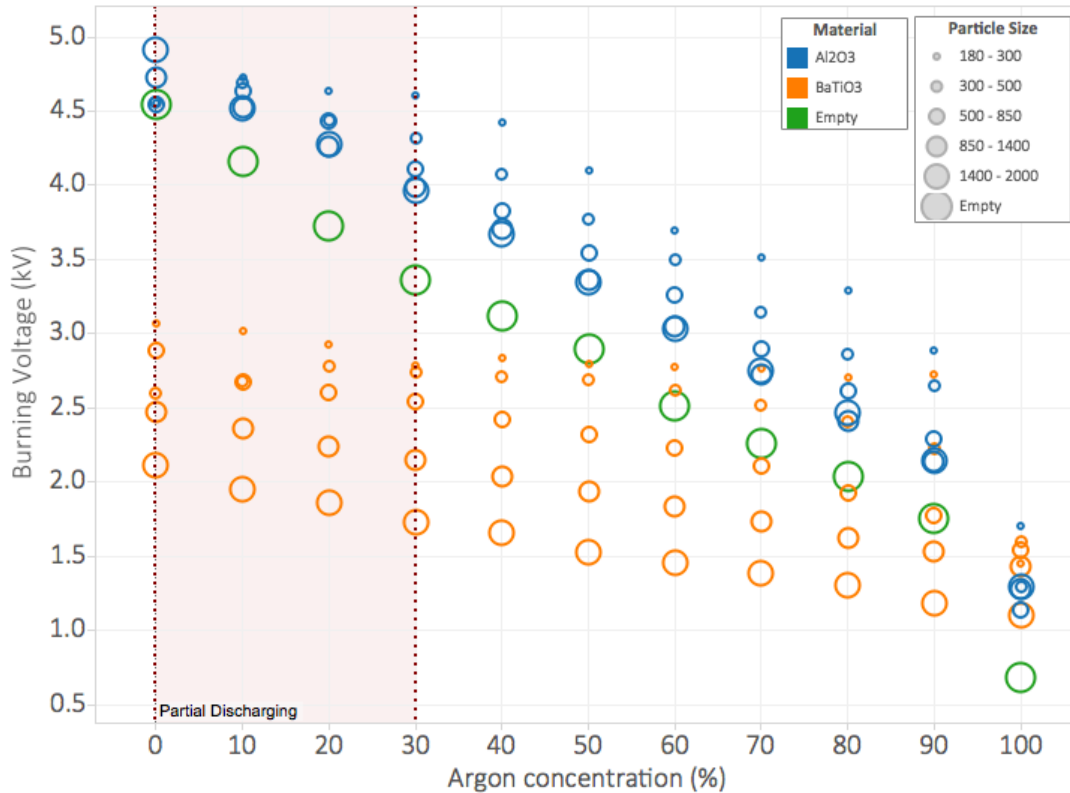
Figure 80: Reactor burning voltage as a function of feed gas argon concentration balanced with CO_2. Applied voltage is 10 kV, with a sine wave at 5 kHz. The "partial discharging" region indicates an area where the data obtained becomes less reliable due to the noise in the Lissajous figure causing problems for the Mathematica based data analysis method. Therefore it is considered that the data obtained in this region is less reliable, particularly for the smallest particle sizes tested.

The first trend to identify from Figure 80 is the almost linear increase in reactor burning voltage with decreasing argon concentration that is observed with every reactor packing condition. The only exception to this linearity is the difference between 100% Ar, and 90% Ar – 10% CO_2. This can be explained by the dramatic differences in electron transport properties between Ar and CO_2, i.e. the electron mean free path in CO_2 being much shorter than Ar, and the presence of excited states that are excited by low electron energy electrons in CO_2. Therefore the addition of a small concentration of CO_2 has a dramatic effect on burning voltage.

Also the data shows that, as predicted, there is a strong relationship between packing particle size and burning voltage. From the data presented here the trend is strongest with the BaTiO$_3$ packed reactor. Take, for example 1400 – 2000 μm BaTiO$_3$ particles, at 60% Ar – 40% CO_2 feed gas composition, the burning voltage is 1.45 (±0.09) kV. With 180 – 300 μm particles, at the same gas composition, measured burning voltage is 2.78 (±0.20) kV, a 90% increase over the value obtained for the larger sized particle and an absolute increase of 1.3 kV. The difference in burning voltage between particle sizes using the Al$_2$O$_3$ packing is proportionately smaller, but is still significant. Using the same Argon – CO_2 concentration as the example, with 1400 – 2000 μm Al$_2$O$_3$ particles, burning voltage is 3.02 kV (± 0.18) kV, whilst with the 180 – 300 μm burning

voltage is 3.7 (± 0.24) kV. An increase of ~23%, or 0.68 kV absolute. In addition to this, the absolute change in burning voltage between particle sizes appears to be approximately constant from about 30% Ar – 70% CO_2 to 90% Ar – 10% CO_2, with the notable exception of the 180 – 300 μm $BaTiO_3$ particles (See Figure 81 and Figure 82). In this case the increase in burning voltage changes with respect to argon concentration at a much slower rate, although the particles have a much higher initial burning voltage at 90% Ar – 10% CO_2 of 2.7 kV, an increase of ~130% compared to the 1400 – 2000 μm particle sizes.
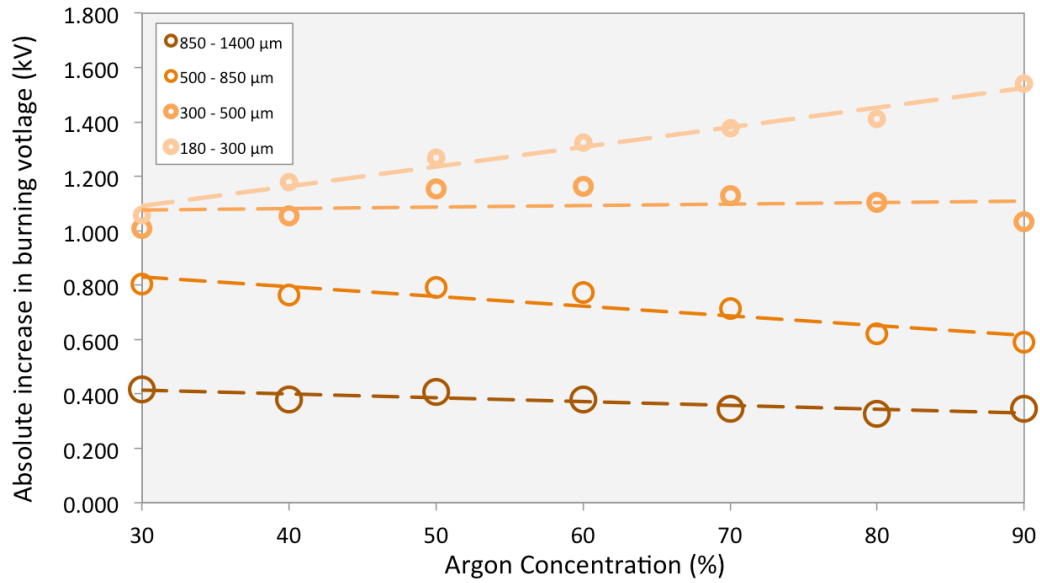
Figure 81: Absolute increase in burning voltage for $BaTiO_3$ particles relative to the 1400 – 2000 μm particles, shown with feed gas argon concentrations between 30 and 90%.
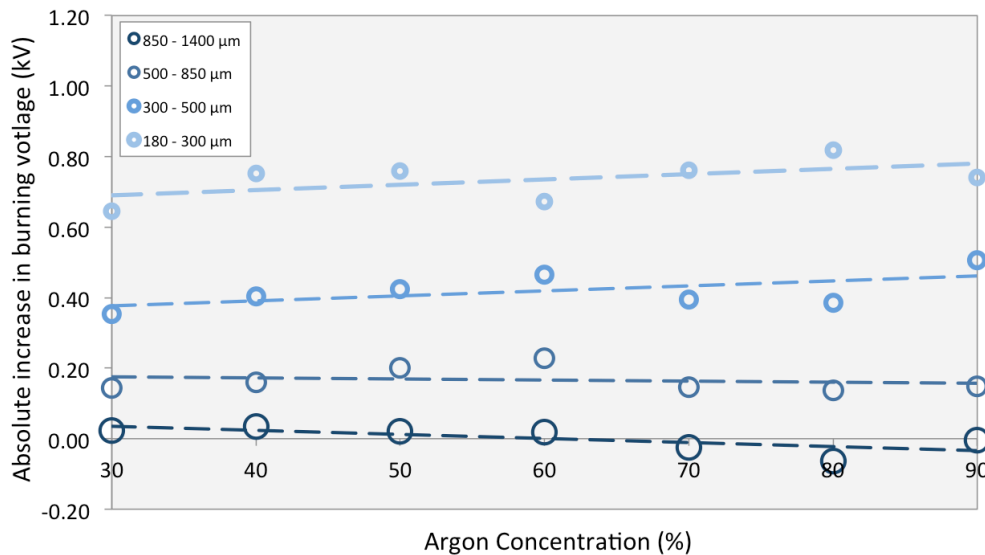
Figure 82: Absolute increase in burning voltage for Al_2O_3 particles relative to the 1400 – 2000 μm particles, shown with feed gas argon concentrations between 30 and 90%.

One of the other interesting results shown in Figure 80 is the relative change in burning voltage compared with an empty reactor. Generally speaking, $BaTiO_3$ leads to a reduction in reactor burning voltage, where as Al_2O_3 causes an increase in burning voltage. The reduction in burning voltage shown by this data with $BaTiO_3$ reflects the experimental results for CO_2 conversion shown in Figure 64, where $BaTiO_3$ still leads to conversion at all applied voltages even in pure CO_2. This data also supports the findings of other research groups where dielectric packing materials are found to decrease reactor breakdown strengths [36, 72, 114, 115]. The increase in burning voltage observed with Al_2O_3 is a more surprising result, as the strengthening of localised electric fields is an enhancement that has generally been attributed to all dielectric reactor packing materials, however this effect has been reported at least once in the literature previously [116]. It may be that although the onset of electrical breakdown is reduced, the burning voltage actually increases.
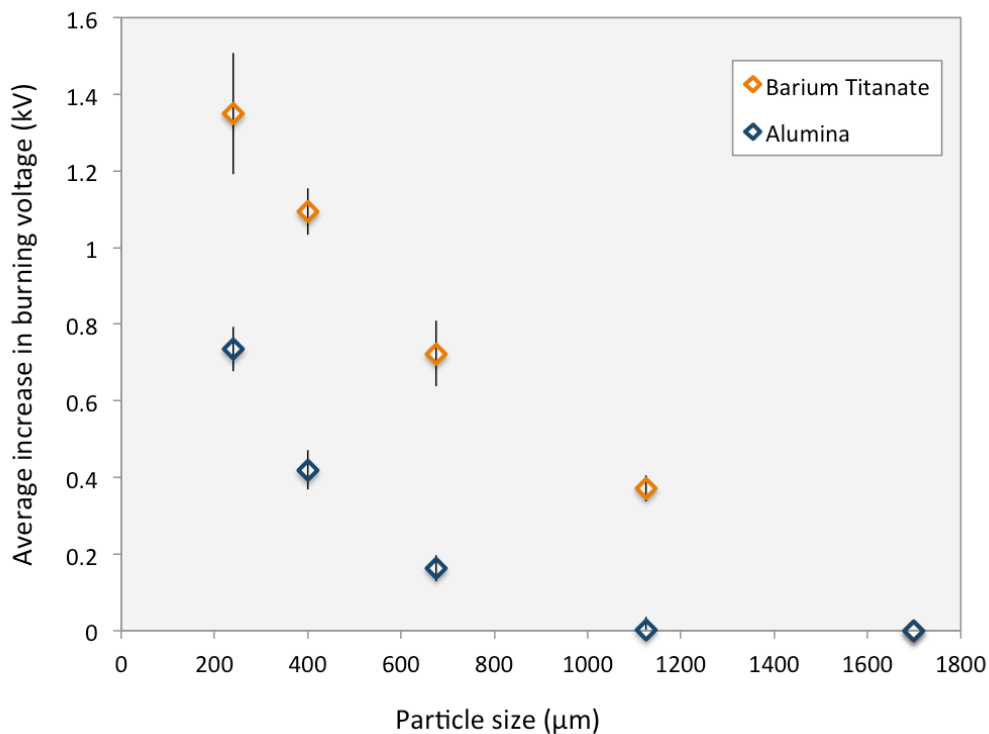
Figure 83: Mean increase in relative reactor burning voltage taken at argon concentrations between 30% - 90% Argon for $BaTiO_3$ and Al_2O_3. Reactor is driven by a 10 kV, 5 kHz sine wave.

Figure 83 shows the mean increase in absolute burning voltage for $BaTIO_3$ and Al_2O_3 packed beds relative to their respective 1400 – 2000 μm particle sizes. Both $BaTiO_3$ and Al_2O_3 show an exponential increase in burning voltage as particle size decreases.

In trying to elucidate the relationship between particle size, packing material, gas composition and applied voltage, other variables that may have an influence on burning voltage must also be considered. These other variables are the gap size, dielectric material used on the electrodes, and the frequency of the applied voltage. As the reactor geometry is fixed, it is not possible to

change the dielectric material or gap size. However, it is possible to easily measure the change in burning voltage by varying the frequency of the applied voltage. Figure 84 shows the burning voltage for a 180 – 300 µm Al_2O_3 packed bed operated with an applied voltage of 10 kV with frequencies in the range of 1 – 10 kHz.
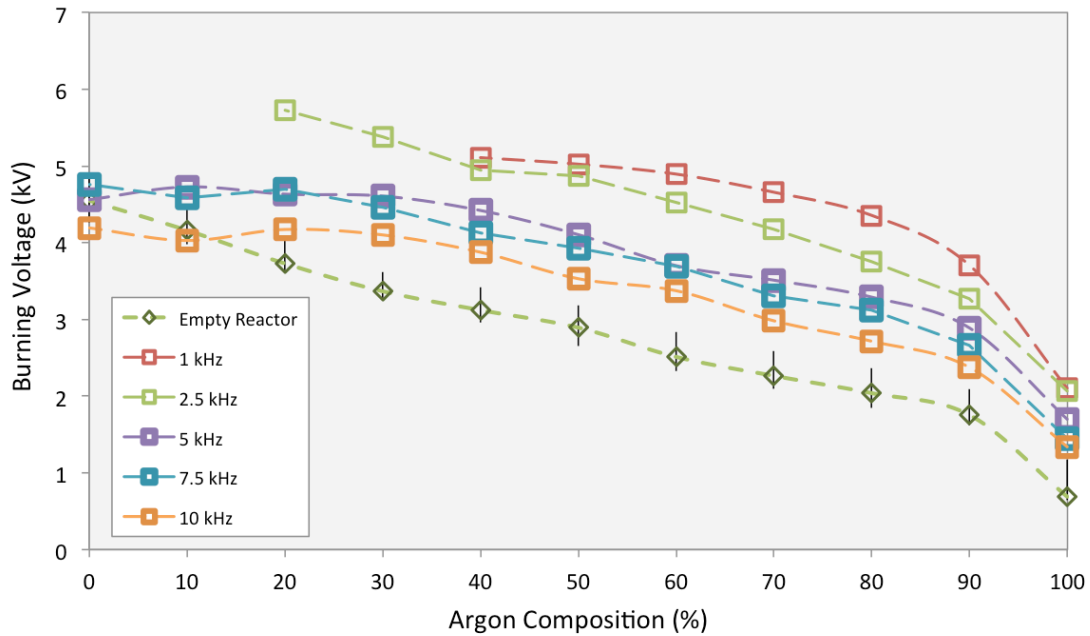
Figure 84: Burning voltage for 180 – 300 µm Al_2O_3 particles as a function of frequency of the AC driving voltage, with argon – CO_2 concentrations varied from 0 – 100 %. The empty reactor case is a reference and is driven by a 5 kHz sine wave. Error bars are not included for all cases as they make the graph difficult to read.

Figure 84 shows that there is a reduction in reactor burning voltage with increasing applied frequency. At frequencies of 2.5 kHz, no plasma discharge is found to occur at argon concentrations less than 20%, and at an applied frequency of 1 kHz, no breakdown occurs with argon concentrations less than 40%. Although the frequency dependence is only tested for the smallest Al_2O_3 particles, it is likely to be representative behavior for all packing materials. The frequency dependent reduction in breakdown voltage is supported by experimental and modeling work carried out by Valdivia-Barrientos et al [90] in a coaxial dielectric barrier discharge reactor with helium, which demonstrates that higher applied frequency reduces breakdown voltage. The authors suggest that this reduction in burning voltage at elevated frequency is due to higher charge accumulation on the dielectric layer, with the residual charge increasing the dielectric voltage relative to the change in the direction of the electric field of the AC applied voltage.

The authors also fit a semi-empirical relationship to their data to calculate breakdown voltage based on the gap capacitance (C_g), dielectric capacitance (C_d), and applied frequency (f), this equation is given by Equation 21:

$$V_{bd} = \frac{1.4 \left(C_d / C_g \right)^2}{\ln \left(f \right)}$$

This relationship can be applied to the experimental data obtained for the case of the empty reactor in this experiment, operating at a frequency of 5,000 Hz with a varying gas composition ranging from 0 – 100% CO_2 in Argon, shown in the plot in Figure 85.
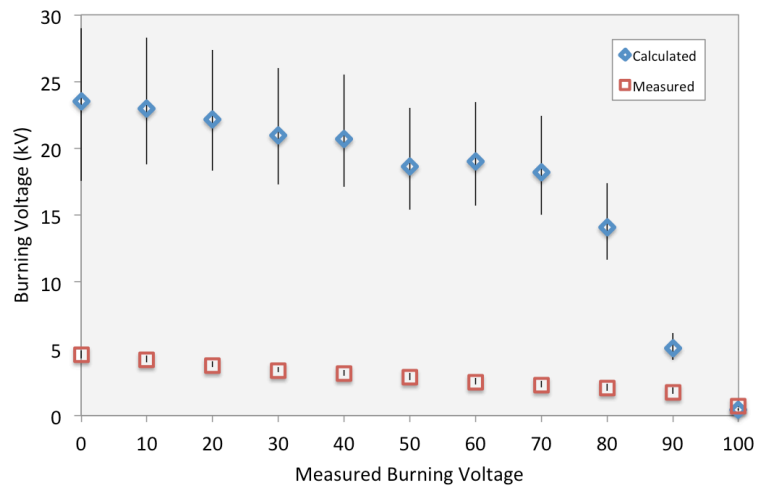
Figure 85: Measured and calculated (Using Equation 21) burning voltage for an unpacked reactor driven by a 5 kHz sine at wave at 10 kV with CO_2 and Argon concentrations ranging from 0 – 100%.

This graph shows that the empirical relationship of Valdivia-Barrientos et al [90] does not apply for the majority of cases tested in this reactor, only the example where pure argon is used is the calculated burning voltage (0.45 kV) close to the experimentally obtained value (0.68 kV). The calculated values from the empirical relationship overestimate the burning voltage by up to ~5 times. Despite this, perhaps the most important feature of this relationship is that the calculated values are non-linear as a function of argon concentration, whilst the experimentally obtained measurements (ignoring the case of 100% argon) are linear. This shows not only that their model cannot be universally applied to all DBDs, but also that it doesn't change linearly if the gas composition is changed. This is because the empirical relationship they obtained is dependent upon capacitance, which is based upon the gas properties when the reactor is not either in the plasma state, or with ions, free electrons or excited species remaining in the gas gap after a discharge has formed. A closer relationship would also have to take into account the gas properties related to electron transport in the gas, which are (to a certain extent) accounted for by the A and B coefficients used in Paschen's law. To determine the relationship for burning voltage in a DBD would require a dedicated study in itself, and so it can be concluded that further research is required into the properties of DBD reactors before the burning voltage relationship for a packed bed DBD can be determined.

The work in this thesis has so far demonstrated that there is a strong relationship between packing particle size and reactor burning voltage, with the burning voltage shown to increase rapidly with decreasing particle size. It is also evident from this thesis that this relationship is additionally dependent upon gas composition, applied frequency and packing materials properties.

6.1.4 Packed bed partial discharging

Moving onto the second question posed in section 5.1.5, "can the benefits of small particle size be realized in all packed bed plasma reactors?" In order to answer this question, the concept of partial reactor discharging must be revisited. The equivalent electrical circuit for partially discharging reactors obtained by Peeters and van de Sanden [95] is derived for usage with conventional DBD (i.e. not packed bed) reactors. In a partially discharging DBD, not all of the residual memory charge stored on the surface of the DBD is transferred to the other electrode during a discharge cycle. As described previously, this is the case where $\zeta_{diel} < C_{diel}$ measured from the Lissajous figure. This same rule applies to packed bed reactors in that cases where the reactor is partially discharging can be determined by this reduced value for ζ_{diel}, and it can be used to quantify to what extent the reactor is partially discharging. However, the implication for the behavior of the reactor is actually slightly different.

In a DBD, once a microdischarge begins on one electrode and the streamer is travelling towards the other electrode, it cannot fail to transfer its charge to the other electrode. On the other hand, with a packed bed reactor, the packing itself has a capacitance, so each individual packing bead acts as a capacitor and can store a charge. Therefore, when a charge is transferred away from an electrode in a packed bed reactor, it doesn't necessarily always reach the opposing electrode. The charge could effectively become trapped within the bed itself, and in this instance the effective dielectric capacitance, ζ_{diel}, would also be less than the value of the dielectric capacitance, C_{diel}. This phenomena of the reduced value for dielectric capacitance indicating a non "fully bridged gap" has been described elsewhere [36, 114]. Previously it has been reported that the inclusion of packing materials assists in charge bridging the electrode gap [36], although in the cited publication this effect is analysed qualitatively based purely on the measured value of ζ_{diel}.

The Peeters [95] equivalent circuit model splits the DBD into discharging and non-discharging sections by two coefficients α and β. The coefficient α has been demonstrated to indicate the areal fraction of the DBD electrode that is not discharging. Conversely, β indicates the electrode areal fraction that is discharging. Equation 22 is used to calculate the value of the coefficient α.

$$\alpha = \frac{C_{diel} - \zeta_{diel}}{C_{diel} - C_{cell}}$$

This equation can be applied to packed bed reactors, but the interpretation of the result is somewhat different. Rather than the value of alpha indicating the areal fraction of the electrode discharging, it indicates the fraction of stored dielectric charge reaching the opposing electrode during a discharge cycle. With this in mind, the alpha values can be calculated for the reactor tested in this thesis, an example of this is shown in Figure 86 for 180 – 300 µm particles and an empty reactor with varying argon and CO_2 composition.
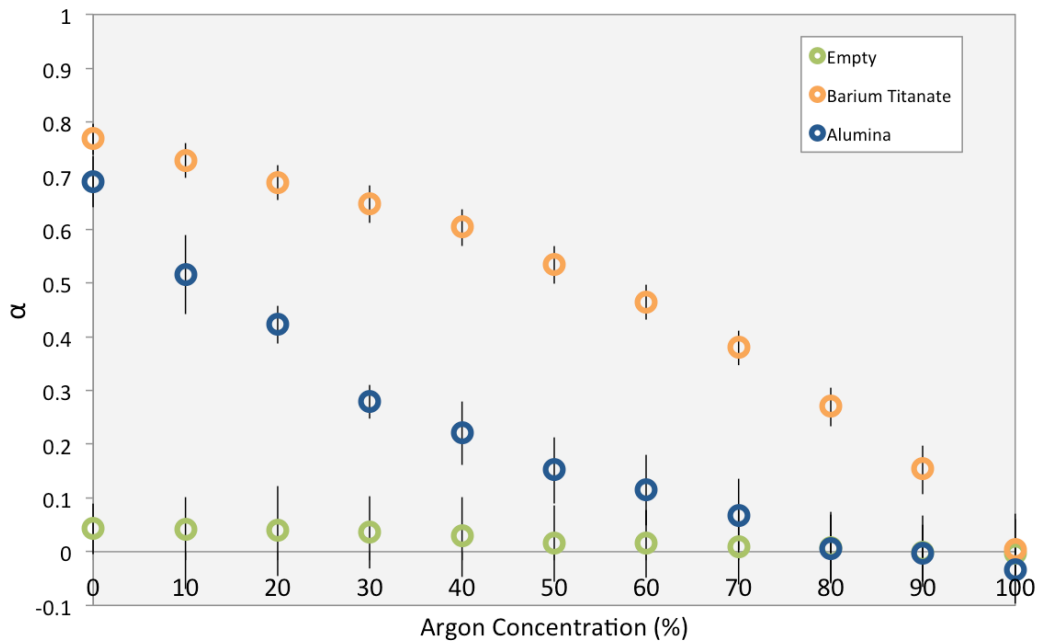
Figure 86: α values for the packed bed reactor at different Ar – CO_2 concentrations. In cases where a packing is used the reactor packing particle size is 180 – 300 µm. The error bars become and some data points cross into giving negative values for α, which is a reflection of the ± pF error on the estimated value of C_{diel}. The reactor is driven by a 5 kHz, 10 kV sine wave.

The results shown in Figure 86 indicate that with the unpacked reactor across all argon – CO_2 concentrations that the reactor is discharging stored charge effectively. The value of α increases to a maximum of ~0.05 in pure CO_2 with the unpacked reactor. When the reactor is charged with either $BaTiO_3$ or Al_2O_3 it can be seen that the value of alpha increases with decreasing Ar concentration. With the $BaTiO_3$, the increase in the value of α with increasing CO_2 concentration is much sharper than that found with Al_2O_3 at high argon concentrations. For all argon concentrations, the value of α in 180 – 300 µm $BaTiO_3$ particles exceed that of Al_2O_3. This effectively means that proportionately less stored dielectric charge is bridged between the electrodes in the $BaTiO_3$ packed reactor, than in the Al_2O_3 reactor and the empty reactors. This may be due to the higher local charge storage capacity of $BaTiO_3$ compared with Al_2O_3 effectively trapping larger charges on its surface. The reduced burning voltage of $BaTiO_3$,

indicating that localised electric field gradients are higher than for the Al_2O_3 case, also supports this hypothesis.

It should be noted however that for the cases at low argon concentrations, less total charge is transferred in the Al_2O_3 packed reactor ($Q_{ptp} \approx 189$ nC) than in the $BaTiO_3$ reactor ($Q_{ptp} \approx 264$ nC) under the conditions for which this experiment was carried out. In addition to this the reactor breakdown properties are highly dependent upon reactor temperature, as well as the previous condition that the reactor was being operated in. The alpha value for 180 – 300 μm Al_2O_3 in this experiment is approximately 0.69 with 100% CO_2 feed gas. In the previous experiment, where CO_2 conversion was measured, it was not possible to ignite a plasma in the bed with a pure CO_2 feed gas, i.e. if measured value of α would have been equal to 1. This ability to operate the reactor in pure CO_2 in this experiment may be due to residual heat from previous experiments allowing the gas to be ionised more easily, or residual charge or metastable plasma species from prior experiments reducing the burning voltage. Either way, future experiments investigating these charge transfer and partial discharging effects should include improved reactor temperature control and measurement, and allow time for reactor cooling periods with the plasma not ignited between measurements.

Figure 87 and Figure 88 show alpha values for different sizes of Al_2O_3 and $BaTiO_3$ as a function of reactor gas composition. Due to the inherent limitation of the set-up in obtaining accurate quantitative data for these alpha values, these figures should be considered more as qualitative rather than quantitative data.
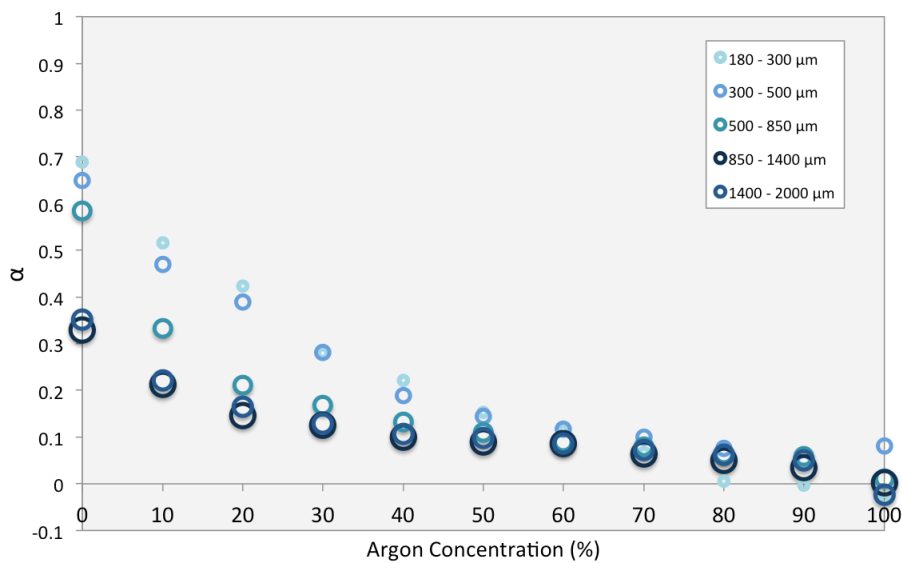
Figure 87: Alpha value for Al_2O_3 particles as a function of argon concentration. Reactor is driven by a 10 kV, 5 kHz Sine wave.

128
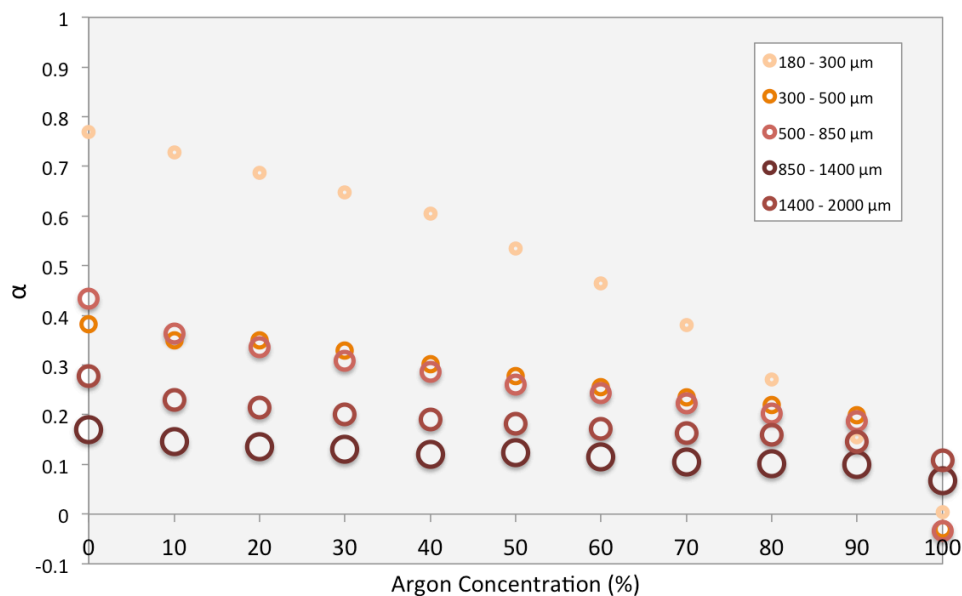
Figure 88: Alpha values for BaTiO₃ particles as a function of argon concentration. Reactor is driven by a 10 kV, 5 kHz sine wave

Both figures show that the value of alpha has a strong size dependence, with smaller particles being more susceptible to causing partial discharging in the reactor. In all conditions with both of these packing materials it can also be seen that the reactor is not fully discharging.

It is apparent from this data that the most likely reason that small particles do not typically perform as anticipated is that the reactor tends to partially discharge more as particle size decreases. Even if it appears that a plasma is being formed in the packed bed, a fraction of the stored charge may be being transferred from one electrode to the other. One of the most important conclusions of this thesis therefore is that analysing the packed bed behavior by measuring reactor capacitances should be performed as a matter of course when studying packed bed plasma reactors. It seems unreasonable to compare potential catalysts and materials against each other, if reactor performance is not comparable in both cases, especially considering that packed bed reactor experiments are predominantly currently at bench scale in order to study the effects of different materials.

So to return to the question, "can the benefits of small particle sizes be applied to all packed bed reactors?" requires the revaluation of the work of other researchers in order to identify **a)** whether it is possible to ignite plasmas in small particle sizes without the addition of noble gases, and **b)** to what extent partial reactor discharging is occurring in the publications on packed bed DBDs of other researchers.

To answer question a) - One of the items of published literature reviewed in section 3.1.3, that of Duan et al [77], shows higher CO_2 conversions in pure CO_2 streams with 180 μm – 250 μm

particles, compared with 250 μm – 420 μm particles. Firstly, this demonstrates that it is possible to generate plasmas in packed beds with small particle sizes. Secondly, it can also be presumed from their high conversion data, that the reactor is not significantly partially discharging, although to be certain the Lissajous figures or reactor capacitances would have to be analysed. The gap space used in their reactor is 0.6 mm, with a maximum applied voltage of 9.13 kV. This equates to an applied field strength of ~15.2 kV/mm. A significantly higher value than the highest applied field strength used in this thesis, ~ 1.68 kV/mm. It is important to note that the applied field strength is not directly indicative of the local field strength between particles in a packed bed reactor (or a DBD), rather it is used simply to compare operating conditions.

And question b) Trying to determine when the reactor is partially discharging in other research from their data is an inherently difficult problem, as it is very rare that capacitance data is reported. However, the experimental conditions used can be evaluated and compared with those tested in this thesis, and those tested by Duan et al [77].

Mei et al [72] and Tu et al [36] are the only authors to publish values for reactor capacitance in their work. Both publications show reduced values for ζ_{diel} compared with C_{diel} under all reactor operating conditions, and both state that this indicates that the reactor is partially discharging. In these publications the effective capacitance is presented as a function of power, even though the electrical breakdown of the reactor is dependent upon the applied potential difference, rather than the power input. In the work of Mei et al [72], the discharge gap is 3 mm and the maximum applied voltage stated is 8.45 kV giving a plasma power output of 40W. Maximum plasma power used is 50 W, so assuming power scales linearly with voltage, this equates to a maximum voltage of ~10.5 kV applied to a 3 mm gap, giving an applied field strength of 3.5 kV/mm. Packing used is 1 mm spherical particles of either $BaTiO_3$ or glass. With $BaTiO_3$, at the highest applied field strength, the value that can be calculated for α is 0.12, where as for glass and the unpacked reactor, these are 0.45 and 0.48 respectively reported at a power of 50 W. It is worth noting that for the same plasma power of 40 W, reactor peak applied voltages are 7.05 kV without packing, 7.65 kV with $BaTiO_3$, and 8.45 kV with the glass beads. It is likely therefore, that if the reactors were compared on the basis of applied voltage that at applied voltages of ~ 8kV, that the value of α in the empty reactor would be lower than in the reactor packed with glass beads. I.e. the glass packing material is blocking charge transfer compared with an unpacked reactor for the same applied voltage.

Performing a similar analysis of Tu et al [36], a maximum voltage of 11 kV is applied to a 4.5 mm gap, giving a maximum applied field strength of 2.44 kV/mm. The NiO / Al_2O_3 packing particles used are randomly shaped and have sizes ranging from 0.85 – 5 mm. At 60 W input power using the NiO / Al_2O_3 catalyst, the value for α is just 0.01 indicating the reactor is almost fully

discharging. For the unpacked reactor, α is 0.32. Although the data isn't published, the authors also note that using unreduced NiO/ Al_2O_3, or Al_2O_3 on its own reduces the transferred charge in the plasma compared to the reduced Ni catalyst, and that these non-conductive packing materials may inhibit charge transfer between the electrodes. This shows that in this case the presence of the Ni catalyst improves charge transfer between the electrodes compared with other packing materials as well as the unpacked reactor.

Evaluating literature where capacitance values or Lissajous figures are not reported, and particle packing size is evaluated as a variable:

- In a very recent conference proceedings, Michielson et al [89] report the reduction of CO_2 from pure streams with the use of different sized (600 – 800, 800 – 900, 900 – 1000, 1000 – 1180, 1250 – 1400, 1600 – 1800, and 2000 – 2240 μm) packing materials (SiO_2, ZrO_2, Al_2O_3, and $BaTiO_3$), packed into a 3.25 mm gap driven by a 7.5 kV peak amplitude power source. This gives an applied field strength of 2 kV/mm. This is higher than the values used in this thesis, but lower than that used by Mei et al. Their results show that CO_2 conversion increase with particle size, and that $BaTiO_3$ yields the highest CO_2 conversion. The results obtained are very similar to those for $BaTiO_3$ shown in Figure 64. There, based on the experimental conditions used being very similar to those used in the aforementioned experiment, it can be presumed that it is highly likely that the reactor was not fully discharging, particularly with the case where smaller particle sizes are used.
- Takaki et al [87] investigating NO removal and / or O_3 production in a $BaTiO_3$ packed reactor using a 10 kV pulse applied to a 10 mm gap (1 kV/mm) using either 3.3 mm spheres, 2.2 mm spheres, and hollow cylindrical pellets (o.d. = 4.1 mm, l = 5mm, i.d. = 1.7 mm). In order of performance, quantified by efficiency, ozone concentration or NO removal, the large cylinders are best, followed by large, then small spheres. However, again due to the electric field strengths applied it is highly likely that the reactor is not fully discharging, particularly with the smallest pellet sizes.

Due to the reactor operating conditions it can be presumed that in the examples cited that the packed bed reactors are not fully discharging. If the example of Duan et al [77] is to be followed, significantly higher applied field strengths than are commonly used in literature are required in order to fully ignite plasma discharges in packed beds, particularly with small particle sizes and electronegative gases. In order to achieve the applied field strengths of Duan et al using the reactor / power supply from this thesis, either the applied potential would have to be increased to 90 kV (for a 6mm gap), or the gap size would have to be reduced to 0.68 mm (for a 10 kV applied voltage).

This is therefore the second major outcome from this thesis, that small particles are likely to be most beneficial for high conversions and efficiencies in packed bed reactors, however much higher applied field strengths need to be applied in order to ensure that the reactor is fully discharging. In order to validate this result, packed bed reactor experiments should be performed in a moderately sized discharge gap (~ 2 mm), with very high applied voltages up to 30 kV. This should allow the testing of a range of particle sizes of packing material with a wide range of applied voltages. This should allow observations to be made regarding transitions in discharge characteristics between point-to-point discharges, surface discharges, or other possibly undocumented discharge mechanisms.

6.1.5   Causes of changes to CO_2 conversion with packing material and size

The final questions posed, "why does CO_2 conversion increase when using small particle sizes in packed bed reactors?" and "why does Al_2O_3 show a significant increase in CO_2 conversion compared with $BaTiO_3$?" are perhaps the most difficult questions to attempt to answer.

There are a number of parameters that change as a consequence of increasing or decreasing particle size. These parameters will have either a positive, negative or neutral effect on CO_2 conversion. It has been demonstrated in section 6.1.3 and 6.1.4 that a decrease in particle size leads to an increase in reactor burning voltage, and an increase in the tendency of the reactor towards partial discharging. Despite this, under high argon concentrations, where the reactor is generally shown to be discharging effectively, small particle sizes yield the highest CO_2 conversions. Table 8 shows a summary of the effect of changing packing particle size or material. This table includes a "resultant variable", that is a property of the reactor that changes as a result of the input variable, as well as the probable net effect on CO_2 conversion and a note on whether or not the effect is experimentally verifiable from the data obtained for this thesis.

Table 8

Input Variable	Resultant Parameter	Probable Net Effect on CO_2 Conversion	Effect Experimentally Verifiable?
Decrease in particle size	Increased surface area to volume ratio for heterogeneous catalytic reactions	⬆ / ?	Surface area could be quantified with further experimentation
Decrease in particle size	Increased number density of contact points between particles, leading to an increase in the number of plasma discharges simultaneously occurring	⬆	Possibly – from oscilloscope data
Decrease in particle size	Greater number density of sharp edges – these may result in a strong localised electric field and lead to formation of discharges	⬆ Weak Contribution	Further experimentation required
Decrease in particle size	Improved gas – plasma contacting. Presuming that the reactor is fully discharging, decreasing particle size is likely to improve gas - plasma contacting. This is linked to the increased number density of contact points between particles, as well as the number density of sharp edges, and the possibility of surface discharges.	⬆⬆ / ⬆ The net effect of multiple variables	Possibly – From Oscilloscope data
Decrease in particle	Reduced residence time – In the reactor tested at a flowrate of 100 ml /min, space	⬇ Weak	Known to have an effect. In this instance

size	time varies between ~ 0.39 and 0.49s. Although residence time is known to be an important parameter, in this circumstance the contribution to decrease in CO_2 conversion is likely to be weak due to the small range of space times between particle sizes.	Contribution	net contribution to CO2 conversion is likely to be weak.
Decrease in particle size	Reduction in void size – This leads to an increase in reactor burning voltage, as well as the possibility of reactor partial discharging	↓↓	Experimentally demonstrated in sections 6.1.3 and 6.1.4
Decrease in particle size	Increased rate of loss of electrons and exited species – leads to lower electron and ion density in packed bed reactors	↓	Further experimentation required
Decrease in particle size	Behaviour of the plasma discharge is very likely to change with a change in particle size. Plasma may change from point-to-point discharges, to a surface discharge or another unidentified mechanism	?	Yes – From oscilloscope data
Decrease in particle size	Change in local electric field strength	?	Possibly too complex to ever be elucidated experimentally. Modeling may help.
Change in material	Possible catalytic activity	↑	Requires further experimentation
Change in material	Change in dielectric constant	?	Requires further experimentation
Change in material	Change in material work function	?	Requires further experimentation
Change in material	Material acidity / basicity	?	Requires further experimentation
Change in material	Increase in porosity / surface area / pore size	↑	Requires further experimentation

Clearly there are many parameters that change as a result of simply changing packing particle size and packing material. Therefore it is not possible to isolate any particular parameter as being the main cause of the change in CO_2 conversion observed in the reactor.

Of the resultant parameters presented in Table 8, the change in the behavior of the reactor is the only parameter that can be further investigated from the data collected. Oscilloscope data can be used to provide an insight into the nature of the discharge in the reactor, specifically

providing information regarding the magnitude, number and duration of current pulses. Further work would have to be carried out in order to quantify these parameters; consequently the oscilloscope data presented here is used solely for qualitative analysis.
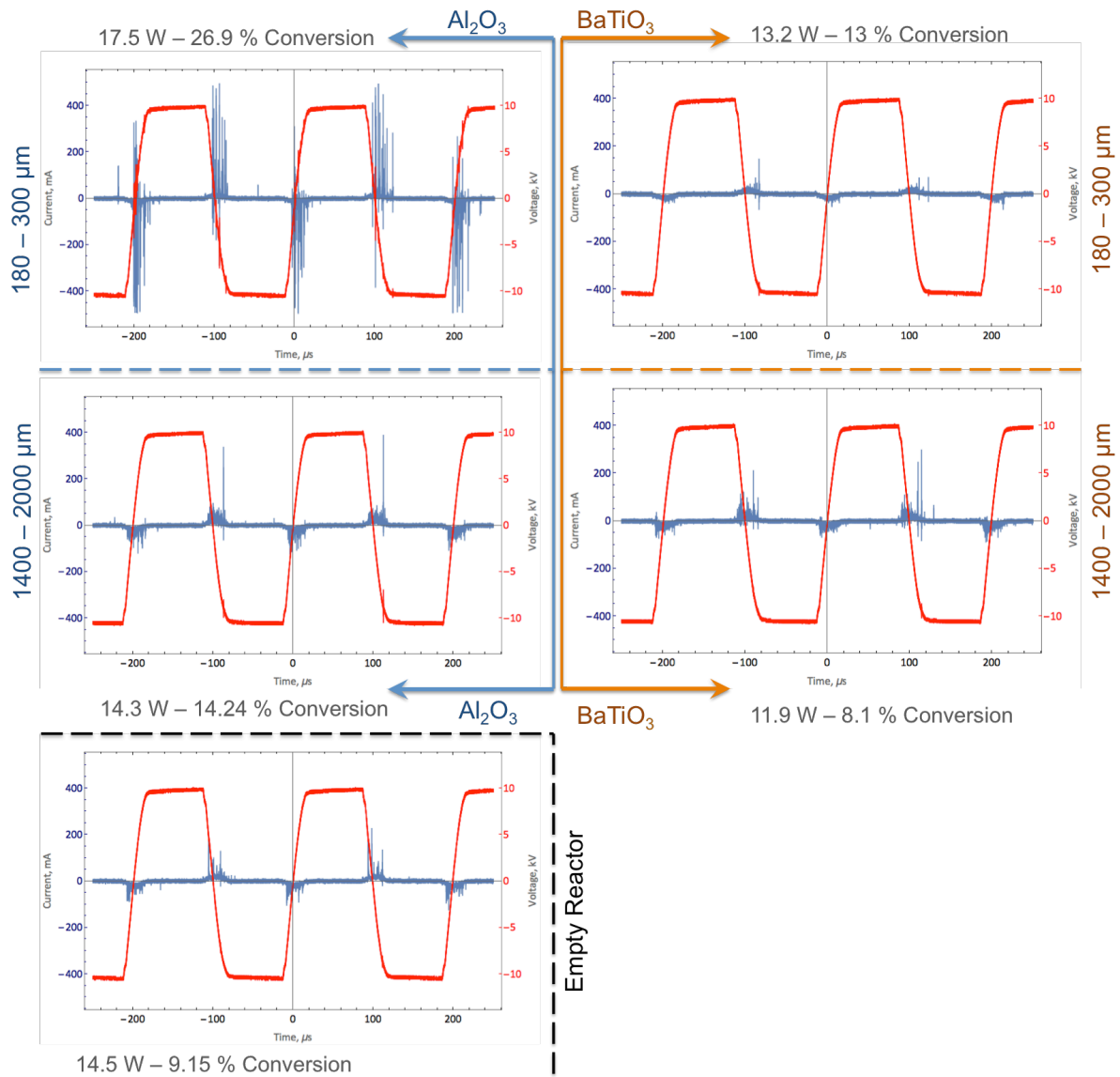
Figure 89: Oscilloscope data showing applied voltage and current data for reactors driven by a 10 kV, 5 kHz square wave. The data presented here is for the experiments where the feed gas composition is 90% Ar – 10% CO_2.

Figure 89 shows oscilloscope data comparing reactors packed with $BaTiO_3$ or Al_2O_3 with particle sizes of either 180 – 300 μm, or 1400 – 2000 μm, as well as an empty reactor. The data is collected for an applied voltage of 10 kV, with a 5 kHz square wave in a gas composition of 90% Ar – 10% CO_2. On each graph the Y-axis is scaled identically, with a range from -500 to +500 mA.

The most apparent feature of this figure is the magnitude of the current pulses in the 180 – 300 μm Al_2O_3 packed bed. Compared with every other reactor set-up the magnitude of the pulses is significantly higher (So much higher that some of the pulses are clipped by the range of the

oscilloscope with the settings used). This reactor shows the highest conversion of CO_2 with a value of 26.9%. In addition to this, the power used in the plasma is much higher, 17.5 W, compared with 13.2 W for 180 – 300 µm $BaTiO_3$ and 14.3 W with 1400 – 2000 µm Al_2O_3. The amplitude of these pulses is much larger than in the non-packed reactor. This shows that the instantaneous charge transferred is much larger during one of these pulses, than can be transferred from one microdiscarge in the unpacked reactor.

Further observations can be made by comparing the behavior of pulse clusters for the 180 – 300 µm Al_2O_3 packed bed and the unpacked reactor, as shown by Figure 90 and Figure 91.

Figure 90: Pulse clusters observed with increasing applied voltage in a 180 – 300 µm Al_2O_3 packed bed driven by a 5 kHz square wave at 10 kV in 90% Ar – 10% CO_2.
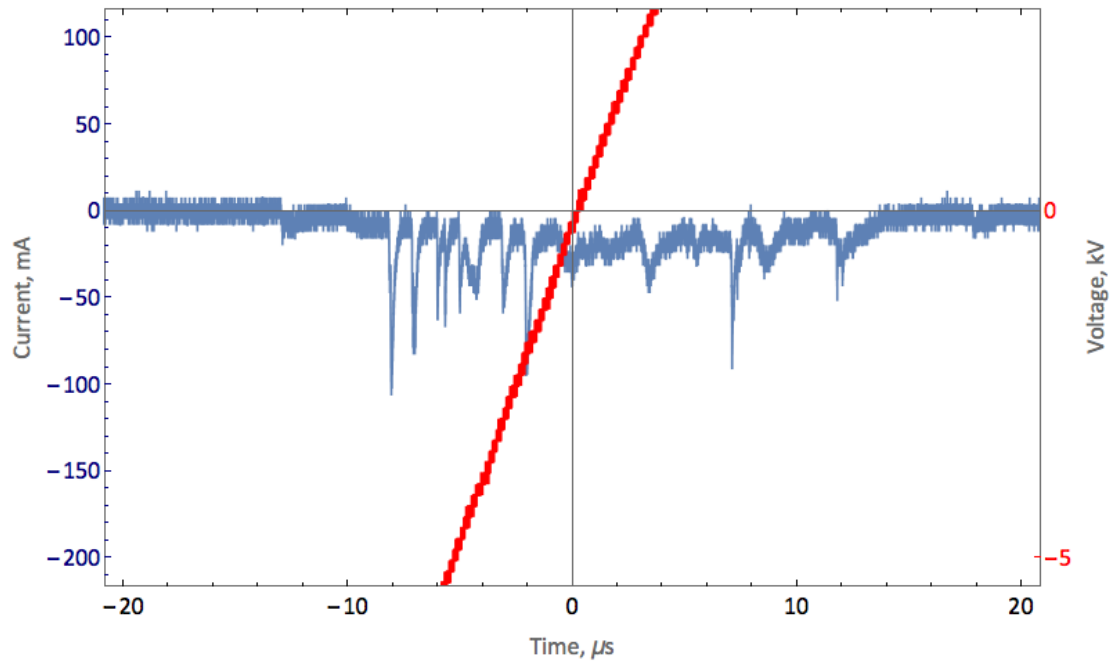
Figure 91: Pulse clusters observed with increasing applied voltage in a non-packed reactor driven by a 5 kHz square wave at 10 kV in 90% Ar − 10% CO_2.

On both Figure 90 and Figure 91, the X-axis is scaled identically for easy comparison, the Y-axis is scaled proportionately to the magnitude of the pulses. Comparing the two figures, there are 3 main differences:

1. The amplitude of the pulses is larger in the Al_2O_3 packed bed than the non-packed reactor

2. There are more pulses during one half discharge cycle in Al_2O_3 packed bed than the non-packed reactor

3. The decay time of pulses in the non-packed bed is longer than those in the Al_2O_3 packed bed

The reduced decay time of the pulses in the packed bed can be explained by the very large plasma − particle interface area very rapidly neutralising charged species present in the plasma. This hypothesis is supported by the pulse cluster data for 1400 − 2000 μm Al_2O_3, shown in Figure 92, where a large fraction of the current pulses observed have a long decay time, similar in time scale to those observed in the non-packed reactor. Indicating that the large voids of the bed allow for longer pulse decay times, due to a lower rate of charge neutralisation.

137
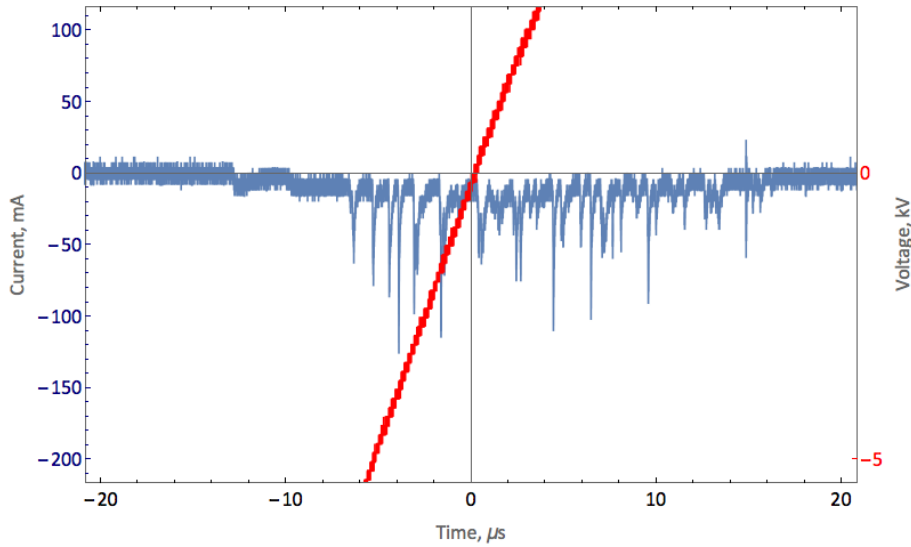
Figure 92: Pulse clusters observed with increasing applied voltage in a $1400 - 2000$ μm Al_2O_3 packed bed driven by a 5 kHz square wave at 10 kV in 90% $Ar - 10\%$ CO_2

The large magnitude of the current pulses is more challenging to explain. Especially when comparing the data obtained to that of the $180 - 300$ μm $BaTiO_3$ packed reactor, shown in Figure 93. The current data from $180 - 300$ μm $BaTiO_3$ packed bed features very few current pulses, the current appears as a continuously drawn current by the reactor. This may be due to the cumulative effect of many very small microdischarges occurring between particles each drawing a small amount of current, as well as a displacement current due to polarisation switching in $BaTiO_3$.
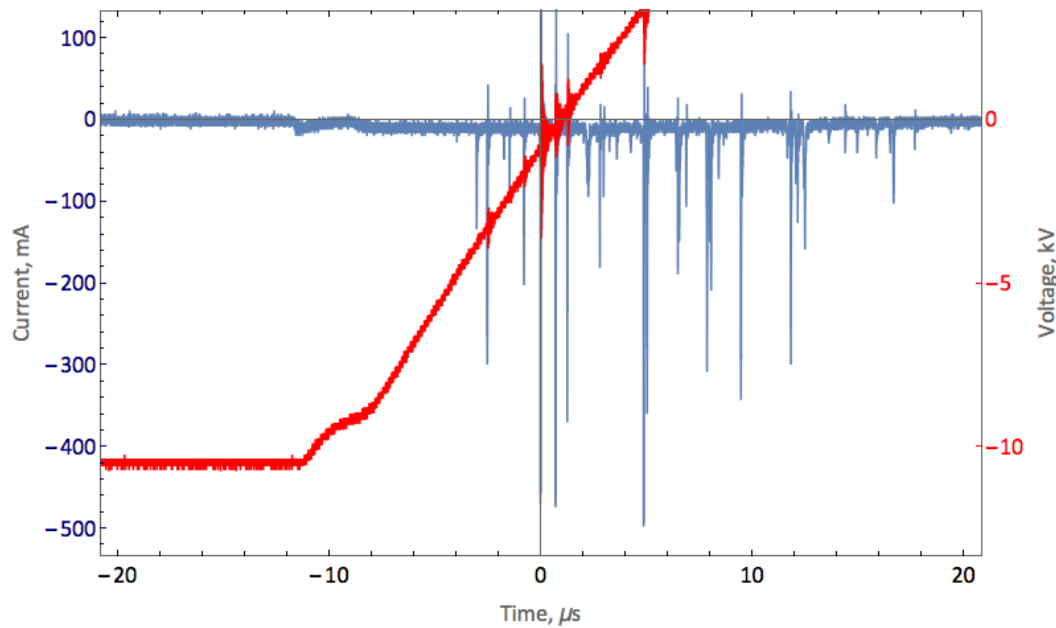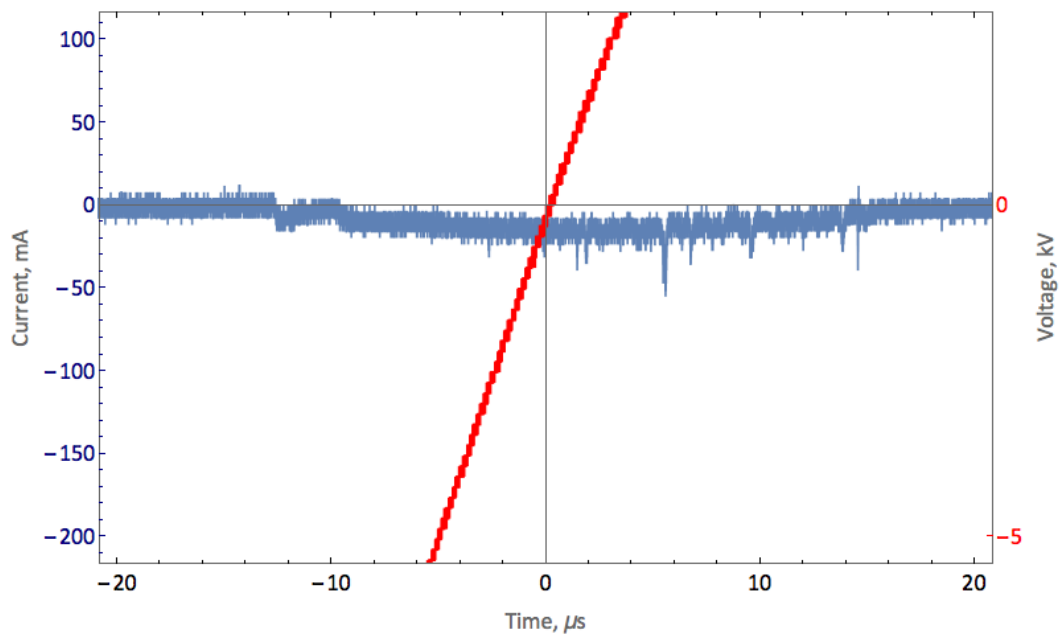

Figure 93: Pulse clusters observed with increasing applied voltage in a $180 - 300$ μm $BaTiO_3$ packed bed driven by a 5 kHz square wave at 10 kV in 90% $Ar - 10\%$ CO_2

The data presented in section 6.1.4 indicated the tendency of the $BaTiO_3$ packed reactor with small particles towards partial reactor discharging. It is likely that under the conditions used in this experiment that the plasma discharge is contained to the regions where particles are touching. It may be that if a larger driving potential was applied to the reactor, that the discharges would expand into the void spaces between particles and the behavior of the reactor may be more similar to the 180 – 300 µm Al_2O_3 packed reactor. Plasma discharge transition from a point-to-point plasma, to a discharge expansion into the void spaces of a $BaTiO_3$ packed reactor has been observed by Tu et al [117] when plasma power is increased. It may be that in the conditions used in this thesis that the potential difference applied is insufficient to cause this transition in discharge behavior to occur. The operational regimes under which this transition in behavior occurs requires further investigation.

In the 180 – 300 µm Al_2O_3 packed bed given the small size of the particles used, coupled with the low dielectric capacity of Al_2O_3 resulting in a low charge storage capacity per particle, the large amplitude current pulses may be the cumulative contribution of the stored charge of many particles dissipating their energy into one high power pulse propagating through the packed bed. This hypothesis is supported by observations made of the reactor whilst it is operating in this condition, where intense filamentary discharges can be seen appearing at different locations in the packed bed. These intense pulses are responsible for the seemingly "noisy" Lissajous figures that were previously shown in Figure 33, indicating that very large amounts of charge are transferred during one of these current pulses. In order to gain a better understanding of discharge phenomena in packed beds, the Lissajous figures and oscilloscope data generated from these experiments requires further analysis.

To return to the questions at the start of this section, there is no certain answer as to why small particles are seemingly beneficial for CO_2 reduction in a packed bed, however it is likely to be caused by improved gas - plasma contacting and a change in plasma discharge behavior. If the material happens to be catalytic in a plasma system, there may be further benefits due to the increased plasma – catalyst interface area.

Addressing the cause of Al_2O_3 packing performance exceeding that of $BaTiO_3$ under conditions when the reactor is discharging well (i.e. α values are low) the mechanism remains uncertain. The $BaTiO_3$ packing needs to be tested with higher applied potential differences in order to determine if the discharge expands more into the void spaces in the reactor. In addition to this, the Al_2O_3 packing should be tested for possible catalytic activity as a plasma activated CO_2 reduction catalyst.

7 Summary & Conclusions

7.1 Summary

This purpose of this research is to investigate the reduction of CO_2 to CO in a packed bed plasma reactor. Upon reviewing the literature, it became clear that the effects of particle size on discharge phenomena in the reactor is both a poorly understood variable and an important controlling factor on the outcomes of the reaction. Research into packed bed reactors for the reduction of CO_2 (and other gas processing reactions) is a growing research topic due to the possibility of including catalytic materials into the plasma discharge region, which is believed to lead to a synergistic enhancement of the performance of both the catalyst and the plasma.

There are possible limitations to packed bed reactors that occur due to the particle size of the packing material used. One of the paradigms of catalysis is the requirement for a high surface area to volume ratio in order to maximise the density of active sites available for reactions. In addition to this, plasma enhanced catalysis is likely to be further constrained by the plasma – catalyst interface area due to the very short lifetime of excited species in the plasma (with lifetimes ranging from ps – μs). These two considerations indicate that small particle sizes would be preferable in a packed bed plasma reactor. On the other hand, Paschen's law can be applied to predict that there is likely to be a minimum particle size in which a discharge can be initiated in the reactor. Paschen's law relates the breakdown voltage of the gas between two parallel plate electrodes with the operating pressure, electrode spacing, gas composition and applied DC voltage. At some small electrode spacings, the breakdown voltage of the gas can be shown to approach infinity due to electrode spacing being within the same order of magnitude as the mean free path of an electron in the gas. Therefore it may not be possible to ignite plasma discharges in a packed bed if the particle size becomes too small. This consideration becomes more important with the use of electronegative or molecular gases, where the mean free path becomes short. This tends to increase the breakdown voltage of the gas as the required field strengths required to accelerate an electron to sufficiently high energies in order to ionise another species and create an electron avalanche become very high.

Consequently the aim of this thesis is:

1. To perform an experiment to observe the effects that a change in particle size has on the outcomes of the CO_2 reduction reaction in a packed bed plasma reactor
2. To use electrical characterization techniques to diagnose the causes of the observed changes

The 1st aim of the thesis was achieved by using a quartz glass coaxial geometry DBD type reactor, featuring a 6mm discharge gap and ~3.5 cm^3 bed volume. The reactor was either tested unpacked, or packed with a BaTiO$_3$ (ε = 4,000 at 25°C and 1,000 Hz) or Al$_2$O$_3$ packing (ε = 9 – 10), with particle sizes of either 180 – 300, 300 – 500, 500 – 850, 850 – 1400, or 1400 – 2000 µm particles. The reactor is driven by a 10 kV maximum amplitude high voltage amplifier, operating at frequencies up to 10 kHz. For the first set of experiments the reactor is always driven by a 5 kHz square wave. The feed gas is CO$_2$ balanced with argon delivered to the reactor at a total flowrate of 100 ml/min, with compositions of 90% Ar – 10% CO$_2$, 50% Ar – 50% CO$_2$, and 100% CO$_2$. Gas conversion and product analysis is quantified using a combination of fourier transform infrared spectroscopy (FTIR) and mass spectrometry (MS). The plasma power is calculated by the "capacitor method", where the potential difference across a monitor capacitor in the ground from the reactor is plotted as function of applied voltage to the reactor. This generates a hysteresis loop known as a Lissajous figure, where the area bound by its perimeter is equal to the energy discharged in the plasma per AC cycle. The value obtained from integration of the Lissajous figure can be multiplied by the operating frequency to obtain the power dissipated in the plasma. This operation is performed in real time using a Labview program that simultaneously operates as a function generator and collects oscilloscope data. The collected voltage, power, temperature, gas composition and CO$_2$ conversion data is used to make observations regarding the performance of the reactor.

To achieve the 2nd aim of the thesis, oscilloscope data obtained during operation of the reactor to characterise properties of the discharge. The characteristics can in turn be used to diagnose the behavior of the plasma in the reactor. The data collected using the oscilloscope consists of applied voltage signal, current pulse signal measured using a current monitor (Rogowski coil), and the potential difference measured across the monitor capacitor. The aforementioned Lissajous figures can also be used to obtain the reactor burning voltge, as well as reactor capacitance data, including the dielectric capacitance, C_{diel}, the cell capacitance, C_{cell}, and the effective dielectric capacitance, ζ_{diel}. The reactor burning voltage is a threshold applied voltage at which plasma discharges begin to form in the reactor during an AC discharge cycle. The reactor capacitances are related to the equivalent electrical circuit of a dielectric barrier discharge reactor, and they can be used as a diagnostic tool to understand when the reactor is partially discharging. "Partial discharging" describes a condition in which the reactor is not transferring all of the stored charge on the dielectric layer to the other electrode during a discharge cycle. The reactor is known to be partially discharging under the condition that the measured value of the dielectric capacitance, (the effective dielectric capacitance, ζ_{diel}), is less than the geometrically determined dielectric capacitance, C_{diel}. Furthermore, this partial discharging behavior can be quantified by the use of the parameter α, derived by Peeters and

van de Sanden [95], which is shown to be equal to the proportion of stored dielectric charge being fully transferred between the reactor electrodes. In addition to the information that can be derived from the Lissajous figure, the voltage and current data can be analysed qualitatively in order to determine the nature of the plasma discharge itself.

The results from the first set of experiments show a number of key, previously unidentified, trends:

- When the feed gas compositions is 90% Ar – 10% CO_2, that the smallest particle sizes (180 – 300 μm) lead to the highest CO_2 conversion in both $BaTiO_3$ and Al_2O_3. For the case of Al_2O_3 the conversion increases by up to 70% with the use of the smallest particle sizes.
- When argon concentration is reduced in the gas mixture, the reactor packed with larger particles yields higher conversion of CO_2 than small particles. Based on the reduced power drawn by the reactor with small particles, this is believed to be due to partial reactor discharging occurring caused by an insufficient applied potential difference to create electrical breakdowns in the void spaces of the packed bed.
- Under the experimental conditions tested, a higher CO_2 conversion can be achieved using the Al_2O_3 packed reactor than the $BaTiO_3$ packed reactor
- No plasma discharge is formed (And hence no CO_2 converted) in the Al_2O_3 packed reactor with particle sizes < 850 μm in pure CO_2 streams. Using the $BaTiO_3$ packed reactor, a plasma can be formed using all particle sizes, applied potential differences and gas compositions.

As a result of these observations, a number of questions were posed. These questions were:

1. What is the relationship between burning voltage, applied voltage, particle size (and shape), gas composition, applied frequency, and choice of packing material?
2. Can the benefits of small particle sizes be realised in all packed bed dielectric barrier discharge reactors?
3. Why do particle size and material properties tested cause an increase or decrease in observed CO_2 conversion?

Using the electrical characterisation data, attempts were made to systematically find an answer to these questions. In order to attempt to answer the first question, the reactor burning voltage was evaluated as a function of the different experimental parameters. As has previously been reported elsewhere, the addition of increasing admixtures of CO_2 in Ar causes an increase in the burning voltage of the reactor. In addition to this an increase in driving frequency is also found to decrease the burning voltage. $BaTiO_3$ is found to significantly decrease the reactor burning voltage, whilst Al_2O_3 causes an increase in the burning voltage compared with a non-packed

reactor. A previously unseen result is found to occur, and the first major outcome of this thesis; decreasing particle size is found to significantly increase reactor burning voltage. When comparing 1400 – 2000 µm to 180 – 300 µm particles, $BaTiO_3$ burning voltage increases up to 130%. This increase in burning voltage is attributed to the decrease in void size in the packed bed. The relationship between experimental parameters in order to find a design equation for packed bed DBDs is not achievable with the data obtained, as it would be a complicated function of many variables.

In order to answer the 2nd question, "can the benefits of small particle sizes be realised in all packed bed dielectric barrier discharge reactors?" The concept of partial reactor discharging was used to explore under what circumstances the reactor tested in this thesis was operating under optimal, fully discharging conditions. It was found that small particle sizes increase the tendency of the reactor towards partially discharging behavior. It was suggested that as each particle can act as a capacitor, charges become trapped in the packed bed whilst being transferred between electrodes. It was also found that partial discharging tends to occur to a greater extent with $BaTiO_3$ compared with Al_2O_3. This is likely to be due to the higher dielectric capacity of the material being able to store a greater density of surface charge.

Previously published literature by other authors was reviewed. An example from literature of plasma discharges forming in pure CO_2 streams in small particles (180 – 250 µm, and 250 – 420 µm) at very high electric field gradients is cited to demonstrate that it is possible. The work of this thesis is subsequently compared to the work of other researchers, using the partial discharging parameter, α, to investigate the operation of their reactors. It was found that in a number of publications, packing materials were being compared despite the reactor not fully discharging in all circumstances. There are two suggestions for researchers working with packed bed reactors based on these findings, and these are the second outcome of this thesis:

1. As a matter of course when carrying out experiments with packed bed reactor discharges the partial discharging of the reactor should be quantified in order to allow a more fair comparison between materials tested.
2. In order to benefit from the advantages of using small particle sizes, higher electric field strengths need to be applied, either by increasing the applied voltage or decrease the gap size used in the reactors.

Finally, to attempt to answer the 3rd question, "Why do particle size and material properties tested cause an increase or decrease in observed CO_2 conversion? The two variables were evaluated in order to determine the resultant parameters that they change. Although it was determined that the range of parameters is too large to come to a specific conclusion, further observations were made about the nature of the plasma discharges occurring in the packed bed.

Oscilloscope data of applied voltages and the plasma current data were evaluated qualitatively. It was found that the behavior of the plasma discharge changes significantly between different particle sizes and packing materials. Very high magnitude, intense pulses are found to occur in the 180 – 300 μm Al_2O_3 packed bed when using 90% Ar – 10% CO_2 feed gas composition, that do not occur when other particle sizes are packed into the reactor. It is hypothesized that these intense pulses are caused by the cumulative effect of the stored charge of many particles dissipating their stored energy into high amplitude, intense pulses carrying a large amount of charge. This effect is not observed with the $BaTiO_3$ particles, but this may be due to the large capacitance of the material reducing effective charge transfer through the bed. The results of the attempt to answer the final question from the data obtained are inconclusive. However, new observations have been made that require further investigation in order to provide a further incite into the behavior of packed bed reactors.

7.2 Limitations of Study

The work carried out in this study has a number of limitations. It is not expected that the limitations of the work performed will have a significant impact on the outcomes of the thesis. There are a number of problems with experimental design:

1. The design of the reactor allows plasma discharges to form outside of the packed bed, this will have had an effect on the electrical measurements made. Stray discharges are still observed despite attempts to minimize their presence, for example through smoothing hard edges and electrode contact points, and using silicone sealant on the outside of the ground electrode. This becomes a particular problem at very high argon concentrations. This will have had an effect on the measurement of capacitances, and burning voltages, but the overall effect is likely to be very small and would not change the important trends observed from the data.

2. Temperature control and measurement should be improved, particularly for measurement of electrical characteristics. Capacitance and burning voltage can be seen to change as the reactor changes in temperature, again this effect would not significantly change the trends observed, but does have an impact on the accuracy of the measurements. Ideally, temperature would be measured from inside the packed bed and would be recorded simultaneously with reactor power.

3. The Mathematica program used to extract data from Lissajous figures needs to be improved. The Mathematica method used currently does not operate very well when the applied voltage to the reactor is low. Currently, it operates by using a least squares method to fit four linear plots to a large set of data, which effectively introduces

problems due to the signal to noise ratio of the data obtained. Instead, this program should separate out the data into individual AC cycles, fit the Lissajous figure, and take the average values of a large number of cycles. This should significantly improve the accuracy of the measurements taken.

4. In an ideal study of the effects of particle size, the shape of the particles should be kept as spherical, although this would become very difficult with smaller particle sizes. Particles that have edges with a high radius of curvature are believed to introduce the possibility of electrical breakdowns occurring at those edges due to very high electric field strengths. Using perfectly spherical particles would affect the results obtained, possibly reducing the relative increase in burning voltage at small particle sizes due to the larger void spaces between particles. Overall, it doesn't change the validity of the results obtained in this thesis.

7.3 Conclusions

There are a number of key conclusions that can be made from the work of this thesis:

1. In packed bed plasma reactors smaller particle sizes (On the order of 100s of μm) are beneficial for conversion of CO_2 to CO, compared with larger particle sizes, provided that a discharge can be generated in the particle bed. This exact cause of the increase in CO_2 conversion is not certain, but it may be due to improved plasma – gas contacting, increased surface – plasma interface area for surface reactions, or a change in the plasma discharge behavior.

2. With randomly shaped particles, as particle size decreases the burning voltage increases rapidly.

3. The tendency of packed bed reactors towards partial discharging increases with decreasing particle size, this is likely to be due to plasma discharges not forming in the void spaces of the particles. As a result of this phenomena, it is recommended that the partial discharging behavior of packed bed plasma reactors should be quantified using the equivalent circuit (or a packed bed equivalent) for partially discharging reactors derived by Peeters and van de Sanden [95]

4. A previously unobserved discharge phenomena in packed bed reactors with small particle sizes may have been observed, although further work is required in order to verify this observation.

8 Suggestions for Future Work

Whilst I was doing the work for this thesis there were many occasions when I would find myself thinking, "What if…?"

In order to accelerate the progress of packed bed plasma research, some fundamental problems need to be addressed. As stated very early into this thesis, the behavior of packed bed reactors is currently very poorly understood. Significant progress is being made with understanding and identifying catalyst – plasma interactions, whilst progress on understanding the dynamics of packed bed plasmas is very slow. I believe this is a problem that needs to be addressed if catalytic plasma reactors are to ever make it out of the laboratory and into industrial use. There are very few direct comparisons that can be made between results obtained with different catalytic experiments, therefore there needs to be a mechanism for benchmarking results obtained in different reactors.

Some of my suggestions for future work reflect a requirement for fundamental research, whilst others are suggestions for novel approaches to drive progress forwards by potentially opening new avenues of research.

8.1 Improving plasma properties in packed bed reactors

It has been demonstrated that packed bed reactors using small particle sizes are likely to be most beneficial for CO_2 conversion if discharges can be ignited in the void spaces of the particles. When increasingly small particle sizes are used, the large plasma – wall interface area will increase the loss rate of electrons, ions and excited species. Therefore, in order to have high electron and ion densities in order to maintain the plasma discharge the effects of materials with low work functions should be investigated. When an ion or electron collides with a material with a low work function, if the energy of that ion or electron exceeds the work function of the material, one or more electrons will be emitted back into the plasma. In my opinion, this is an essential piece of research that may have a significant impact if it can lead to a significant improvement in electron densities in packed bed reactors

8.2 Discharge phenomena in packed beds

The formation and mechanism of discharges in packed bed DBDs is very much unknown. High speed photography, high speed optical emission spectroscopy, and electrical characterisation could be used. It would be interesting to observe plasma formation around single pellets,

stacked pellets and packed beds arranged in monolayers, or thin layers dependent upon particle size. Discharge behavior should be studied varying applied field strength, gas composition, packing material, and applied frequency.

8.3 Catalytic activity of γ-Al₂O₃ for CO₂ reduction in non-thermal plasmas

A question that keeps recurring amongst discussion between myself and other researchers is the possibility that γ-Al_2O_3 might be catalytic for CO_2 reduction in plasma. The work of Roland et al [82] demonstrating that a paramagnetic surface species is formed in γ-Al_2O_3 when it is subjected to non-thermal plasma might indicate that it can become catalytic towards CO_2 reduction, which may explain some of the surprisingly good results that have been observed using Al_2O_3 for CO_2 reduction. In terms of methodology to test this hypothesis, plasma DRIFTS-MS recently demonstrated at QUB [83], in-situ Raman spectroscopy, molecular beam mass spectrometry, and optical emissions spectroscopy could all be useful. I would also be interested in using DRIFTS-MS to measure changes in the relative height of vibrational lines of CO_2 and CO on the surfaces of potential catalysts. As far as I am aware, this has not been demonstrated previously.

8.4 Larger scale testing of packed bed reactors

The majority of publications on packed bed reactors are performed using very small reactors with packed bed sizes of no more than 3 – 20 ml. I would be very interested to see some of these reactors operated on a slightly larger scale, perhaps about a 100 – 300 ml sized reactor. As demonstrated by this thesis, gap sizes should be kept small (0.5 – 2mm perhaps) with high driving voltages (60 – 120 kV peak to peak), with powers of 500 W to 2 kW. Driving frequencies should also be significantly increased from those studied in this thesis, perhaps up to 150 kHz. Although the work of this thesis recommends the use of small particles for studying packed bed reactor materials, pressure drop will become an important factor when the reactor is scaled up significantly. Structured catalyst monoliths designed specifically for plasma reactors should be developed to optimise gas contacting, gas flow through the bed, and catalytic performance.

8.5 In-situ oxygen separation from CO₂ plasma reduction

This is a project that has attracted some interest already [118, 119], and that I have also done some work on myself. Solid oxide electrolysis cells could be coupled with non-thermal plasma technologies in order to actively remove oxygen from the reaction site as it is being created. If

this was operated at high temperature for co-electrolysis (CO_2 and H_2O) there could be many potential benefits, including direct reforming to fuels. The high temperature of operation is likely to reduce the power required to generate a plasma to a fraction of the normally required energy input [120, 121]. In addition to this, the plasma may be used to improve reaction kinetics, negate the requirement for a catalyst, help overcome kinetic limitations due to rates of gas diffusion, and potentially even address problems of solid oxide cell durability.

9 Appendix

9.1 Labview Program

The purpose of the Labview program is to operate as a function generator, and to collect, analyse and save oscilloscope data. Each Labview program is made up of a number of virtual instruments (VIs). In the images shown in figures Figure 94 toFigure 96 the function of clusters of VIs are described to breakdown the function of the overall program into its constituent components. Figure 97 shows the front panel of the Labview program during operation.

Its operation can be split into 3 independent subprograms:

1. Function generator (Figure 94)
2. Oscilloscope + Analysis (Figure 95)
3. File Management (Figure 96)
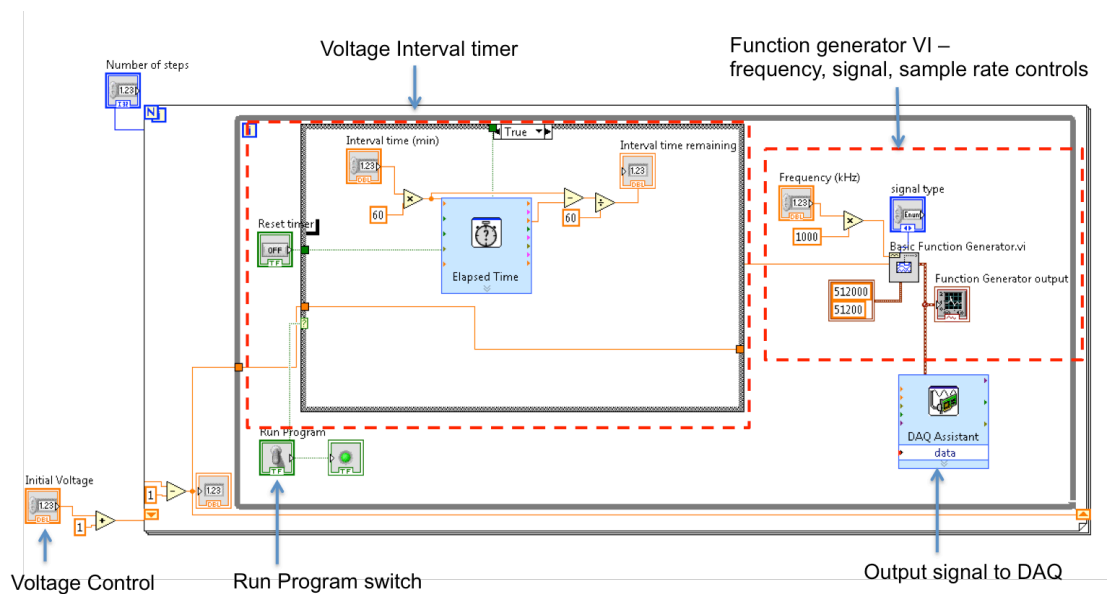
Figure 94: Function Generator Labview Sub-program
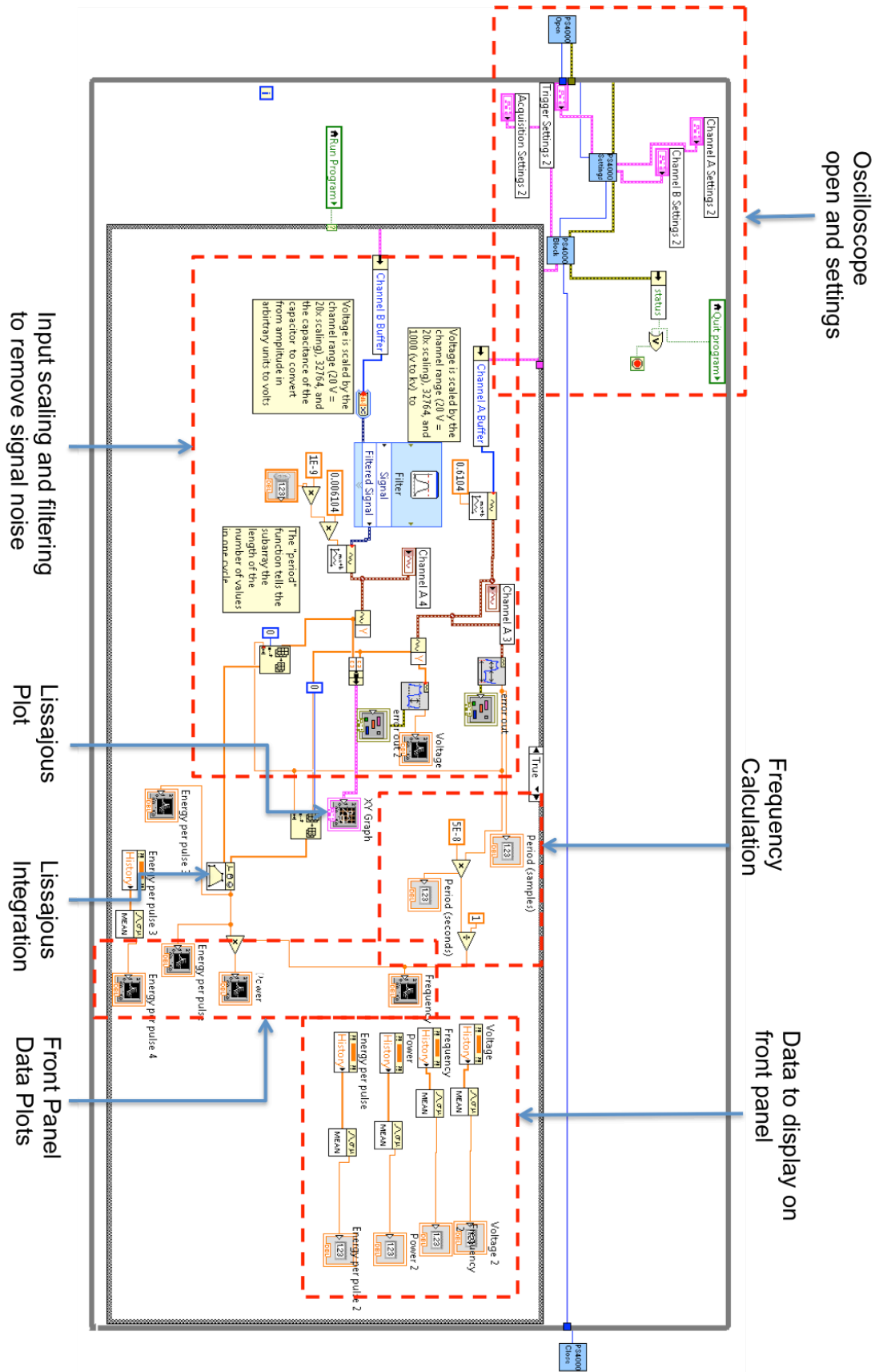
Figure 95: Oscilloscope and data analysis sub-program

File save – front panel interface

Data write timer

file path (use dialog)

open or create

10000

Voltage
History
MEAN

Frequency
History
MEAN

%5.2f

Power
History
MEAN

Quit program

Data to save – format and
number of decimal places

Figure 96: File management sub-program

151

Figure 97: View of complete program front panel in operation

9.2 Mathematica program for analysis of Lissajous figures

A step-by-step annotated guide to the Mathematica code used to extract data from the Lissajous figures is given below, with some sample data included.

Mathematica Program for analysis

Setting up directory to operate in

```
In[189]:= SetDirectory[NotebookDirectory[]]

Out[189]= /Users/TomButterworth/Documents/PhD/Experimental Data/Lissajous Data/Al2O3 300 500

In[190]:= FileNames["*", %]

Out[190]= {/Users/TomButterworth/Documents/PhD/Experimental Data/Lissajous
            Data/Al2O3 300 500/10 Ar 90 co2 5 khz sine 10 kv 35 dc.csv,
          /Users/TomButterworth/Documents/PhD/Experimental Data/Lissajous
            Data/Al2O3 300 500/20 Ar 80 co2 5 khz sine 10 kv 70 dc.csv,
          /Users/TomButterworth/Documents/PhD/Experimental Data/Lissajous
            Data/Al2O3 300 500/30 Ar 70 co2 5 khz sine 10 kv 75 dc.csv,
          /Users/TomButterworth/Documents/PhD/Experimental Data/Lissajous
            Data/Al2O3 300 500/40 Ar 60 co2 5 khz sine 10 kv 78 dc.csv,
          /Users/TomButterworth/Documents/PhD/Experimental Data/Lissajous
            Data/Al2O3 300 500/50 Ar 50 co2 5 khz sine 10 kv 79 dc.csv,
          /Users/TomButterworth/Documents/PhD/Experimental Data/Lissajous
            Data/Al2O3 300 500/60 Ar 40 co2 5 khz sine 10 kv 78 dc.csv,
          /Users/TomButterworth/Documents/PhD/Experimental Data/Lissajous
            Data/Al2O3 300 500/70 Ar 30 co2 5 khz sine 10 kv 76 dc.csv,
          /Users/TomButterworth/Documents/PhD/Experimental Data/Lissajous
            Data/Al2O3 300 500/80 Ar 20 co2 5 khz sine 10 kv 72 dc.csv,
          /Users/TomButterworth/Documents/PhD/Experimental Data/Lissajous
            Data/Al2O3 300 500/90 Ar 10 co2 5 khz sine 10 kv 62 dc.csv,
          /Users/TomButterworth/Documents/PhD/Experimental Data/Lissajous
            Data/Al2O3 300 500/90 Ar 10 co2 5 khz sine 10 kv 68 dc.csv,
          /Users/TomButterworth/Documents/PhD/Experimental Data/Lissajous
            Data/Al2O3 300 500/90 Ar 10 co2 5 khz sine 10 kv 70 dc.csv,
          /Users/TomButterworth/Documents/PhD/Experimental Data/Lissajous
            Data/Al2O3 300 500/Lissajous test annotated.nb,
          /Users/TomButterworth/Documents/PhD/Experimental Data/Lissajous
            Data/Al2O3 300 500/Pure Ar co2 5 khz sine 10 kv 50 dc.csv,
          /Users/TomButterworth/Documents/PhD/Experimental Data/Lissajous
            Data/Al2O3 300 500/Pure Ar co2 5 khz sine 10 kv 50 dc.nb,
          /Users/TomButterworth/Documents/PhD/Experimental Data/Lissajous
            Data/Al2O3 300 500/Pure co2 5 khz sine 10 kv 32 dc.csv}
```
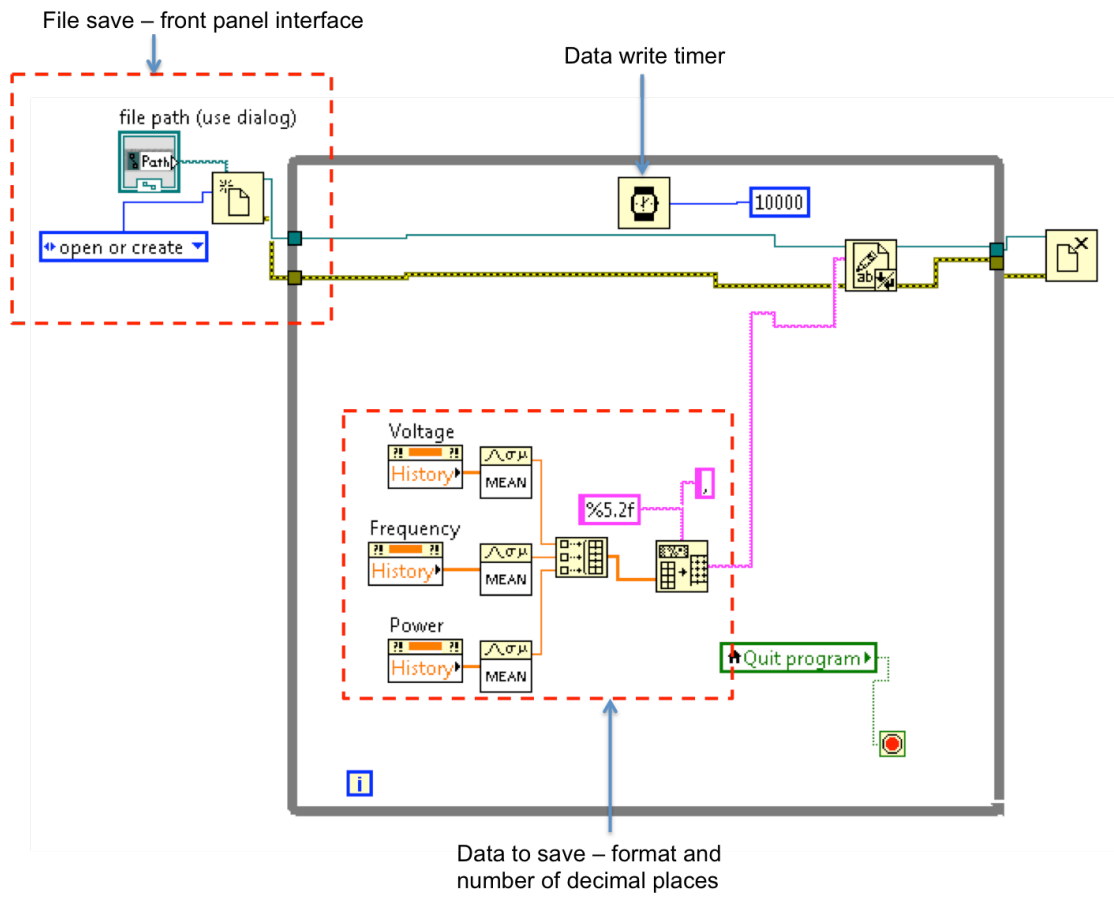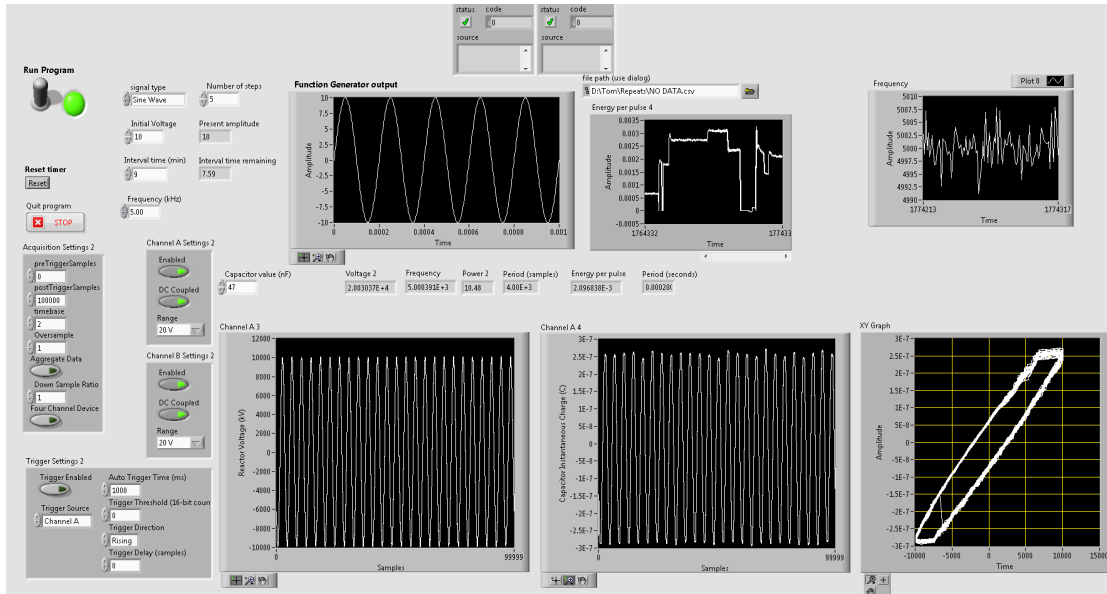
Entry of variables that are used in the program

```
In[191]:= scale = 47
          frequency = 5000

Out[191]= 47

Out[192]= 5000
```

Trimming data so that only the values of interested are selected

```
In[193]:= raw = Import[
              "/Users/TomButterworth/Documents/PhD/Experimental Data/Lissajous
                Data/Al2O3 300 500/80 Ar 20 co2 5 khz sine 10 kv 72 dc.csv"
            ];

In[195]:= clip = raw[[4 ;;]];

In[196]:= charge = clip[[All, 3]];
          xypairs = Transpose[{clip[[All, 2]], charge}];
```

Removing non-numerical data points, e.g. where the value is infinite due to data clipping

```
In[198]:= dataRough = Cases[xypairs[[1 ;; -1 ;; 10]], {_Real, _Real}];
         dataPlot = ListPlot[dataRough, PlotStyle → Lighter[Blue, 0.7]];
```

Data smoothing using the Savitzky-Golay method

```
In[200]:= k = SavitzkyGolayMatrix[{10}, 2];
         ListPlot[k]
```
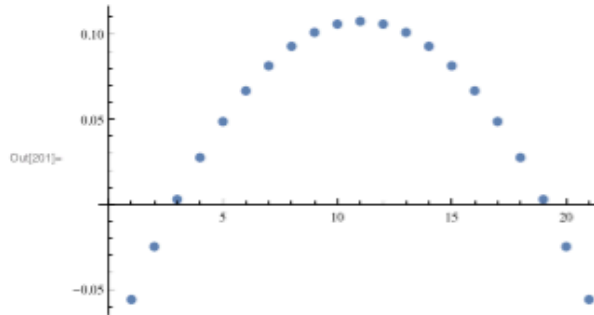

Test Lissajous plot showing raw data (blue dots) and smoothed data (red dots)

```
In[202]:= data = Transpose[{voltage = ListConvolve[k, dataRough[[All, 1]]],
            current = ListConvolve[k, dataRough[[All, 2]]]}];
         Show[smoothDataPlot = ListPlot[data, PlotStyle → Red], dataPlot]
```
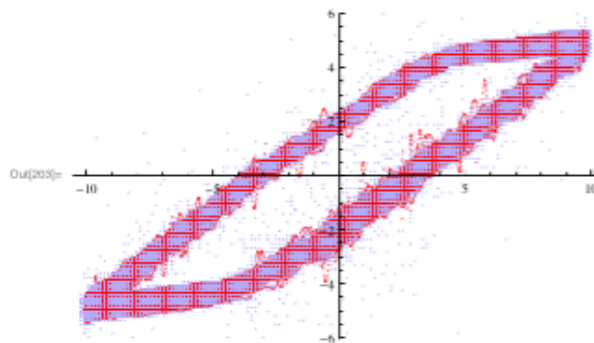

These functions split the data into positive and negative x and y values

```
In[207]:= PosX[y_] := Cases[y, {x_, _} /; x > 0]
         PosY[y_] := Cases[y, {_, x_} /; x > 0]
         NegX[y_] := Cases[y, {x_, _} /; x < 0]
         NegY[y_] := Cases[y, {_, x_} /; x < 0]
```

In[213]:= `PosX[data] // ListPlot`

Out[213]=
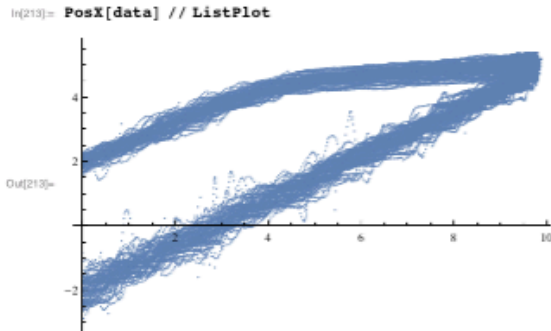
These functions find the nearest data points to the various axis intercepts

```
In[211]:= distY[{a_, _}, {b_, _}] := Abs[b - a]
         distX[{_, a_}, {_, b_}] := Abs[b - a]
```

```
In[215]:= PosXInt = Mean[Nearest[PosX[data], {0, 0}, DistanceFunction → distX]]
         NegXInt = Mean[Nearest[NegX[data], {0, 0}, DistanceFunction → distX]]
         PosYInt = Mean[Nearest[PosY[data], {0, 0}, DistanceFunction → distY]]
         NegYInt = Mean[Nearest[NegY[data], {0, 0}, DistanceFunction → distY]]
```

Out[215]= {3.40761, 0.}

Out[216]= {-2.99089, 0.}

Out[217]= {0., 1.93131}

Out[218]= {0., -1.837}

These find the maxima and minima of the Lissajous figure

```
In[220]:= maxPos = data[[First[FirstPosition[data, Max[data[[All, 1]]]]]]]
         minPos = data[[First[FirstPosition[data, Min[data[[All, 1]]]]]]]
         maxPosAvg = Mean[maxPosNear = Nearest[data, maxPos, 100]]
         minPosAvg = Mean[minPosNear = Nearest[data, minPos, 100]]
```

Out[220]= {9.88893, 5.16926}

Out[221]= {-10.1343, -5.02779}

Out[222]= {9.82396, 5.15751}

Out[223]= {-10.0946, -5.0291}

Visualise the points of interest

```
In[224]:= intercepts =
         ListPlot[{PosXInt, NegXInt, PosYInt, NegYInt, maxPosAvg, minPosAvg}, PlotStyle → Red];
```

In[225]:= `Show[ListPlot[data], intercepts]`
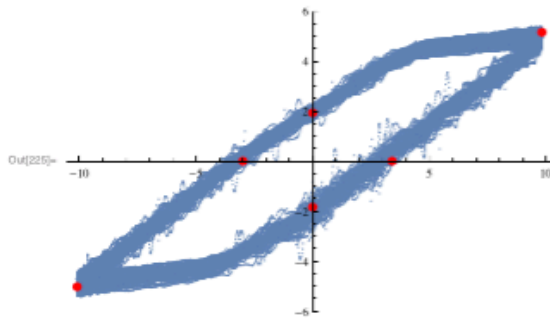
Fit a linear model to each section of data

In[228]:=
```
reg1prelim = {minPosAvg, NegYInt};
reg2prelim = {maxPosAvg, PosXInt};
reg3prelim = {maxPosAvg, PosYInt};
reg4prelim = {minPosAvg, NegXInt};
```

In[230]:=
```
reg1 = LinearModelFit[reg1prelim, f, f];
reg2 = LinearModelFit[reg2prelim, f, f];
reg3 = LinearModelFit[reg3prelim, f, f];
reg4 = LinearModelFit[reg4prelim, f, f];
```

Begin to define the regions in which the Lissajous plot should be defined

In[234]:=
```
low = 0.9
high = 0.6
```

Out[234]= `0.9`

Out[235]= `0.6`

In[236]:=
```
regNeglmp = low * minPosAvg[[1]];
regNeghmp = high * minPosAvg[[1]];
regPoslmp = low * maxPosAvg[[1]];
regPoshmp = high * maxPosAvg[[1]];
```

In[240]:=
```
p1a = {{regNeglmp, reg1[regNeglmp]}};
p1b = {{regNeghmp, reg1[regNeghmp]}};
p2 = {{regPoslmp, reg2[regPoslmp]}};
p3a = {{regPoslmp, reg3[regPoslmp]}};
p3b = {{regPoshmp, reg3[regPoshmp]}};
p4 = {{regNeglmp, reg4[regNeglmp]}};
```

Test plot to see how the Lissajous figure is developing

```
In[246]:= points = ListPlot[{p1a, p1b, p2, p3a, p3b, p4}, PlotStyle → Black];
        mp = Plot[reg1[f], {f, minPosAvg[[1]], NegYInt[[1]]}, PlotStyle → Darker[Green]];
        Show[ListPlot[data], intercepts, mp, points]
```


Out[248]=
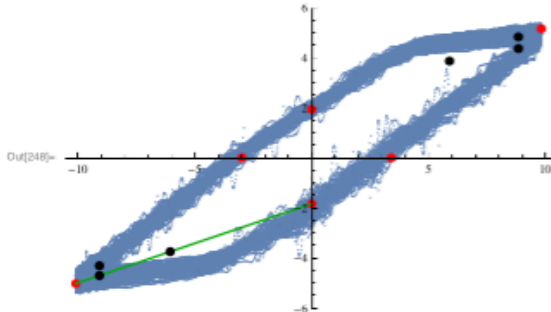
All good so far! Using the points defined in black, a new region is defined above or below these points where the linear models should be fitted for the Lissajous data.

```
In[249]:= yLp1a[z_] := Cases[z, {_, y_} /; y < p1a[[1, 2]]]
        yLp1b[z_] := Cases[z, {_, y_} /; y < p1b[[1, 2]]]
        yLp2[z_] := Cases[z, {_, y_} /; y < p2[[1, 2]]]
        yGp3a[z_] := Cases[z, {_, y_} /; y > p3a[[1, 2]]]
        yGp3b[z_] := Cases[z, {_, y_} /; y > p3b[[1, 2]]]
        yGp4[z_] := Cases[z, {_, y_} /; y > p4[[1, 2]]]

In[255]:= Np1a = Mean[Nearest[yLp1a[data], p1a[[1]], 200, DistanceFunction → distY]];
        Np1b = Mean[Nearest[yLp1b[data], p1b[[1]], 200, DistanceFunction → distY]];
        Np2 = Mean[Nearest[yLp2[data], p2[[1]], 200, DistanceFunction → distY]];
        Np3a = Mean[Nearest[yGp3a[data], p3a[[1]], 200, DistanceFunction → distY]];
        Np3b = Mean[Nearest[yGp3b[data], p3b[[1]], 200, DistanceFunction → distY]];
        Np4 = Mean[Nearest[yGp4[data], p4[[1]], 200, DistanceFunction → distY]];

In[261]:= Np = {Np1a, Np1b, Np2, Np3a, Np3b, Np4};

In[264]:= reg1new = {Np1a, Np1b};
        reg2new = {NegYInt, Np2};
        reg3new = {Np3a, Np3b};
        reg4new = {PosYInt, Np4};

In[268]:= nr1 = LinearModelFit[reg1new, f, f];
        nr2 = LinearModelFit[reg2new, f, f];
        nr3 = LinearModelFit[reg3new, f, f];
        nr4 = LinearModelFit[reg4new, f, f];
```

Make a plot to test if everything makes sense

```
In[272]:= mpr1 = Plot[nr1[f], {f, minPosAvg[[1]] - 5, 3}, PlotStyle → {Dashed, Darker[Orange]}];
        mpr2 = Plot[nr2[f], {f, -5, maxPosAvg[[1]] + 1}, PlotStyle → {Dashed, Darker[Orange]}];
        mpr3 = Plot[nr3[f], {f, -2, maxPosAvg[[1]] + 1}, PlotStyle → {Dashed, Darker[Orange]}];
        mpr4 = Plot[nr4[f], {f, minPosAvg[[1]] - 2, 3}, PlotStyle → {Dashed, Darker[Orange]}];
```

```
In[399]:= Show[dataPlot, mpr1, mpr2, mpr3, mpr4,
           plotNp, intercepts, PlotRange → {{-11, 11}, {-7, 7}}]
```
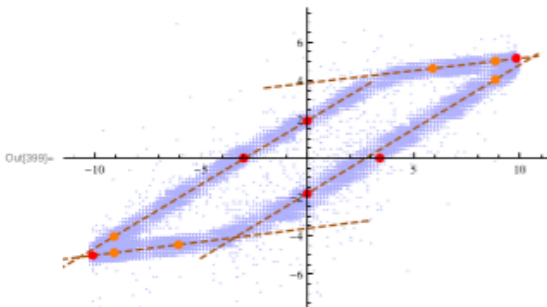

Still looking good. Approximate Lissajous figure is fitted to data. Now a more accurate Lissajous figure should be fitted to the data. Start by finding the intersections of the Lissajous linear lines, and use these to define "regions" in which to search for data.

```
In[277]:= m1 = Normal[nr1];
           m2 = Normal[nr2];
           m3 = Normal[nr3];
           m4 = Normal[nr4];

In[281]:= i12 = Flatten[{x12 = f /. Solve[m1 == m2], y12 = m1 /. Solve[m1 == m2]}];
           i23 = Flatten[{x23 = f /. Solve[m2 == m3], y23 = m2 /. Solve[m2 == m3]}];
           i34 = Flatten[{x34 = f /. Solve[m3 == m4], y34 = m3 /. Solve[m3 == m4]}];
           i41 = Flatten[{x41 = f /. Solve[m4 == m1], y41 = m4 /. Solve[m4 == m1]}];

In[285]:= intersections = ListPlot[{i12, i23, i34, i41}, PlotStyle → Darker[Green, 0.7]];

In[286]:= Show[dataPlot, mpr1, mpr2, mpr3, mpr4, intersections]
```
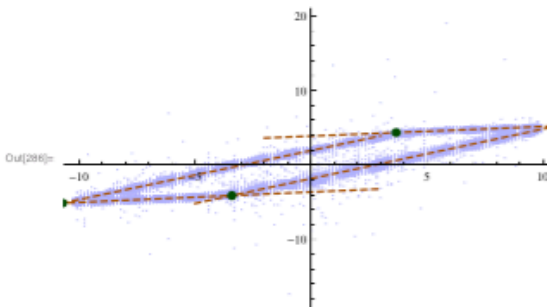

Add / Subtract a certain percentage range to the intersection and define an area that runs between each data point in which to search for data for the Lissajous plot

```
In[287]:= s = {1, 0.8};
           h = {1, 1.1};
```

158

```
In[289]:= i12min = i12 * h;
          i12max = i12 * s;
          i23min = i23 * s;
          i23max = i23 * h;
          i34min = i34 * s;
          i34max = i34 * h;
          i41min = i41 * h;
          i41max = i41 * s;

In[297]:= sNegLow = {1, 1.2};
          sNegHigh = {1, 1.2};
          hNegLow = {1, 0.9};
          hNegHigh = {1, 0.75};
          sPosLow = {1, 0.8};
          sPosHigh = {1, 0.85};
          hPosLow = {1, 1.2};
          hPosHigh = {1, 1.2};

In[305]:= i12minLow = i12 * sNegLow;
          i12maxLow = i12 * hNegLow;
          i12minHigh = i12 * sNegHigh;
          i12maxHigh = i12 * hNegHigh;
          i23minLow = i23 * sPosLow;
          i23maxLow = i23 * hPosLow;
          i23minHigh = i23 * sPosHigh;
          i23maxHigh = i23 * hPosHigh;
          i34minLow = i34 * sPosLow;
          i34maxLow = i34 * hPosLow;
          i34minHigh = i34 * sPosHigh;
          i34maxHigh = i34 * hPosHigh;
          i41minLow = i41 * sNegLow;
          i41maxLow = i41 * hNegLow;
          i41minHigh = i41 * sNegHigh;
          i41maxHigh = i41 * hNegHigh;

In[321]:= r1 = Polygon[{i41minLow, i12minLow, i12maxLow, i41maxLow}];
          r2 = Polygon[{i12minHigh, i23minLow, i23maxLow, i12maxHigh}];
          r3 = Polygon[{i34minHigh, i23minHigh, i23maxHigh, i34maxHigh}];
          r4 = Polygon[{i41minHigh, i34minLow, i34maxLow, i41maxHigh}];

In[327]:= r1f = Select[dataRough, RegionMember[r1]];
          r2f = Select[dataRough, RegionMember[r2]];
          r3f = Select[dataRough, RegionMember[r3]];
          r4f = Select[dataRough, RegionMember[r4]];
```

Use least squares method to fit linear models to the data found within the defined region and set-up plots of Lissajous figure

```
In[331]:= lmn1 = Normal[lm1 = LinearModelFit[r1f, f, f]];
          lmn2 = Normal[lm2 = LinearModelFit[r2f, f, f]];
          lmn3 = Normal[lm3 = LinearModelFit[r3f, f, f]];
          lmn4 = Normal[lm4 = LinearModelFit[r4f, f, f]];

In[335]:= I1 = Flatten[{X1 = f /. Solve[Normal[lmn1 == lmn4]], y1 = lmn4 /. Solve[lmn1 == lmn4]}];
          I2 = Flatten[{X2 = f /. Solve[Normal[lmn1 == lmn2]], y2 = lmn1 /. Solve[lmn1 == lmn2]}];
          I3 = Flatten[{X3 = f /. Solve[Normal[lmn2 == lmn3]], y3 = lmn2 /. Solve[lmn2 == lmn3]}];
          I4 = Flatten[{X4 = f /. Solve[Normal[lmn3 == lmn4]], y4 = lmn3 /. Solve[lmn3 == lmn4]}];

In[339]:= Plm1 = Plot[lm1[f], {f, X1[[1]], X2[[1]]}, PlotStyle → Red, PlotRange → All]
          Plm2 = Plot[lm2[f], {f, X2[[1]], X3[[1]]}, PlotStyle → Red, PlotRange → All];
          Plm3 = Plot[lm3[f], {f, X4[[1]], X3[[1]]}, PlotStyle → Red, PlotRange → All];
          Plm4 = Plot[lm4[f], {f, X1[[1]], X4[[1]]}, PlotStyle → Red, PlotRange → All];
```

```
In[360]:= RDP = ListPlot[Transpose[{dataRough[[All, 1]], dataRough[[All, 2]] * scale}],
        PlotStyle -> Lighter[Red, 0.7]];
      PLm1c = Plot[lmn1 * scale, {f, X1[[1]], X2[[1]]}];
      PLm2c = Plot[lmn2 * scale, {f, X2[[1]], X3[[1]]}];
      PLm3c = Plot[lmn3 * scale, {f, X4[[1]], X3[[1]]}];
      PLm4c = Plot[lmn4 * scale, {f, X1[[1]], X4[[1]]}];
```

Show that Lissajous plot fits raw data

```
Show[RDP, PLm1c, PLm2c, PLm3c, PLm4c,
 AxesLabel -> {"Voltage, kV", "Charge, nC"}, ImageSize -> Large,
 LabelStyle -> Directive[Bold, Medium], PlotRange -> {{-11, 11}, {-320, 300}}]
```


Out[422]=
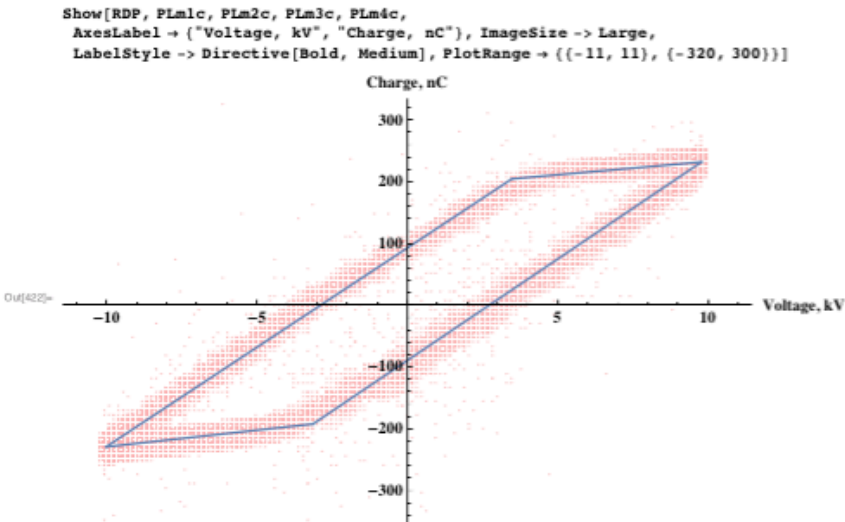
Extract information such as line gradients, intercepts and errors

```
In[366]:= a = {ax = First[f /. Solve[lmn1 == lmn4]], ay = (lm1[ax] * scale)};
      b = {bx = First[f /. Solve[lmn1 == lmn2]], by = (lm2[bx] * scale)};
      c = {cx = First[f /. Solve[lmn2 == lmn3]], cy = (lm3[cx] * scale)};
      d = {dx = First[f /. Solve[lmn3 == lmn4]], dy = (lm4[dx] * scale)};
      e1 = Quantile[resid1 = lm1["FitResiduals"] * scale, {0.95, 0.05}]
      e2 = Quantile[resid2 = lm2["FitResiduals"] * scale, {0.95, 0.05}];
      e3 = Quantile[resid3 = lm3["FitResiduals"] * scale, {0.95, 0.05}];
      e4 = Quantile[resid4 = lm4["FitResiduals"] * scale, {0.95, 0.05}];
      ah = {ax, (ay + ((e1 + e4) / 2))[[1]]};
      al = {ax, (ay + ((e1 + e4) / 2))[[2]]};
      bh = {bx, (by + ((e1 + e2) / 2))[[1]]};
      bl = {bx, (by + ((e1 + e2) / 2))[[2]]};
      ch = {cx, (cy + ((e2 + e3) / 2))[[1]]};
      cl = {cx, (cy + ((e2 + e3) / 2))[[2]]};
      dh = {dx, (dy + ((e3 + e4) / 2))[[1]]};
      dl = {dx, (dy + ((e3 + e4) / 2))[[2]]};

Out[370]= {14.8228, -16.4747}

In[382]:= BDEPosTest[z_] := Cases[z, {x_, y_} /; x > 0 && (-0.2) < y < (0.2)]
      BDENegTest[z_] := Cases[z, {x_, y_} /; x < 0 && (-0.2) < y < (0.2)]
      BDEPos = Quantile[BDEPosTest[dataRough][[All, 1]], {0.90, 0.10}];
      BDENeg = Quantile[BDENegTest[dataRough][[All, 1]], {0.90, 0.10}]

Out[385]= {-2.67717, -3.77953}
```

```
In[386]:= eplot1 =
    ListLinePlot[{{ah, bh, ch}, {al, bl, cl}}, Filling → {1 → {2}}, PlotStyle → None];
  eplot2 = ListLinePlot[{{ah, dh, ch}, {al, dl, cl}},
      Filling → {1 → {2}}, PlotStyle → None];
  zp = ListPlot[{ah, al, bh, bl, ch, cl, dh, dl}, PlotStyle → Black];
```

Prepare data for exportable format to Excel

```
In[390]:= TableForm[{
    First[
     BDPm = f /. Solve[Normal[lmn2 == 0]]],
    BDPsg = First[PosXInt],
    BDPosH = BDEPos[[1]],
    BDPosL = BDEPos[[2]],
    BDNm = -1 * First[f /. Solve[Normal[lmn4 == 0]]],
    BDNsg = -1 * First[NegXInt],
    BDNegH = -1 * BDENeg[[1]],
    BDNegL = -1 * BDENeg[[2]],
    (BDPm + BDNm) / 2,
    (BDPsg + BDNsg) / 2,
    Cap1 = ∂ₜlmn1 * scale,
    Cap2 = ∂ₜlmn2 * scale,
    Cap3 = ∂ₜlmn3 * scale,
    Cap4 = ∂ₜlmn4 * scale,
    a[[1]],
    a[[2]],
    ah[[2]],
    al[[2]],
    b[[1]],
    b[[2]],
    bh[[2]],
    bl[[2]],
    c[[1]],
    c[[2]],
    ch[[2]],
    cl[[2]],
    d[[1]],
    d[[2]],
    dh[[2]],
    dl[[2]],
    Qtrans = (First[lmn3 - lmn1] * scale),
    Qp2p = c[[2]] - a[[2]],
    Qd = d[[2]] - a[[2]],
    Power = frequency * ((EuclideanDistance[a, c] * EuclideanDistance[b, d]) / (2 * (10^8)))
    },
    TableDirections → Row]
```

Out[390]//TableForm=
```
2.7266  3.40761  3.46457  2.20473  2.88046  2.99089  2.67717  3.77953  2.80353  3.19925  5.369
```

9.3 FTIR Stepwise Calibration method

The steps used to calibrate the FTIR for carbon monoxide are outlined below:

i. Ensure that the FTIR is set-up as correctly, and the mass spectrometer is in continuous ion monitoring mode and is correctly set-up. (See section MASS SPECTROMETER)

ii. Flush the experimental rig with argon to remove any other gases that may be contained within any of the lines or the gas cell itself. The mass spectrometer will show that the species concentration of all gases has stabilised once the system is completely purged with argon.

iii. Change the argon flowrate to 100 ml/min and after the mass spectrometer is once again stable, run a background scan using the FTIR.

iv. Set the FTIR to "slow kinetics" mode and begin taking samples. In this mode the FTIR can be set to take a sample every minute, for any number of repeats. The number of samples should be selected so that it will run for the duration of the FTIR calibration run.

v. Set the argon flowrate to 99 ml/min, and the CO flowrate to 1 ml/min. These will be the flowrates used for the 1% CO calibration. Allow the mass spectrometer readings to stabilise, Once stabilisation has been reached leave the FTIR to continue for a minimum of 5 samples.

vi. Change the gas flowrates to 98 ml/min Ar, and 2 ml/min CO. Repeat step v. for each gas sample until a CO concentration of 5%, (5 ml/min CO, in 95 ml/min Ar) is reached. At this point the gas flow can be switched off.

vii. Using the FTIR software, the CO peak should be selected and added as a "new component". Then the peak boundaries should be defined, as described in Figure 43. The 5 stable values for each different gas concentration should be selected, and the corresponding concentration data should be entered into the calibration database.

viii. Finally, either a linear or quadratic relationship between species concentration and peak area should be selected. Although the Beer-Lambert law is a linear relationship, a quadratic relationship can often provide a more accurate fit for the data.

10 References

[1]   N. Stern, "The Stern Review on the Economics of Climate Change: Executive Summary," L. HM Treasury, Ed., ed, 2006.

[2]   C. John, N. Dana, A. G. Sarah, R. Mark, W. Bärbel, P. Rob, "Quantifying the consensus on anthropogenic global warming in the scientific literature," *Environmental Research Letters,* vol. 8, p. 024024, 2013.

[3]   Ipcc, *Climate Change 2014: Impacts, Adaptation, and Vulnerability. Part A: Global and Sectoral Aspects. Contribution of Working Group II to the Fifth Assessment Report of the Intergovernmental Panel on Climate Change [Field, C.B., V.R. Barros, DJ. Dokken, KJ. Mach, M.D. Mastrandrea, T.E. Bilir, M. Chatterjee, K.L. Ebi, Y.O. Estrada, R.C. Genova, B. Girma, E.S. Kissel, A.N. Levy, S. MacCracken, P.R. Mastrandrea, and L.L. White (eds.)].* Cambridge, United Kingdom and New York, NY, USA: Cambridge University Press, 2014.

[4]   IPCC, "IPCC Fourth assesment report: Climate Change 2007 (AR4)," Intergovernmental Panel on Climate Change2007.

[5]   United Nations, "Kyoto Protocol to the United Nations Framework Convention on Climate Change," ed, 1998.

[6]   United Nationations Climate Change, "Report of the Conference of the Parties on its sixteenth session, held in Cancun from 29 November to 10 December 2010. Addendum Part 2: Action taken by the Conference of the Parties at its sixteenth session," 2011.

[7]   Her Majestey's Government of the United Kingdom, "Climate Change Act 2008," ed, 2008.

[8]   Department of Energy and Climate Change, "2013 UK Greenhouse Gas Emissions, Provisional Figures and 2012 UK Greenhouse Gas Emissions, Final Figures by Fuel Type and End-User," Department of Energy and Climate Change, Ed., ed: Crown copyright 2014.

[9]   United States Energy Adminsitration, "International Energy Outlook 2011," 2011.

[10]   K. Armstrong, G. Dowson, and P. Styring, "Recent Advances in Catalysis for Carbon Dioxide Utilization," *The Catalyst Review,* vol. 26, pp. 6 - 13, 2013.

[11]   R. Garnaut, "The Garnaut Climate Change Review: Final Report," ed: Cambridge University Press, 2008.

[12]   D. Pakhare and J. Spivey, "A review of dry (CO_2) reforming of methane over noble metal catalysts," *Chemical Society Reviews,* vol. 43, pp. 7813-7837, 2014.

[13]   X. Tao, M. Bai, X. Li, H. Long, S. Shang, Y. Yin, "CH_4–CO_2 reforming by plasma – challenges and opportunities," *Progress in Energy and Combustion Science,* vol. 37, pp. 113-124, 4// 2011.

[14]   M. Carmo, D. L. Fritz, J. Mergel, and D. Stolten, "A comprehensive review on PEM water electrolysis," *International Journal of Hydrogen Energy,* vol. 38, pp. 4901-4934, 4/22/ 2013.

[15]   C. Graves, S. D. Ebbesen, M. Mogensen, and K. S. Lackner, "Sustainable hydrocarbon fuels by recycling CO_2 and H_2O with renewable or nuclear energy," *Renewable and Sustainable Energy Reviews,* vol. 15, pp. 1-23, 1// 2011.

[16]   A. Fridman, *Plasma Chemistry*: Cambridge University Press, 2008.

[17]   Y. P. Raizer, *Gas Discharge Physics*: Springer Berlin Hedielberg, 2011.

[18]   Y. Itikawa, "Cross Sections for Electron Collisions with Carbon Dioxide," *Journal of Physical and Chemical Reference Data,* vol. 31, pp. 749-767, 2002.

[19]   Y.-G. Ángel, C. José, and L. A. Luís, "An update of argon inelastic cross sections for plasma discharges," *Journal of Physics D: Applied Physics,* vol. 38, p. 1588, 2005.

[20]   A. Fridman and L. A. Kennedy, *Plasma Physics and Engineering*: Taylor & Francis, 2004.

[21]   R. Aerts, T. Martens, and A. Bogaerts, "Influence of Vibrational States on CO_2 Splitting by Dielectric Barrier Discharges," *The Journal of Physical Chemistry C,* vol. 116, pp. 23257-23273, 2012/11/08 2012.

[22]   S. Scherer. (2009, 4/3/2015). *Water is blue ... because water is blue.*

[23]   K. R. Parker, *Apppplied Electrostatic Precipitation*: Springer Science and Business media, 1996.

[24]   P. K. Chu and X. P. Lu, *Low Temperature Plasma Technology: Methods and Applications*: CRC Press, 2013.

[25]   D. Z. Pai, D. A. Lacoste, and C. O. Laux, "Transitions between corona, glow, and spark regimes of nanosecond repetitively pulsed discharges in air at atmospheric pressure," *Journal of Applied Physics,* vol. 107, p. 093303, 2010.

[26]   J. Chen and J. Davidson, "Model of the Negative DC Corona Plasma: Comparison to the Positive DC Corona Plasma," *Plasma Chemistry and Plasma Processing,* vol. 23, pp. 83-102, 2003/03/01 2003.

[27]   J. Chen and J. Davidson, "Electron Density and Energy Distributions in the Positive DC Corona: Interpretation for Corona-Enhanced Chemical Reactions," *Plasma Chemistry and Plasma Processing,* vol. 22, pp. 199-224, 2002/06/01 2002.

[28]   J. Chang, x, Shih, P. A. Lawless, and T. Yamamoto, "Corona discharge processes," *Plasma Science, IEEE Transactions on,* vol. 19, pp. 1152-1166, 1991.

[29]   J. R. Roth, *Industrial plasma engineering: Volume 2: Applications to nonthermal plasma processing*: CRC Press, 1995.

[30]   J. P. Hartnett, A. Fridman, and Y. I. Cho, *Transport phenomena in plasma: 40 (Advances in Heat Transfer)*: Academic Press, 2007.

[31]   U. Kogelschatz, "Dielectric-Barrier Discharges: Their History, Discharge Physics, and Industrial Applications," *Plasma Chemistry and Plasma Processing,* vol. 23, pp. 1-46, 2003/03/01 2003.

[32]   F. Holzer, F. D. Kopinke, and U. Roland, "Influence of Ferroelectric Materials and Catalysts on the Performance of Non-Thermal Plasma (NTP) for the Removal of Air Pollutants," *Plasma Chemistry and Plasma Processing,* vol. 25, pp. 595-611, 2005/12/01 2005.

[33]   J. S. Chang, A. Chakrabarti, and K. Urashima, "The Effects of Barium Titanate Pellet Shapes on the Gas Discharge Characteristics of Ferroelectric Packed Bed Reactors," presented at the Electrical Insulation and Dielectric Phenomena, Atlanta, GA, 1998.

[34]   L. F. Spencer and A. D. Gallimore, "CO_2 dissociation in an atmospheric pressure plasma/catalyst system: a study of efficiency," *Plasma Sources Science and Technology,* vol. 22, p. 015019, 2013.

[35]   E. C. Neyts and A. Bogaerts, "Understanding plasma catalysis through modelling and simulation—a review," *Journal of Physics D: Applied Physics,* vol. 47, p. 224010, 2014.

[36]   T. Xin, J. G. Helen, V. T. Martyn, A. G. Peter, and J. C. Whitehead, "Dry reforming of methane over a Ni/Al$_2$O$_3$ catalyst in a coaxial dielectric barrier discharge reactor," *Journal of Physics D: Applied Physics,* vol. 44, p. 274007, 2011.

[37]   T. Nozaki and K. Okazaki, "Non-thermal plasma catalysis of methane: Principles, energy efficiency, and applications," *Catalysis Today,* vol. 211, pp. 29-38, 8/1/ 2013.

[38]   H. L. Chen, H. M. Lee, and S. H. Chen, "Review of Packed-Bed Plasma Reactor for Ozone Generation and Air Pollution Control," *Industrial & Engineering Chemistry Research,* vol. 47, pp. 2122-2130, 2008/04/01 2008.

[39]   L. Pardo and J. Ricote, *Multifunctional polycrystalline Ferroelectric Materials: processing and properties*: Springer, 2011.

[40]   A. K. Tagantsev, L. E. Cross, and J. Fousek, *Domains in ferroic crystals and thin films*: Springer, 2010.

[41]   Y. E. Krasik, A. Dunaevsky, J. Felsteiner, A. Krokhmal, and S. Dorfman, "Ferroelectric plasma sources and their applications," in *Plasma Science, 2000. ICOPS 2000. IEEE Conference Record - Abstracts. The 27th IEEE International Conference on*, 2000, p. 235.

[42]   G. Rosenman, D. Shur, Y. E. Krasik, and A. Dunaevsky, "Electron emission from ferroelectrics," *Journal of Applied Physics,* vol. 88, p. 6109, 2000.

[43]   M. A. Kemp and S. D. Kovaleski, "Piezoelectric-Resonance Effect in a Radio-Frequency-Driven Ferroelectric Plasma Source," *Plasma Science, IEEE Transactions on,* vol. 35, pp. 578-581, 2007.

[44]   A. Meiners, M. Leck, and B. Abel, "Efficiency enhancement of a dielectric barrier plasma discharge by dielectric barrier optimization," *Review of Scientific Instruments,* vol. 81, p. 113507, 2010.

[45]   S. Mitea, M. Zeleznik, M. D. Bowden, P. W. May, N. A. Fox, J. N. Hart, "Generation of microdischarges in diamond substrates," *Plasma Sources Science and Technology,* vol. 21, p. 022001, 2012.

[46]   T. Chang, S. Lou, H. Chen, C. Chen, C. Lee, N. Tai, "Enhancing the plasma illumination behaviour of microplasma devices using microcrystalline/ultra-nanocrystalline hybrid diamond materials as cathodes," *Nanoscale,* vol. 5, pp. 7467-7475, 2013.

[47]   T. Takamatsu, K. Uehara, Y. Sasaki, H. Miyahara, Y. Matsumura, A. Iwasawa*, et al.*, "Investigation of reactive species using various gas plasmas," *RSC Advances,* vol. 4, pp. 39901-39905, 2014.

[48]   R. I. Asisov, A. Fridman, V. K. Givotov, E. G. Krasheninnikov, B. I. Patrushev, B. V. Potapkin, "Carbon Dioxide Dissociation in Non-Equilbrium Plasma," in *5th International Symposium on Plasma Chemistry*, Edinburgh, 1981, p. 774.

[49]   S. Tiago, B. Nikolay, G. Thomas, and S. Rony, "Optical characterization of a microwave pulsed discharge used for dissociation of CO$_2$," *Plasma Sources Science and Technology,* vol. 23, p. 025009, 2014.

[50]   A. Indarto, D. R. Yang, J.-W. Choi, H. Lee, and H. K. Song, "Gliding arc plasma processing of CO$_2$ conversion," *Journal of Hazardous Materials,* vol. 146, pp. 309-315, 7/19/ 2007.

[51]   T. Nunnally, K. Gutsol, A. Rabinovich, A. Fridman, A. Gutsol, and A. Kemoun, "Dissociation of CO$_2$ in a low current gliding arc plasmatron," *Journal of Physics D: Applied Physics,* vol. 44, p. 274009, 2011.

[52]   N. Boukhalfa, A. Goldman, and M. Goldman, "CO$_2$ to CO conversion in corona discharges," in *8th International Symposium on Plasma Chemsitry*, 1987, p. 797.

[53]   I. Maezono and J. S. Chang, "Reduction of CO_2 from combustion gases by DC corona torches," in *Industry Applications Society Annual Meeting, 1988., Conference Record of the 1988 IEEE*, 1988, pp. 1636-1640 vol.2.

[54]   G. Zheng, J. Jiang, Y. Wu, R. Zhang, and H. Hou, "The Mutual Conversion of CO_2 and CO in Dielectric Barrier Discharge (DBD)," *Plasma Chemistry and Plasma Processing,* vol. 23, pp. 59-68, 2003/03/01 2003.

[55]   J.-Y. Wang, G.-G. Xia, A. Huang, S. L. Suib, Y. Hayashi, and H. Matsumoto, "CO_2 Decomposition Using Glow Discharge Plasmas," *Journal of Catalysis,* vol. 185, pp. 152-159, 7/1/ 1999.

[56]   S. L. Brock, M. Marquez, S. L. Suib, Y. Hayashi, and H. Matsumoto, "Plasma Decomposition of CO_2 in the Presence of Metal Catalysts," *Journal of Catalysis,* vol. 180, pp. 225-233, 12/10/ 1998.

[57]   J. Amouroux, S. Cavadias, and A. Doubla, "Carbon Dioxide reduction by non-equilibrium electrocatalysis plasma reactor," *IOP Conference Series: Materials Science and Engineering,* vol. 19, p. 012005, 2011.

[58]   M. Ramakers, I. Michielsen, R. Aerts, V. Meynen, and A. Bogaerts, "Effect of argon or helium on the CO_2 conversion in a dielectric barrier discharge," *Plasma Processes and Polymers,* pp. n/a-n/a, 2015.

[59]   G. Horváth, J. D. Skalný, and N. J. Mason, "FTIR study of decomposition of carbon dioxide in dc corona discharges," *Journal of Physics D: Applied Physics,* vol. 41, p. 225207, 2008.

[60]   F. Pontiga, H. Moreno, K. Hadji, K. Yanallah, and A. Castellanos, "Experimental study of positive corona discharge in mixtures of CO_2 and N_2," in *ESCAMPIG XXI*, Viana do Castelo, Portugal, 2012.

[61]   M. Marcela, "Dc corona discharges in CO_2 and air," *Journal of Physics D: Applied Physics,* vol. 31, p. 1865, 1998.

[62]   T. Mikoviny, M. Kocan, S. Matejcik, N. J. Mason, and J. D. Skalny, "Experimental study of negative corona discharge in pure carbon dioxide and its mixtures with oxygen," *Journal of Physics D: Applied Physics,* vol. 37, p. 64, 2004.

[63]   F. Pontiga, K. Yanallah, H. Moreno, K. Hadji, and A. Castella, "Negative corona discharge in mixtures of CO_2 and N_2: modeling and experiments," in *International Symposium on Plasma Chemistry 20*, 2011, p. 394.

[64]   M. S. Bak, S. Im, and M. Cappelli, "Nanosecond-pulsed discharge plasma splitting of carbon dioxide," *Plasma Science, IEEE Transactions on,* vol. 43, pp. 1002-1007, 2015.

[65]   Y. Wen and X. Jiang, "Decomposition of CO_2 Using Pulsed Corona Discharges Combined with Catalyst," *Plasma Chemistry and Plasma Processing,* vol. 21, pp. 665-678, 2001/12/01 2001.

[66]   C. J. .Liu, L. Lobbann, and R. Mallinson, "Modification of nay zeolite in a corona discharge and its application for the reduction of carbon dioxide," in *Greenhouse gas control technologies*, ed, 1999, pp. 1153 - 1166.

[67]   P. Sabine, V. Bert, T. Xin, B. Christophe De, M. Tom, P. Dragana, "Conversion of carbon dioxide to value-added chemicals in atmospheric pressure dielectric barrier discharges," *Plasma Sources Science and Technology,* vol. 19, p. 034015, 2010.

[68]   R. Snoeckx, Y. X. Zeng, X. Tu, and A. Bogaerts, "Plasma-based dry reforming: improving the conversion and energy efficiency in a dielectric barrier discharge," *RSC Advances,* vol. 5, pp. 29799-29808, 2015.

[69]   C.-J. Liang, "In-situ Impedance Spectroscopy Studies of the Plasma Electrolytic Oxidation Coating Process," PhD PhD, Materials Science and Enginerring University of Sheffield,

http://etheses.whiterose.ac.uk/4519/1/Chen-Jui Liang Thesis - In-situ Impedance Spectroscopy Studies of the Plasma Electrolytic Oxidation Coating Process.pdf, 2013.

[70] R. Li, Y. Yamaguchi, S. Yin, Q. Tang, and T. Sato, "Influence of dielectric barrier materials to the behavior of dielectric barrier discharge plasma for CO_2 decomposition," *Solid State Ionics,* vol. 172, pp. 235-238, 8/31/ 2004.

[71] R. Li, Q. Tang, S. Yin, and T. Sato, "Plasma catalysis for CO_2 decomposition by using different dielectric materials," *Fuel Processing Technology,* vol. 87, pp. 617-622, 7// 2006.

[72] M. Danhua, Z. Xinbo, H. Ya-Ling, D. Y. Joseph, and T. Xin, "Plasma-assisted conversion of CO_2 in a dielectric barrier discharge reactor: understanding the effect of packing materials," *Plasma Sources Science and Technology,* vol. 24, p. 015011, 2015.

[73] Q. Yu, M. Kong, T. Liu, J. Fei, and X. Zheng, "Characteristics of the Decomposition of CO_2 in a Dielectric Packed-Bed Plasma Reactor," *Plasma Chemistry and Plasma Processing,* vol. 32, pp. 153-163, 2012/02/01 2012.

[74] S. Mahammadunnisa, E. L. Reddy, D. Ray, C. Subrahmanyam, and J. C. Whitehead, "CO_2 reduction to syngas and carbon nanofibres by plasma-assisted in situ decomposition of water," *International Journal of Greenhouse Gas Control,* vol. 16, pp. 361-363, 8// 2013.

[75] K. Jogan, A. Mizuno, T. Yamamoto, J-S. Chang,"The effect of residence time on the CO_2 reduction from combustion flue gases by an AC ferroelectric packed bed reactor," *Industry Applications, IEEE Transactions on,* vol. 29, pp. 876-881, 1993.

[76] S. Futamura and H. Kabashima, "Synthesis Gas Production from CO_2 and H_2O with Nonthermal Plasma," in *Studies in Surface Science and Catalysis.* vol. Volume 153, J.-S. C. Sang-Eon Park and L. Kyu-Wan, Eds., ed: Elsevier, 2004, pp. 119-124.

[77] X. Duan, Z. Hu, Y. Li, and B. Wang, "Effect of dielectric packing materials on the decomposition of carbon dioxide using DBD microplasma reactor," *AIChE Journal,* vol. 61, pp. 898-903, 2015.

[78] L. G. Devi and G. Krishnamurthy, "TiO_2- and $BaTiO_3$-Assisted Photocatalytic Degradation of Selected Chloroorganic Compounds in Aqueous Medium: Correlation of Reactivity/Orientation Effects of Substituent Groups of the Pollutant Molecule on the Degradation Rate," *The Journal of Physical Chemistry A,* vol. 115, pp. 460-469, 2011/02/03 2011.

[79] M. Cabrejas Manchado, J. M. Guil, A. Perez Masia, A. Ruiz Paniego, and J. M. Trejo Menayo, "Adsorption of H_2, O_2, CO, and CO_2 on a .gamma.-Alumina: Volumetric and Calorimetric Studies," *Langmuir,* vol. 10, pp. 685-691, 1994/03/01 1994.

[80] O. Dewaele and G. F. Froment, "TAP study of the sorption of CO and CO_2 on γ Al_2O_3," *Applied Catalysis A: General,* vol. 185, pp. 203-210, 9/20/ 1999.

[81] U. Roland, F. Holzer, A. Pöppl, and F. D. Kopinke, "Combination of non-thermal plasma and heterogeneous catalysis for oxidation of volatile organic compounds: Part 3. Electron paramagnetic resonance (EPR) studies of plasma-treated porous alumina," *Applied Catalysis B: Environmental,* vol. 58, pp. 227-234, 6/28/ 2005.

[82] U. Roland, F. Holzer, and F. D. Kopinke, "Combination of non-thermal plasma and heterogeneous catalysis for oxidation of volatile organic compounds: Part 2. Ozone decomposition and deactivation of γ -Al_2O_3," *Applied Catalysis B: Environmental,* vol. 58, pp. 217-226, 6/28/ 2005.

[83] C. E. Stere, W. Adress, R. Burch, S. Chansai, A. Goguet, W. G. Graham*,* "Probing a Non-Thermal Plasma Activated Heterogeneously Catalyzed Reaction Using in Situ DRIFTS-MS," *ACS Catalysis,* vol. 5, pp. 956-964, 2015/02/06 2015.

[84]   K. Hensel, S. Katsura, and A. Mizuno, "DC microdischarges inside porous ceramics," *Plasma Science, IEEE Transactions on,* vol. 33, pp. 574-575, 2005.

[85]   K. Hensel, "Microdischarges in ceramic foams and honeycombs," *The European Physical Journal D,* vol. 54, pp. 141-148, 2009/08/01 2009.

[86]   J. S. Chang, A. Chakrabarti, K. Urashima, and M. Arai, "The effects of barium titanate pellet shapes on the gas discharge characteristics of ferroelectric packed bed reactors," in *Electrical Insulation and Dielectric Phenomena, 1998. Annual Report. Conference on*, 1998, pp. 485-488 vol. 2.

[87]   K. Takaki, S. Takahashi, S. Mukaigawa, T. Fujiwara, K. Sugawara, and T. Sugawara, "Influence of Pellet Shape of Ferro-Electric Packed-Bed Plasma Reactor on Ozone Generation and NO Removal," *International Journal of Plasma Environmental Science & Technolog,* vol. 3, 2009.

[88]   E. L. Reddy, V. M. Biju, and C. Subrahmanyam, "Hydrogen production from hydrogen sulfide in a packed-bed DBD reactor," *International Journal of Hydrogen Energy,* vol. 37, pp. 8217-8222, 5// 2012.

[89]   I. Michieslsen, K. V. Laer, Y. Uytdenhouwen, V. Meynen, and A. Bogaerts, "Packing effect of SiO_2, ZrO_2 and Al_2O_3 beads on CO_2 conversion in a packed-bed DBD reactor," in *22nd Interational Symposium on Plasma Chemistry*, Antwerp, Belgium, 2015.

[90]   R. Valdivia-Barrientos, J. Pacheco-Sotelo, M. Pacheco-Pacheco, J. S. Benítez-Read, and R. López-Callejas, "Analysis and electrical modelling of a cylindrical DBD configuration at different operating frequencies," *Plasma Sources Science and Technology,* vol. 15, p. 237, 2006.

[91]   H. E. Wagner, R. Brandenburg, K. V. Kozlov, A. Sonnenfeld, P. Michel, and J. F. Behnke, "The barrier discharge: basic properties and applications to surface treatment," *Vacuum,* vol. 71, pp. 417-436, 5/19/ 2003.

[92]   T. C. Manley, "The Electric Characteristics of the Ozonator Discharge," *Transaction of the Electrochemical Society,* pp. 83 - 96, 1943.

[93]   F. Zoran and J. C. John, "Microdischarge behaviour in the silent discharge of nitrogen - oxygen and water - air mixtures," *Journal of Physics D: Applied Physics,* vol. 30, p. 817, 1997.

[94]   A. V. Pipa, J. Koskulics, R. Brandenburg, and T. Hoder, "The simplest equivalent circuit of a pulsed dielectric barrier discharge and the determination of the gas gap charge transfer," *Review of Scientific Instruments,* vol. 83 p. 115112, 2012.

[95]   F. J. J. Peeters and M. C. M. v. d. Sanden, "The influence of partial surface discharging on the electrical characterization of DBDs," *Plasma Sources Science and Technology,* vol. 24, p. 015016, 2015.

[96]   E. Hughes, *Electrical and Electronic Technology*, 9th ed.: Pearson Education, 2005.

[97]   J. Kriegseis, B. Möller, S. Grundmann, and C. Tropea, "Capacitance and power consumption quantification of dielectric barrier discharge (DBD) plasma actuators," *Journal of Electrostatics,* vol. 69, pp. 302-312, 8// 2011.

[98]   D. E. Ashpis, M. C. Laun, and E. L. Griebeler, "Progress Toward Accurate Measurements of Power Consumptions of DBD Plasma Actuators," http://www.sti.nasa.gov NASA/TM— 2012-217449, 2012.

[99]   K. P. Francke, R. Rudolph, and H. Miessner, "Design and Operating Characteristics of a Simple and Reliable DBD Reactor for Use with Atmospheric Air," *Plasma Chemistry and Plasma Processing,* vol. 23, pp. 47-57, 2003/03/01 2003.

[100] P. Reichen, A. Sonnenfeld, and R. Ph Rudolf von, "Discharge expansion in barrier discharge arrangements at low applied voltages," *Plasma Sources Science and Technology,* vol. 20, p. 055015, 2011.

[101] S. Futamura, A. Zhang, and T. Yamamoto, "Behavior of N_2 and nitrogen oxides in nonthermal plasma chemical processing of hazardous air pollutants," *Industry Applications, IEEE Transactions on,* vol. 36, pp. 1507-1514, 2000.

[102] A. Savitzky and M. J. E. Golay, "Smoothing and Differentiation of Data by Simplified Least Squares Procedures," *Analytical Chemistry,* vol. 36, pp. 1627-1639, 1964/07/01 1964.

[103] F. Brehmer, S. Welzel, M. C. M. v. d. Sanden, and R. Engeln, "CO and byproduct formation during CO2 reduction in dielectric barrier discharges," *Journal of Applied Physics,* vol. 116, p. 123303, 2014.

[104] B. Eliasson, M. Hirth, and U. Kogelschatz, "Ozone synthesis from oxygen in dielectric barrier discharges," *Journal of Physics D: Applied Physics,* vol. 20, p. 1421, 1987.

[105] Dow Chemaical Company. (1964, 12/8/2014). *Carbon Dioxide - Infrared Spectrum.*

[106] Dow Chemical Company(1964, 12/8/2014). *Carbon Monoxide - Infrared Spectrum.*

[107] Dow Chemical Company (1969, 12/8/2014). *Ozone - Infrared Spectrum.*

[108] Dow Chemical Company. (1969, 12/8/2014). *Water (liquid) - Infrared Spectrum.*

[109] Dow Chemical Company (2009, 12/8/2014). *Water (liquid) - Infrared Spectrum.*

[110] H. Bader and J. Hoigné, "Determination of ozone in water by the indigo method," *Water Research,* vol. 15, pp. 449-456, // 1981.

[111] "Hiden QGA - Quantitative Gas Analysis system," H. Analytical, Ed., ed. http://www.hidenanalytical.com/en/docman/presentations/807-qga.

[112] M. G. Harwood, P. Popper, and D. Rushman, "Curie Point of Barium Titanate," *Nature,* vol. 160, pp. 58 - 59, 1947.

[113] H. S. Uhm, S. J. Jung, and S. K. Hyoung, "Influence of Gas Temperature on Electrical Breakdown in Cylindrical Electrodes," *Journal of the Korean Physical Society,* vol. 42, pp. 989-993, 2003.

[114] X. Tu, B. Verheyde, S. Corthals, S. Paulussen, and B. F. Sels, "Effect of packing solid material on characteristics of helium dielectric barrier discharge at atmospheric pressure," *Physics of Plasma,* vol. 18, p. 080702, 2011.

[115] K. Woo Seok, P. Jin Myung, K. Yongho, and H. Sang Hee, "Numerical study on influences of barrier arrangements on dielectric barrier discharge characteristics," *Plasma Science, IEEE Transactions on,* vol. 31, pp. 504-510, 2003.

[116] K. Schmidt-Szalowski, S. Jodzis, K. Krawczyk, M. Mlotek, and A. Gorska, "Non-equilibrium plasma processes in heterogeneous systems at atmospheric pressure," *Current Topics in Catalysis,* pp. 39 - 68, 2006.

[117] T. Xin, H. J. Gallon, and J. C. Whitehead, "Transition Behavior of Packed-Bed Dielectric Barrier Discharge in Argon," *Plasma Science, IEEE Transactions on,* vol. 39, pp. 2172-2173, 2011.

[118] S. Mori, N. Matsuura, L. L. Tun, M. Suzuki, "Synergistic Decomposition of CO_2 by Hybridization of a Dielectric Barrier Discharge Reactor and a Solid Oxide Electrolyser Cell," *KAGAKU KOGAKU RONBUNSHU,* vol. 37, pp. 114-119, 2011.

[119] S. Mori, N. Matsuura, L. L. Tun, and M. Suzuki, "Synthesis of nanocarbon materials by PECVD: challenges to direct synthesis via CO_2 reduction using plasma-SOEC hybrid reactor," in *International Symposium on Plasma Chemistry*, Antwerp, Belgium, 2015.

[120]   A. Gutsol, A. Rabinovich, and A. Fridman, "Combustion-assisted plasma in fuel conversion," *Journal of Physics D: Applied Physics,* vol. 44, p. 274001, 2011.

[121]   M. S. Lee, I. G. Koo, J. H. Kim, and W. M. Lee, "Electrochemical hydrogen pumping from high temperature plasma-chemical reactor involving H_2O/SO_2 gas mixture," *International Journal of Hydrogen Energy,* vol. 34, pp. 40-47, 1// 2009.